R-826

FINAL REPORT
VOLUME I

EVALUATION OF SELECTED STRAPDOWN INERTIAL INSTRUMENTS AND PULSE TORQUE LOOPS

by

J.S. Sinkiewicz, J. Feldman, C.B. Lory

July 1974

(NASA-CR-120427) EVALUATION OF SELECTED STRAPDOWN INERTIAL INSTRUMENTS AND PULSE TORQUE LOOPS, VOLUME 1 Final Report (Draper (Charles Stark) Lab., Inc.) N74-32099
CSCL 17G G3/21 Unclas 47874

The Charles Stark Draper Laboratory, Inc.
Cambridge, Massachusetts 02139

R-826

FINAL REPORT
VOLUME I

EVALUATION OF SELECTED STRAPDOWN INERTIAL INSTRUMENTS AND PULSE TORQUE LOOPS

by

J.S. Sinkiewicz

J. Feldman

C.B. Lory

July 1974

THE CHARLES STARK DRAPER LABORATORY, INC.
CAMBRIDGE, MASSACHUSETTS
02139

Approved: N. Sears Date: 7-31-74

N. Sears

/

ACKNOWLEDGEMENTS

This report was prepared by the Charles Stark Draper Laboratory under Contract NAS12-2033 for the George C. Marshall Space Flight Center of the National Aeronautics and Space Administration.

The work reported under this program was originally sponsored by the NASA Electronics Research Center and has been continued by the George C. Marshall Space Flight Center. Mr. B.J. Doran and Mr. B.J. Gaines have with imagination and foresight, broadened the scope of the project to provide an effective balance between theory and testing. Appreciation is also extended to Mr. Clyde Jones, the contract Technical Monitor, for his support of the Experimental Studies of Body Mounted Gyroscope Design Techniques Program.

This phase of the final report is the combined effort of the following authors:

VOLUME I

CHAPTER 1	C.B. Lory
CHAPTER 2	J. Feldman
CHAPTER 3	J.S. Sinkiewicz
CHAPTER 4	J.S. Sinkiewicz J. Feldman
CHAPTER 5	J.S. Sinkiewicz
APPENDIX A	J. Feldman
APPENDIX B	C.B. Lory

Individuals responsible for the engineering of specific portions of the tasks are identified and their significant contributions acknowledged.

Jerold Gilmore, Division Leader, provided technical supervision and substantial inputs to the final report.

Eugene Salamin contributed significantly in the areas of analysis and test. He developed the analyses for the torquer nonlinearity (Section 4.3), the anisoelasticity effects (Section 2.4.5), Appendices A and B, and the on-line computer capability that processed the dynamic test data.

George Bukow contributed the analysis of an electromagnetic suspension and substantial editorial comments.

William Sartanowicz and William Trosky, gyroscope test technicians, deserve special commendation for their test support.

In the preparation of the Final Report, the contributions of both Stephen Helfant and Roscoe Cooper in the editing and preparation of the document for publication were invaluable.

The efforts of Aldo Bonaventura and Linda Willy in preparing the technical illustrations and of Carol Lynde in preparing the text input to the computer are also acknowledged and appreciated.

Recognition is directed to the staff of the CSDL Publications Department for their help in the composition and printing of this report.

R-826

FINAL REPORT
VOLUME I

STRAPDOWN EVALUATION OF SELECTED INERTIAL INSTRUMENTS AND PULSE TORQUE LOOPS

ABSTRACT

Design, operational and performance variations between ternary, binary and forced-binary pulse torque loops are presented. A fill-in binary loop which combines the constant power advantage of binary with the low sampling error of ternary is also discussed.

The effects of different output-axis supports on the performance of a single-degree-of-freedom, floated gyroscope under a strapdown environment are illustrated. Three types of output-axis supports are discussed: pivot-dithered jewel, ball bearing and electromagnetic.

A test evaluation on a Kearfott 2544 single-degree-of-freedom, strapdown gyroscope operating with a pulse torque loop, under constant rates and angular oscillatory inputs is described and the results presented.

Contributions of the gyroscope's torque generator and the torque-to-balance electronics on scale factor variation with rate are illustrated for a SDF 18 IRIG Mod-B strapdown gyroscope operating with various pulse rebalance loops. Also discussed are methods of reducing this scale factor variation with rate by adjusting the tuning network which shunts the torque coil.

A simplified analysis illustrating the principles of operation of the Teledyne two-degree-of-freedom, elastically-supported, tuned gyroscope and the results of a static and constant rate test evaluation of that instrument are presented.

by

J.S. Sinkiewicz
J. Feldman
C.B. Lory

July 1974

TABLE OF CONTENTS

TABLE OF CONTENTS (cont)

TABLE OF CONTENTS (cont)

TABLE OF CONTENTS (cont)

LIST OF ILLUSTRATIONS

LIST OF TABLES

PREFACE

This document is the final report submitted to satisfy the contractual requirements of NAS 12-2033 and to provide a complete description of the work accomplished under the contract from its inception in November, 1968 to completion of the work effort in November, 1973. A total of five years was devoted to the Experimental Studies of Body Mounted Gyroscope Design Techniques Program.

Initial Tasks (November 1968 to October 1971)

The original contract Work Statement defined six tasks, items 1 through 6, connected with the performance evaluation of a Honeywell GG334 gyroscope operating with a pulse-torque electronic test module. The design of this electronic module permitted operation in either a ternary or a binary mode and included an optional quantizer compensation feature. Evaluation called for single-axis testing to determine the effect of the quantizer loop compensation with steady state and transient inputs using the pulse-torque electronic test module and a customer furnished UAC forced limit cycle, pulse rebalance module (GFE). The UAC module was never provided so all testing was accomplished using the CSDL module. These tasks also included test plan development and dynamic testing in a single and two-axis oscillatory environment with the same combinations of loop electronics. The results of this work effort have been reported and widely distributed in CSDL Report E2618, dated October, 1971. The major results are summarized below.

Follow-on Tasks (October 1971 to June 1972)

Modification 6 to Contract NAS 12-2033 added applicable Tasks A through D. Task A, accomplished during this period, required the development and test confirmation of analytical models of the dynamic errors, with emphasis on an explanation for the lock-in phenomenum and the resulting effect of these dynamic errors on torque-to-balance applications. The results of this work effort have been reported and distributed in MIT/CSDL Report T-566, dated June 1973. The major results are summarized below.

Follow-on Tasks (June 1972 to November 1973)

The remaining tasks, B and C, from Contract Modification 6, and Tasks 1 through 3 from Modification 8 are covered in Volume I of this report. Task D was subsequently eliminated and replaced by Task 1, Modification 8. Tasks 4, 5 and 6 are covered in Volume II. A short description of the contents of each chapter in Volumes I and II follows.

VOLUME I

Chapter 1

Pulse-Torque Loop Comparisons - Task 3

This chapter covers the analysis, test results and evaluation of the available pulse torque-to-balance loops, i.e. ternary, binary, forced binary and fill-in binary.

Chapter 2

Output-Axis Suspensions for Strapdown Gyroscopes - Task 2

This chapter discusses and compares the performance, integrity and environmental response of three different gyro output-axis support designs: ball bearing, pivot-dithered jewel, and electromagnetic.

Chapter 3

Static and Dynamic Testing of the Kearfott 2544

Single-Degree-of-Freedom Strapdown Gyroscope - Task 2

This chapter reports the results of a test evaluation performed on the Kearfott Model 2544 gyroscope operating in a strapdown configuration and exposed to static and dynamic environments.

Chapter 4

Testing of the Magnetically-Suspended C.S. Draper

Laboratory 18 IRIG Mod-B - Tasks B and C

This chapter describes the results of a test evaluation performed on the 18 IRIG Mod-B and defines the torquer non-linearities and the optimization of torquer tuning techniques for that instrument.

Chapter 5

Test Evaluation of the Teledyne

Two-Degree-of-Freedom Strapdown Gyroscope - Task 1

This chapter reports the results of static and constant rate tests performed on the Teledyne SDG instrument. Planned single and two-axis oscillatory testing were not attempted because of inadequate performance of the GFE analog loop and the A/D readout system.

VOLUME II

Standardized Strapdown, Inertial Component Modularity Study - Tasks 4, 5, and 6.

This volume describes the concept of a standardized, modularized, strapdown system design, its requirements and trade-off analyses. It discusses design principles and techniques for the mechanical layout, component selection, processing and thermal control to achieve the required performance ranges. Projected costs, weights and volumes are presented.

SUMMARY

An analysis and test program was performed during the past five years by CSDL to better define the performance of inertial components operating with digital and analog torque-to-balance loops in a dynamic environment. The gyroscopes tested included:

Honeywell	GG334
Kearfott	2544
CSDL	18 IRIG Mod-B
Teledyne	Two-Degree-of-Freedom, SDG-2

Tests were conducted with ternary, binary, forced binary, and analog torque-to-balance loops.

The instrument and torque-to-balance loop tests were performed under static, constant rate and single-axis oscillatory inputs using modified gyro laboratory test equipment with an on-line computer for data reduction and test control. The two-axis oscillatory tests were performed with an angular oscillator that was constructed from an available Apollo inertial measurement unit. Analog and digital simulations of the various instruments, torque-to-balance loops and dynamic environments were utilized in support of the instrument test programs.

The significant program achievements are summarized for the four previously issued reports, E-2618, T-526, T-541 and T-566 and for each chapter of Volumes I and II as follows.

A. CSDL Report E-2618, Work Statement Items 1-6

The results obtained and the conclusions drawn from this investigation are summarized as follows:

1. Using the MIT ternary torque-to-balance loop, the Honeywell GG334A (S/N C5) exhibited the following performance:
   a) SF stability - at 3600 Hz interrogation frequency for 50 hours - 10 ppm
   b) SF variation with rate - 1/8 to 1 rad/s at interrogation frequencies of 3600, 7200 and 14,400 Hz - 125 ppm
   c) SF variation with rate - with the torquer tuned for minimum variation with rate at a 3600 Hz interrogation frequency - 60 ppm

d) Drift Stability - 1 month testing

   1. Bias - 0.07 deg/h
   2. ADSRA - 0.01 deg/h/g
   3. ADIA - 0.16 deg/h/g

2. Design and assembly practices affecting the performance of PM torquers are described and analyzed. SG-to-TG alignment and torque coil material choice represent the most critical factors.

3. Thermal affects are also a source of torquer scale factor variation with rate.

4. A torquer tuned to be resistive to the current switch is independent of interrogation frequencies from 3.6 to 14.4 kHz.

5. Tuning can be accomplished to minimize scale factor variation with rate at a fixed interrogation frequency. This however degrades the SF. performance at other interrogation frequencies.

6. Compensation for command torque lags reduced sampling errors and improved resolution, confirming the analytical studies.

7. Single-axis angular oscillatory testing noted a discrepancy with the presently accepted theoretical model which considers the wheel structural compliance.

8. Two-axis, open loop angular oscillatory tests on the Honeywell GG334 gyro confirmed the theoretical analysis presented in T-526.

9. Two-axis angular oscillatory tests were performed on the Honeywell GG334 gyro operating with a ternary torque-to-balance loop. Analysis was developed to explain much of the closed loop angular oscillatory data.

10. Lock-in, a new gyro-torque loop dynamic error source was identified. This phenomena occurs under two-axis angular oscillatory inputs to a gyroscope. For some amplitude and phases of inputs, the gyroscope can not detect low level input-axis rates.

B. CSDL Report T-526 Work Statement - Item 5

This report modeled the performance of a single-degree-of-freedom gyroscope under single-axis and multiaxis angular oscillatory inputs for open loop and analog torque-to-balance loop operation of the gyro. Dynamic error sources such as output-axis coupling, anisoinertia, coning and cross coupled rectification are analyzed in detail. Normalized plots using the parameters of the Honeywell GG334 gyro were presented for each of the dynamic error sources.

C. CSDL Report T-541 Statement of Work - Item 5

This report presented an evaluation of the two-axis angular vibrator constructed by CSDL for the multiaxis angular oscillatory testing of the Honeywell GG334 gyroscope. The report describes the test fixture's mechanical configuration, dynamic response, cross coupling errors and performance.

D. CSDL Report T-566 - Work Statement Task A

The results obtained, and the conclusions drawn from this investigation are summarized as follows.

When a single-degree-of-freedom gyroscope experiences angular oscillatory inputs about two axes, an erroneous equivalent input axis rate is measured. These apparent input rates obtained for a gyroscope operating open loop under sinusoidal oscillations have been extensively analyzed, i.e. CSDL Report T-526 and test verified as shown in CSDL Report E-2618. However, when the instrument is operating in a pulse rebalance loop under an angular oscillatory input, nonlinear equations of motion result, and closed form analytical solutions are not possible. To support the two-axis angular oscillatory testing performed on the Honeywell GG334 gyro operating with a ternary torque-to-balance loop as reported in E-2618, digital simulations of a single-degree-of-freedom gyro were created. These simulations exercised various types of angular inputs and torque-to-balance loop mechanizations. The simulation results confirmed the previous multiaxis angular oscillatory test data, or in areas of disagreement, retesting confirmed the digitally simulated analysis. This digital simulation explained the lock-in phenomena and showed that dynamic error sources can be effectively analyzed and compensated in system applications.

E. Volume I, Chapter 1 - Task 3

The content and conclusions contained in Chapter 1 are summarized as follows.

1. A tutorial analytic description of the operation of the general form of the integrated feedback loop as used in a strapdown gyro application is presented. This includes each of the following component elements.
   a) Constant current source
   b) Current switches
   c) Electromagnetic integrator (gyro)
   d) Analog signal processor
   e) Comparator(s) and voltage source(s)
   f) Digital logic and clock.

2. A description of each of the four types of integrated feedback loops (delta modulators) studied, i.e. binary, ternary, forced binary, and fill-in binary is presented. Operating characteristics, performance and test data are shown for each type. Comparison of these parameters shows that the ternary loop has the lowest sampling error, that the difference between positive and negative SF in binary and forced-binary loops results in a bias drift, that with nearly constant power dissipation in the torquer, the binary loops show the lowest variation in SF with input rate, and that the fill-in binary combines the nearly constant power operation of binary with the low sampling error of the ternary loops.

3. A description of pulse torque loop - gyroscope testing procedures is provided. The specific tests consist of the following.
   1. SF deviation
      a) Variation with rate
      b) Instability
   2. Drift instability
   3. Moding pattern statistics.

F. Volume I, Chapter 2 - Task 2

The content and conclusions contained in Chapter 2 are summarized as follows.

1. A description is provided of three different gyro output-axis suspension designs as exemplified by three specific instruments as follows.
   a) Pivot-dithered jewel - Honeywell GG334
   b) Ball bearing - Kearfott 2544
   c) Electromagnetic - CSDL 18 IRIG Mod-B.

Contributions to gyro drift and axis misalignments are analyzed for each suspension design.

2. Testing was performed to evaluate SF stability, variation with rate, IA alignment, and static and dynamic drift stability. The evaluation determined that the magnetic suspension provided the best SF stability, IA alignment and short-term drift stability. The results obtained were the following:

	Stability		
	SF (ppm)	IA Alignment ($\widehat{sec}$)	Short Term Drift (deg/h)
Magnetic	3	0.5	< 0.0015
Pivot-Dithered Jewel	10	8	< 0.003
Ball Bearing	50-200	7	< 0.015

G. Volume I, Chapter 3 - Task 2

The content and conclusions contained in Chapter 3 are summarized as follows.

The chapter includes a description of the Kearfott Model 2544 gyroscope and the test facilities employed in the test program. A series of static and constant rate input tests were performed to establish instrument integrity and a performance baseline. Results show a bias drift stability of 0.015 deg/h and repeatability in the bias coefficient with cooldowns and wheel starts and stops of 0.1 - 0.2 deg/h. The stability of ADIA and ADSRA was 0.015 and 0.09 deg/h/g, respectively for a continuous 55-hr. test. The repeatability in these coefficients was 0.16 and 0.19 deg/h/g, respectively. A drift uncertainty also resulted from a change in torquer input power. The SG-to-TG misalignment of approximately 10 mrad resulted in a relatively large ac torquer sensitivity of -.003 $deg/h/mA^2$. SF performance with constant rate input revealed a sensitivity to input power and the SF magnitude changed randomly between and during tests regardless of the loop employed.

Performance measured under an angular oscillatory environment with a ternary torque-to-balance loop showed that the indicated drift rate measurement is dependent to a large extent on the accurate extraction of the positive and negative scale factor difference. This difference is a function of the instrument and/or the pulse rebalance loop; IA and OA test results agree with the theoretical analysis to within the instrument's drift uncertainty; the IA-SA test results showed the same agreement with theoretical predictions and also demonstrated the effects of anisoinertia and cross coupling on the drift measurement.

H. Volume I, Chapter 4 - Tasks B and C

The content and conclusions contained in Chapter 4 are summarized as follows.

A description of the CSDL 18 IRIG Mod-B gyroscope is provided followed by a discussion of the torque generator and electronics loop contribution to scale factor variations with input rates. A third section discusses methods and a criteria for torquer tuning and the effects of these tuning approaches on the scale factor variation with rate. Angular oscillatory tests performed on the CSDL 18 IRIG Mod-B are presented. It was found that error terms obtained in an angular oscillatory environment were commensurate with data obtained from the other single-degree-of-freedom, floated instruments tested.

I. Volume I, Chapter 5 - Task D

The content and conclusions contained in Chapter 5 are summarized as follows.

The Teledyne SDG-2, dry, two-degree-of-freedom, elastically-supported, tuned gyroscope is described and the basic theory of operation of this type of gyroscope and its rebalance loop electronics are presented. The chapter also provides a description of the test facility utilized in the test program. Test results showing performance data for all important static test parameters are included. Static drift performance met specifications. Torquer performance exhibited major sensitivities to input power in response to both transient and steady state input variations. The A/D readout system and the analog rebalance loop did not provide sufficient accuracy and/or stability to permit meaningful testing in a dynamic environment. Forty watts of torquer input power is required for restoring the rotor when input-axis rates of 100 deg/s are applied. This high power requirement would impose a severe burden on the electronic and possibly the thermal designer.

J. Volume II - Tasks 4, 5 and 6.

Volume II presents the results of a preliminary strapdown modularity study, including the significant gain achieved in reducing the cost of ownership through the ease of maintenance, increased reliability and producibility. It shows that three classes of modules (high, moderate and low performance) would be required to meet system requirements. A group of candidate inertial instruments representing the three performance classes is presented and the incompatibilities between candidates which must be addressed in a standardization program are discussed. The electronic design, hybrid packaging and thermal control considerations applicable to the three module performance classes are developed and a recommended hardware demonstration program is defined.

CHAPTER 1
PULSE-TORQUE LOOP COMPARISONS

1.1 INTRODUCTION

Under contracts from NASA/MSFC we evaluated various gyroscopic instruments operating in a strapdown environment. The evaluation determined: the effects of the output axis support (sumarized in Chapter 2), the interaction of the gyro and a dynamic environment (reported in E2618 and T566), and the effects of the torque generator characteristics on its dynamic performance (E2618 and Chapter 4). Tests for these effects were performed with a ternary torque-to-balance loop. Since the dynamic performance is significantly affected by the type of loop selected, test effort was directed to evaluate the performance of various pulse-torque loops. The results of the preliminary pulse-torque loop study are presented in this chapter.

The central role of digital computers in modern guidance systems requires that one obtain digital measurement of parameters. Thus the conversion of the primary transducers, the inertial instruments, to digital measuring equipment is an important instrumentation problem. Fifteen years or so ago, this was accomplished for floated, pendulous accelerometers as designed for the SINS and Apollo programs. Mounted on a gyro-stabilized, gimbal-mounted platform, the accelerometers were controlled in what is called a pulse-torque loop. This combination of instrument and electronics was intended to measure changes in velocity and communicate them by discrete pulses. The gyroscopes, in contrast, were used as analog indicators of angular displacement, providing error signals to the gimbal servos. Since then, the implementation of strapdown guidance systems has required digital measurements by the gyros as well. This chapter describes methods by which digital inertial measurements are obtained, concentrating on the rate-integrating, single-degree-of-freedom, floated gyro with a permanent-magnet torque generator and a high-resolution signal generator mounted on the output axis of the float.

In using a gyroscope, one forms a measurement system by applying torque about the output axis equal and opposite to the precession torque. Applying the opposing torque by calibrated means produces a measurement of the inertial stimulus. In a pulsed-torque loop, one obtains accurate knowledge of the opposing torque by precise control of electric charge through the torque generator. High precision is presently achieved by switching a stable direct current through the torque-generator coil for a fixed period of time to form a pulse. Having constant current for constant time, each pulse commanded results in a fixed increment of electric charge flowing

through the coil. Eventually, every pulse results in a constant increment in float angle away from the path it would otherwise follow. The job in designing or evaluating this type of system is to find the best way to apply pulses so that the measurement of angular displacement is made by counting them.

In the past, engineers have analyzed this system as a positional servomechanism. They knew that some function of float angle must be used to achieve equality of opposing torques, at least on the average. Their concept of the system is shown in Fig. 1.1-1. The form is that of a servo regulator which attempts to keep the float stationary in its case. There is a tendency to consider that the primary purpose of the system is to rebalance the float. By this line of reasoning, most have followed Chow[1*] in using describing functions to analyze the nonlinearity and sampling delays. We must suggest that they are misapplying Chow's pioneer work. He was analyzing the positional servomechanism of Fig. 1.1-2. Describing function analysis leads to sinusoidal analysis, analysis of the frequency response. The primary purpose of the digital torque-to-balance loop, however, is to perform an analog-to-digital conversion of the input, i.e. to represent to a computer a real-time history of the input. There the sampling and nonlinearity are intentional and desirable. Frequency response is not of much use to evaluate the functioning of the loop as a quantizer. Describing functions fail to give useful measures of error to aid in design improvement.

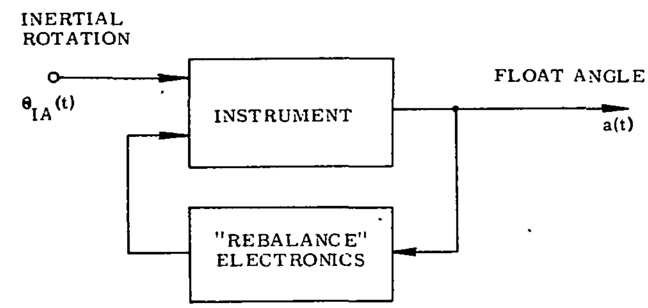

Fig. 1.1-1 Positional Servomechanism Concept

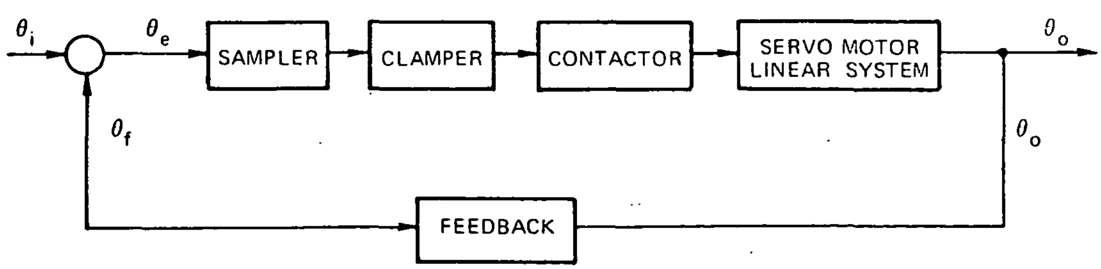

Fig. 1.1-2 Block Diagram of the Servomechanism
(Chow, Fig. II-1 p. 6)

*All references are at the end of the Chapter.

The instruments in our own view must perform two essential functions, regardless of the type of loop. The inertial element and signal generator form a transducer which changes mechanical motion into an electrical signal; and the torque generator, float, and signal generator are used additionally as the integrator in a feedback-type analog-to-digital converter. We conceive of these processes as shown in Fig. 1.1-3, with an inertial transducer and an analog-to-digital converter. The transducer input, $\theta_{IA}(t)$, called the command, is the independent physical rotation of the case we wish to measure. The transducer and any filter chosen to improve the signal-to-noise ratio converts this rotation to an electrical reference-input signal, $r(t)$, which is to be quantized. This signal is then converted to a pulse train, $c^*(t)$, called the controlled variable. In Section 1.2 we will describe the components that carry out the necessary functions, and we will show (Fig. 1.2-13) how they are arranged to correspond to Fig. 1.1-3. A complete measuring system (Fig. 1.1-4) also includes an indirectly controlled system; this is a counter which accumulates a count of $c^*(t)$ as $q(t)$, usually in a digital computer.

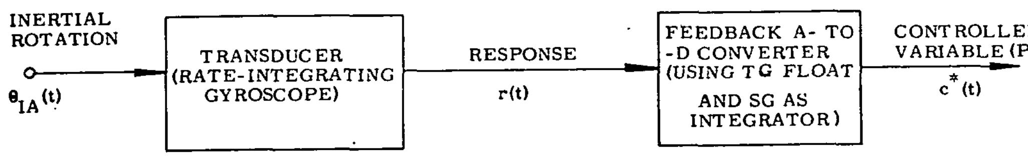

Fig. 1.1-3 Inertial Measurement System Concept

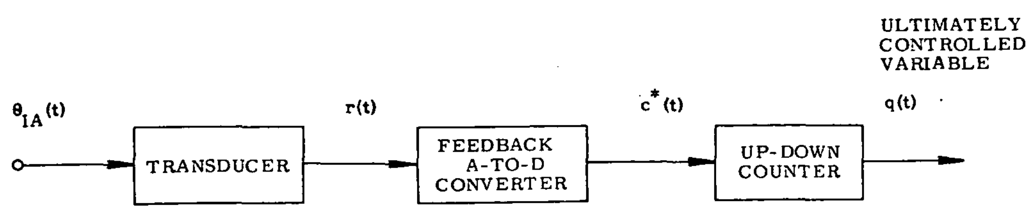

Fig. 1.1-4 Complete Measuring System

1.2 GENERAL PULSE-TORQUE LOOP MECHANIZATION

The general mechanization of the pulse-torque electronics (PTE) and a gyroscope to form a feedback analog-to-digital converter is shown in Fig. 1.2-1. It has the following major parts:

1. Constant-current source
2. Current switches
3. Electromechanical integrator (Gyro)
4. Analog signal processor
5. Comparator(s) and voltage source(s)
6. Digital logic and clock

We shall describe briefly how each functions.

1.2.1 Constant-Current Source

The constant-current source maintains direct current into the current switches and load in order that equal charges will flow during equal time intervals. As shown in Fig. 1.2-2, this is achieved by a feedback current regulator in which the precision dc, I_L, flows in series through 1.) a control transistor, 2.) the load (including the current switches), and 3.) a current-sampling resistor. The voltage difference between the sampling-resistor drop and a reference source is amplified greatly and fed back to drive the control transistor. In the reference source, a high-quality zener diode draws current from the 28-volt supply through a dropping resistor to produce a stable EMF of about six volts. (The voltage divider shown, which divides the precision voltage reference by about three, is a feature of the United Aircraft forced-binary PTE only.) To be useful in a high quality PTE, the current source must be constant within a few parts per million. This precision depends chiefly on the constancy of the reference diode, of the voltage divider, and of the sampling resistor.

1.2.2 Current Switches

The current switches consist of reversing switches and, for ternary, an on-off switch. Reversing of a load such as a dc motor is achieved as in Fig. 1.2-3 using a double-pole double-throw switch. Load current will flow from left to right or vice versa depending on the switch position. Similar control is obtained in the PTE using high-speed transistors. Two transistors are biased full on and two are cut off as shown in Fig. 1.2-4 giving current flow from left to right in the load.

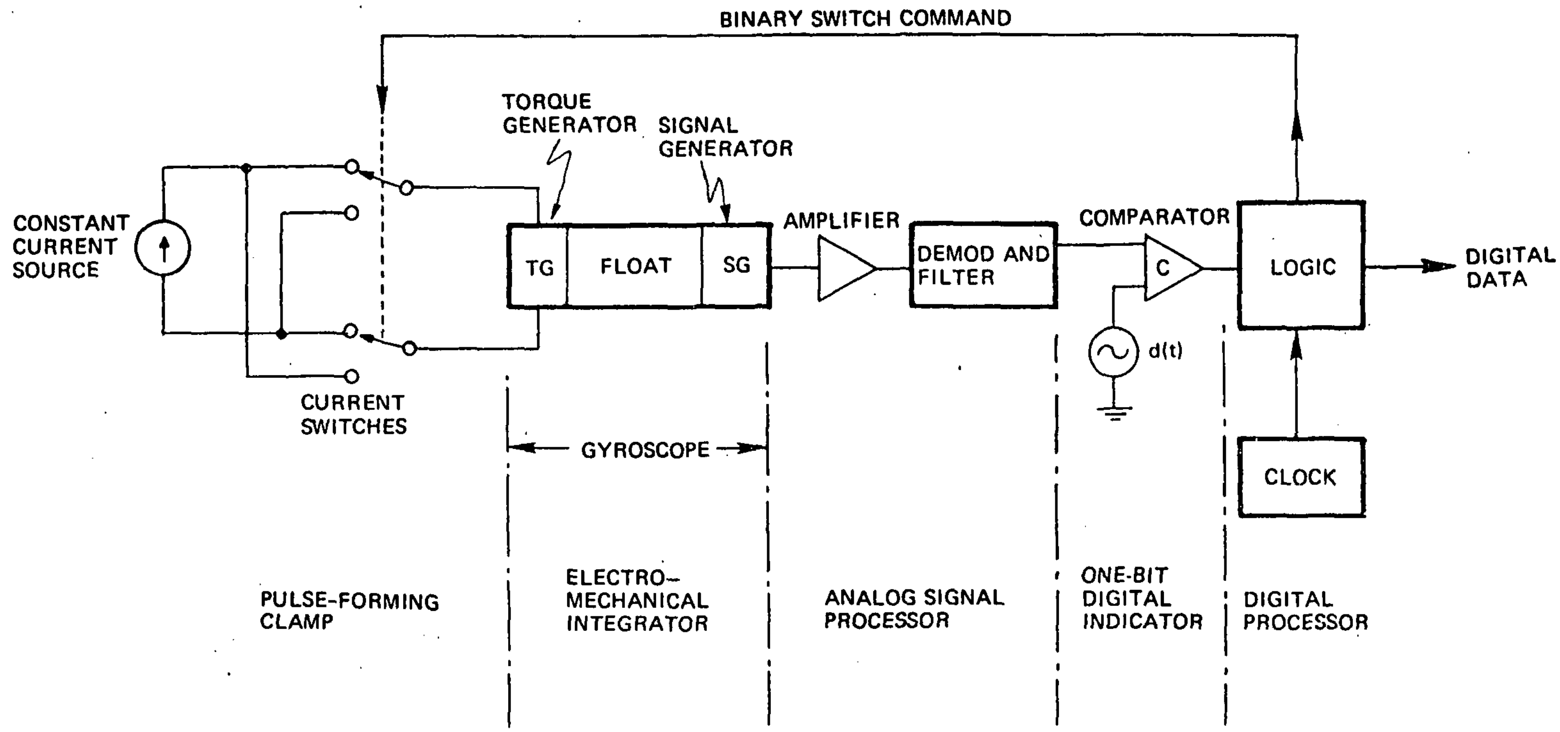

Fig. 1.2-1 General PTL Mechanization

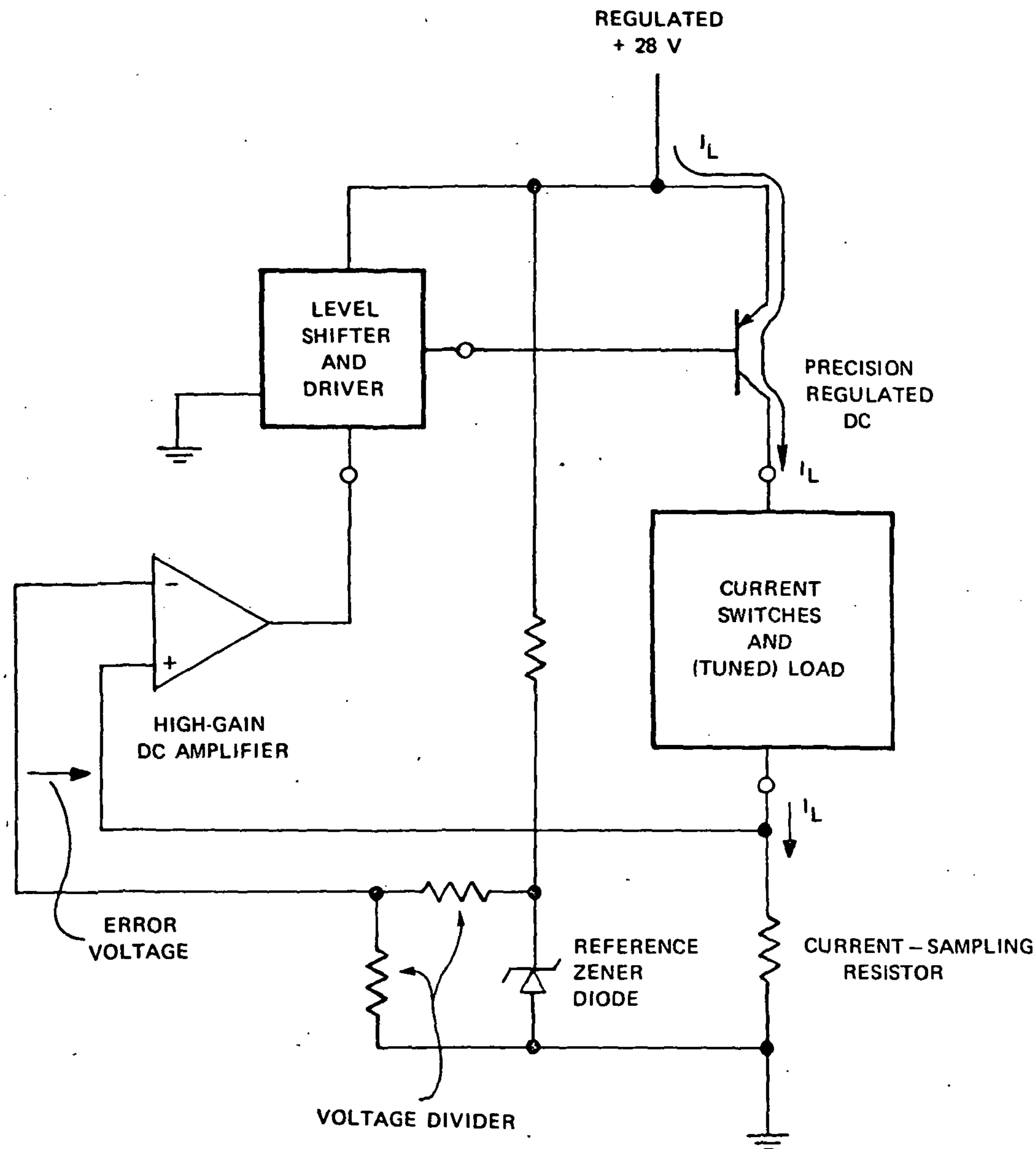

Fig. 1.2-2 Constant Current Source

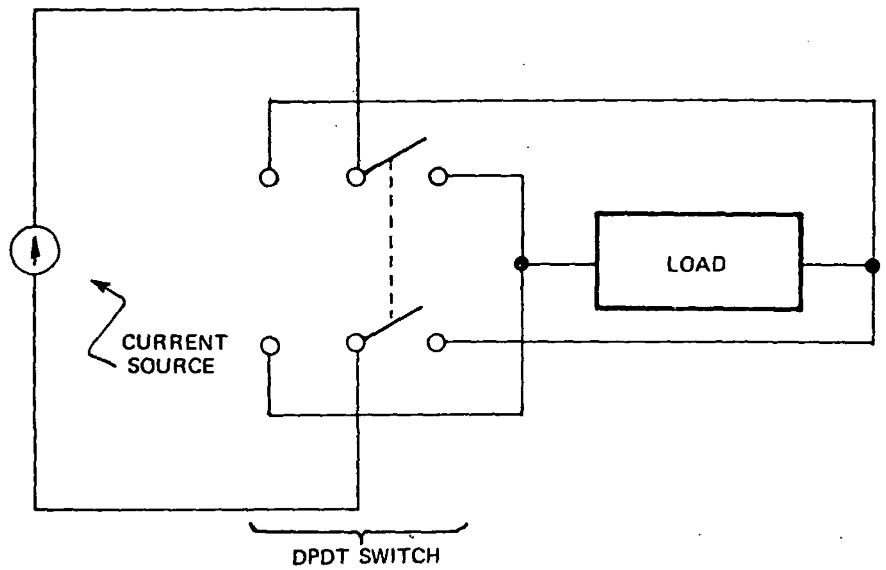

Fig. 1.2-3 Simple Reversing Switch

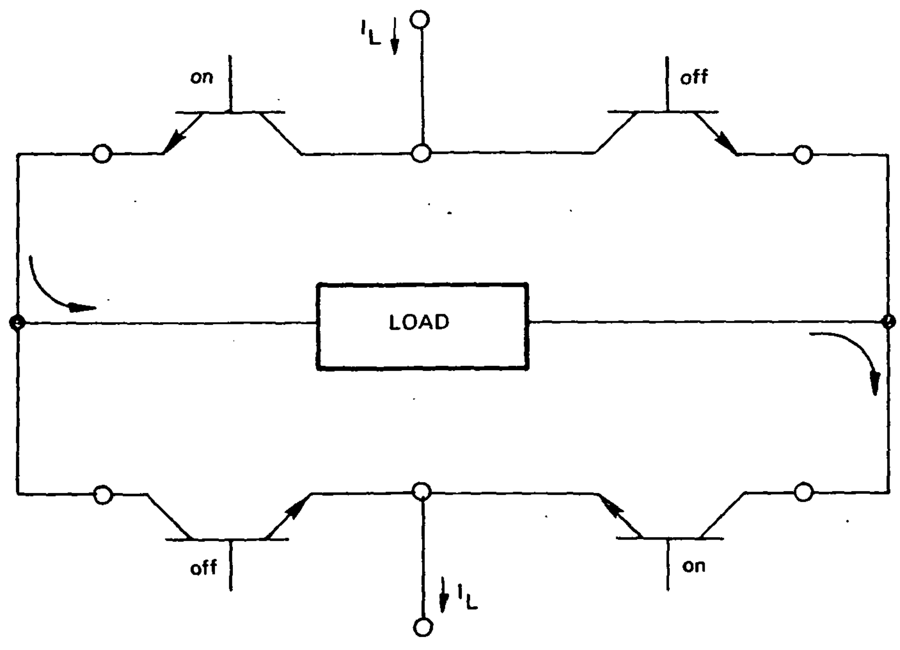

Fig. 1.2-4 Transistor Reversing Switch

Complementing the on and off states reverses the load current. For a ternary PTE, an additional pair of transistors is required to route the current either through the reversing switch and load or through a dummy load as in Fig. 1.2-5.

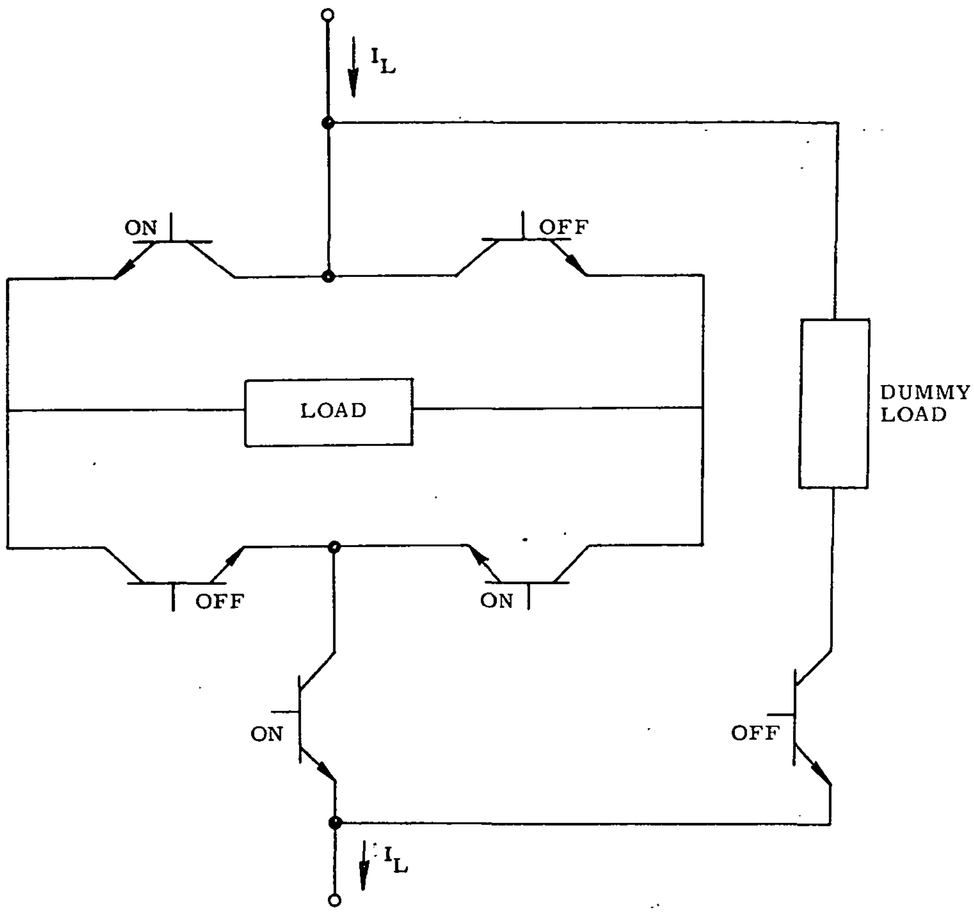

Fig. 1.2-5 Current Switches for Ternary Logic

The principal requirements for such switches are rapid switching and freedom from unwanted current paths. The rapid switching is required to get consistent timing and to keep the area under the current transients so small that the constant current source doesn't saturate. Unwanted current paths are: 1.) any which carry current through the load but not through the current-sampling resistor or 2.) any paths which pass through the resistor but not through the load. As an example of such current switches, Hamilton Standard's reversing switch is shown in Figs. 1.2-6 and 1.2-7. The switch is shown with one of its two driver transistors. Several unwanted current paths in the two complimentary positions are indicated. These are eliminated in a more complex switch by using floated dc supplies to drive the switching transistors.

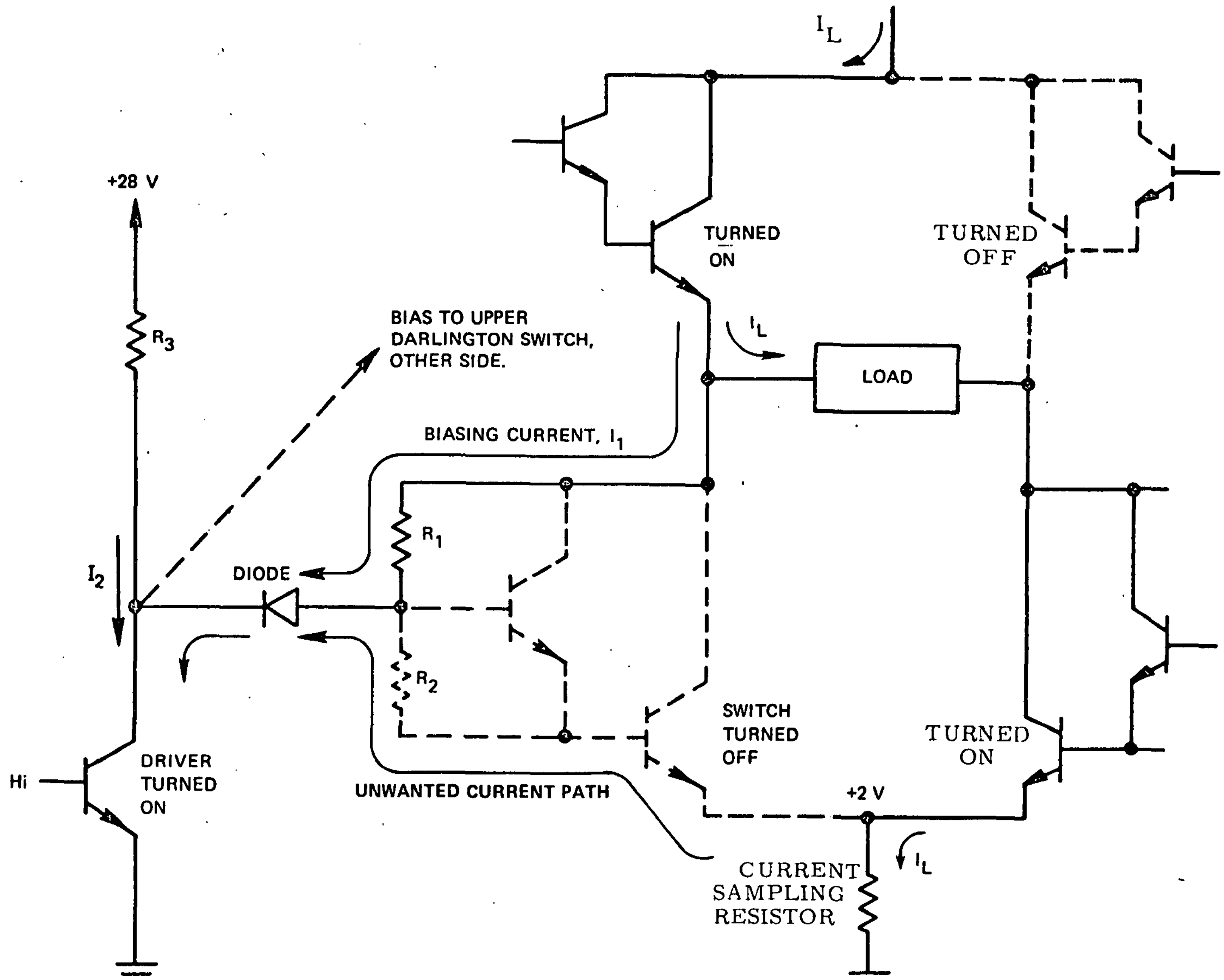

Fig. 1.2-6 United Aircraft Reversing Switch Showing Driver Turned On.

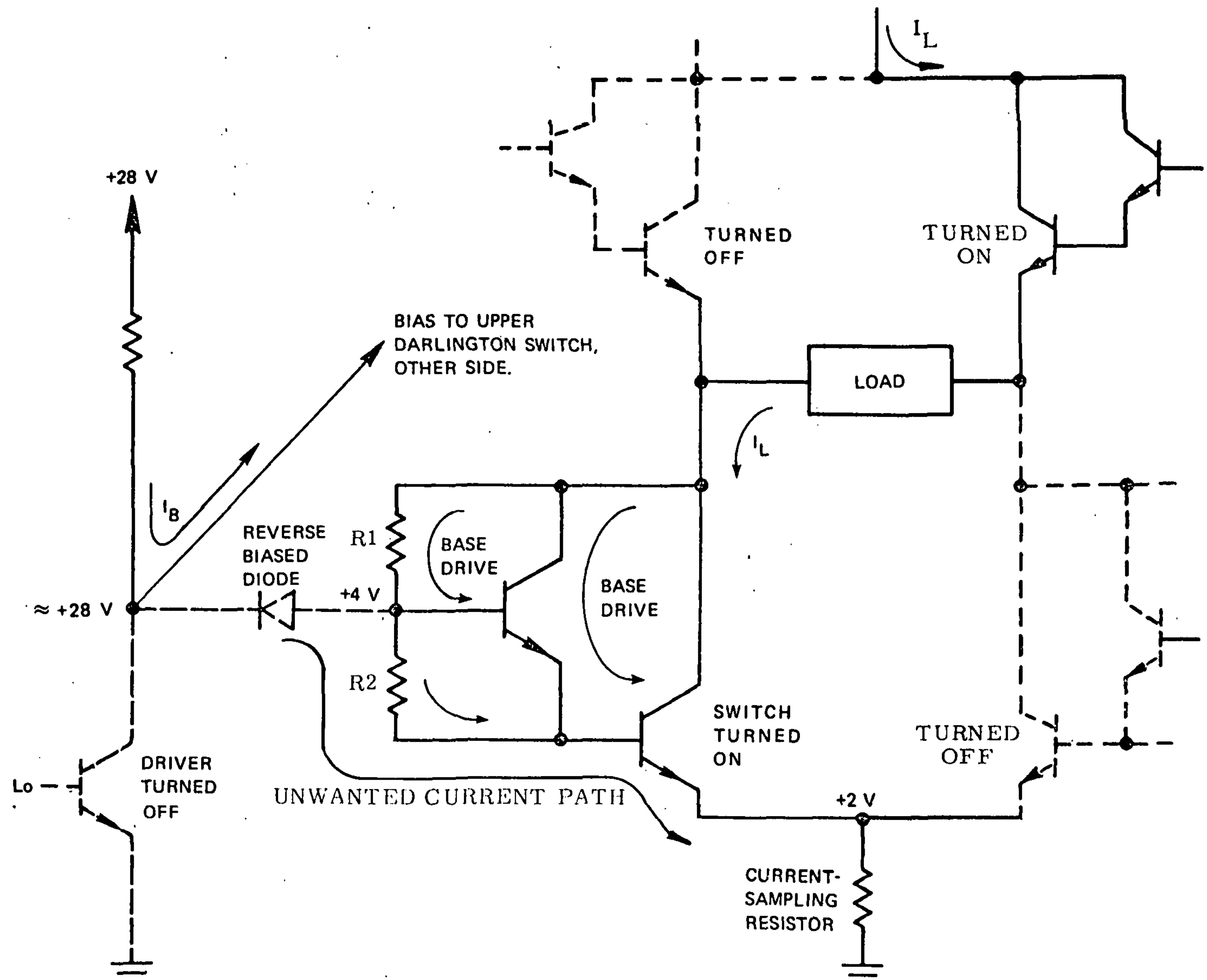

Fig. 1.2-7 United Aircraft Reversing Switch Showing Driver Turned Off.

1.2.3 Electromechanical Integrator (Gyro Float)

A single-degree-of-freedom, floated inertial instrument consists of a spinning wheel mounted within a torsional viscous integrator. As shown in Fig. 1.2-8, the integrator takes the form of a cylindric float mounted on pivots within a close-fitting case. The space between the case and the float is filled with a dense, viscous, homogenous fluid. The equation of motion for such a simple single-axis torsional system is

$$m(t) + f(t) - C\frac{d\,a(t)}{dt} - K\,a(t) = I\frac{d^2\,a(t)}{d\,t^2} \qquad (1.1)$$

where

- $m(t)$ - is the moment applied by the TG.
- $f(t)$ - is the sum of all parasitic torques such as bearing friction, unbalance, anisoinertia, etc.
- $a(t)$ - is the angular position of the float with respect to the case.
- C = the viscous drag coefficient.
- K = the spring rate of any elastic restraint.
- I = the cylinder's moment of inertia about its axis of symmetry.

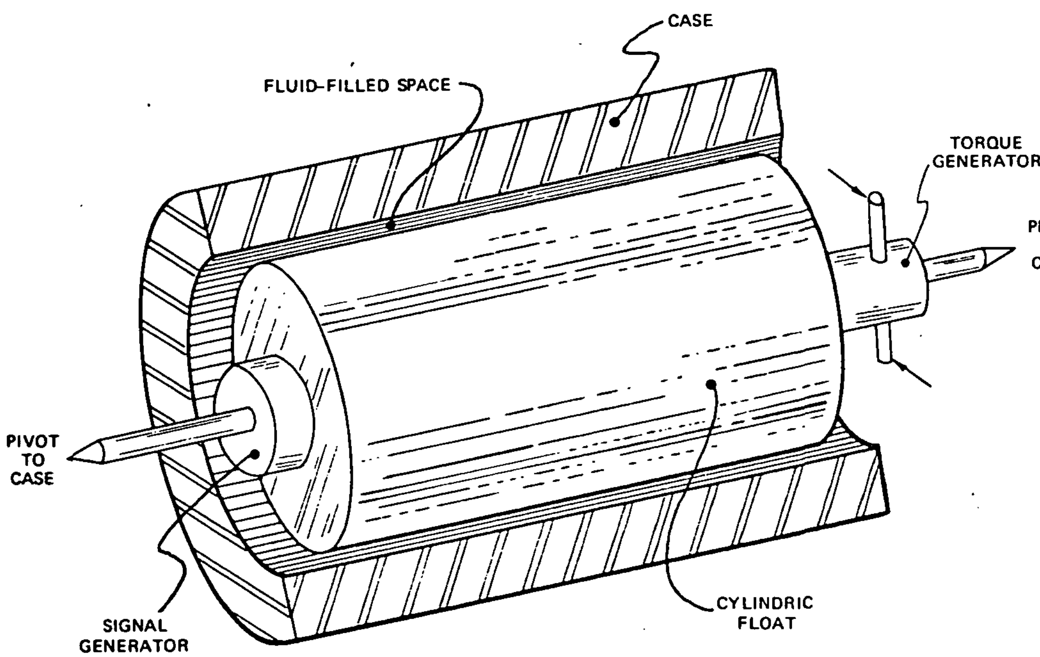

Fig. 1.2-8 Viscous Torsional Integrator

One of the major advantages of using the gyro float as the feedback integrator is that the parasitic torques and the elastic restraint can be made exceedingly small. Moreover, they are chargable to the gyroscope in its role as a transducer and thus can be entirely ignored here. The moment of inertia, however, causes a first-order lag in the float response to any torque. We will ignore it here since we previously showed that any such lags operating on the TG input can be compensated so as not to affect the quantizer.[2,3] Hence in the feedback path, we treat the float as an ideal integrator having the equation

$$m(t) = C \frac{d\,a(t)}{dt} \tag{1.2}$$

By integrating this equation, one obtains the integral of the applied torque.

$$a(t) = \frac{1}{C} \int_0^t m(\tau)\, d\tau + a(0) \tag{1.3}$$

When a spinning wheel is mounted within the cylindric float of the integrator just described, an inertial instrument is formed. An elementary gyroscope is drawn in Fig. 1.2-9. If the gimbal shown is replaced by the hollow cyclindric float of Fig. 1.2-8, as in Fig. 1.2-10, the cyclinder and its pivots then serve simultaneously as part of the integrator and as a gimbal for the gyro.

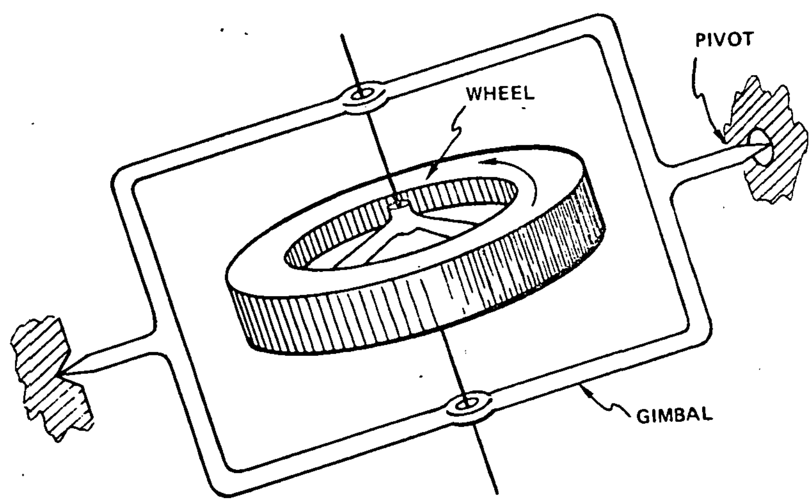

Fig. 1.2-9 Elementary Gyroscope

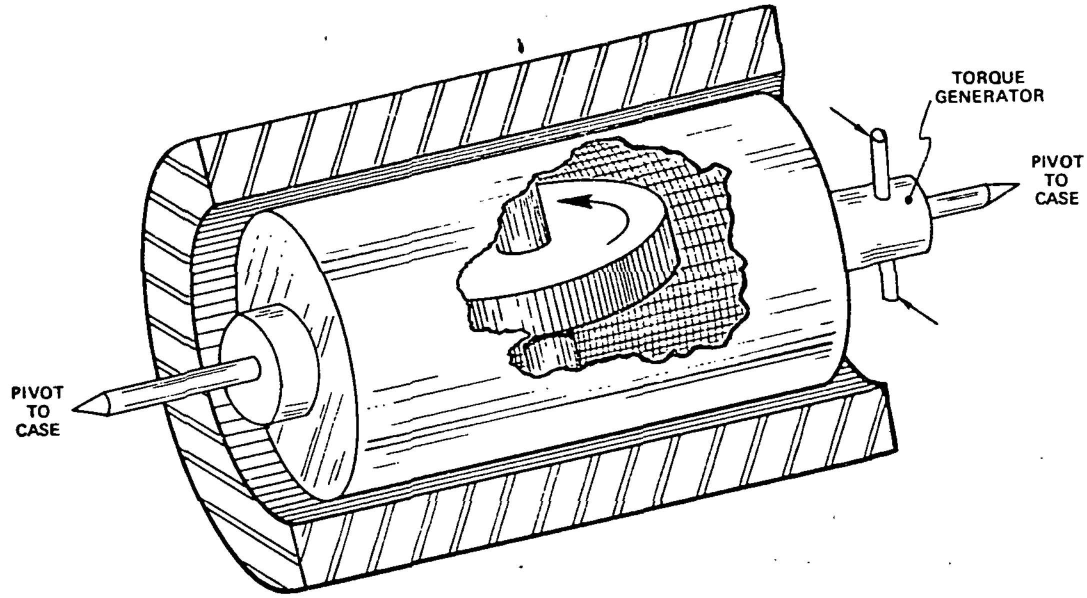

Fig. 1.2-10 Elementary Gyro Mounted in Viscous Torsional Integrator

1.2.4 Analog Signal Processor

The analog signal processor consists of the amplifiers and filters between the SG and the comparator(s). If, as is usual, an ac SG is used, a demodulator is also included. The principal use of signal processing, other than demodulation, is to keep a high signal-to-noise ratio both by preamplification and by noise discrimination. If the gyro has a significantly large uncompensated lag, the filtering must be a compromise between rejecting noise and limiting moding.

1.2.5 Comparators and Voltage Sources

One or more comparators perform the vital function in the PTE of communicating the status of the analog signal to the logic. A comparator forms the function sign(z) when z is the difference between two inputs, x and y. The sign function is defined as:

$$\mathrm{sign}(z) = \begin{cases} 1, & z > 0 \\ 0, & z < 0 \end{cases} \qquad (1.4)$$

Such a comparator forms the basic device which converts analog information into binary digits in any analog-to-digital converter.

Only one comparator is needed in general with binary current switches and logic (Fig. 1.2-1). In a simple binary delta modulator the voltage source, d(t), is zero at all times. In Section 1.4 we shall describe the United Aircraft forced binary PTE, which has a saw-toothed waveform for this source. When ternary current switches and logic are used, two comparators (Fig. 1.2-11) are needed. The voltage sources $d_1(t)$ and $d_2(t)$ are usually constant, nonzero voltage levels.

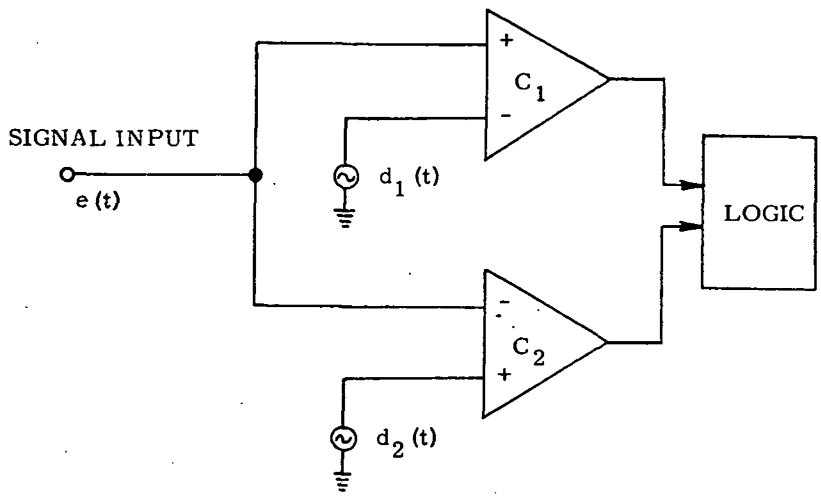

Fig. 1.2-11 Comparators for Ternary Logic

1.2.6 Digital Logic and Clock

In a sense there are no general forms of logic and timing in pulse-torque electronics: the differences in these elements determine whether a loop is binary or ternary or forced-binary or whatever. Understanding of the different schemes will be enhanced, however, if we recognize that the necessary processes can be stated in general terms. Consider the mechanization as in Fig. 1.2-12. This has the same elements as Fig. 1.2-1 redrawn to fit the form of Fig. 1.1-3. (Notice that in this form the gyro is shown twice in order to show explicitly its separate use as a transducer and as an integrator.) The basic purposes of the logic are:

1. to sense the condition of the analog error signal via the status of the comparator(s),

2. to act in synchronism with timing pulses from an electronic clock,

3. to control the switches carrying current to the torque generator by deciding whether to switch or not at each clock pulse, and

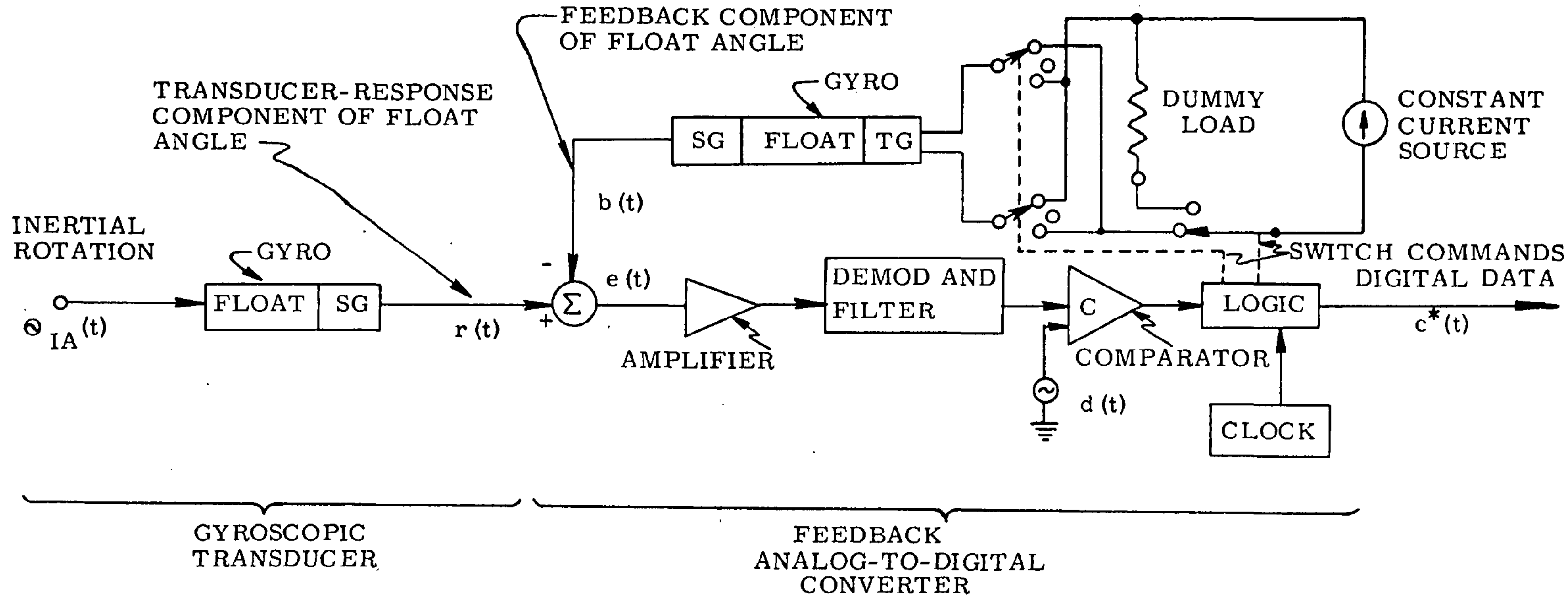

Fig. 1.2-12 General Mechanization of PTL Showing Separate Functions of Gyro

4. to gate out pulses as data (usually called $\Delta\theta$ pulses for a gyro) so as to communicate best the significance of the decision made for the torque-generator switches.

These general processes will be made specific in the sections below which describe the different types of pulse-torque loops.

1.3 DELTA MODULATORS

1.3.1 Ternary

A ternary delta modulator is a communications device which converts an analog signal into increments of equal weight. At regular time intervals, the device issues a code for plus one, minus one, or zero in such a fashion that a count or accumulation of the output code is a representation of the input signal. The basic rule governing its operation is that this count of its output be as close as possible to the signal to be quantized.

Let us deduce the essential processes required in a delta modulator. The device can be organized as shown in Fig. 1.3-1. The central component is a logical decision maker which issues output impulses as needed. The sampled output, $c^*(t)$, is integrated to form a feedback signal, $b(t)$. As shown in Fig. 1.3-2, the actuating (or error) signal, $e(t)$, is the difference between input $r(t)$ and $b(t)$. The time scale has been chosen so that one period of the clock is one unit of time. A decision is required at time t_o^- (a time just before t_o) whether to put out a positive unit pulse, a negative unit pulse, or none. If only the instantaneous value of $e(t)$ is used in the decision (i.e., neither past or future values influence it), the control should minimize the difference between $r(t_o)$ and $b(t_o^+)$ by selection of the outputs +1, -1, or 0. As illustrated, the decision can be based on the difference between $r(t_o)$ and $b(t_o^-)$. The best decision is found by comparing this difference to constants of plus and minus one-half and producing controlled output $c^*(t_o)$ which is

a.) a plus pulse if the difference is greater than one-half,
b.) a minus pulse if the difference is less than minus one-half, or
c.) no pulse if the difference is from minus one-half to plus one-half.

An idealized ternary delta modulator is constructed with logic and an integration in a feedback configuration as shown in Fig. 1.3-3. Fig. 1.3-4 illustrates the signal response of such a system for an arbitrary input $r(t)$ as depicted. The idealization is that the control $c^*(t)$ to the integrator (gyro) is an impulse into an integrator

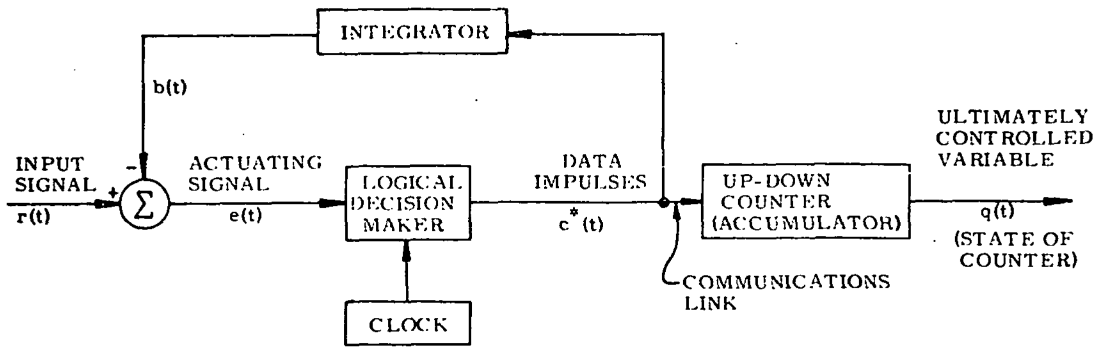

Fig. 1.3-1 Organization of Delta Modulator

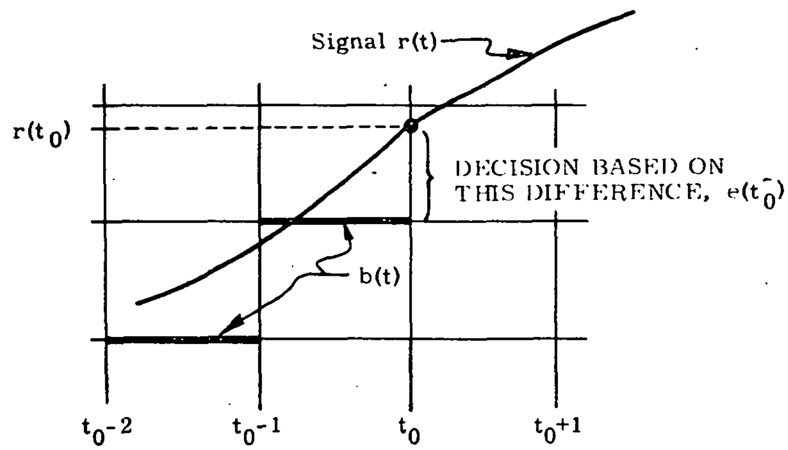

Fig. 1.3-2 Actuating Difference

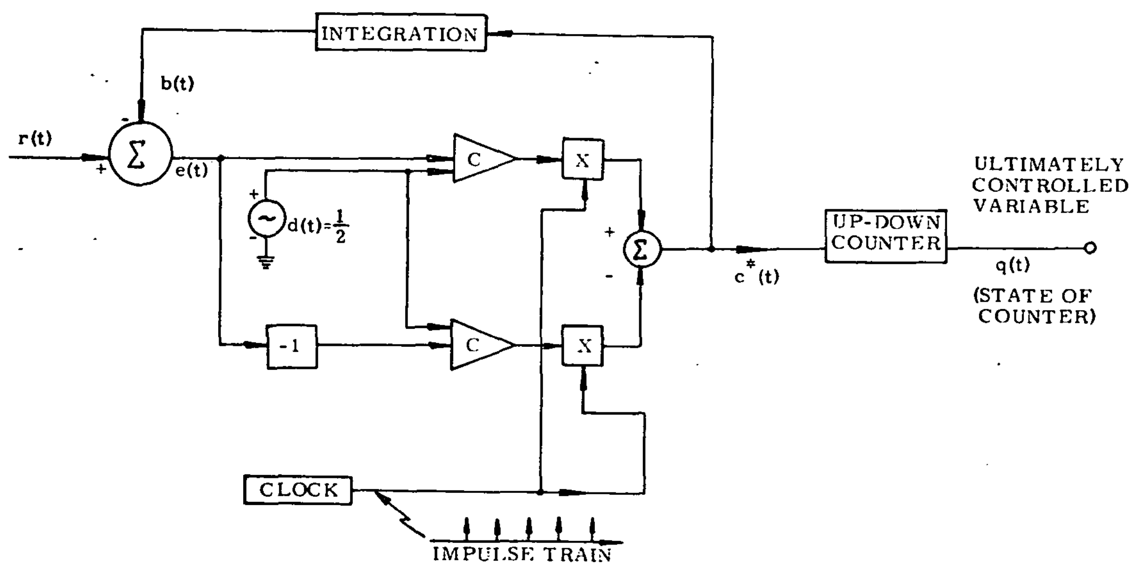

Fig. 1.3-3 Idealized Ternary Delta Modulator

yielding a step response at b(t). A plus or minus data pulse is formed if the actuating signal, e(t), is more than plus one half or less than minus one half when a clock pulse arrives. The feedback signal, b(t), is formed as an integration of the impulsive data and therefore has the same waveform as q(t), a count of the data pulses. Hence the apparatus operates to keep b(t) close to the analog input reference signal, r(t).

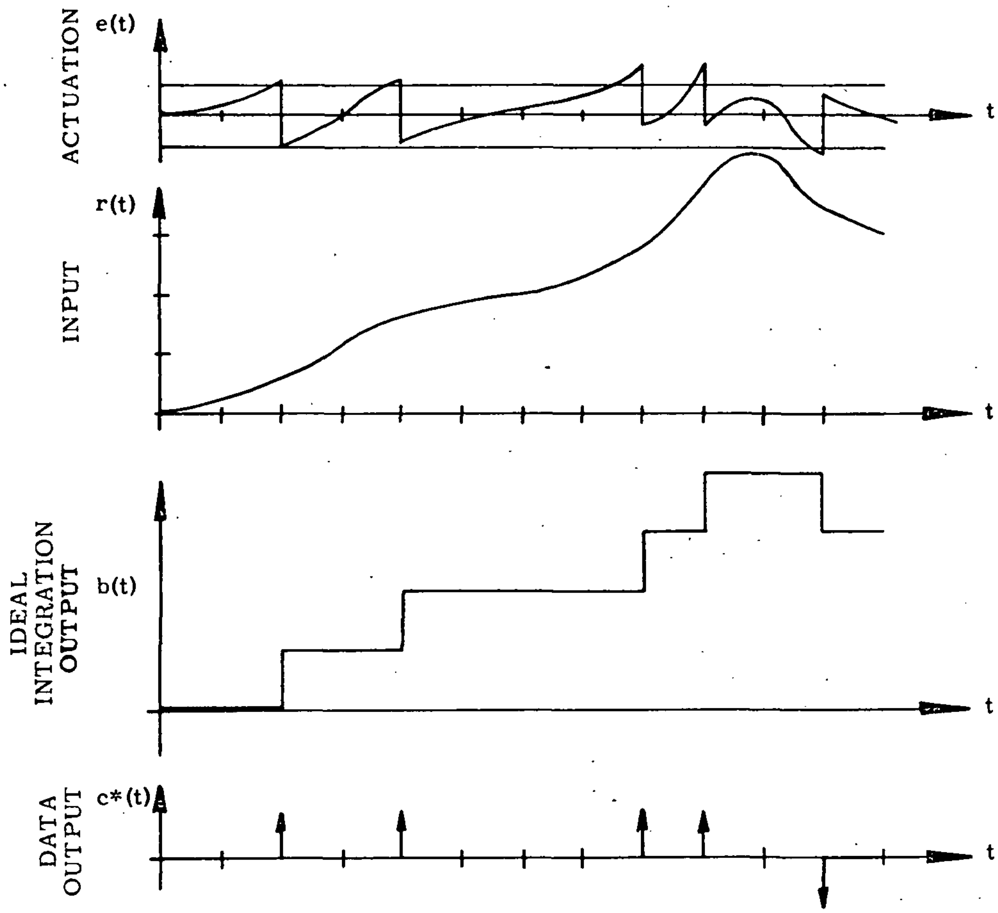

Fig. 1.3-4 Idealized Ternary Delta Modulator Waveforms

One can compare Fig. 1.3-3 to Fig. 1.2-12 to see that a ternary pulse-torque loop can operate as a ternary delta modulator. The constant current source and current switches form a finite-width pulse which is integrated by the gyroscope in the feedback loop. Although the feedback from the gyro does not jump instantaneously to a new value at each clock pulse as an ideal integration responds to impulses, it will arrive via a one-period ramp as in Fig. 1.3-5, which is just as good. The real device will also have a deadzone somewhat greater than plus or minus one-half in order to prevent frequent triggering of pulses by small noise signals.

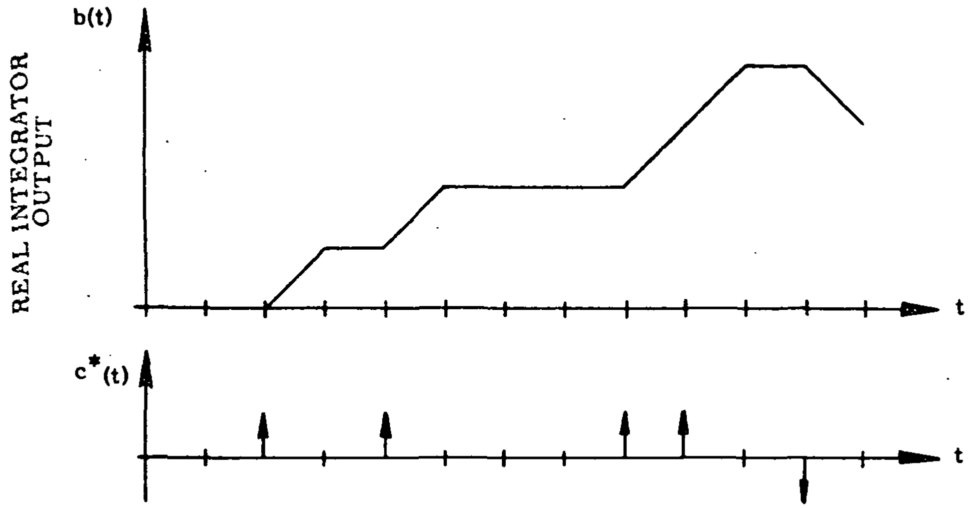

Fig. 1.3-5 Waveforms With Real Integrator (Gyro)

The operation of a ternary delta modulator is most easily understood when the input has constant rate and the loop is compensated to avoid problems with the gyro time constant. If the input rate normalized to the maximum rate is a constant designated V, the patterns of the actuating signal, e(t), are composed of straight lines as shown in Fig. 1.3-6. The case shown is for V positive. As an example of the patterns which result, Fig. 1.3-7 shows the actuating signal and the thresholds when V is three eighths. The same signal and the pulses produced are shown in Fig. 1.3-8. Note that for V a rational fraction, the pattern is periodic with the minimum possible period.

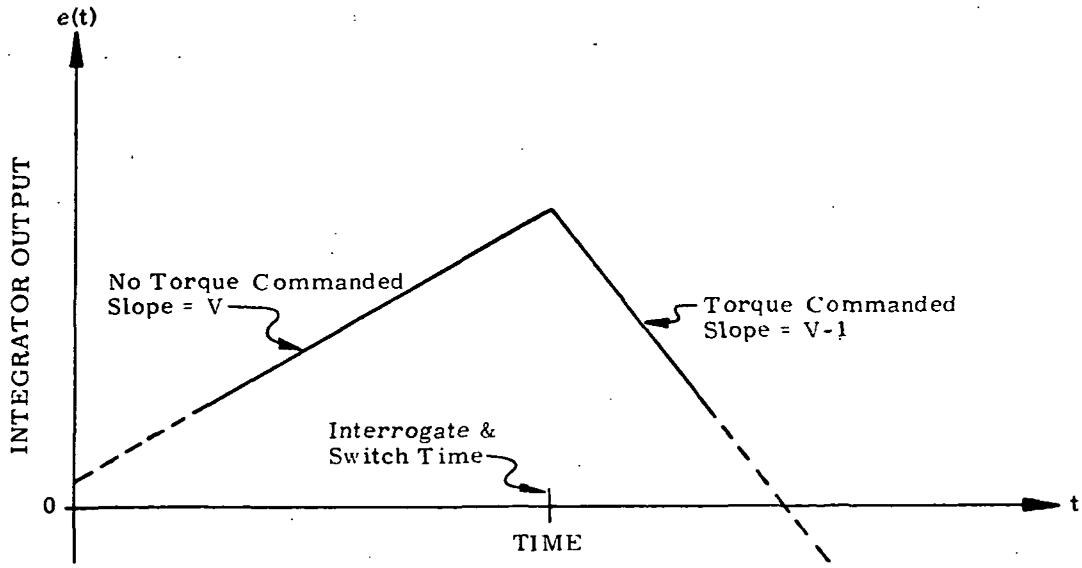

Fig. 1.3-6 Actuating (Error) Signal for a Ternary Delta Modulator at Constant Input Rate, V

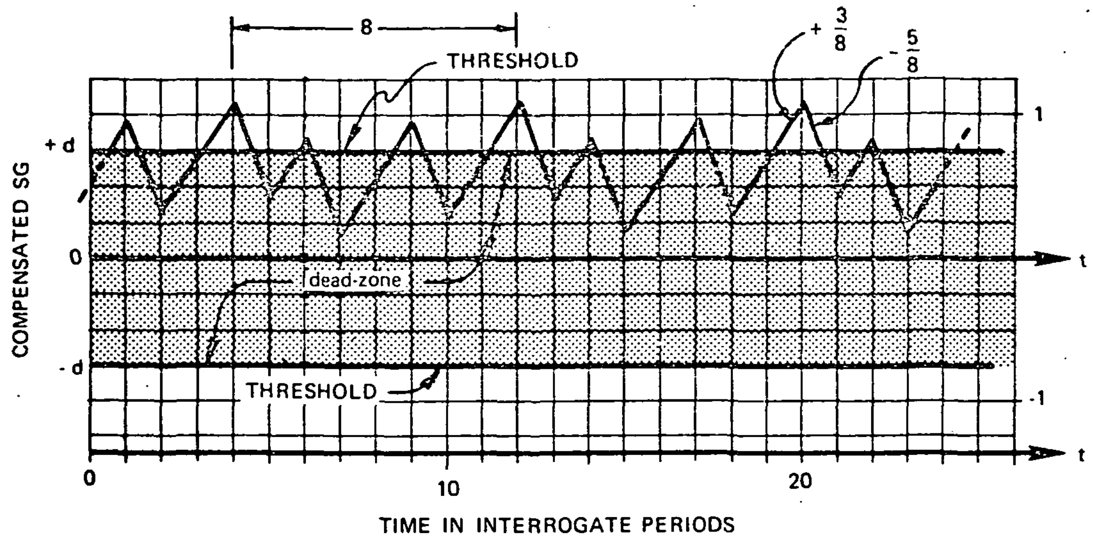

Fig. 1.3-7 Actuating Signal and Deadzone,Ternary Loop

The ternary pulse-torque loop has been used extensively by CSDL, Honeywell, and other system designers for a number of years with gyroscopes and accelerometers. Our primary tests for MSFC study used this type of loop. Since it has small sampling and quantization errors, ternary has been used where fine quantization is required. Its major disadvantage is that power into the torque generator varies with the input rate.

1.3.2 SIRU Ternary

The gyro pulse-torque loop used in a CSDL system, SIRU, is a hybrid of a ternary delta modulator and an additional analog-to-digital converter. The extra converter samples the actuating signal just after the decision whether to apply a pulse is made. It encodes this sample to three bits finer than the weight of a torque pulse and transmits the result. The use of this finer data increases the static resolution by a factor of eight(to 5.5 arc seconds in a one-rad/s loop.) Since the sampling for this converter is at the same rate as the torque pulse decisions, the sampling error remains at one torque pulse (44 arc seconds) when rotating at one rad/sec. For details on the SIRU loop mechanization, see Reference 4.

1.3.3 Binary

A binary delta modulator is a communications device which converts an analog signal into increments of equal weight. At regular time intervals the device issues a plus code or a minus code in such a fashion that a count of these outputs is a representation in digital form of the analog input.

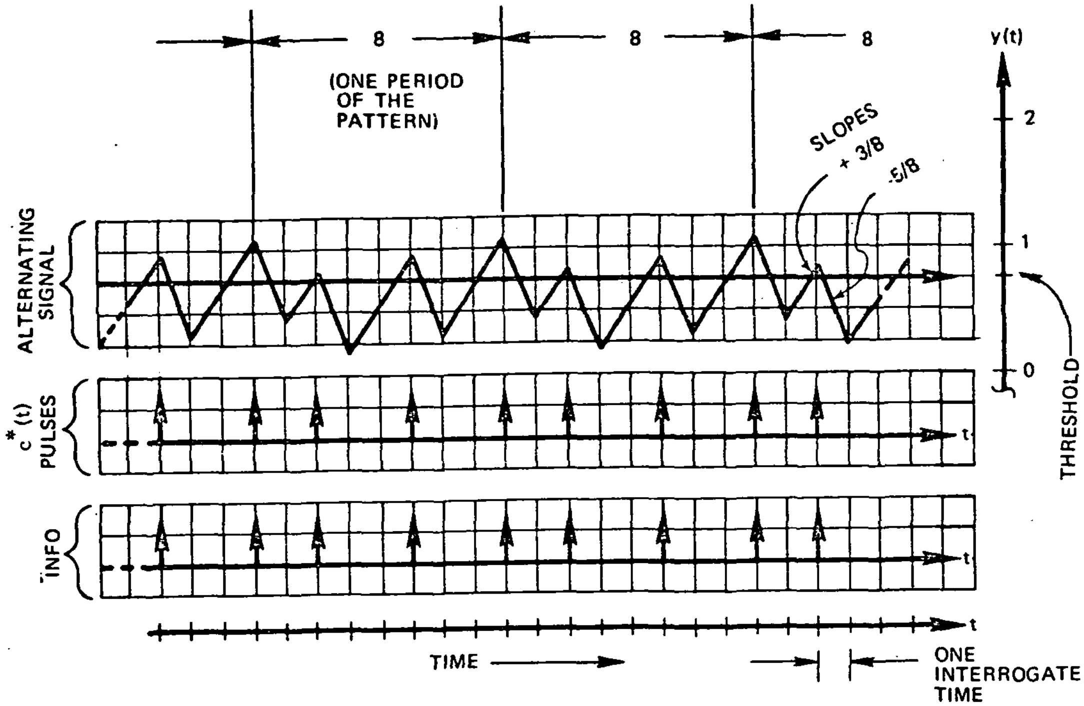

Fig. 1.3-8 Ternary Operation at 3/8th of Maximum Input

A delta modulator of this sort is constructed with logic circuits and an integration in a feedback configuration as shown in Fig. 1.3-9. A plus or a minus pulse is formed when each clock pulse arrives depending whether the actuating signal is positive or negative. The feedback signal, b(t), is formed as an integration of the data impulses, which has the same waveform as q(t), a count of the data. The device operates to keep b(t) and thus q(t) as close to r(t) as possible within the restriction that either a plus or minus pulse must occur at each clock time whether it is needed or not. One can compare Fig. 1.3-9 to Fig. 1.2-12 to see that a binary pulse-torque loop can operate as a binary delta modulator. The constant current source and current switches act like a zero-order hold (a boxcar clamp) causing the integration by the float to produce a ramp output to the new value rather than a step.

The operation of a binary delta modulator is most easily understood when the input has constant rate. If the input rate normalized to maximum rate is a constant, V, the patterns of the actuating signal, e(t), are composed of straight lines as shown in Figure 1.3-10. As an example of the operation, Fig. 1.3-11 shows the actuating signal and pulse patterns for V equal to plus three eighths. The information contained in the binary pulses C*(t) is gotten by leaving out any pulse which disagrees in sign with the pulse before it. A circuit to accomplish this with logic is shown in

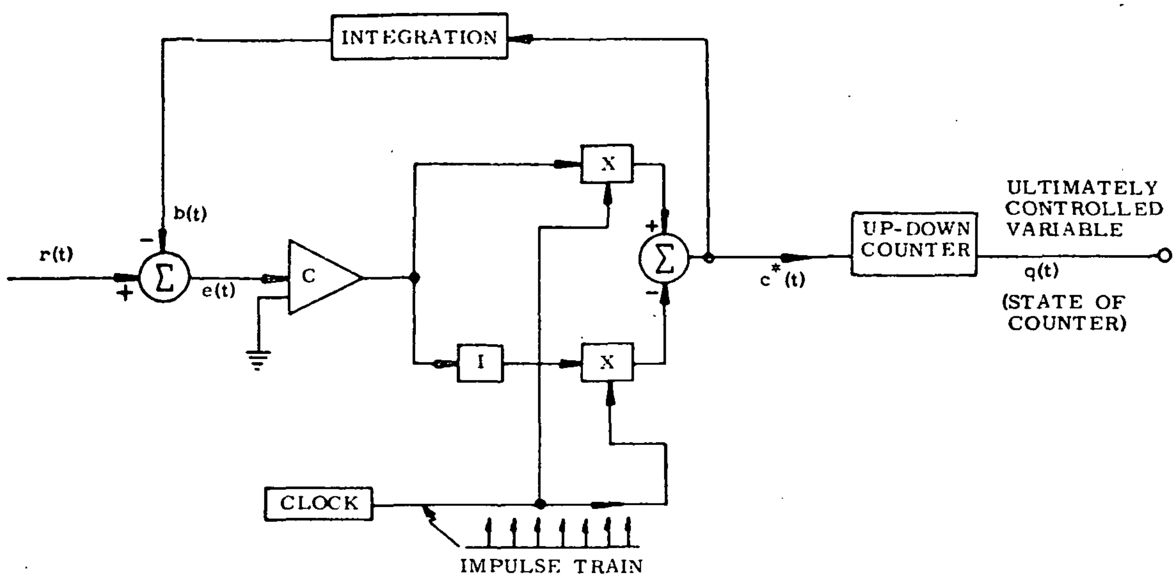

Fig. 1.3-9 Binary Delta Modulator

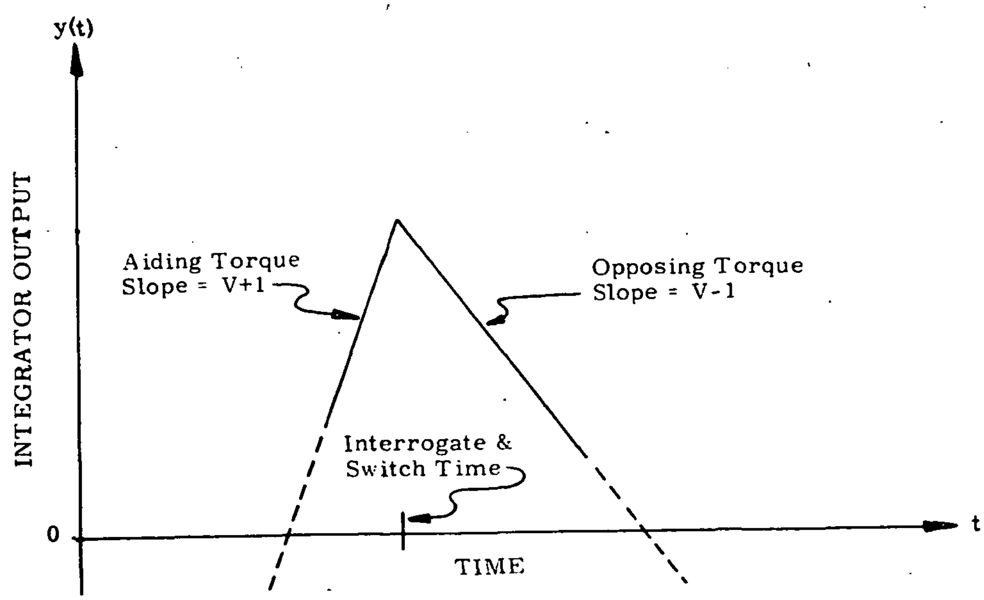

Fig. 1.3-10 Actuating (Error) Signal for a Binary Delta Modulator at Constant Input Rate, V

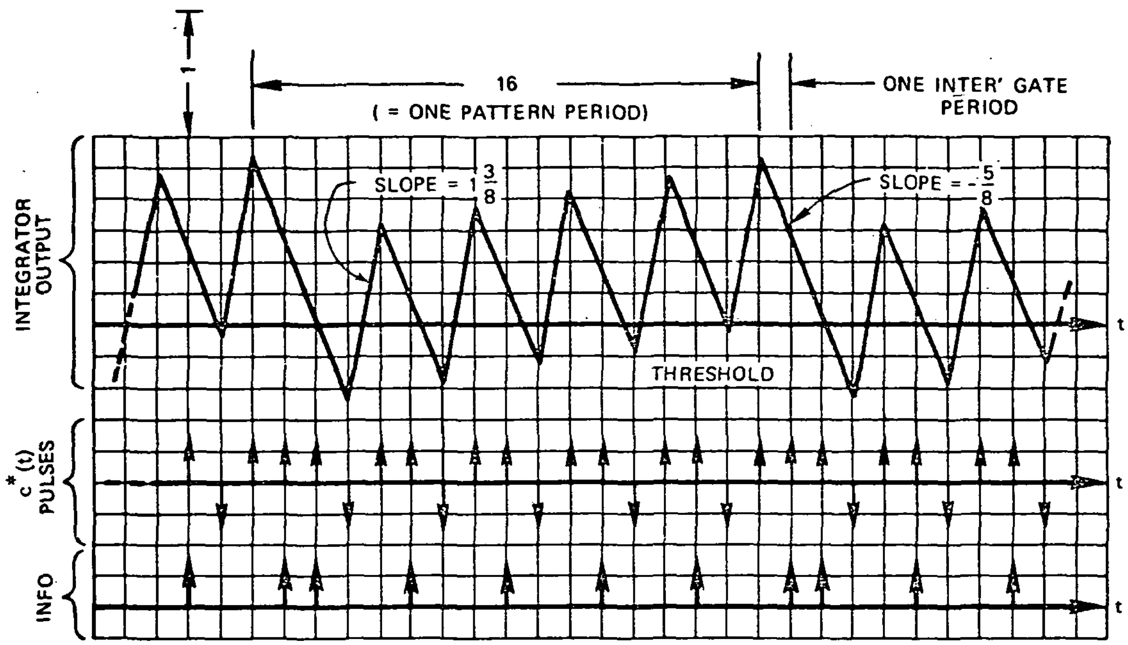

Fig. 1.3-11 Binary Operation at 3/8th of Maximum Input

Fig. 1.3-12. The first flip-flop stores the sign of each pulse. When the clock pulse arrives subsequently, it transfers the sign to the second flip-flop. Its condition then enables output of pulses of the same sign but sends pulses of the opposite sign into the bit bucket.

Binary loops are used principally because they dissapate nearly constant heat in the torque generator. If the scale factor or gyro drift varies with TG power, then binary operation is desirable. Disadvantages of binary include data delays and mode-related deadzones. The first happens because the zero-input moding may occur so as to interfere with interpretation of the data. Any pulse generated which disagrees with the pulse immediately before does not communicate a rotation. If in fact the pulse should have communicated data, the message is delayed until the next interrogate time. We have shown[5] that this delay averages one interrogate period longer than the delays in ternary.

The mode-related deadzones come from more complex phenomena. They occur when two adjacent mode patterns develop biases in opposing directions. In our loop study we were using a compensated loop, so the modes involved were 1:1 and 2:2. A 1:1 binary mode consists of alternating plus and minus pulses. A 2:2 binary mode is pairs of plus pulses alternating with pairs of minus pulses. The deadzone

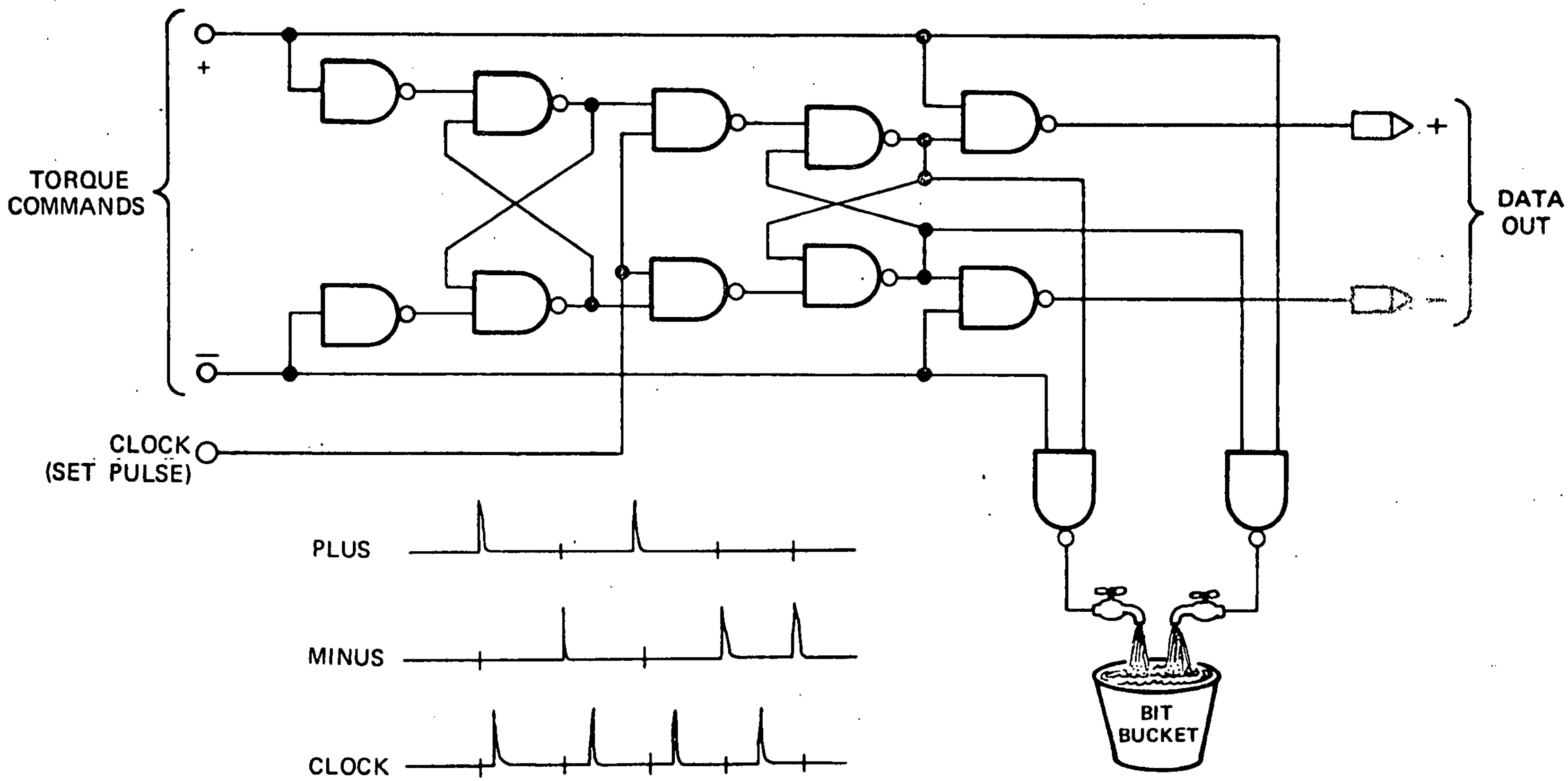

Fig. 1.3-12 Zero Mode Suppressor

occurs when the 1:1 mode drifts so as to favor 2:2 moding, but the 2:2 mode drifts in the opposite direction and so as to favor 1:1 moding. Noise at the comparator (even a small amount) makes it possible to operate with a mixture of the two modes. E. Salamin of this labaratory has shown that the drift difference, D, between the modes is:

$$D = K I_o^2 \left[\frac{\tau}{T} \quad \frac{2 \tanh^3(T/2\tau)}{1 + \tanh^2(T/2\tau)} \right] \qquad (1.5)$$

where:

K	= the TG current-squared sensitivity in deg/h per mA^2.
I_o	= the magnitude of the current pulse in mA
T	= the duration of the current pulse.
τ	= the torque-generator coil time constant.

The function in the brackets is sketched in Fig. 1.3-13. To show the importance of the deadzone, consider the example of a GG334 gyro we tested which had a misalignment between the TG and SG of a milliradian. This gave a current-squared sensitivity, K, of 0.0003 deg/h per mA^2. In the vicinity of the broad maximum in Fig. 1.3-13, this produces almost two deg/h deadzone at a current of 150 mA. Since the current-squared sensitivity, K, is proportional to TG-SG misalignment, the deadzone would be measurable even at a misalignment of 0.01 mrad.

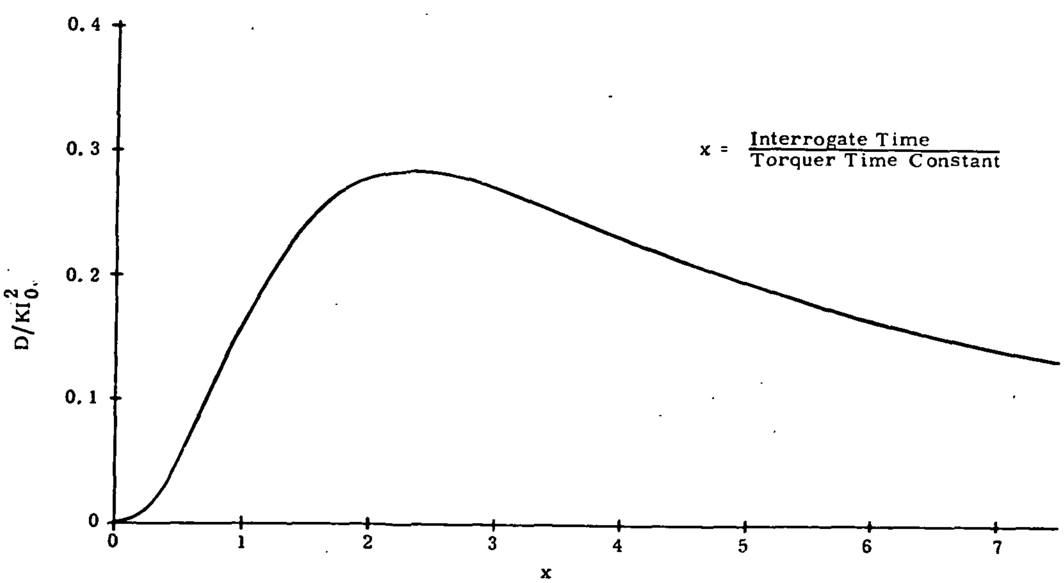

Fig. 1.3-13 Drift Difference Between 1:1 and 2:2 Modes

1.3.4 Fill-In Binary (FIB)

Fill-in binary is a delta type of pulse-torque quantizer which acts upon the instrument with a binary (reversing) switch, but which generates data as if it be ternary. This scheme therefore achieves nearly constant heating in the torque generator, an advantage of binary current switching, while avoiding the mode-related dead zone and data delay of binary. Logic for a fill-in binary quantizer was designed and constructed as a modification to the breadboard SIRU pulse-torque electronics.

The nature of FIB (fill-in binary) is to fib about the actual commands of current into the torque generator; that is, it does not necessarily communicate data corresponding to each pulse to the feedback elements. Instead, the spaces which would occur in ternary are filled in with current pulses of alternating sign without transmitting any data. These white lies are harmless so long as they average to zero and are prevented from interfering with formation of the ternary output. If this is accomplished, the data output format is indistinguishable from that of a ternary PTE. As a consequence, FIB logic can replace ternary in a guidance system without system modification. It also has the same sampling error as ternary rather than the larger amount of ordinary binary. We shall explain the concept of the FIB quantizer and give data from tests using FIB on a SIRU gyro module (containing an 18 IRIG Mod B).

As described in Section 1.3.3, binary delta modulators have two problems which up to now have seemed inherent to binary. First, the mixing of informative pulses with arbitrary pulses (required to achieve binary operation) inevitably delays communication of some information until it can be distinguished from the zero mode pattern of the quantizer. Second, the bias of the switch-TG combination can be pattern sensitive, giving a deadzone for low input rates. The FIB logic described here cures the moding (sampling) delays and the pattern-associated deadzone, thus proving that they are not intrinsic to binary delta modulation of inertial instruments.

The logic starts with an <u>ordinary ternary</u> interrogation section having two comparators with thresholds at, say, plus and minus 3/4 of a pulse. By itself, this would give a pulse pattern like Fig. 1.3-14 in response to 3/8 of maximum input rate. (This figure is a copy of Fig. 1.3-8.) When no output data is required, the task of the FIB logic is to call for a feedback pulse but to block data to the computer. The filled-in feedback must alternate in sign in order to minimize its effects on the loop.

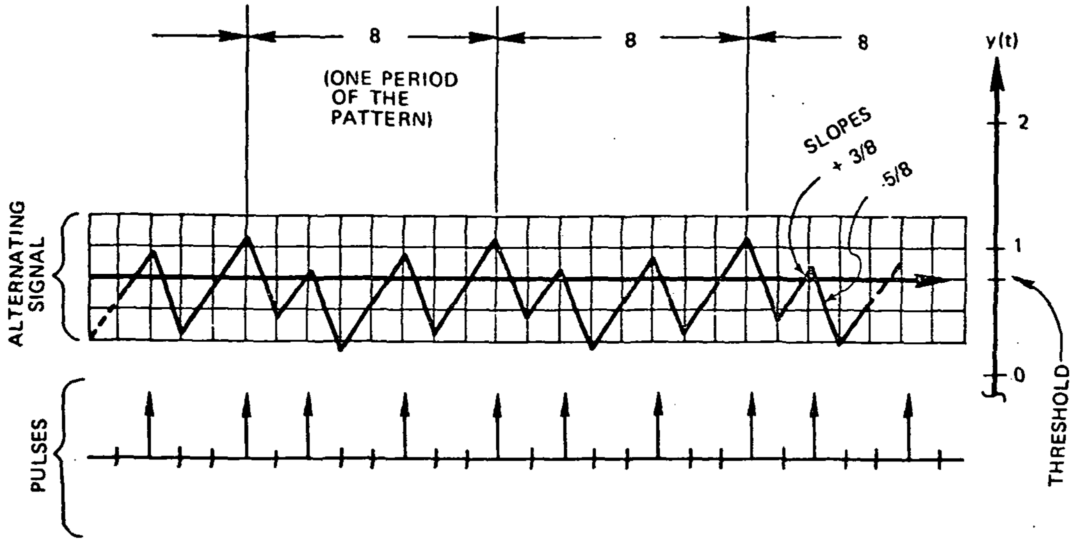

Fig. 1.3-14 Ternary Data Pulses

The idea of fill-in binary can be easily illustrated. Take a red pencil and fill in on *Fig. 1.3-14* the periods having no torque command, with alternating plus and minus pulses. The added pulses are to alternate in sign regardless of intervening pulses commanded by the interrogator. The two correct solutions are shown in Figures 1.3-15 and 1.3-16. A significant characteristic of these patterns is that, although the data has a period of eight interrogate cycles, the filled-in pattern has a period of 16.

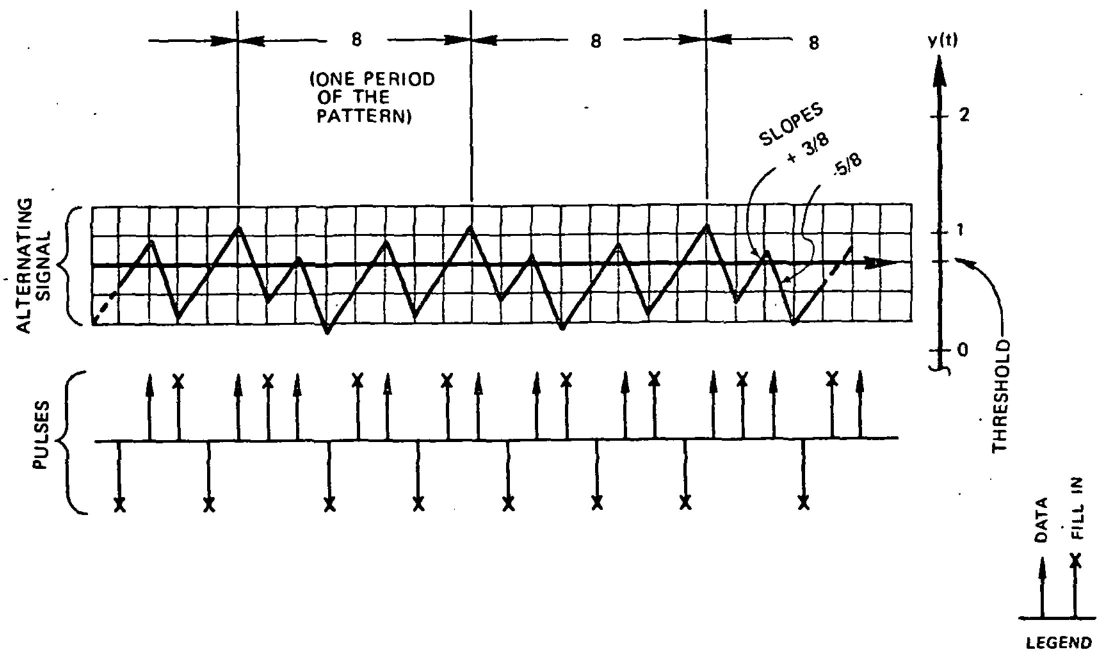

Fig. 1.3-15 Fill-In Binary Pulses (Case 1)

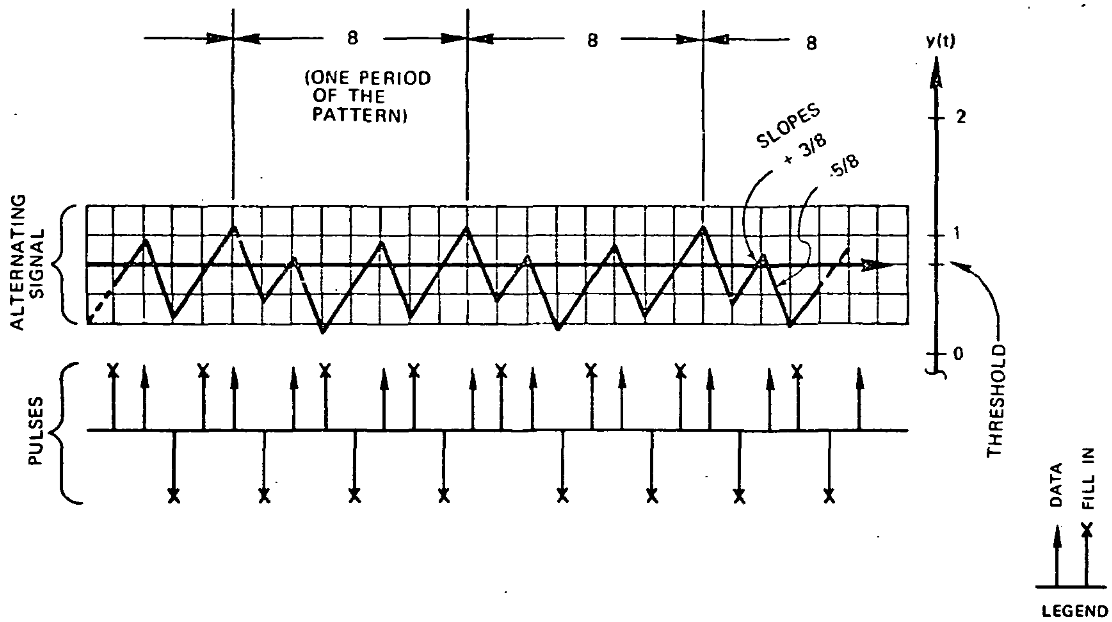

Fig. 1.3-16 Fill-In Binary Pulses (Case 2)

The only complication in the implementation of the FIB system is that, if uncorrected, the filled-in pulses would move the actuating signal out of the deadzone and trigger extraneous pulses. To prevent this, we add an offset of plus or minus one-half pulse to the thresholds, the sign depending on the sign of the fill-in pulse. In effect, this gives a zero moding pattern like that in Fig. 1.3-17 where the actuating signal, e(t), and the thresholds move in parallel lines.

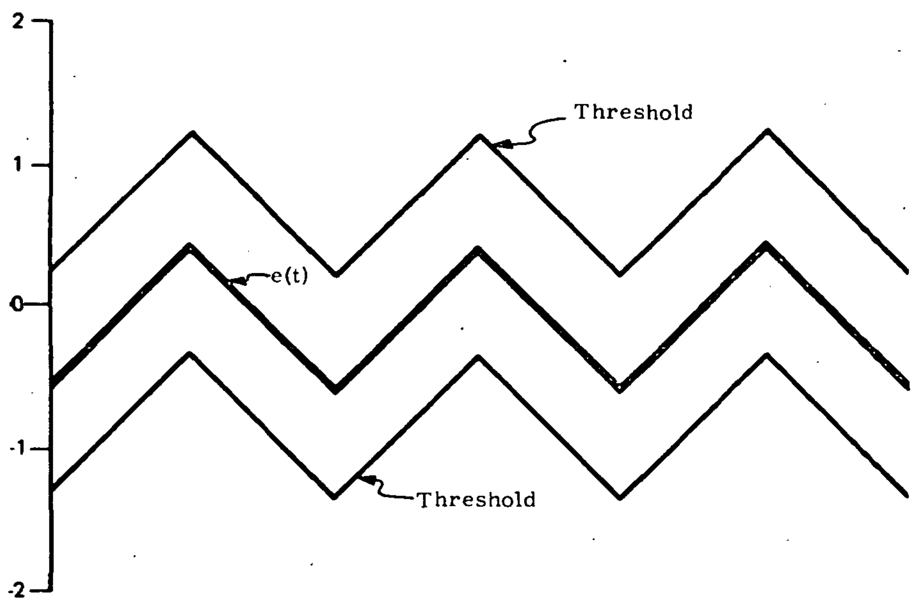

Fig. 1.3-17 Threshold Offsets for Fill-In Binary

A FIB system was built as a modification to the SIRU ternary bread-board PTE to show the feasibility of FIB. The current switch in these electronics has a 15/16 duty cycle: that is, torque is commanded for less than the time available for a pulse. Such a "forced reset" system assures that every pulse has a turn on and a turn off regardless of the presence or absence of neighboring pulses of either sign. When the PTE is converted to binary to demonstrate the feasibility of FIB, the forced reset gives an extremely high switching rate even when static. As a result, drift stability was found to be poor, but good enough to run meaningful nonlinearity tests. Figure 1.3-18 shows the scale-factor deviation versus rate first for ternary and then for FIB. One can see that the linearity is excellent except for the uncorrected bias drift which affects the lower rates. As just explained, the bias effects are to be expected with this switch. The feasibility of fill-in binary is illustrated well.

1.4 *UNITED AIRCRAFT FORCED BINARY LOOP*

1.4.1 Introduction

Getting high resolution with a simple delta modulator requires many small pulses. If at the same time one needs a high maximum rebalance rate, the small pulses must be short. But more and shorter pulses mean high switching rates which make it difficult to keep short-time stability. With a binary loop, such a difficulty is costly because the highest switching rate for binary delta modulators comes when the instrument is stationary. A forced binary PTE is a design which avoids high switching rates by bunching the short pulses into continuous groups and switching at a constant, less-frequent rate. Higher static resolution at a given switching rate is achieved by forced binary at a cost of larger sampling errors.

The PTE which CSDL test evaluated and which we call forced binary was designed and built by the Hamilton Standard Division of United Aircraft. These electronics reverse the current into the gyro torque generator at the start of a fixed one-millisecond data cycle. Then once and only once during each millisecond, the current is reversed again. Because the timing of the latter reversal varies with the rotational rate of the gyro, forced binary is often called width-modulated binary. The width is not continuously varied in an analog fashion: rather, the concept of smaller pulses grouped together is maintained by enabling the reversal at 64 discrete times marked off evenly by the clock.

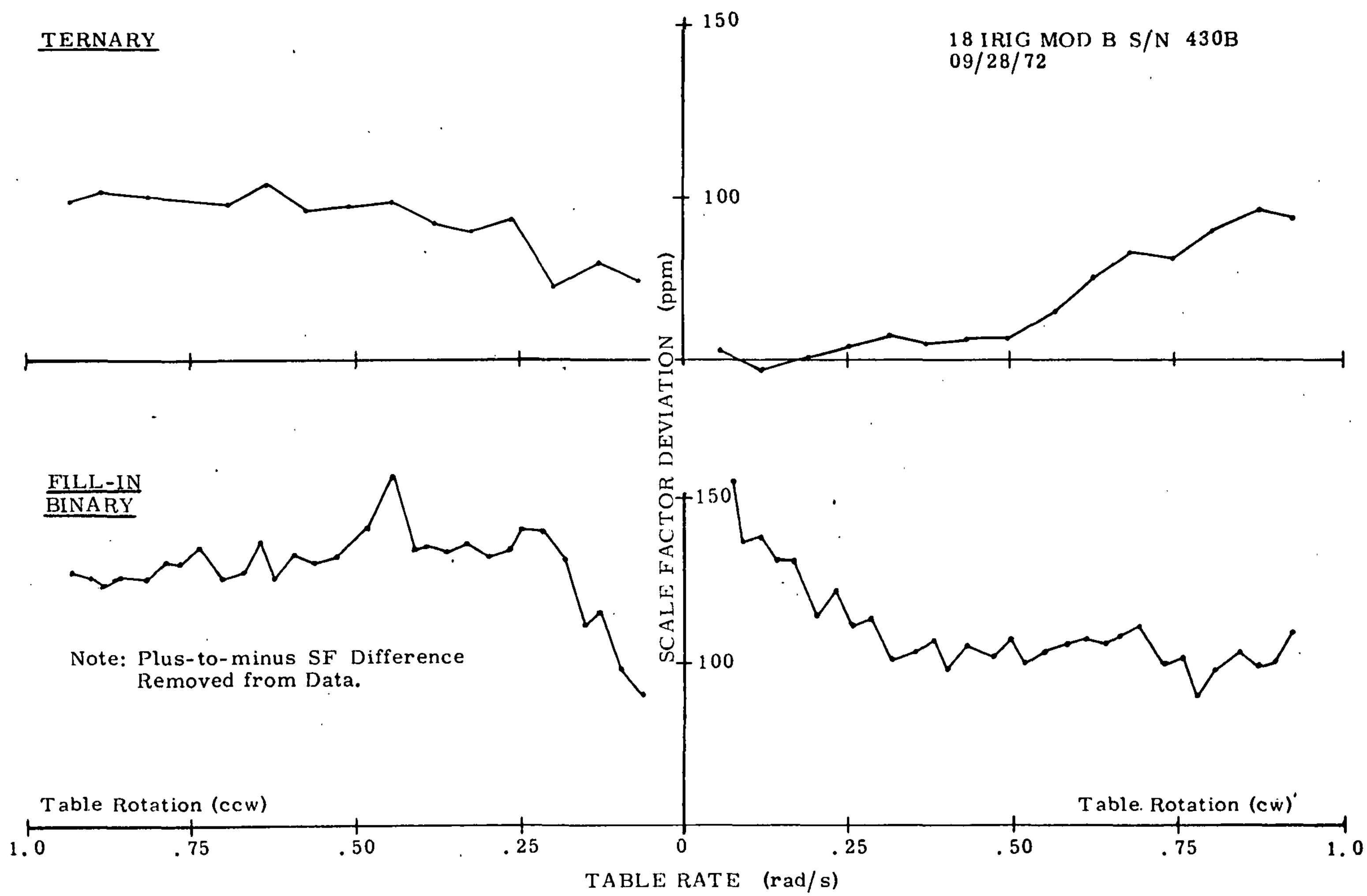

Fig. 1.3-18 Fill-In Binary Nonlinearity

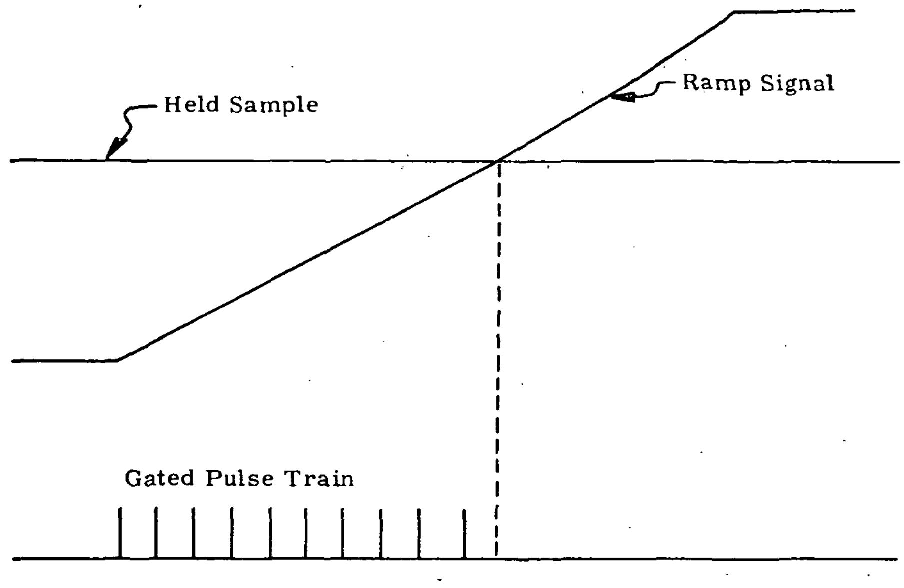

Fig. 1.4-1 Operation of a Time-Analog Digital Converter

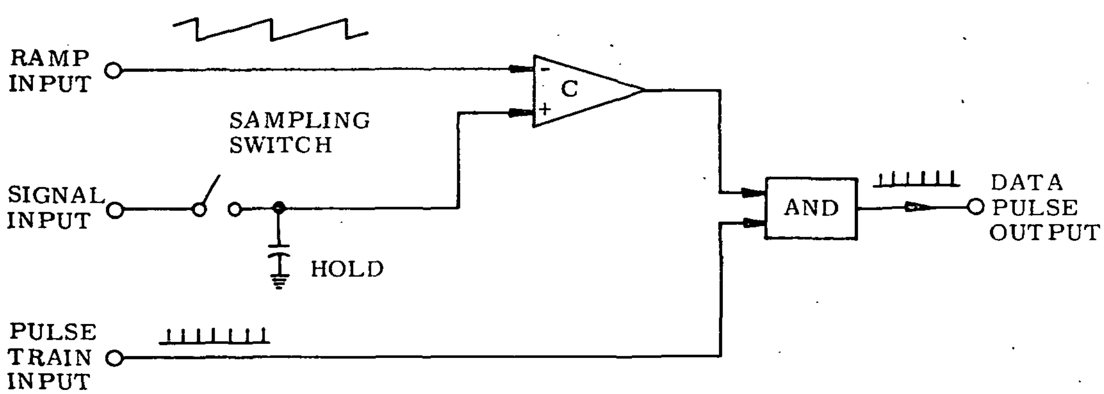

Fig. 1.4-2 Time-Analog Digital Converter

1.4.2 Forced Binary Loop Mechanization

The general mechanization of the forced binary loop was described in Section 1.2. Additional information on the logic and timing which are special to this loop will be given here.

The forced binary PTE works in a way similar to the operation of a time-analog digital converter. In such a converter, a ramp signal is compared to a sample of the signal as in Fig. 1.4-1. A pulse train, started at the same time as the ramp, is counted until the ramp gets larger than the sample. At that time the count is halted. Figure 1.4-2 shows how this is mechanized. The length of time that the comparator is enabling (keeping the AND gate open) is proportional to or analogous to the magnitude of the held signal.

We speculate that the forced binary PTL evolved from the time-analog digital converters: this is the only way we can satisfactorily explain the presence of the ramp signal in the loop. In the forced binary loop, one enables the comparator only at integral times as indicated by a pulses arriving from the clock. This process is shown as a torque-command synchronizer in Fig. 1.4-3. As shown there, the designers have found it unnecessary to retain the sample and hold in the loop. To consider the equipment in Fig. 1.4-3 adequately, we must think of it being included as the logic in the PTL of Fig. 1.2-1 or Fig. 1.2-12. When we do, a curious fact becomes evident: we have formed a feedback type analog-to-digital converter using the gyro as the feedback integrator, but we have retained the ramp signal and the data format of a time-analog digital converter. A problem of this loop is that, without the sample and hold, there is no distinct time in the data cycle when the data can be said to be correct.

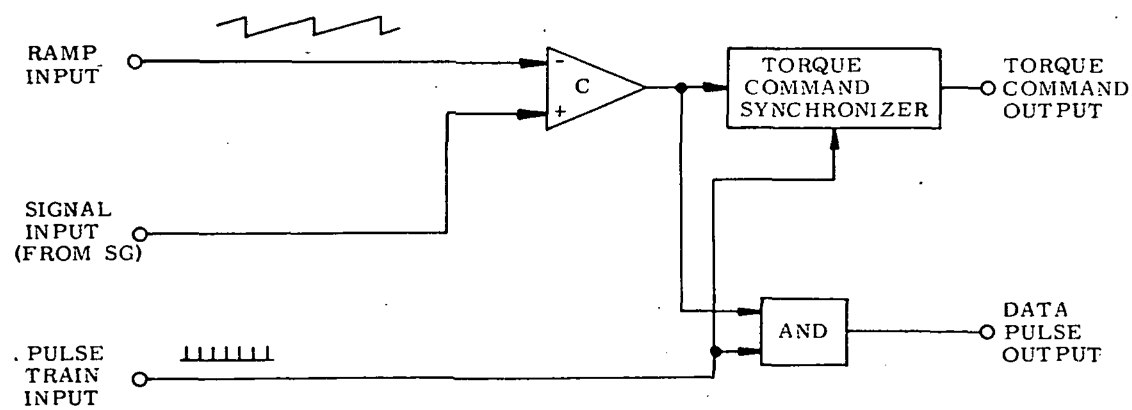

Fig. 1.4-3 Forced Binary PTL Logic

The forced binary PTE is timed and synchronized from a 4096-kilohertz crystal-controlled oscillator. From this, four signals are supplied to the logic: a 64,000-pulses-per-second (64 kp/s) square-wave clock with 50% duty cycle, a sync pulse once every millisecond, and two "blanking" signals which also have a one-millisecond period. The blanking signals serve to assure that at least two data pulses in each direction are included in each cycle. The forms and relative phases of these signals are shown in Fig. 1.4-4. We have defined time zero in each cycle as that when all timing signals have an edge. In each one-millisecond data cycle, the loop generates one measurement using the logic shown in Fig. 1.4-5. A complete data cycle with the gyro stationary is drawn in Fig. 1.4-6 showing the torque command, the data pulses, the analog input from the comparator, and the timing signals.

1.4.3 Resolution and Sampling Errors

The resolution of this loop is illustrated in Fig. 1.4-7. Two data cycles are shown, one for a null or stationary condition and one for the next adjacent condition. It is shown that the resolution is two increments of torque rather than one as often stated. A further explanation of the resolution is given in Table 1.4-I.

TABLE 1.4-I

Forced Binary Data Format

DATA PLUSES	CW PULSES	CCW PULSES	NET PULSES
2	2	62	60 CCW
30	30	34	4 CCW
31	31	33	2 CCW
32*	32	32	0
33*	33	31	2 CW
34	34	30	4 CW
62	62	2	60 CW

* Illustrated in Fig. 1.4-7.

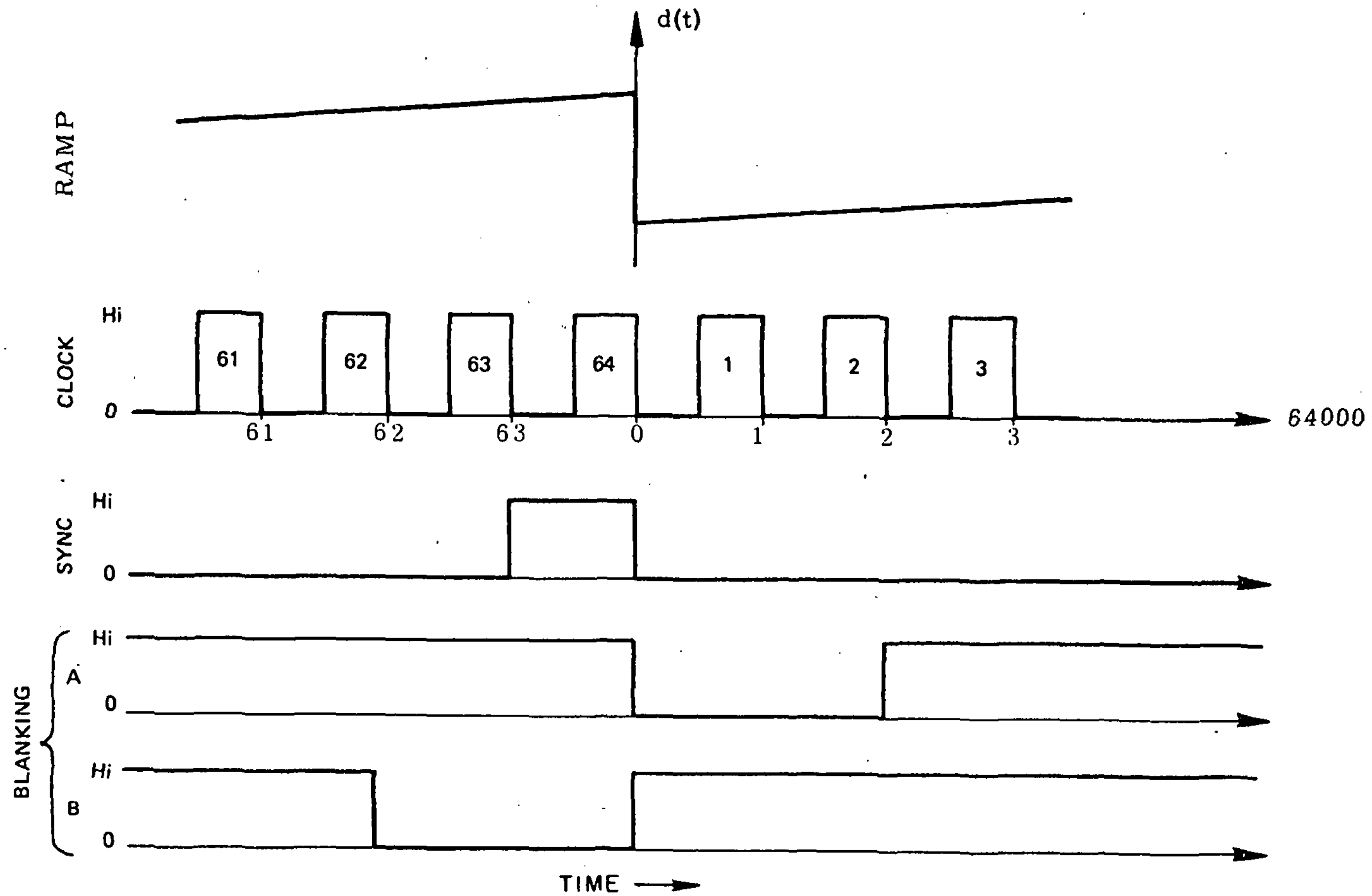

Fig. 1.4-4 Forced Binary Timing Signals

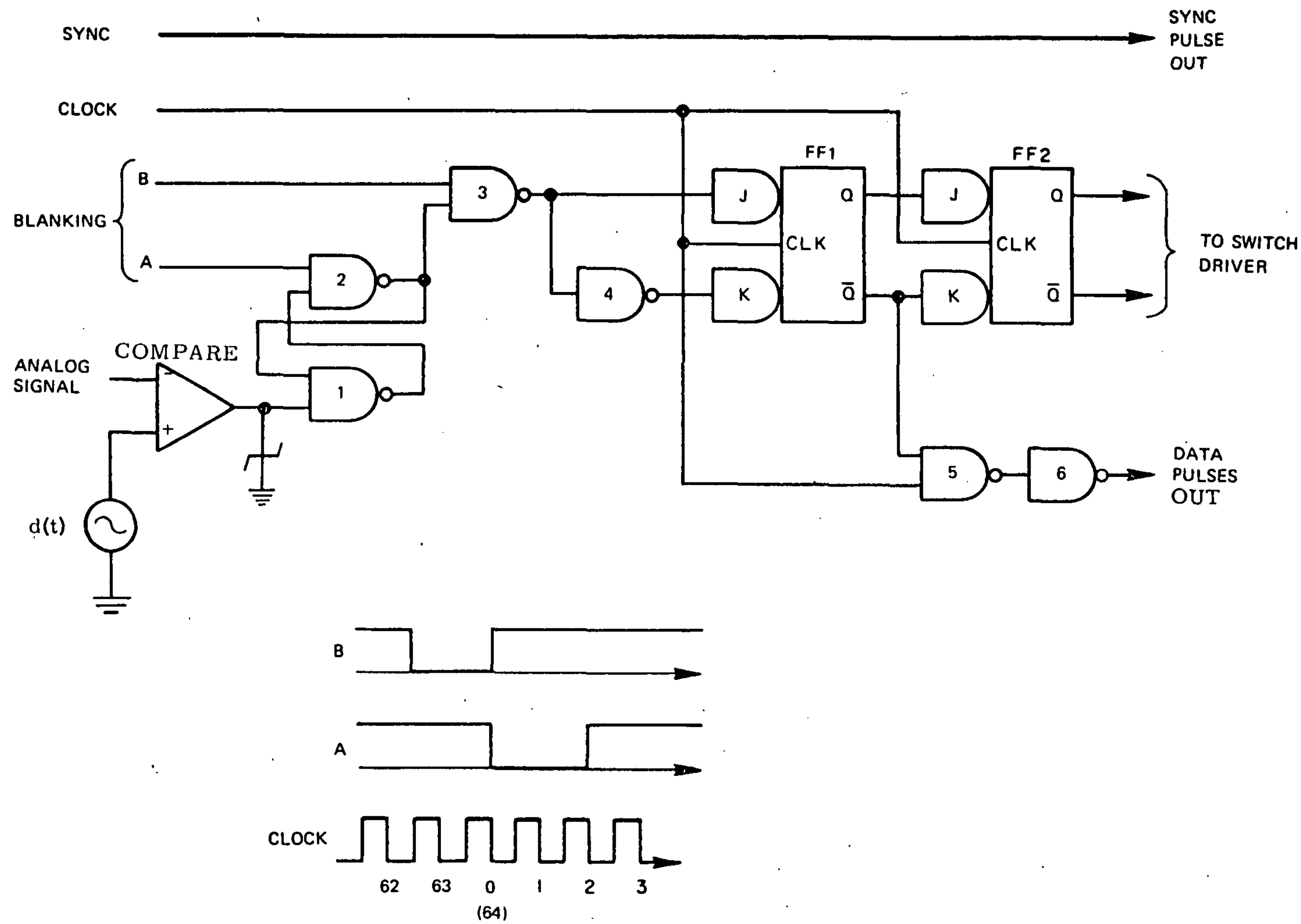

Fig. 1.4-5 Forced Binary Logic

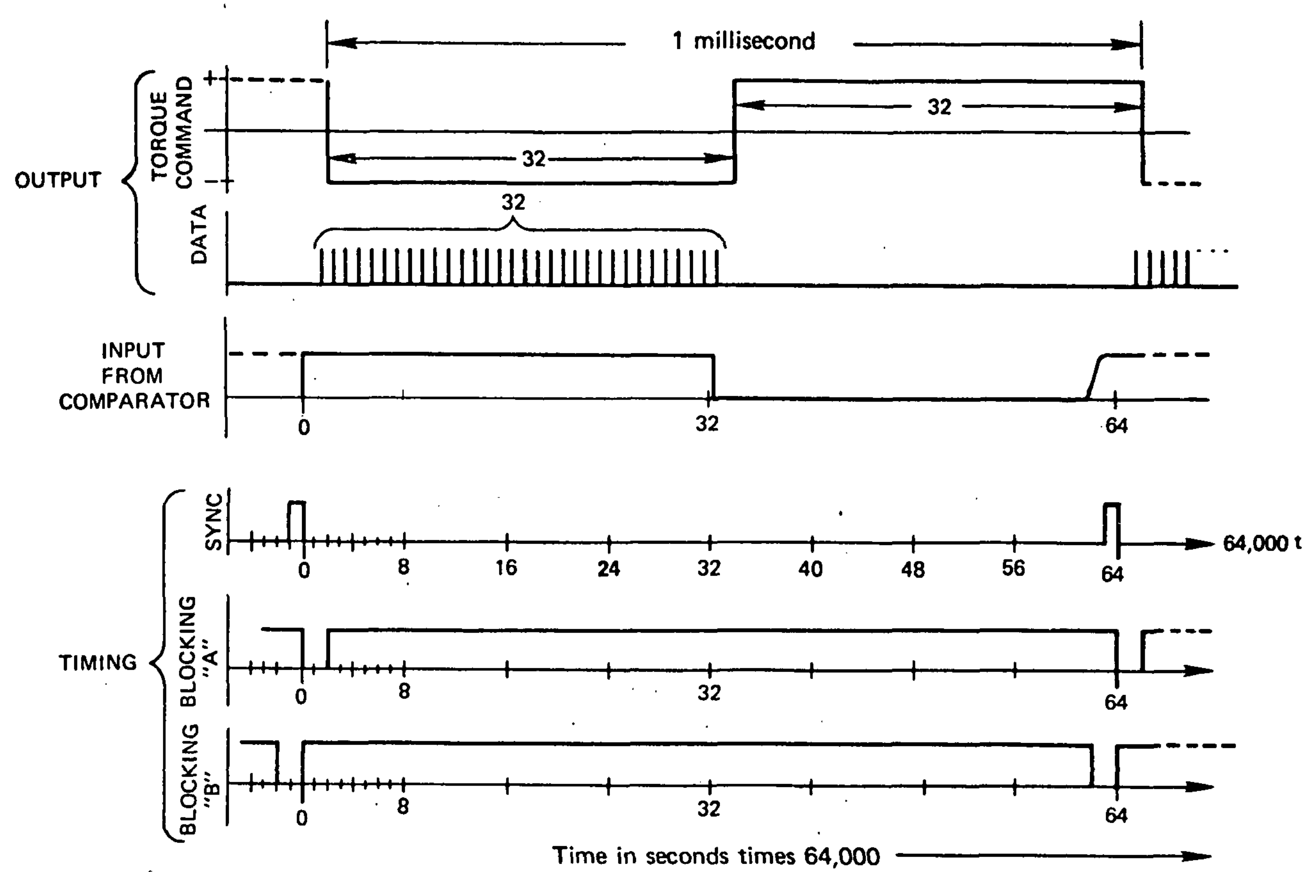

Fig. 1.4-6 Forced Binary Timing and Data when Stationary

(a) Stationary

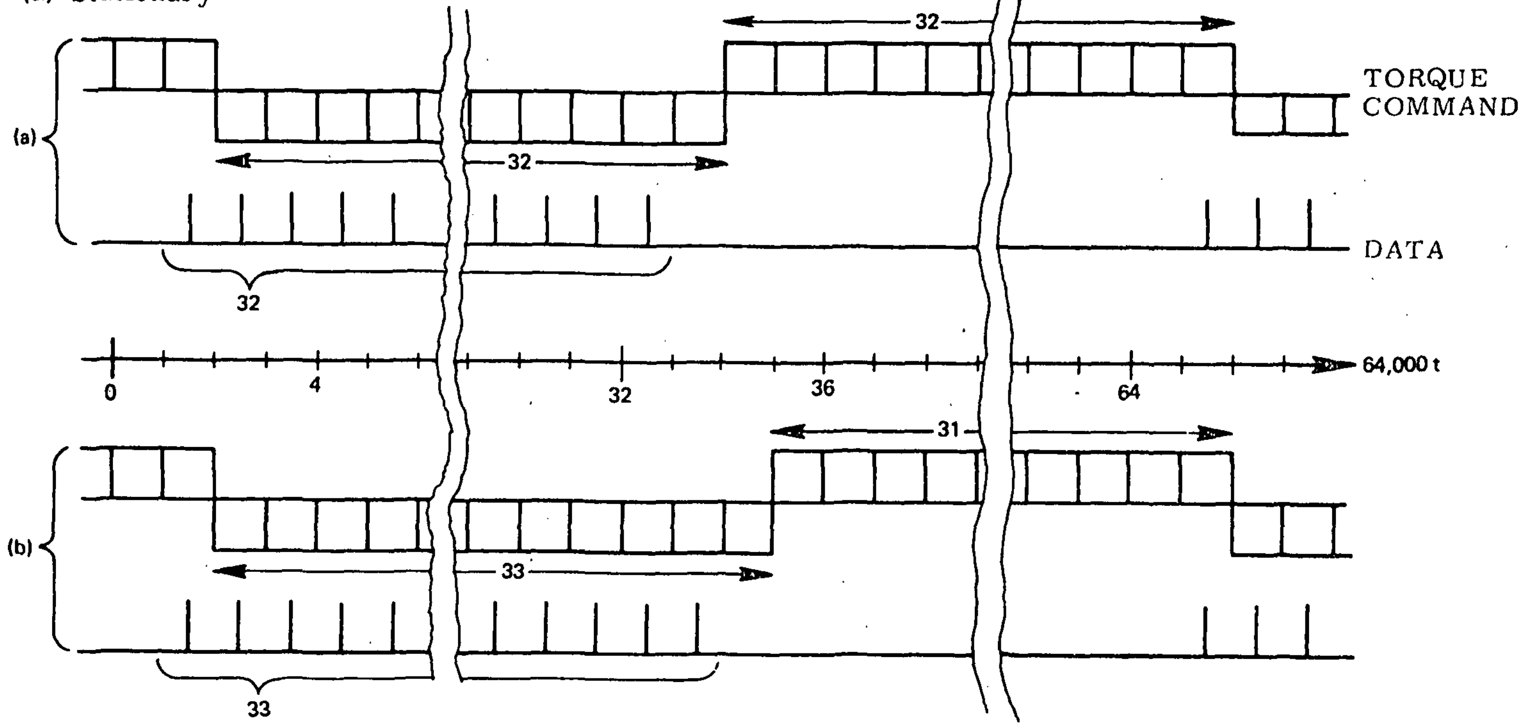

(b) One bit from null: motion indicated = 33-31 = $\underline{\underline{2}}$ increments

Fig. 1.4-7 Forced Binary Torque Generator Current and Data Pulses Showing Resolution

One problem with a forced binary PTL is that it has relatively large sampling error. The sampling errors for this loop outweigh the resolution errors at any significant rate. Sampling error occurs in a sampled data system when measurements are required at random times during the sample period. The error is the change in the measured variable between the time when the measurement is desired and the time when actual sampling takes place. Sampling and resolution errors are shown for the forced binary loop in Fig. 1.4-8(a). Fig. 1.4-8(b) shows the same errors for a SIRU ternary loop if it were to carry the same torque-coil current. It is clear that the forced binary cannot compete with SIRU (which samples every 206 microseconds) except at extremely low input rates.

1.4.4 Forced Binary Loop Tests

The principal testing of the forced-binary PTE was accomplished while connected to an 18 IRIG Mod B made by this laboratory. This inertial rate-integrating gyroscope was designed for our own strapdown inertial reference unit (SIRU). It is a size-eighteen instrument having electromagnetic suspension to restrain the float to a single degree of freedom. It has a microsyn signal generator to indicate float angle. In a strapdown mode, precession torque about its output axis is opposed by that from a permanent-magnet, moving-coil (d'Arsonval) torque generator. Table 1.4-II lists important constants for the 18 IRIG Mod B when used with 0.1 amperes coil current. The individual 18 IRIG Mod. B used was Serial Number 430B. It was chosen because it has an excellent history of stable performance over many months.

1.4.4.1 Scale-Factor Nonlinearity. The data for the forced binary nonlinearity will now be given. Fig. 1.4-9 shows scale factor deviation between plus and minus one half a radian per second. Each point is a 4-minute test and the entire range was repeated to give four complete curves in about 10 hours. As one can see, the linearity is good but the repeatability only fair. One of these curves from May 7th is shown in Fig. 1.4-10 along with two later runs taken after a shutdown of the PTE. The shift in scale factor at that time has not been explained, but since it was not repeatable, it may have been from an extraneous cause. Notice that the data from May 9th and 11th agree with each other as well as the May 7th runs agree with each other.

1.4.4.2 Scale-Factor Instability. The scale factor was measured repeatedly overnight at 0.1 radians per second with twenty revolutions per data point on two successive nights. The data is plotted in Fig. 1.4-11 to show the stability of scale factor.

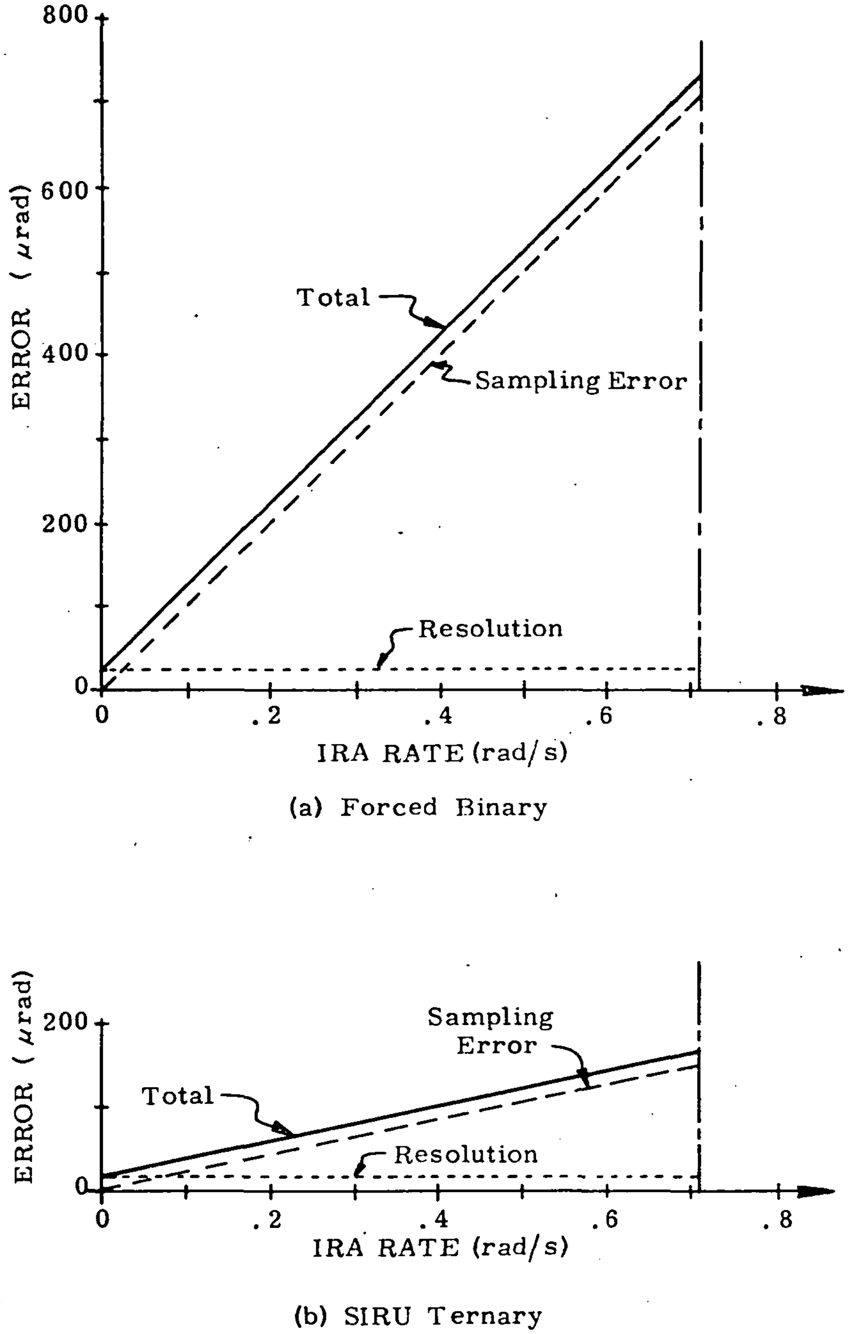

Fig. 1.4-8 Total Quantizer Error

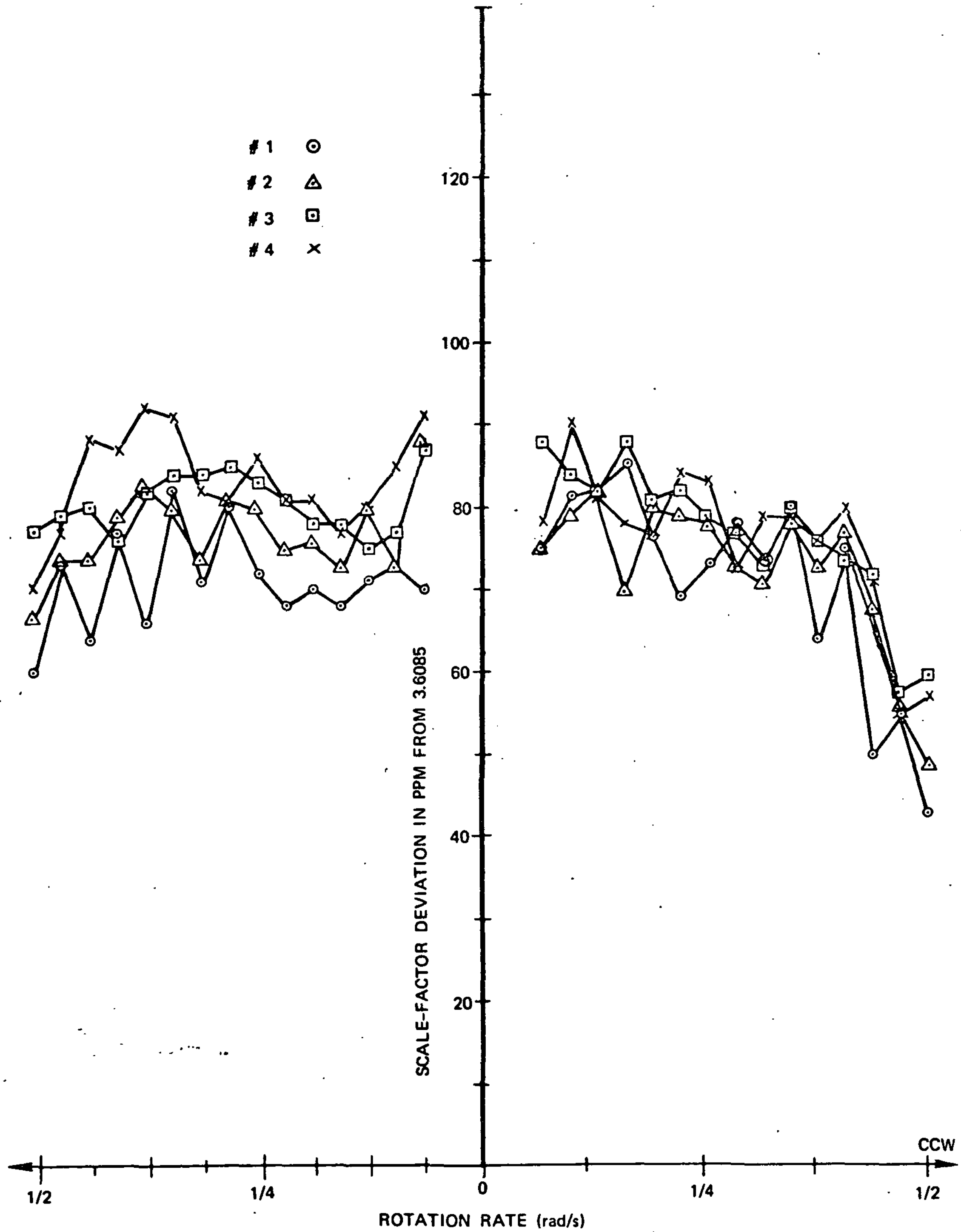

Fig. 1.4-9 Forced Binary Nonlinearity (Four Consecutive Runs)

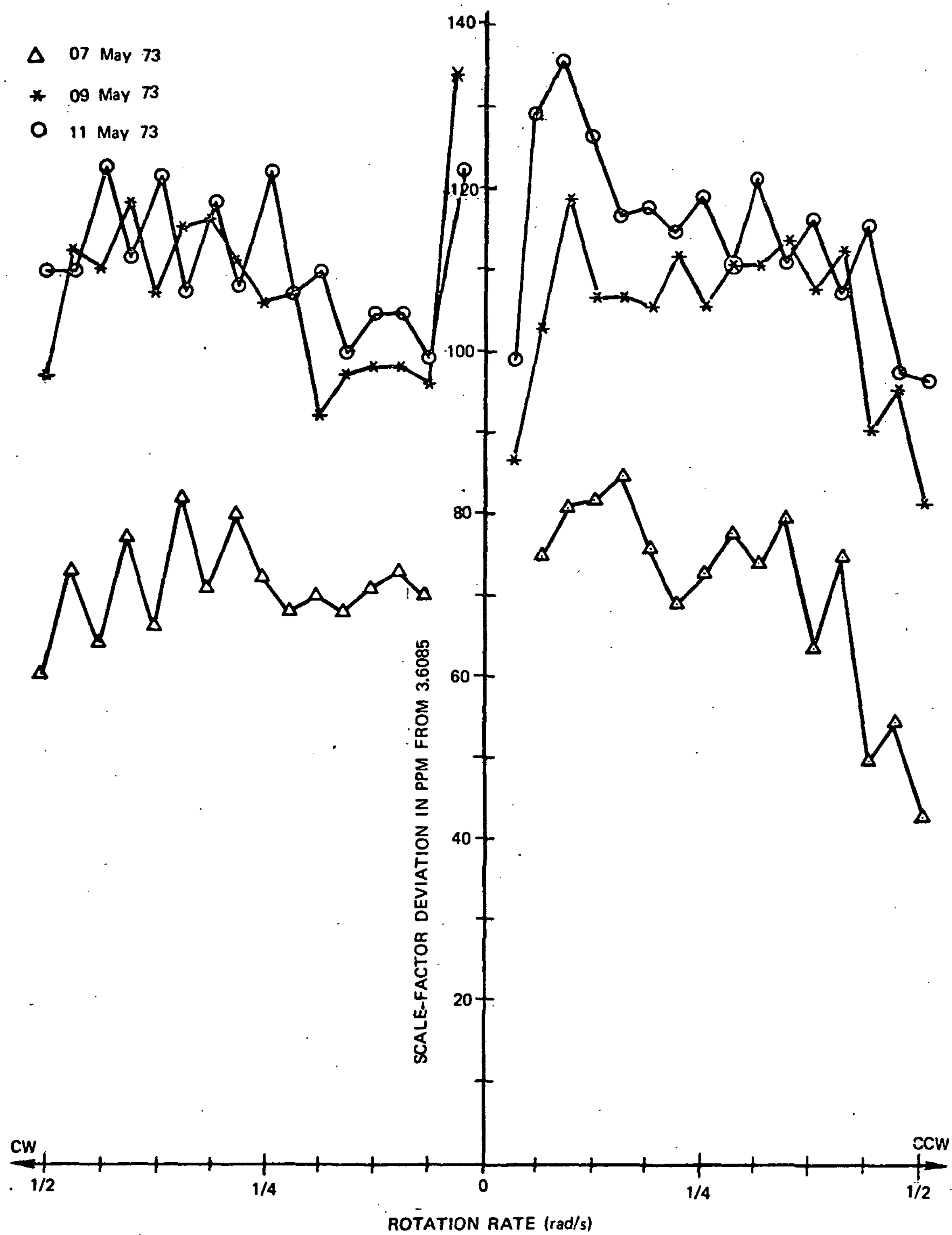

Fig. 1.4-10 Forced Binary Nonlinearity (Three Different Days)

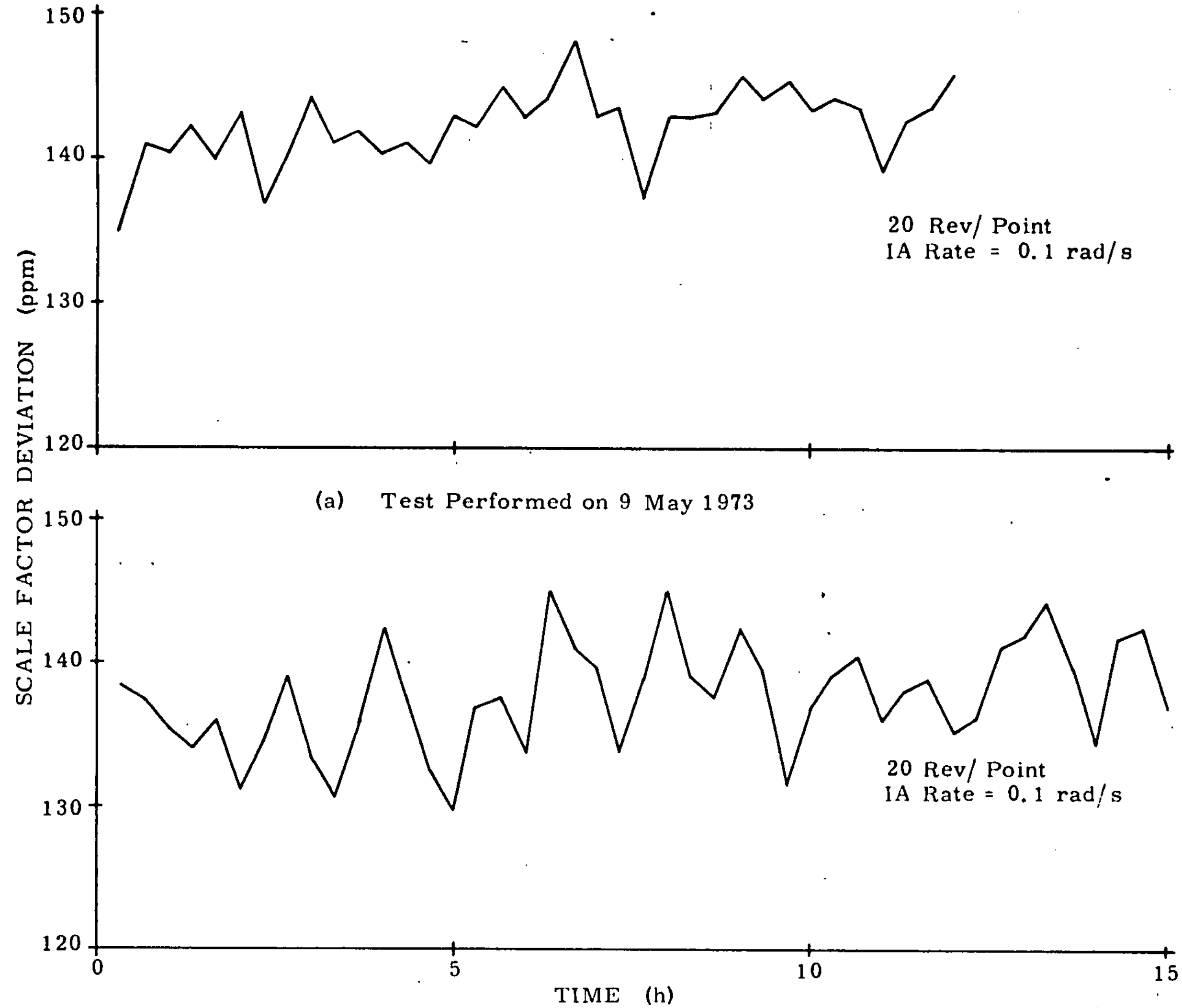

(a) Test Performed on 9 May 1973

(b) Test Performed on 10 May 1973

Fig. 1.4-11 Scale Factor Stability—Forced Binary Loop

This data does not have a discernable ramp or trend. It seems to us that the variations in scale factor in this form is consistant with the variations between consecutive nonlinearity tests. The variation is about 20 to 25 ppm pk-pk overall.

1.4.4.3 Static Instability. Results of the static instability test are shown in Fig. 1.4-12. In the main section of the figure, a graph of data counts per 15 minute interval is given. At the right-hand side is a frequency count of the numbers which occurred. The spread of the data is unexpectedly large. Being suspicious that the loop might be moding badly, we immediately ran a pulse pattern test with the gyro remaining stationary with results as in Table 1.4-III. The broad spread in mode pattern shown in the table explains the lack of static stability. Because the moding can be narrowed with better loop compensation, the lack of static stability could be improved and might not then be a serious problem. Zero-input moding and bias instabilities are still worse for binary than for ternary.

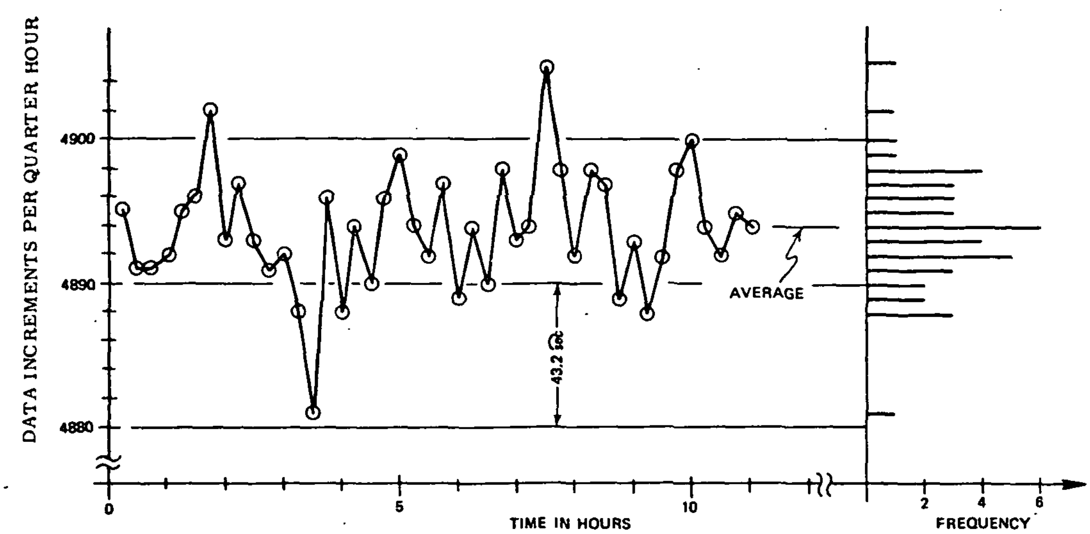

Fig. 1.4-12 Static Stability—Forced Binary Loop

TABLE 1.4-II

Important Constants of the 18 IRIG Mod B at 100 mA TG Current

Spin angular momentum, H,	150,000 dyne-cm sec/rad
Output-axis moment of inertia, I,	220 $gm\text{-}cm^2$
Output-axis damping, C,	700,000 dyne-cm sec/rad
Characteristic time, I/C,	315 microsec
Scale factor	7.62 rad/coulomb
Scale factor (at 15/16 duty cycle)	7.15 rad/coulomb

TABLE 1.4-III

Null Moding at Time of Static Instability Test

Data Count	Frequency
28	9
29	99
30	887
31	3245
32	4096
33	3319
34	878
35	102
36	10

1.5 PULSE-TORQUE LOOP TESTING

This section is a description of tests normally run to evaluate a pulse-torque loop (PTL). These tests include:

1. Scale-Factor Deviation
   a. Nonlinearity
   b. Instability
2. Drift Instability
3. Moding-Pattern Statistics

Each test uses a minicomputer to control equipment, collect data, and reduce data to engineering units.

1.5.1 Scale-Factor Deviation Tests

Scale factor is measured by rotating the gyro around its input axis by some precisely known angle and counting the increments of angle communicated by the gyro and PTE. We mount the gyro on a rate table with its input axis along the table axis and vertical. Rotation rate is under computer program control via a digital-to-analog converter. Table position is measured using a printed-circuit resolver and associated electronics which generate a pulse for each degree of travel. To attain maximum accuracy, each test is run over integral revolutions. Timing pulses are counted during the rotation so that motion of the earth and gyro drift can be accounted for in the known reference angle. Note in this latter regard that operation of the gyro with a binary loop can alter bias substantially: part of the test, therefore, must be to infer the closed-loop bias from the distinctive nonlinearity caused by uncorrected bias.

Sampling error is the dominant uncertainty in the scale-factor test of a PTE above about five percent of its maximum rebalance rate. This error can be quite significant with a forced-binary PTE because of the relatively infrequent sampling. Considering that this error increases with rate, one must increase in proportion the angle measured to maintain constant fractional error, requiring a constant time of test subject to the restriction to integral revolutions. Thus each test runs for a specified minimum length of time and then finishes out a full revolution.

1.5.1.1 Scale-Factor Nonlinearity Test. Scale-factor nonlinearity as used here is any variation of measured scale factor as a function of input-axis rotation rate. Our data is calculated as deviation from a given nominal scale factor in parts per million of the given value.

The linearity test program measures scale factor at sixteen equally-spaced angular rates in each direction. The rates are at sixteenths of a maximum commanded by the operator. Data typed out after each rate are direction, rate in radians per second, scale-factor deviation in parts per million, and the number of revolutions. At the end of all 32 points, a plot of scale-factor deviation versus rate is composed and drawn by the computer program.

1.5.1.2 Scale-Factor Instability Test. Scale-factor instability is defined here as the variation of scale factor with time when measuring at fixed rate and assuming constant drift. If, during an instability test, the gyro drift is found to be changing, the data is usually judged erroneous. In testing a binary loop, however, scale-factor shifts may result in a variation of plus-to-minus scale-factor difference. In a fixed-rate test, one can't distinguish between plus-to-minus difference and other changes in scale factor. The scale-factor instability for binary PTE's is reported without any distinction of cause. The static-instability test to be described next, however, can give some better insight into these instabilities.

1.5.2 Drift-Instability Test

Instability of drift is measured with the pulse-torque loop closed and the rate table held stationary. Data pulses per period of time (15 minutes or so) are counted repeatedly for a long time to determine how steadily the gyro and PTE can measure the earth's rotation.

1.5.3 Moding-Pattern Statistics

Moding- pattern tests measure statistics of the patterns in which pulses occur. This is done by counting the frequency of all the distinct patterns which occur during the test. For a ternary or fill-in binary loop below half rate, a pattern is defined as 1.) the number of consecutive on pulses, and 2.) the number of consecutive off pulses which immediately follow. Above half rate, the sequence of a pattern is the number of off pulses followed by the number of on pulses. For a binary delta modulator, the same test as ternary is used after eliminating the zero-rate moding. For a forced-binary loop, each different count of data pulses in a data cycle is considered a distinct pattern to be counted.

1.6 SUMMARY

This chapter describes the mechanizations and presented test results for the binary, ternary, and forced-binary torque-to-balance loops. The operating characteristics, performance, and representative test data were presented. It was shown that the ternary loop has a lower sampling error than the binary or forced-binary loops. For a system requiring continuous fine quantized data a ternary system is most applicable.

The binary and forced-binary systems have a bias drift due to the difference between the positive and negative scale factor. An instability in this scale factor difference causes a bias instability. Therefore, the binary loops will typically have a greater bias instability than ternary. However, the binary loops dissipate nearly constant power in the torque generator and, thus, have a smaller variation of scale factor with rate than the ternary type loop.

The chapter also described a hybrid fill-in-binary loop, which combines the constant power advantage of binary with the low sampling error of ternary. This loop as well as other loop mechanizations are possible for specific applications or improved performance.

REFERENCES

1. Chow, C.K.. Contactor Servomechanisms Employing Sampled Data, Ph.D. Thesis, School of Electrical Engineering, Cornell University, June 1953.

2. Lory, C.B., Compensation of Pulse-Rebalanced Inertial Instruments, M.S. Thesis, M.I.T. Department of Aeronautics and Astronautics, CSDL Report T-495, January 1968.

3. Lory, C.B., Feldman, J., and Sinkiewicz, J.S., Dynamic Testing of a Single-Degree-of-Freedom Gyroscope, CSDL Report E-2618, Section 2.1.2, October 1971.

4. Cooper, R., and Shuck, T., SIRU Development–Final Report–Gyro Module, CSDL Report R-746, Vol. II, June 1973.

5. Lory, op cit, pp 29-32.

CHAPTER 2

OUTPUT AXIS SUSPENSIONS FOR STRAPDOWN GYROSCOPES

2.1 INTRODUCTION

This program studied the effects of output axis (OA) suspensions on the performance of a gyroscope when used in a strapdown mode. Three types of OA suspensions were evaluated: pivot and dithered jewel (Honeywell GG334), magnetic (C. S. Draper Laboratory 18 IRIG Mod-B), and ball bearing (Kearfott 2544).

The results reported are based on tests of twelve 18 IRIG Mod B magnetically-suspended instruments, two GG334 pivot-dithered jewel units and one Kearfott 2544 ball-bearing suspension instrument. Because of the limited sample, the results should not be considered as describing the behavior of all instruments in the families tested. The results serve only as a guide for evaluation of OA suspension differences.

2.2 TYPES OF SUSPENSION

2.2.1 Magnetic Suspension[1]

Magnetically-suspended instruments make use of quasi-elastic magnetic supports to properly position the neutrally buoyant float within the case. A diagram of the magnetic suspension is shown in Fig. 2.2-1. Radial and axial centering is produced by action of the suspension magnetic field on the tapered surface of the rotor (Fig. 2.2-2).

A schematic of the suspension circuit is shown in Fig. 2.2-3. The four suspension coil pairs (P_1 & P_8, P_4 & P_5, P_3 & P_2, and P_6 & P_7) represent the effective inductances along orthogonal axes. The capacitors are typically mounted external to the instrument and provide the proper tuning so that stable magnetic restoring forces on the rotor will be obtained.

The underlying basis for the suspension circuit is the force exerted by an electromagnet:

$$F_r = \frac{1}{2} i^2 \frac{dl}{dg} \tag{2.1}$$

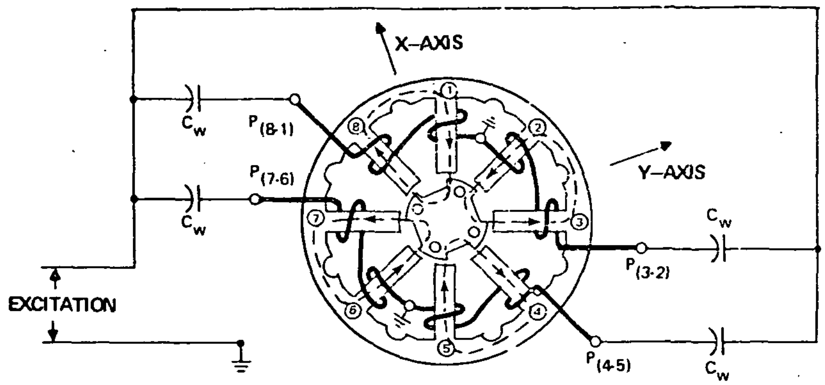

Fig. 2.2-1 Cross Section of One End of Instrument's Magnetic Suspension

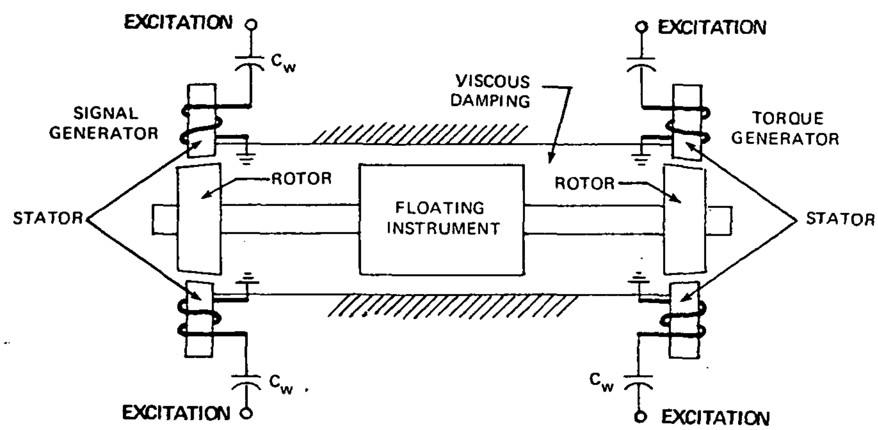

Fig. 2.2-2 Pictorial Representation of Magnetic Suspension

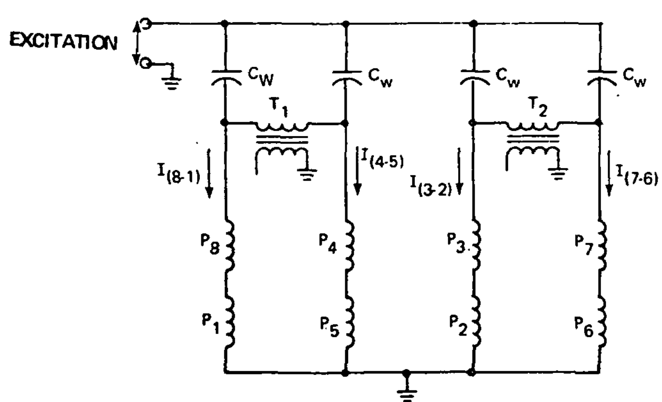

Fig. 2.2-3 Schematic of One End of Instrument's Magnetic Suspension

where:

F_r	=	restraining force on the rotor due to a stator pole
i	=	current in a stator winding
l	=	inductance of a stator winding
g	=	air-gap length

To establish a relationship between the suspension stiffness, or dF_r/dg, and the circuit parameters requires considerable algebraic manipulation[2]. The results of the derivations are summarized in Appendix A.

2.2.2 Pivot and Dithered-Jewel Suspension

The GG334 gyroscope uses piezoelectric dither plates to which ring jewels are mounted as its OA suspension. Two polarized, barium titanate/zirconate disks with polarities as shown in Fig. 2.2-4 are bonded together to form the dither plates. A ring jewel is mounted in the center of each disk assembly.

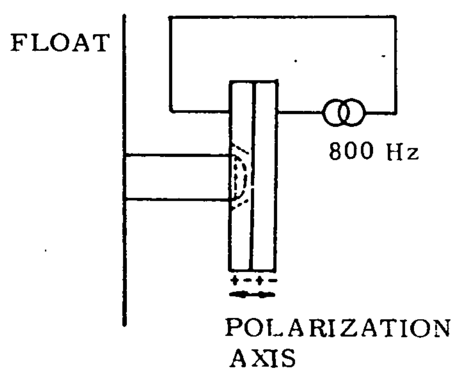

Fig. 2.2-4 Schematic of Piezoelectric Dither Disk Suspension

With the application of voltage, one disk expands while the other contracts, producing a "bender" mode of operation analogous to that of a bimetal strip. By utilizing the spin-motor excitation as the input voltage for the dither plate, a high frequency, 800 Hz dither is obtained. The ring jewel is thus placed in constant motion (with an amplitude of 100 microinches) relative to the pivot, resulting in a dynamic, low friction suspension.

2.2.3 Ball-Bearing Output Axis Support

Figure 2.2-5 shows a cross sectional representation of the ball-bearing OA support used on the Kearfott 2544 gyroscope. Since the friction of the ball bearing is a rolling friction, it will be less than the sliding friction obtained with a simple pivot jewel suspension.

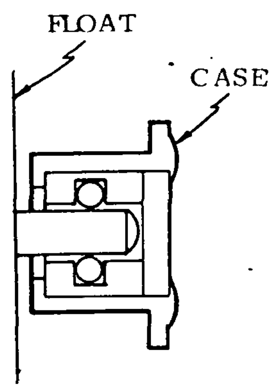

Fig. 2.2-5 Pivot and Ball Bearing Suspension

2.3 ANALYSIS OF OUTPUT AXIS UNCERTAINTY

2.3.1 Introduction

In the SDF gyro the OA suspension constrains the instrument's float axes with respect to the case reference axes.

The quality of this geometric restraint reflects in the performance of the gyroscope in that:

1. Sensing errors due to the float's geometric alignment uncertainties with respect to the case measurement reference axes may occur,

2. Sensing and torquing errors may result due to gap geometry changes that cause magnetic field variations, etc.,
3. The restraint technique itself may introduce frictional torque uncertainties about the OA axis which correspond to equivalent drift uncertainties.

Any inertial grade gyroscope must have low OA frictional uncertainty torques and maintain a fixed orientation between its case and float to ensure high level performance. A few sample calculations will better illustrate the magnitude of the frictional torques.

2.3.2 Output Axis Friction

2.3.2.1 Drift Uncertainty with Applied Output Axis Rate. When a gyroscope is subjected to an OA rate, the OA suspension is radially loaded due to the gyroscopic torque developed (OA rate times angular momentum). This torque can, in turn, produce a frictional uncertainty torque about the OA. The resulting frictional uncertainty drift rate is given by the following relationship:

$$W_f = \frac{\mu d W_{OA}}{L} \tag{2.2}$$

where:

W_f	=	drift error due to OA friction (rad/s)
μ	=	coefficient of friction
d	=	diameter of OA pivot (cm)
L	=	distance between the two OA supports (cm)
W_{OA}	=	angular rate about the OA (rad/s)

Note that the drift uncertainty due to OA friction is independent of the gyroscope angular momentum, but depends only on the geometry of the OA support and the OA rate. For low OA rates the drift error due to OA friction is small (less than 10^{-4} deg/h for the Kearfott 2544 or the Honeywell GG334 for an OA rate equal to earth rate, assuming the coefficient of friction is 0.0005). For a larger OA rate a proportionally larger drift error will occur. For an OA rate of 1 rad/s the theoretical drift error due to OA friction is approximately 1.2 deg/h for the Kearfott 2544 or the Honeywell GG334. Thus under this 1 rad/s OA rate the instrument could theoretically not detect IA rates of less than 1.2 deg/h. Under larger IA rates, the instrument will respond to the rate, but will have an error in the measurement of IA rate due to this OA friction. For example if both the IA and OA rates are 1

rad/s (assuming the same coefficient of friction as obtained for low OA loads) the frictional uncertainty torque will cause a 60 ppm scale factor error. If the IA rate is ten times the OA rate the OA friction will cause a scale factor error of less than 1 ppm. During a scale factor test, the IA is aligned with the rate vector and a very small OA rate would be expected. For a scale factor test OA friction should cause errors of much less than 1 ppm. For an instrument with a magnetic suspension, this error does not occur unless the OA rate exceeds the suspension capability.

2.3.2.2 Drift Uncertainty due to Flotation Error. When an imperfectly floated gyroscope is subjected to a linear acceleration, an OA frictional uncertainty torque is produced. The magnitude of this frictional drift uncertainty for a linear acceleration perpendicular to OA (rad/s) is given by:

$$D_f = \frac{r\mu UTa}{H} \tag{2.3}$$

where:

r	=	radius of OA pivot (cm)
μ	=	coefficient of friction
U	=	unfloated mass/^{o}F (gm/^{o}F)
T	=	difference between operating and floatation temperature (^{o}F)
H	=	angular momentum (gm-cm^2/s)
a	=	input acceleration (cm/sec^2)

Assuming a coefficient of friction of 0.0005, an error from floatation of 2^{o}F and a one g acceleration, a theoretical frictional uncertainty of .0014 deg/h would occur for the Kearfott 2544 and .0025 deg/h for the Honeywell GG334. For a magnetically suspended instrument, this error does not occur unless the magnetic suspension capability is exceeded by the radial acceleration acting on the unfloated mass.

2.3.3 Alignment Uncertainty

Due to the mechanical clearance in an OA suspension, an uncertainty in the location of the IA with respect to the case can occur. The magnitude of this alignment uncertainty is given by

$$e = \frac{2C_d}{L} \tag{2.4}$$

where:

e	=	alignment uncertainty (rad)
C_d	=	diametrical clearance of the OA support (in.)
L	=	length between OA supports (in.)

For the geometry of the Kearfott 2544 gyroscope (C_d = 30 microinches and and L = 2 inches), an IA alignment uncertainty of 6 seconds of arc is expected. For the geometry of the Honeywell GG334 gyroscope (C_d = 30 microinches, L = 3 inches), an IA alignment uncertainty of 4 seconds of arc is expected.

There is a displacement between the case and float of a magnetic suspension instrument under a dynamic environment. The float location is repeatable for a fixed input. Even though there is a change in IA position of a magnetic suspension instrument under dynamic inputs, there is not an uncertainty in the IA alignment.

2.3.4 Signal Generator and Torque Generator Gap Changes

A dynamic environment which results in float-to-case displacement changes both the signal generator and torque generator magnetic gaps. The signal generator gap change may cause a null shift and may change the magnitude of signal generator quadrature signal.

The torque generator sensitivity will change if the magnetic gap changes. A torque generator sensitivity change as large as 1 ppm per microinch of radial displacement was noted on some permanent-magnet torque generators[3]. Thus, to ensure small changes in torquer sensitivity, the OA suspension should restrict the radial travel. The diametrical clearance of 30 microinches for both the Kearfott 2544 and Honeywell GG334 should for a well designed permanent magnet TG ensure that the change in scale factor due to gap change would be less than 30 ppm. With careful design a small torque generator sensitivity change with radial displacement can be obtained. For example, in the present 18 IRIG Mod-B, tests have shown that for its torquer a radial travel of 400 microinches results in a sensitivity change of less 25 ppm. In general, care must be taken in the design of the torque generator to ensure low torquer sensitivity changes with radial displacement.

2.4 TEST TECHNIQUE AND TEST RESULTS

2.4.1 Pulse Torque-to-Balance Scale Factor Determination

For the three types of suspensions, the evaluation compared scale factor stability, scale factor rate linearity, IA alignment, drift stability and performance under a dynamic environment. All data except drift stability was measured on a ternary pulse torque-to-balance loop. The drift stabilities were measured in a stable azimuth test mode.

Pulse torque scale factor was measured using the test setup shown in Fig. 2.4-1. The gyroscope was operated in a ternary pulse torque-to-balance loop where each readout pulse corresponds to an incremental IA rotational angle. The computer counts these readout and table angle pulses, computationally removes the effect of earth rate and gyroscope drift and calculates the pulse torque scale factor (where scale factor is defined as the incremental IA angle per pulse). The computer can sequence the table through a number of rates with a digital-to-analog converter to determine scale factor variation, with IA rate.

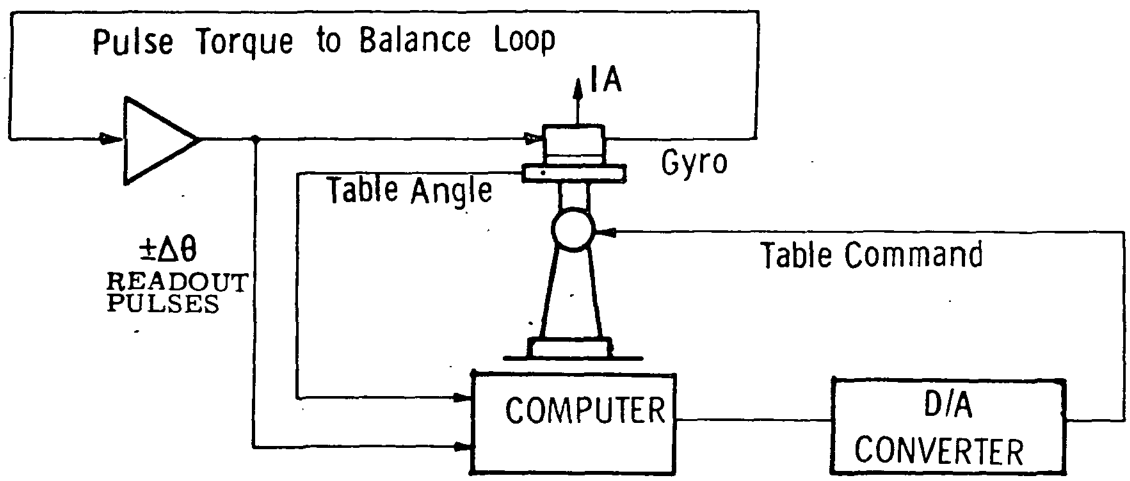

$$\text{Scale Factor (SF)} = \frac{\text{Input Angle}}{\text{Pulse}}$$

Fig. 2.4-1 Pulse Torque-to-Balance Scale Factor Test

Figure 2.4-2 (plotted to different scales) presents ternary loop scale factor stability for the three instruments. The magnetic suspension instrument had the best stability (3 ppm peak-to-peak for sixty (60) hours); the pivot dithered-jewel had the second best stability (10 ppm peak-to-peak for fifty (50) hours); and the ball-bearing OA suspension had the poorest data (50 ppm peak-to-peak for seven (7) hours). As shown in Section 2.3.2.1, less than 1 ppm of the scale factor instability for the 2544 and GG334 gyros could be caused by OA friction. As shown in Section 2.3.4, 30 ppm of scale factor uncertainty are possible due to uncertainty in the torquer gap for the 2544 and GG334. Thus, their scale factor instabilities could be caused primarily by torquer sensitivity changes with gap changes, an effect which could be reduced in an improved design. In addition, the Kearfott 2544 exhibited a consistent history of torquer instabilities. These are discussed in detail in Chapter 3. This scale factor instability is probably not the result of its OA support but reflects design problems for this specific instrument.

2.4.2 Scale Factor Rate Linearity

The variations in torque loop scale factor with rate for the three OA suspensions are shown in Fig. 2.4-3. Studies described in Chapter 4 of this report show that the scale factor changes with rate are primarily due to the torque loop, power dissipation in the torque coil and the torque-coil tuning. The differences in scale factor linearity for the three gyroscopes are not significant and probably result from the differences in the above three areas.

2.4.3 Drift Stability

The drift stability of a gyroscope is proportional to its OA. Since the magnetic suspension prevents OA friction, a gyroscope with this type of OA suspension should yield better drift stability than either a ball bearing or dithered jewel OA support.

Short-term bias stability was measured for the three types of friction. Instruments in a stable azimuth mode. The test measured drift stability for approximately one hour and tests were performed for various orientations with respect to gravity on each instrument. Suspension loads resulted from the quantity of unfloated mass. The error from floatation temperature was less than $2^{\circ}F$. The magnetic suspension had the best short-term stability (less than 0.0015 deg/h); the pivot-dithered jewel suspension had the second best performance (less than 0.003 deg/h); and the ball-bearing suspension had the poorest stability (less than 0.015 deg/h). These test results agree with the theoretical calculation for an OA friction uncertainty (Section 2.3.2.2) for the GG334, and are an order of magnitude poorer

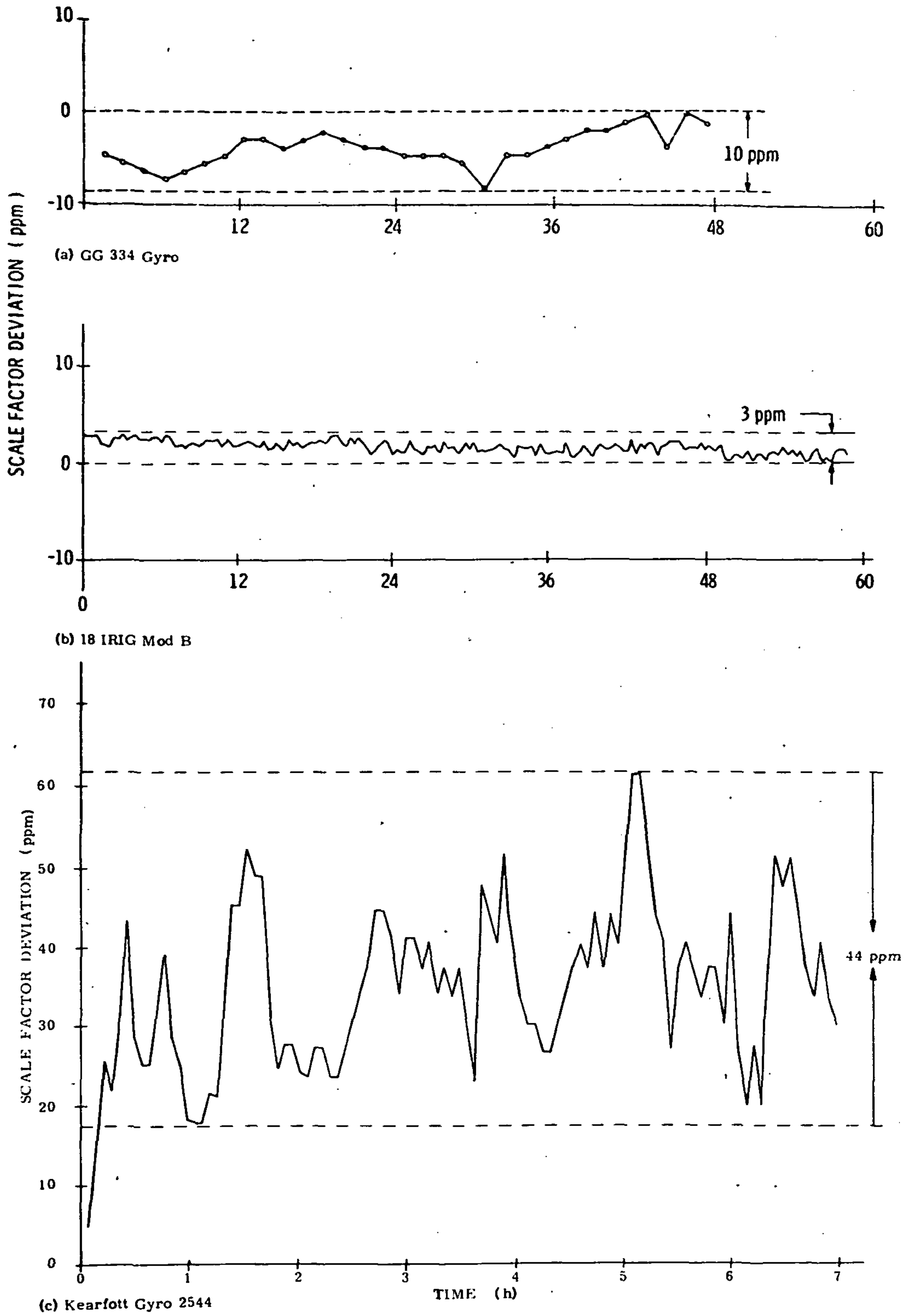

Fig. 2.4-2 Scale Factor Stability - Ternary Loop

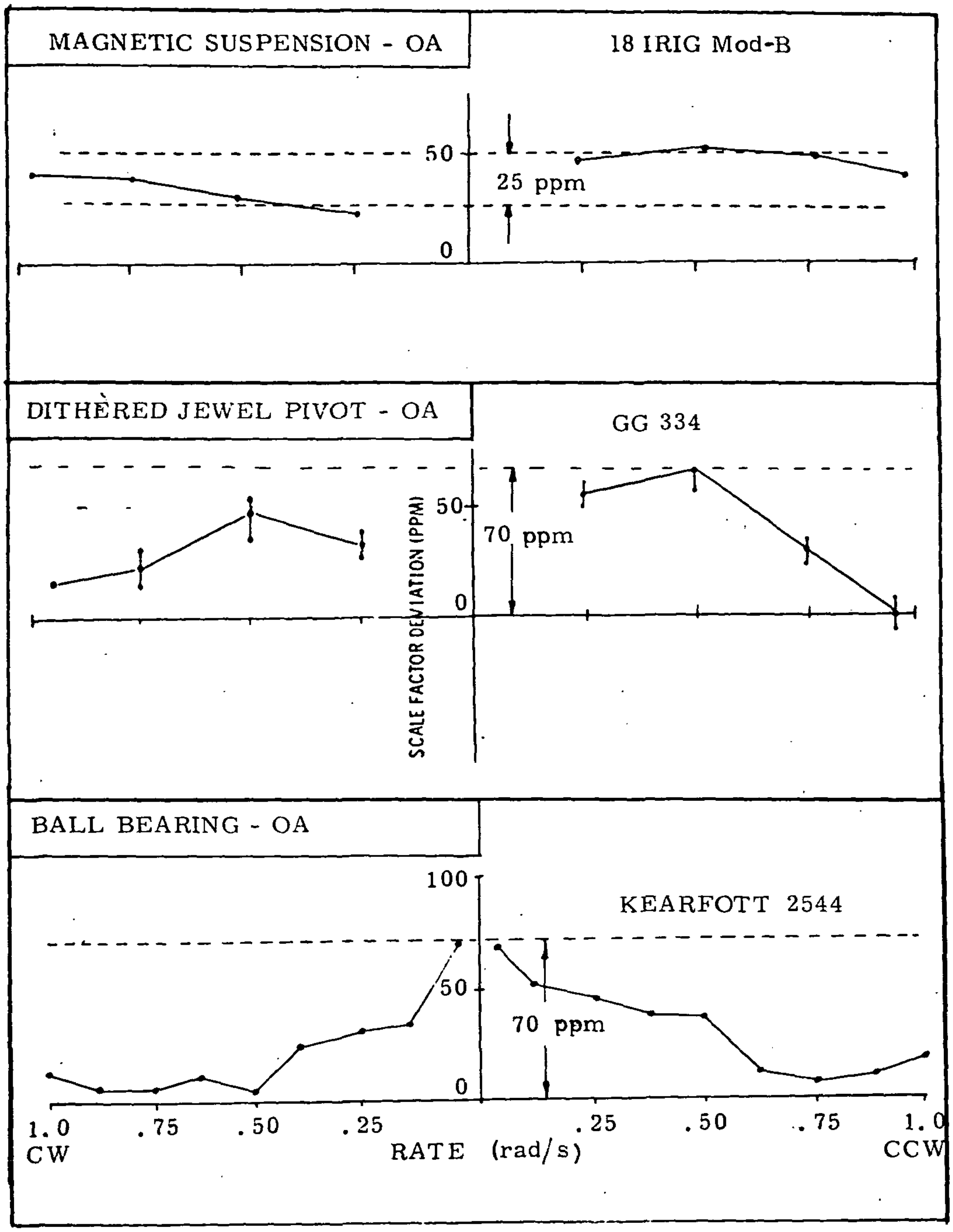

Fig. 2.4-3 Scale Factor Rate Linearity-Ternary Loop

than the calculations for the Kearfott 2544. This would indicate that the drift instability for the Kearfott 2544 is due to an effect other than OA friction, or its coefficient of friction is an order of magnitude greater than anticipated.

2.4.4 Input-Axis Alignment

Due to the clearance between the float and its case an uncertainty can exist in the location of the IA. This clearance will differ for each type of OA support. The ball-bearing and pivot-dithered jewel suspensions have an unrestrained "free play" OA, while the OA for the magnetic suspension are elastically restrained. A rate applied to the instrument's case about its OA will cause a torque on the float about its IA. This will result in motion within the OA clearance for the ball-bearing or pivot-dithered jewel suspensions or restrained motion for the magnetic suspension. Figure 2.4-4 illustrates the test setup used to measure the effects of OA rate on the gyroscope IA position. Since the OA is not parallel to the table axis, a component of table rate is sensed by the gyroscope IA. (This is actually a misalignment of the IA about the spin reference axis (SRA)). When the table is rotated at a constant rate, the component of OA rate, causes a torque about the IA. The float will move due to the clearance or suspension stiffness and an uncertainty in IA misalignment about the spin axis (SA) could result.

Figure 2.4-5 shows the results for the three suspensions driven at various OA rates. The magnetic suspension had a linear change with rate with an uncertainty of less than 0.1 second of arc. The change was repeatable and could be minimized by suspension capacitor adjustment (see Section 2.4.5). The pivot-dithered jewel had an uncertainty of 8 seconds of arc, while the ball bearing had an uncertainty of 7 seconds of arc. It should be noted for dithered and ball-bearing OA supported units, the alignment would vary between these uncertainties from test to test, and a different alignment versus rate curve would result in each case, bounded by these uncertainties. These magnitudes correspond reasonably well to those predicted in Section 2.3.3 for the ball-bearing suspension, and indicate a jewel to pivot clearance of 60 microinches for the pivot-dithered jewel suspension.

2.4.5 Magnetic Suspension Behavior under Output-Axis Rate

When a magnetically-suspended gyroscope is rotated about its OA, the IA alignment about the SRA also changes. Test results will now be presented for this magnetic suspension characteristic and methods of reducing the alignment change will be discussed. The theoretical analysis for this effect on the 18 IRIG Mod-B magnetic suspension is shown by Salamin in Appendix A.

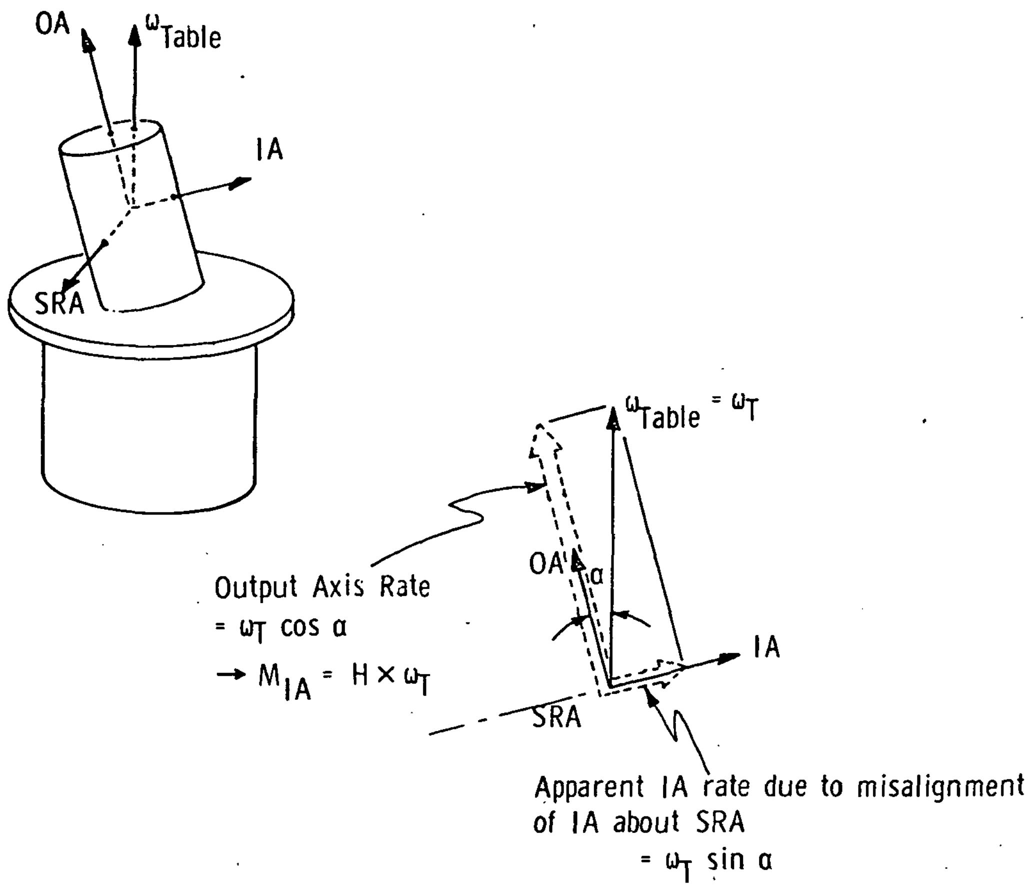

Fig. 2.4-4 Measurement of Input Axis Misalignment

An 18 IRIG (magnetic suspension) was rotated about its OA at rates up to 1 rad/s and was operated in a pulse torque-to-balance mode. The number of torque pulses per table revolution yields the misalignment of the gyroscope IA from the plane perpendicular to the table axis. This result is shown in the upper half of Fig. 2.4-6 where it is seen that this misalignment angle changed essentially linearly by 4 seconds of arc between the extremes of input.

Why this phenomenon occurred posed a problem: an input rate about the OA requires a torque about IA to be supplied by the suspension. This torque is a function of rate so there will be a rate dependent rotation of the float about IA with no attendent IA alignment change. However, we experimentally observed an IA alignment change, i.e., a rotation of the float about SRA. The IA alignment change would have required a suspension torque about SRA, but there is no apparent origin for such a torque.

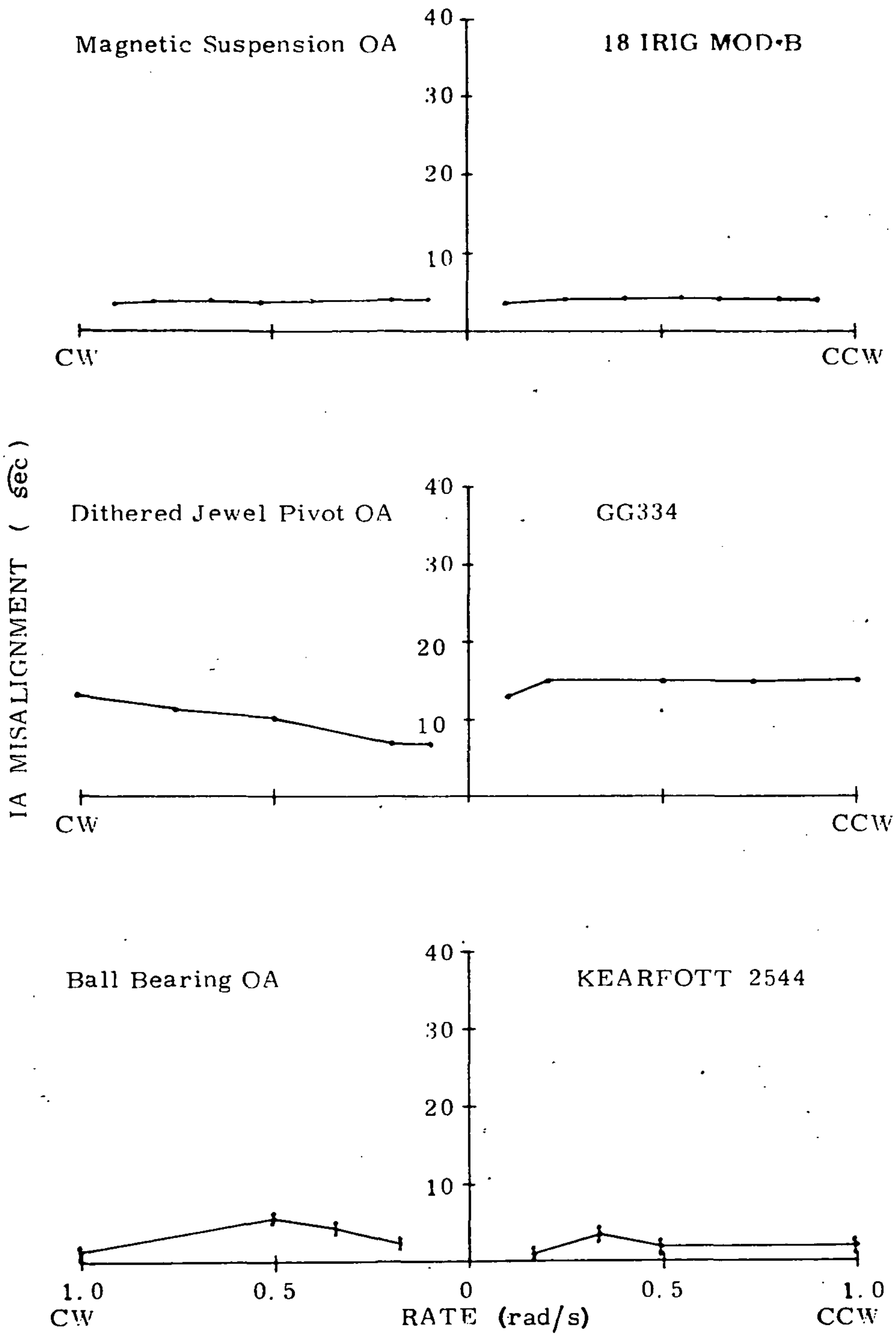

Fig. 2.4-5 Change in Apparent IA Misalignment vs Output Axis Rate

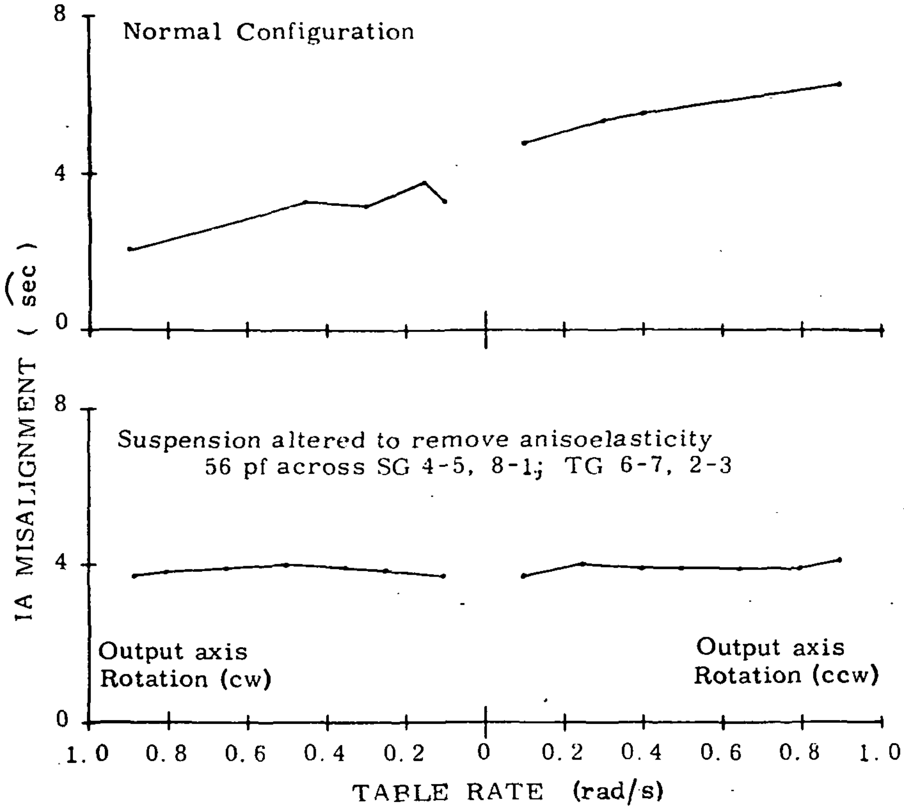

Fig. 2.4-6 Change in Apparent IA Misalignment vs Output Axis Rate-Magnetic Suspension

The answer to this problem is that the torque purely about IA causes a rotational displacement partly about SRA because of anisoelasticity of the suspension, i.e., the suspension stiffness in two principal directions is different. That is, the suspension force gradients in all directions are not equal.

Figure 2.4-7 shows a simplified diagram of the magnetic suspension. Each spring represents two adjacent poles (shown in Fig. 2.2-1) which are in series with the same working capacitor. If the springs all had the same coefficient of elasticity no IA alignment shifts would be observed. Changing the capacitor will change the stiffness of the springs corresponding to a pole pair. By changing a set of four of the eight capacitors corresponding to axis (e.g., 6-7, 2-3 on SG end and 4-5, 8-1 on the TG end) as indicated in Fig. 2.4-7, by equal amounts, the elasticity of suspension can be modified to equal the spring constant of the other axis. An anisoelastic suspension is then achieved without changing the equilibrium position of the float.

To demonstrate the suspension anisoelasticity effect an extra 610 pF was added to the nominal 14 nanofarads (nF) on the gyroscope in test. The results are shown in Fig. 2.4-8. The IA alignment about SRA changed by 45 seconds of arc over the extremes of input.

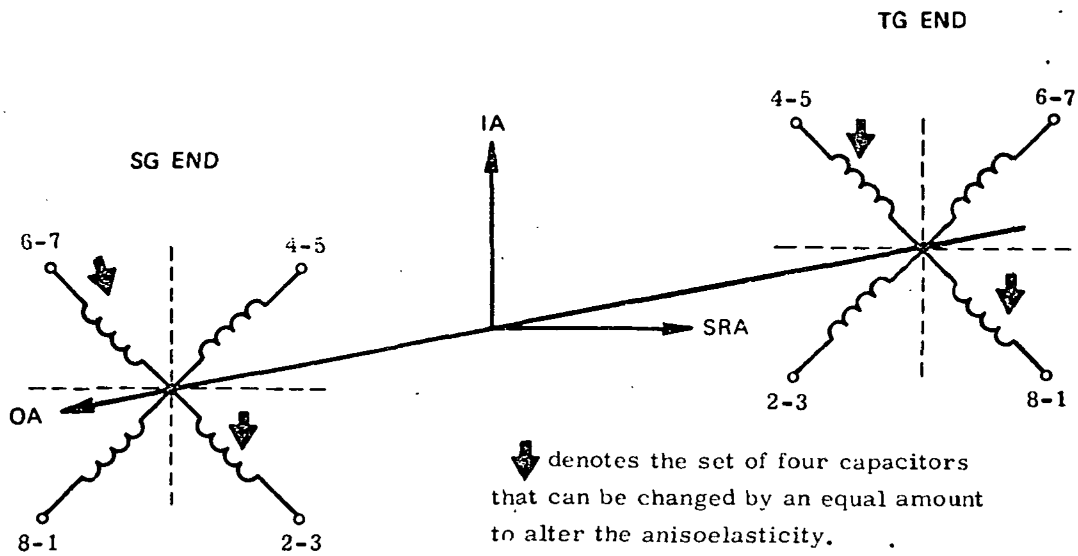

Fig. 2.4-7 Simplified Diagram of Float Suspension

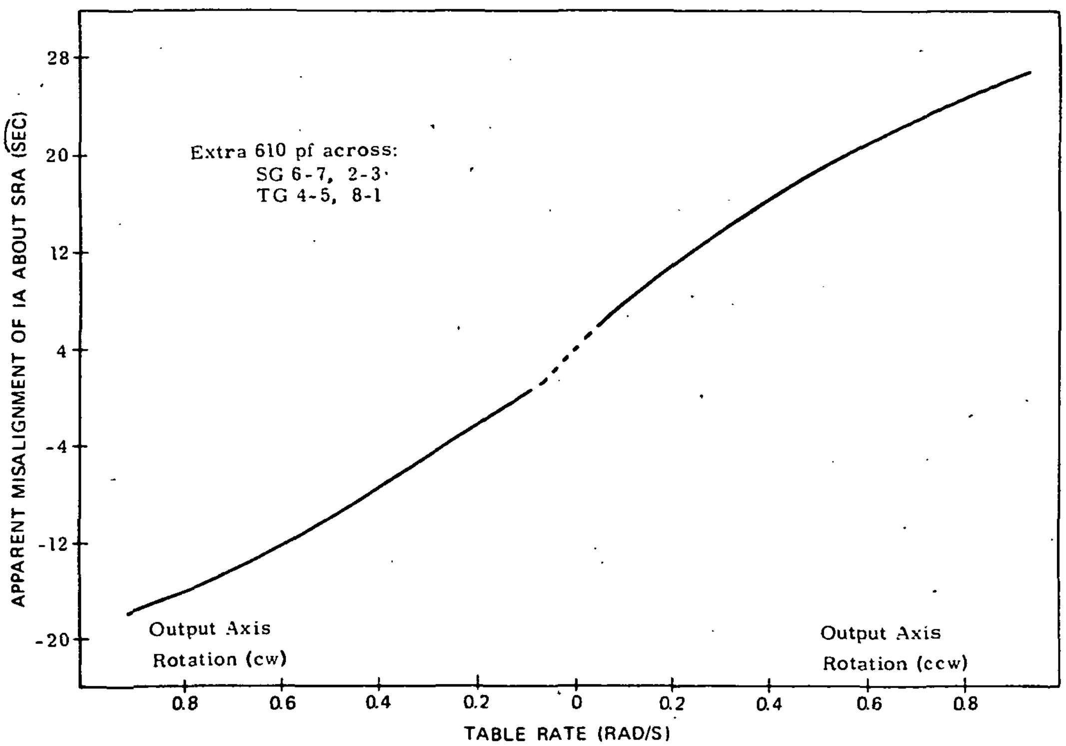

Fig. 2.4-8 Change in Apparent IA Misalignment vs Output Axis Rate-Modified Magnetic Suspension

By linear extrapolation from the two results described in Figs. 2.4-6 and 2.4-8 one would expect that the anisoelasticity would be eliminated by adding in parallel an extra 56 pF to the other set of four capacitors. With this change the resultant IA alignment about SRA, Fig. 2.4-6 lower curve, was reduced to about 0.4 second of arc over the extremes of input.

It is also seen from these three tests that the IA alignments at zero table rate was within 0.8 second of arc of each other demonstrating that the stiffness changes were achieved without altering the equilibrium position of the float.

A theoretical analysis (Appendix A) calculates the change in IA alignment (about SRA) due to an unbalance in the suspension capacitors. The theoretical analysis agreed well with the above test results.

It was seen that the anisoelasticity in the unit under test could be removed by a change of 56 pF out of 14 nF, or 0.4 percent, in four of the working capacitors. Since the tolerance on the suspension capacitors require equality of the eight capacitors to be within 0.5 percent, it is quite reasonable that the anisoelasticity obtained may be due to capacitor mismatch.

In conclusion, the phenomenon of float rotation about SRA under OA rate can be attributed to suspension anisoelasticity and can be eliminated by trimming the suspension capacitors. To change the anisoelasticity and nothing else requires an equal change in four capacitors. Other types of changes to capacitors can have effects such as translation and rotation of the float equilibrium position.

2.4.6 Oscillatory Testing

The three instruments were all tested under single axis IA, OA and IA-SRA oscillations. The test results do not differ for the three types of suspensions, and are more dependent on the characteristics of the torque loop. These dynamic test results are discussed in greater detail in Chapters 3 and 4 of this report.

2.5 SUMMARY AND CONCLUSIONS

The results of the test evaluation of the three output axis supports are summarized in Table 2.5-I. We believe the results may be typical for these types of suspensions. Due to the limited tests the results should not be expected to categorize all instruments of this class. The magnetic suspension instrument had the best scale factor stability, alignment stability and short-term drift stability.

Table 2.5-I

Summary of Test Results on Output Axis Suspensions

	OUTPUT AXIS SUSPENSIONS		
	MAGNETIC SUSPENSION	DITHERED JEWEL-PIVOT	BALL BEARING
SF Stability** (ppm) (without turn-off)	3	10	50-200
SF Rate Linearity**	Same	Same	Same
IA Alignment Stability (sec)	0.5	8	7
Short Term Drift Stability* (deg/h)	<0.0015	<0.003	<0.015

* After calibration and continuous operation (no shutdown) measured in stable azimuth mode.

**Measured with ternary torque-to-balance loop.

The pivot dithered jewel suspension had a scale factor stability of 10 ppm, a short-term drift stability of less than 0.003 deg/h, and an IA alignment stability of eight seconds of arc. These levels of alignment drift and scale factor stabilities are adequate for many applications (i.e., boosters). The ball-bearing OA suspension had an alignment stability of seven seconds of arc, and a short term drift stability of better than 0.015 deg/h. The ball-bearing unit had 50 to 200 ppm of scale factor instability due to other causes and thus could not be evaluated for suspension effects on scale factor. The drift and alignment stabilities for the ball-bearing OA suspension instruments are also adequate for many applications. The greater stabilities obtained with the magnetic suspension would be applicable to precision attitude reference system applications.

REFERENCES

1. Bukow, G., The PIPA (Pulsed Integrating Pendulous Accelerometer), CSDL Report E-2334, September 1968.

2. Gilinson, Jr., P.J., Denhard, W.G., and Frasier, R.H., A Magnetic Support for Floated Inertial Instruments, CSDL Report R-277, April 1960.

3. Gilmore, J.P., et al, Control, Guidance, and Navigation for Advanced Manned Missions, Vol. IV, Inertial Subsystem (Structure Mounted Studies), CSDL Report R-600, January 1968.

CHAPTER 3

STATIC AND DYNAMIC TESTING OF
THE KEARFOTT 2544
SINGLE-DEGREE-OF-FREEDOM
STRAPDOWN GYROSCOPE

3.1 INTRODUCTION AND BACKGROUND

3.1.1 Introduction

This chapter describes the C.S. Draper Laboratory test evaluation performed on the Singer Kearfott 2544 gyroscope in both static and dynamic environments. A description of the instrument and the test facilities precede the discussion of the test results.

The static test evaluation established instrument integrity and formed a performance baseline. The initial tests measured the unit's drift stability and repeatability in both an inertial reference (servo) and pulse torque-to-balance mode. Next, tests were run to evaluate the instrument's performance under constant rate inputs. These tests determined the dc and pulse torque (ternary and binary) scale factor stability and deviation with rate.

The dynamic test evaluation determined the apparent average drift rate indicated by a pulse-rebalanced gyroscope when subjected to angular oscillations. This apparent drift rate results from the gyroscope, the rebalance loop and their interaction. Test data, supported by an analysis, shows the gyroscopic response for single-axis and in-phase,two-axis oscillations.

The results and conclusions for this test phase, are based upon a sequence of evaluation tests performed on one instrument. They do not attempt to categorize the Kearfott 2544 family.

3.1.2 The Kearfott 2544 Gyroscope

The Kearfott 2544 gyroscope is a floated, single-degree-of-freedom, strapdown instrument. Figure 3.1-1 shows its dimensions and electrical schematic, and Tables 3.1-I and 3.1-II list a number of its operational and performance parameters as quoted by Singer-Kearfott Systems Division. (Publishing of this performance data in this report does not infer CSDL verification except as indicated in the text.) Its

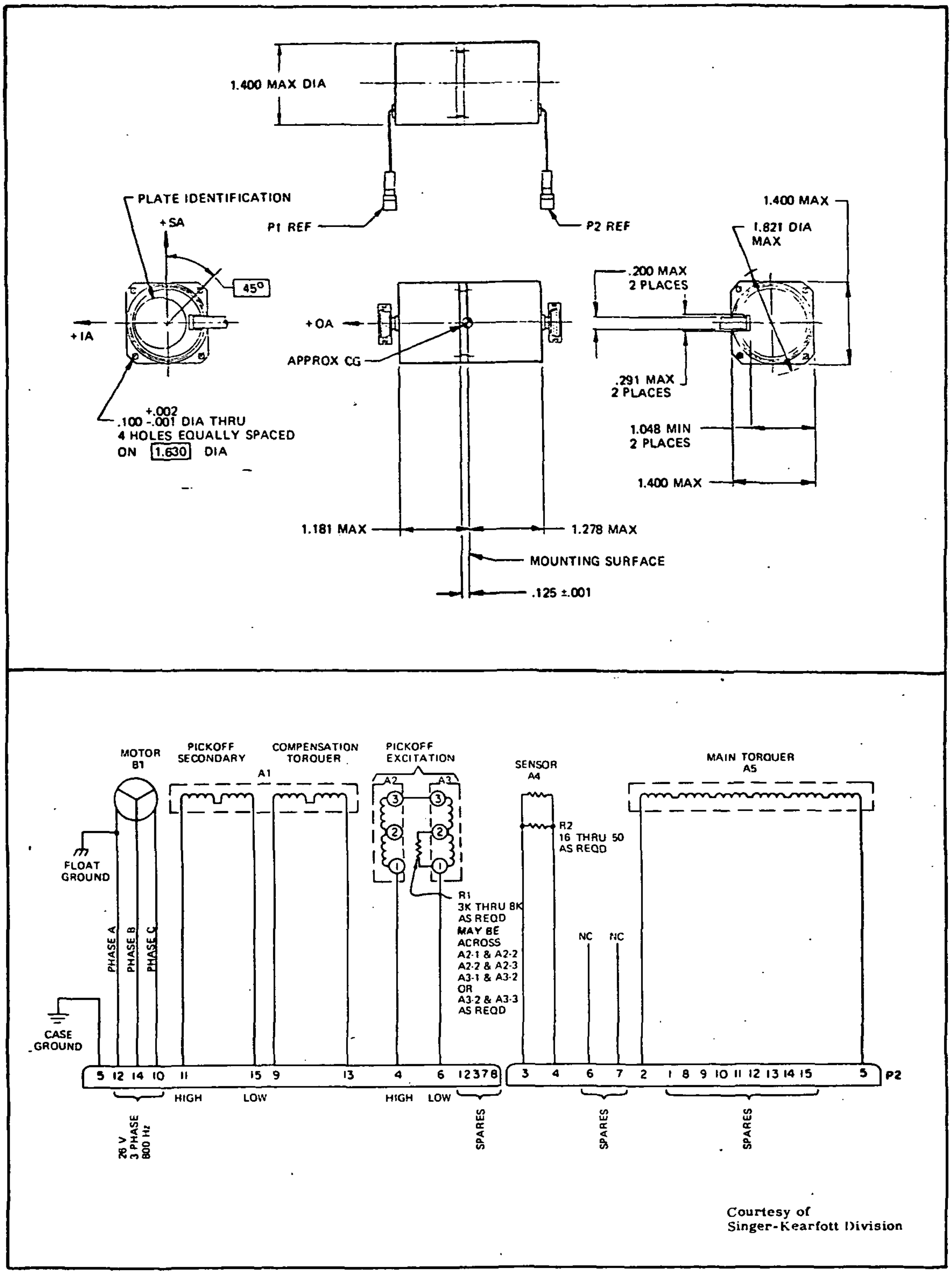

Fig. 3.1-1 Kearfott 2544- Outline Dimensions and Schematic Diagram

Table 3.1 - I
Kearfott 2544-Performance and Environmental Nominal Characteristics*

PARAMETER	2544	
Angular Momentum (H)	6×10^4	$gm\text{-}cm^2/s$
Output Axis Damping (C)	3×10^5	dyne-cm-s
Input Axis Inertia	104.2	$gm\text{-}cm^2$
Output Axis Inertia (I)	60	$gm\text{-}cm^2$
Spin Axis Inertia		
Total	108.9	$gm\text{-}cm^2$
Rotor	25.2	$gm\text{-}cm^2$
Characteristic Time (I/C)	0.0002	s
Gimbal Freedom	±0.375	deg
Operating Temperature	160	^oF
Size		
Length	2.46	in.
Diameter	1.4	in.
Weight	0.64	lb
Spin Motor Power		
Start	3.5	W
Run	2.5	W
Torque Generator		
Sensitivity	1600	deg/h/mA
Maximum Torquing Rate (continuous)	1.75	rad/s
Time Constant	0.00004	s
Auxiliary Torque Generator		
Scale Factor	135	deg/h/mA
Heaters	None	
Telemetry Sensor		
Resistance at Operating Temp.	814.1	Ω
Pickoff Sensitivity	238	mV/deg
Pickoff Preamplifier Time Constant	0.000055	s

* As published by Singer-Kearfott Division (Ref. 1, pp. 6-12)

Table 3.1 - II
Kearfott 2544-Mechanical and Dynamic Nominal Characteristics*

PARAMETER	2544
Fixed Torque	
Magnitude	± 2.0 deg/h
Stability	
Day-to-Day	± 0.1 deg/h
One Year	± 0.45 deg/h
Random Drift (OAV)	0.01 deg/h (1σ)
G-Sensitive Torque	
Magnitude	3.0 deg/h/g
Stability	
Day-to-Day	± 0.15 deg/h/g
One Year	± 1.0 deg/h/g
G^2-Sensitive Drift	
Anisoelastic (10-2000 Hz)	0.05 deg/h/g^2
Environmental Capability	
Storage Temperature	0 to 200 °F
Vibration (peak)	50 g
Acceleration	150 g
Shock	200 g

* As published by Singer-Kearfott Division (Ref. 1, pp. 6-12)

ball-bearing wheel rotates at 24,000 rpm, developing an angular momentum of 60,000 g-cm^2/s. A four-pole, 800-Hz, three-phase synchronous motor drives the wheel. The wheel and motor structure are mounted in an hermetically-sealed, cylindrical float surrounded by high density fluid. The output-axis alignment is maintained by ball bearings. The instrument requires an external heat source to maintain operating temperature. The thermal path is through the instrument's center mounting flange from the external heater. At operating temperature, the float is near neutral buoyancy.

The signal generator (SG) consists of an air-core, differential transformer that is excited with 9.0V (rms) at 19.2 kHz. Its output is proportional in magnitude and phase to the angular position of the float about the output axis. The torque generator (TG) consists of a case-fixed, permanent magnet with two independent windings mounted on the gyroscope float. The high sensitivity winding is used in

the pulse-rebalance loop. The winding with the lower sensitivity is available for use in compensating for earth rate or gyroscope drift.

3.2 STATIC AND CONSTANT-RATE TESTS

Initially, component level, inertial reference (servo) mode tests on the 2544 gyroscope were conducted to establish the unit's drift stability (long and short term) and repeatability. The tests were run with two different signal generator excitations. The tests run with the SG excitation of 9.0V (rms) at 19.2 kHz, provided a performance comparison with past Kearfott data. The tests run with the SG excitation of 8.0V (rms) at 9.6 kHz, enabled a comparative basis for evaluating the instrument's performance with the ternary and forced-binary torque-to-balance loops. The constant-rate tests determined dc and pulse torque (ternary and binary) scale factor (SF) stability and deviation with rate.

Determination of the gyroscope and loop performance, over the full spectrum of strapdown inputs, is necessary to adequately simulate performance for a system application. It should be noted that the 2544 gyroscope is a typical single-degree-of-freedom, floated instrument. Test findings are generally applicable to many similar gyroscopes. Performance problems presented provide insight for further gyroscope and electronic design improvement.

3.2.1 Static and Constant-Rate Test Facility

The static and constant-rate test facility consists of a gyroscope rate table and a console adapted for this program. A block diagram illustrating the functional elements of the controls, various test monitors, and support equipment is shown in Fig. 3.2-1. The drift evaluation tests were performed in both an inertial reference (servo) mode and a fixed position pulse-rebalance mode. In the inertial-reference mode the servo loop drives the table to oppose earth rate and gyroscope drift. In the pulse-rebalance mode the instrument is oriented in a fixed position and the pulse torque-to-balance loop (PTBL) applies pulses of current to the torque coil at a rate proportional to the gyroscope drift and input rate. For ternary scale-factor stability and scale factor (SF) deviation with rate testing, the table was driven at the desired rate and the number of gyroscope incremental angle pulses ($\Delta\theta$) were counted for a preset accumulation of table angle pulses generated by the table-angle readout. Since the outputs (table angle and gyroscope pulses) from this test occur as pulses, they can be interfaced directly to a digital computer allowing for on-line computation of the test data. Figure 3.2-2 illustrates the method used to perform this function with a small PDP-8/L computer. A computer program, while accounting

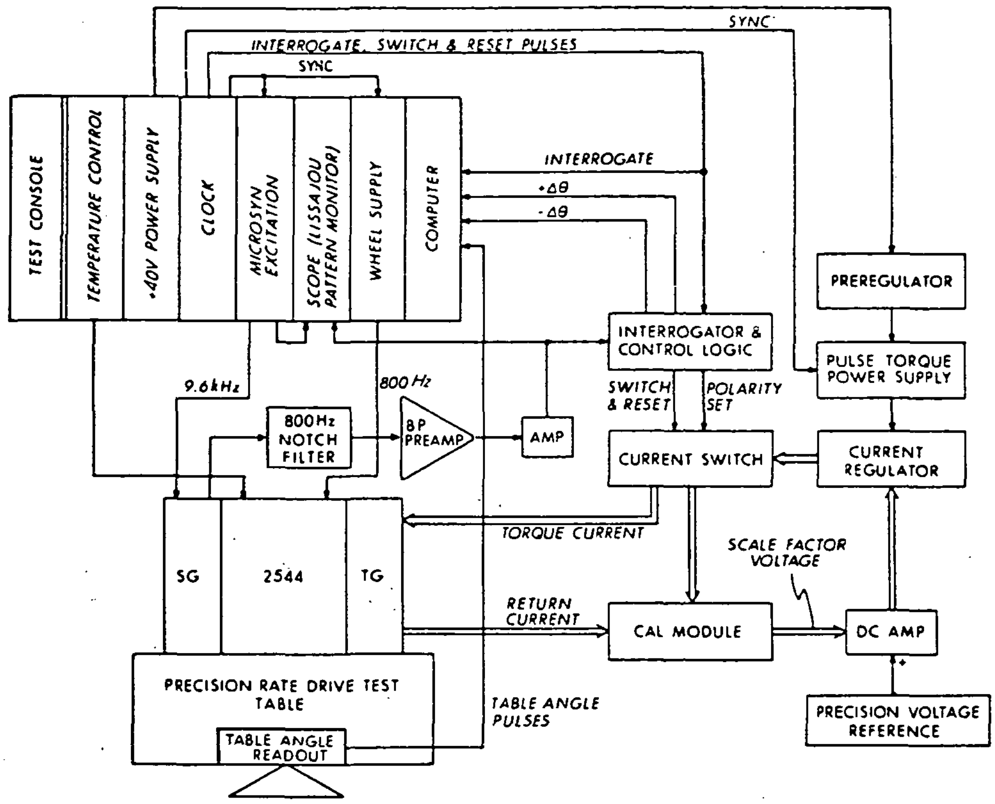

Fig. 3.2-1 Gyroscope in Pulse Torque Electronic Test Setup

for earth rate and gyroscope drift, calculates torque scale factor (input angle per pulse) and average table rate repeatedly during the test.

The test facility and data acquisition system was modified to accomodate a forced-binary loop. The gyroscope interfaces to the pulse torque loops were designed so that the ternary and forced-binary loops could be interchanged. This provided a means of obtaining comparative performance data on the two loops using the same instrument and test facility. A discussion of the principles of operation of a ternary and forced-binary loop is presented in Chapter 1.

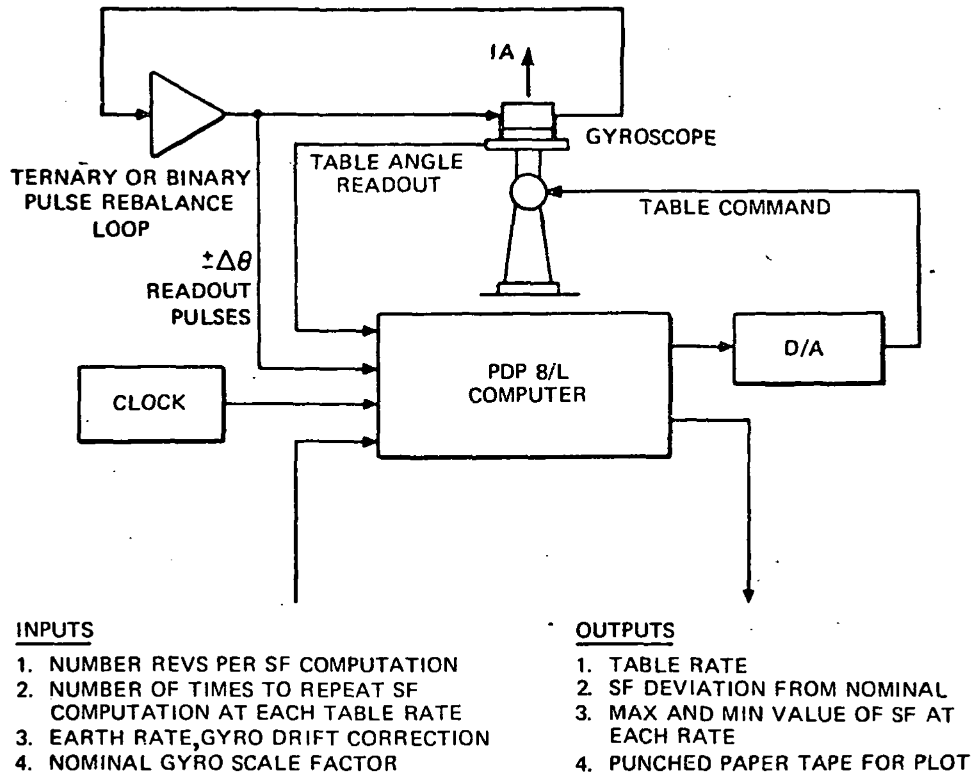

Fig. 3.2-2 On-Line Scale Factor Determination

3.2.2 Static and Constant-Rate Test Results

The static and constant-rate tests run on the 2544 gyroscope are described in this section. The measurements include:

1. Static Tests
   a. Gyroscope Drift Performance
      1. Inertial reference servo (input axis-vertical and horizontal)
      2. Stable azimuth
      3. Drift rate change after an applied input-axis rate
      4. Bias and acceleration drift in the following modes:
         a. Inertial reference servo
         b. Pulse torque-to-balance
   b. Signal generator harmonic analysis
   c. AC torque generator sensitivity

C-2

2. Constant-Rate Tests

a. DC torque-generator sensitivity
   1. Stability
   2. Linearity
b. Scale Factor (ternary)
   1. Stability
   2. Scale factor transient after an input-axis rate change
   3. Deviation with rate
c. Scale Factor (forced-binary)
   1. Stability
   2. Deviation with rate

3.2.2.1 Static Tests. The static tests measured the instrument's drift performance. The bias drift stability with the unit in continuous operation for 55 hours was 0.015 deg/h. The repeatability in the bias coefficient across cooldowns and wheel turn-off to turn-on was approximately 0.1 to 0.2 deg/h. The drifts due to an acceleration along the input axis (ADIA) and the spin reference axis (ADSRA) showed a stability of 0.015 and 0.09 deg/h/g, respectively for a continuous operation 55-hour test. The repeatability in these terms across cooldowns and wheel turn-off to turn-on was 0.16 and 0.19 deg/h/g, respectively. The unit also exhibited a drift uncertainty that occurred after a change in input power to the torquer.

3.2.2.1.1 Inertial Reference Servo. Figure 3.2-3 shows an input axis (IA) vertical-down inertial reference mode test. The constant term consisting of bias drift (BD), acceleration sensitive drift along IA (ADIA), and spin-axis, input-axis compliance (K_{SI}) is -3.903 deg/h. The average point-to-point stability was approximately 0.015 deg/h for 55 hours. In this test the gyroscope drift rate was sampled at one-degree table-angle intervals for 558 degrees of table rotation. The downward trend of the data is believed to be a result of a gyroscope thermal control problem. A similar servo test was run with IA oriented horizontal-south (Fig. 3.2-4). The drift showed an uncertainty range of 0.015 to 0.09 deg/h for 317 degrees of table rotation. A 56-hour, horizontal-servo test yielded similar drift performance.

3.2.2.1.2 Stable Azimuth. The short term drift stability was measured with the output axis (OA) oriented vertically-up. In this test mode the major portion of the input rate and the gyroscope drift is cancelled by applying an accurate level of dc to the torquer while the instrument's SG is servoed to the table drive motor. The drift rate of the table is measured by the analog output of a resolver. The continuous short term (less than one hour) drift stability for this unit had a one sigma value of 0.015 deg/h.

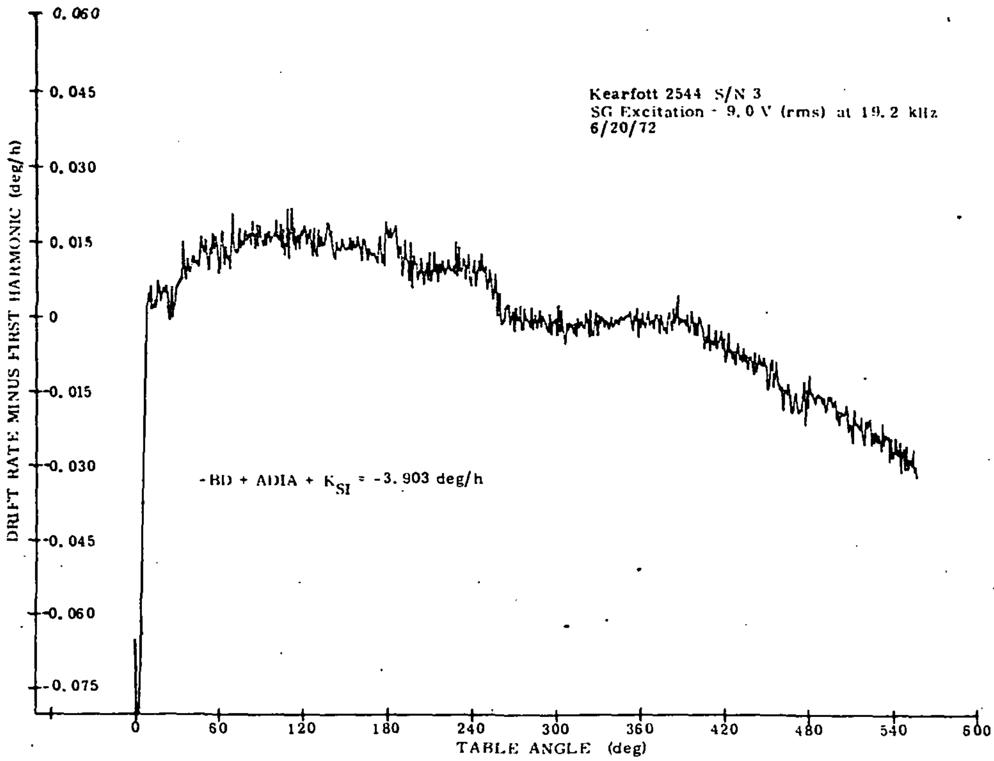

Fig. 3.2-3 Inertial Reference Servo Test-IA Vertical

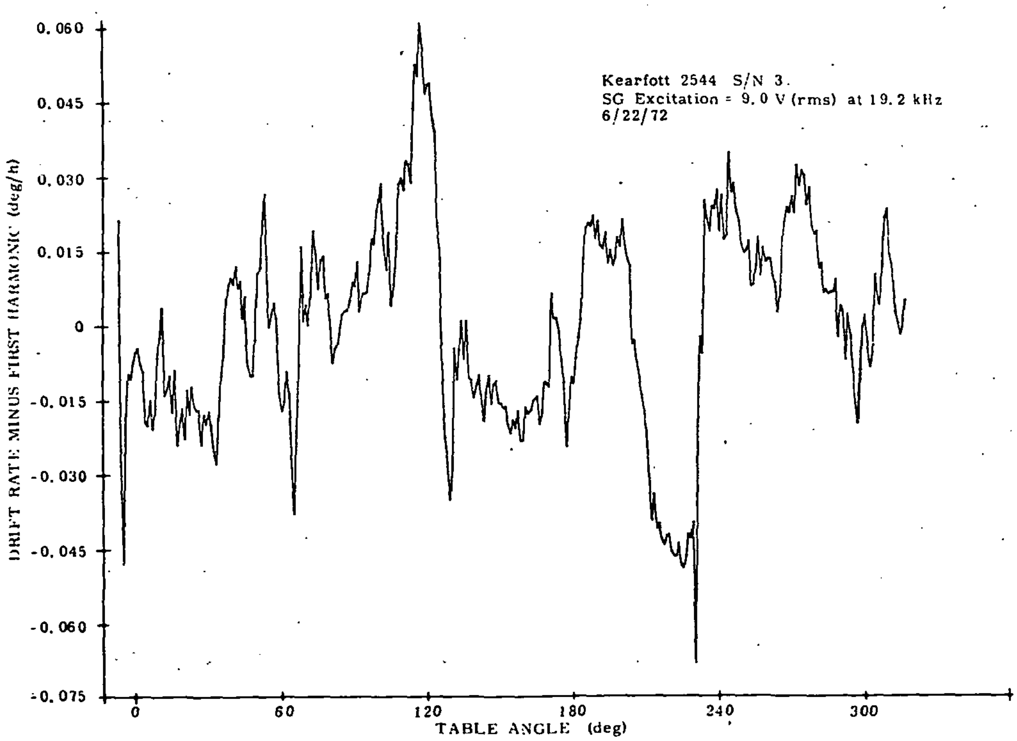

Fig. 3.2-4 Inertial Reference Servo Test-IA Horizontal

3.2.2.1.3 Drift-Rate Change after an IA Rate Input. The instrument's drift uncertainty across an input rate was measured to obtain a base line for dynamic tests. Figure 3.2-5 shows the gyroscope drift (-BD+ADIA), under earth-rate input, recorded before and after the gyroscope was torqued to compensate for an applied input-axis rate of 1.0 rad/s for one hour. The drift, measured with a ternary torque-to-balance loop, changed by 0.12 deg/h after the high-torque rate and required 9 hours to settle to its initial value. The drift change across an input-axis rate, could have been caused by thermal gradients induced in the torque coil and damping fluid.

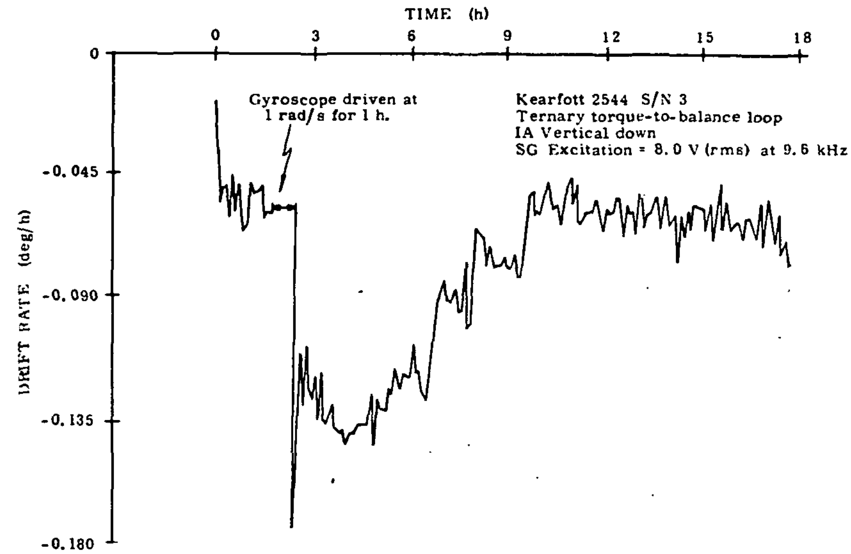

Fig. 3.2-5 Drift Rate Change after an IA Rate Input

3.2.2.1.4 Bias and Acceleration Drift Measurements. The 2544 (S/N 3) bias and acceleration drift terms were measured in both an inertial reference (servo) and PTBL mode. The measurements were also performed at two different signal-generator excitations. The initial tests were performed with an SG excitation of 9.0V (rms) at 19.2 kHz. These tests were run to insure instrument integrity at the nominal excitation frequency. The second set of tests were performed with an SG excitation of 8.0V (rms) at 9.6 kHz. This SG excitation enabled the instrument to be interfaced to an existing ternary-pulse loop. The acceleration insensitive drift (BD) and the drifts due to an acceleration along the spin reference axis (ADSRA), the input axis (ADIA) and the output axis (ADOA) are tabulated in Table 3.2-I for data obtained in the two test modes. Between tests, the wheel was turned off and the unit cooled down. The acceleration sensitive terms showed a typical peak-to-peak spread of 0.19, 0.16 and 0.17 deg/h/g, respectively. The bias drift showed a peak-to-peak spread of 0.079 and 0.017 deg/h in the two test modes for the respective SG excitations. The drift uncertainties obtained for these tests do not correlate with the measurement loop used. This range of instability was typical for this 2544 instrument.

Table 3.2 - I
Bias and Acceleration Drift Measurements

SG EXCITATION	9.0V (rms) @ 19.2kHz				8.0V (rms) @ 9.6kHz		
TEST MODE	SERVO	SERVO	SERVO	SERVO	SERVO	PTBL	PTBL
DATE	6/20/72	6/22/72	6/22/72	6/26/72	9/10/72	9/25/72	10/5/72
$BD_{SRA(S)} + K_{IS}/2$ (deg/h)	0.836	0.795	0.860	0.874		1.38	1.209
$BD_{SRA(N)} + K_{IS}/2$ (deg/h)					1.099	1.2	1.047
$BD_{OA(S)}$ (deg/h)	0.849	0.824					
$BD_{OA(N)}$ (deg/h)					1.129	1.206	1.098
$ADSRA_{(S)}$ (deg/h/g)	0.318	0.305	0.408	0.498		0.695	0.839
$ADSRA_{(N)}$ (deg/h/g)					0.941	0.672	0.707
ADIA (deg/h/g)	-3.089	-3.249			-4.35	-4.19	-4.319
ADOA (deg/h/g)	0.01	0.028	0.027	0.026	0.102	-0.017	0.072

BD_{SRA} — GYROSCOPE BIAS DRIFT FROM SPIN REFERENCE AXIS UP AND DOWN
BD_{OA} — GYROSCOPE BIAS DRIFT FROM OUTPUT AXIS UP AND DOWN
ADSRA, ADIA AND ADOA — ACCELERATION SENSITIVE DRIFT ALONG THE SPIN REFERENCE AXIS, INPUT AXIS AND OUTPUT AXIS, RESPECTIVELY
K_{IS} — INPUT-AXIS, SPIN-AXIS COMPLIANCE COEFFICIENT
(S), (N) — SOUTH AND NORTH INPUT-AXIS ORIENTATION, RESPECTIVELY
PTBL — PULSE TORQUE-TO-BALANCE LOOP

3.2.2.1.5 Signal Generator Harmonic Analysis. A signal generator (SG) harmonic analysis was performed on the 2544 (S/N 3) instrument. This measurement determined the frequencies and amplitudes of noise appearing on the raw SG secondary winding. The harmonic analysis showed that a large amount of 800-Hz wheel noise appeared on the SG output. This noise when related to the SG sensitivity, was equivalent to a 24 second of arc angle about the output axis. This SG wheel noise was reduced through appropriate shielding and filtering so that pulse torque quantization of 5.6 seconds of arc about OA was achieved. Since the filtering reduces the sensing bandwidth and only a percentage of the noise, it has been CSDL's practice on our instruments to reduce the wheel-to-SG noise coupling through instrument design.

3.2.2.1.6 AC Torque Generator Sensitivity. The ac torque generator sensitivity (Fig. 3.2-6) was measured in an inertial reference mode with the float at the signal generator null. A 1 kHz alternating current, that was varied from 0 to 100 mA, excited the torquer. The measured ac sensitivity of -0.003 deg/h/mA^2 was relatively large and corresponds to approximately 10 mrad of signal generator-to-torque generator (SG-to-TG) misalignment for this particular unit. The effect of an instrument's SG-to-TG misalignment on its performance is discussed in reference 2. Kearfott indicated that this misalignment could be easily removed since the permanent magnet can be rotated without disassembling the instrument. (CSDL did not verify or attempt the realignment technique.)

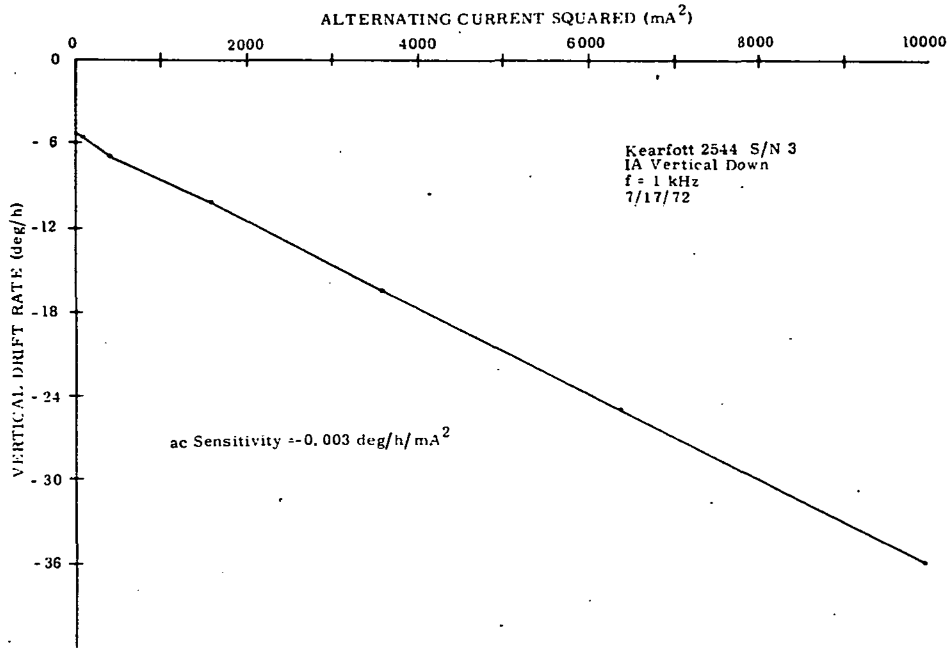

Fig. 3. 2-6 AC Torque Generator Sensitivity

3.2.2.2 Constant-Rate Tests. The constant-rate strapdown tests measured the instrument's dc and pulse torque (ternary and binary) scale factor performance. These measurements included scale factor stability and scale factor deviation with rate. The results showed that the torquer was sensitive to input power. Torque generator sensitivity and/or scale-factor transients evident in the dc and torque-to-balance loop tests were dependent upon the time history of the applied current to the torque coil. Scale factor transients, settling out within minutes, resulted from torquer current changes. Longer scale factor transients, which settled out after a number of hours, could have been due to thermal gradients set up in the instrument as a result of the applied torque-coil current. These gradients could have caused fluid torques and changes in the geometry of the permanent-magnet torquer (air gap), thus changing its sensitivity. The gradients could also have introduced a long duration transient into the thermal control of the unit.

The pulse rebalance SF tests were repeated with a second ternary PTBL to insure that the transient problem was not in the loop hardware. The different gyroscope torque electronics gave the same result. In addition, the tests showed that nominal scale factor magnitude changed randomly between and during testing. The cause of this nonrepeatability was internal to the instrument and was possibly an inherent torquer problem for this specific unit. The following subsections present this data in greater detail.

3.2.2.2.1 DC Torque Generator Sensitivity. The dc stabilities and current linearities of the torquer were determined. These measurements were performed on the instrument itself, independent of the rebalance loop. For the stability tests, a constant current of 30 mA, which corresponds to 0.24 rad/s, was applied to the main torque coil while the gyroscope was servoed in an inertial reference mode. In that mode, the servo loop drives the table to oppose earth rate, gyroscope drift and dc inputs. The dc torquer sensitivity is then calculated, after the effects of gyroscope drift and earth-rate inputs are removed. Figure 3.2-7 shows a 15-hour dc torquer stability test. The torquer sensitivity (S_{TG}) continuously changed at a rate of -11.5 ppm/h. The average point-to-point excursion for this test was 20 ppm. An apparent torquer problem exists that results in a downward trend in torque generator sensitivity.

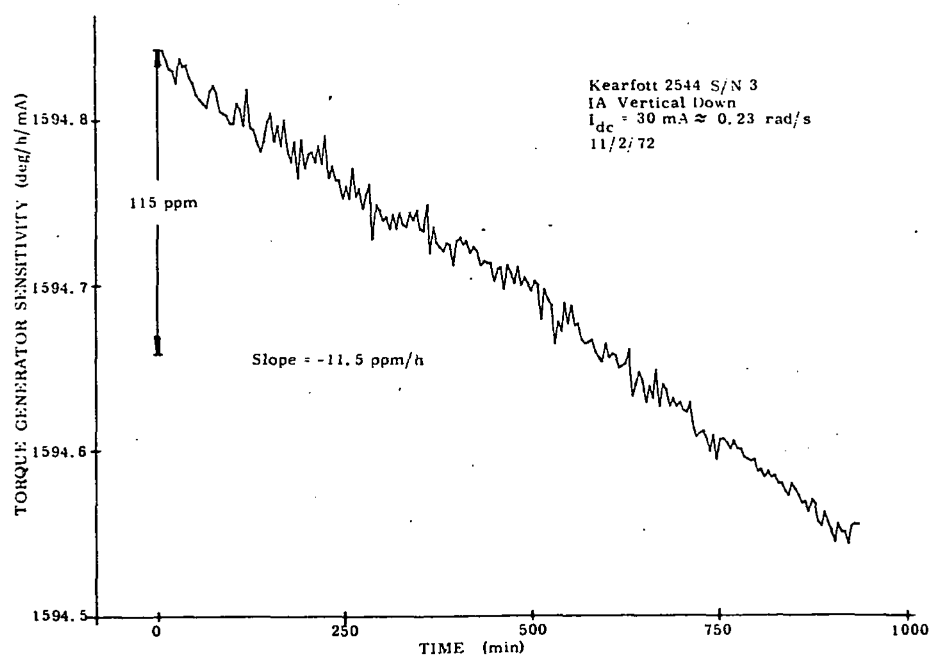

Fig. 3.2-7 DC Torquer Sensitivity

Figure 3.2-8 shows the dc torquer linearity. This test was run with a range of applied direct currents of ±10 to ±80 mA. This applied current range corresponds to an input-rate range of approximately ±0.08 to ±0.65 rad/s. The torque generator sensitivity showed a worst case nonlinearity of approximately 140 ppm for the applied current range. The mechanism causing this dc nonlinearity is discussed in Section 4.3.

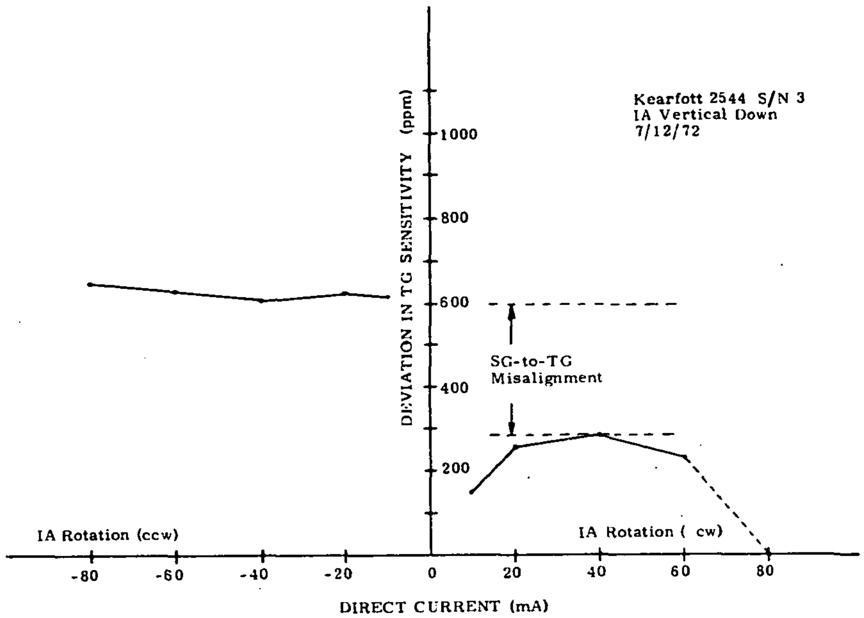

Fig. 3.2-8 DC Torquer Linearity

3.2.2.2.2 Ternary Scale Factor Stability. Constant input rates were applied to the gyroscope with the instrument restrained by a ternary pulse torque-to-balance loop. A 4800 Hz interrogation frequency was used for this pulse-loop configuration with the nominal scale factor adjusted to 44.48 seconds of arc per pulse. An interpolator which further reduced the quantization to 5.6 seconds of arc and a gyroscope lag compensator[2] were mated to the PTBL. The time constants of the gyroscope lag compensator were adjusted to match the 2544 instrument and the main torque coil was tuned with cascaded RC networks to make it appear resistive to the pulse-torque current switch.

Figures 3.2-9 and 3.2-10 show 4-hour and 45-hour scale factor stability tests. In each test the scale factor was averaged over 10 table revolutions. A one pulse uncertainty results in a 3.5 ppm error in scale factor when averaged over 10 table revolutions. Therefore the loop quantization error of ±1 pulse represents 7 ppm.

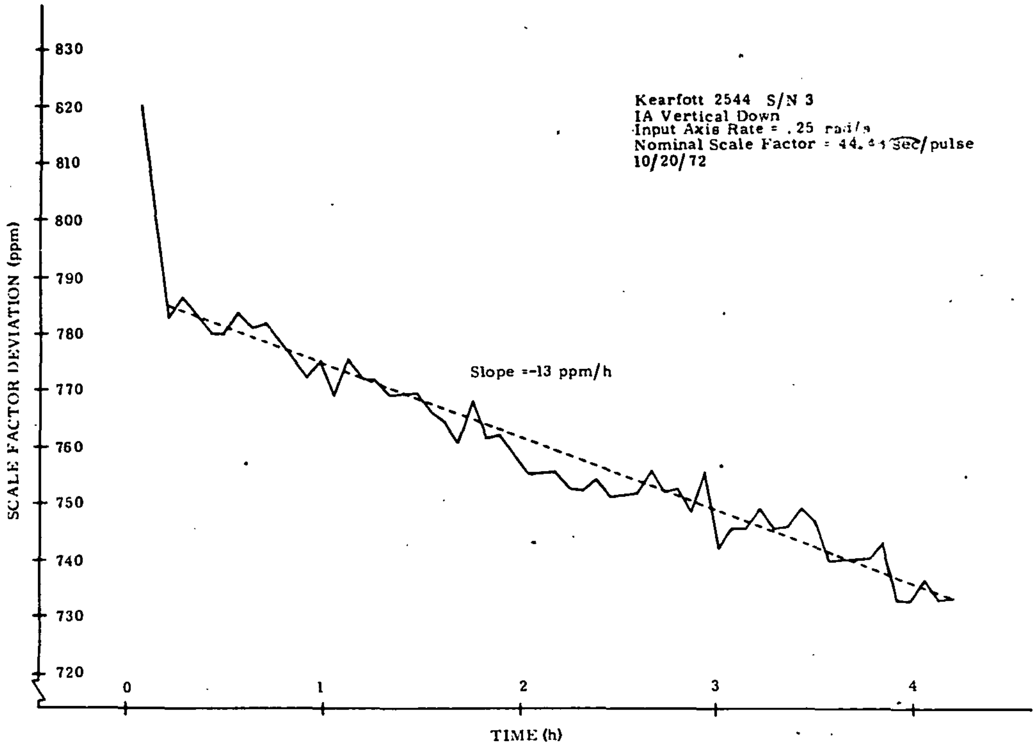

Fig. 3.2-9 Scale Factor Stability (Ternary Loop)

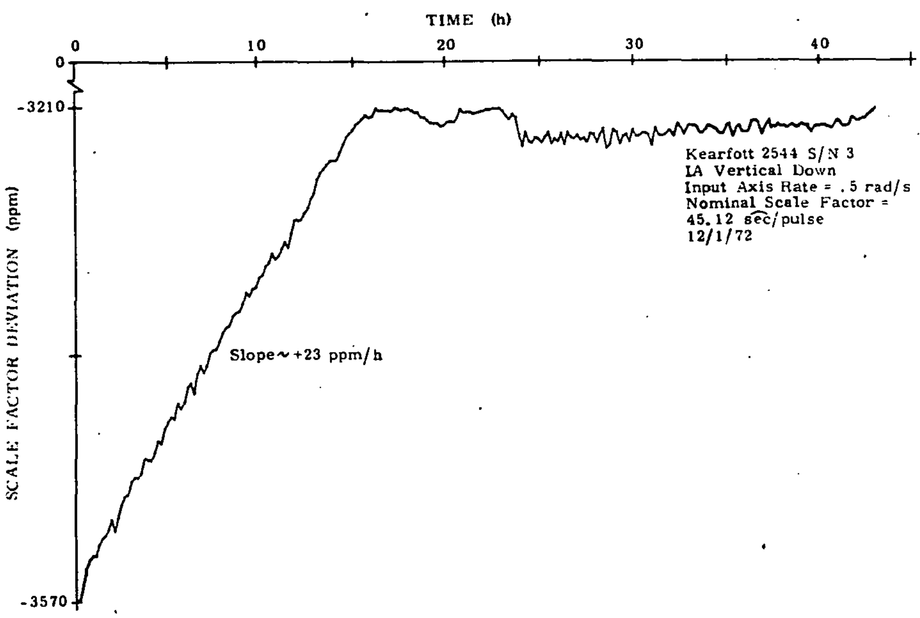

Fig. 3.2-10 Scale Factor Stability (Ternary Loop)

The first ternary SF stability test (Fig. 3.2-9) was run with a constant input rate of 0.25 rad/s. The scale factor decreased at a rate of -13 ppm/h and an average point-to-point excursion of 10 to 15 ppm was obtained. The downward trend in SF was comparable to the trend observed in the dc torquer stability test (Fig. 3.2-7) which was run at a similar input rate of 0.23 rad/s. The next ternary SF stability test (Fig. 3.2-10) was run with a constant input rate of 0.5 rad/s. For this test the SF exhibited a positive slope of 23 ppm/h and settled out after 16 hours. In addition, the nominal scale factor changed by 14,388 ppm between the two tests. The changes in scale factor both in magnitude and slope were attributed to a torquer problem.

Further tests were performed to investigate these torquer abnormalities and to determine the cause of the dc and pulse-torque scale-factor transients. Measurements of scale factor across changes in input-axis rates were obtained. Figures 3.2-11 and 3.2-12 show the deviations in scale factor that resulted from these input rate changes. In Fig. 3.2-11 the SF was initially measured at an input rate of 0.8 rad/s. The applied rate was then gradually reduced to zero over a 1/2-hour interval. After 2 minutes at this zero input rate the applied rate was increased to 0.8 rad/s and the SF was measured for 1-minute samples. The data shows a 6-minute scale factor settling time after the change to the higher rate. The scale factor changed by 75 ppm in that 6-minute interval. Figure 3.2-12 shows the scale factor transients that were caused by alternating the applied input rate to the gyroscope between 0.25 and 0.5 rad/s. These transients showed an average settling characteristic time of approximately 20 minutes.

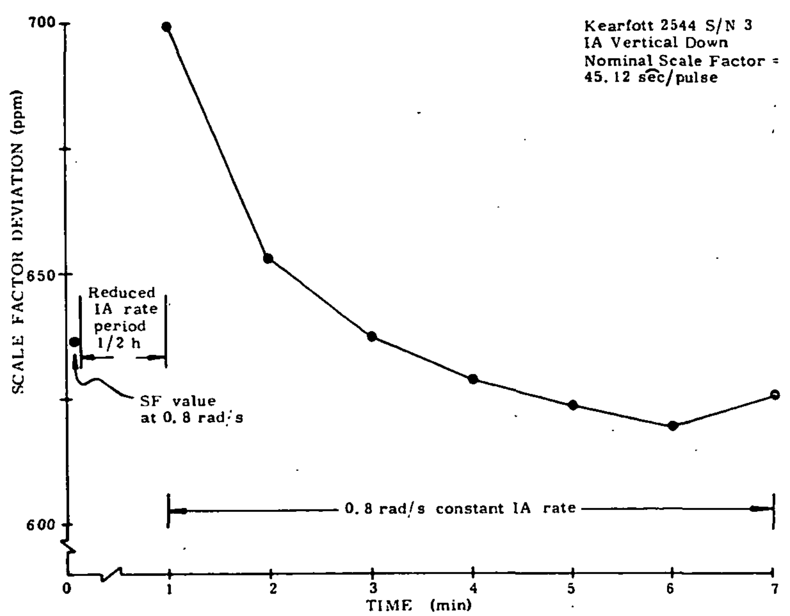

Fig. 3.2-11 Scale Factor Transient after an IA Rate Change

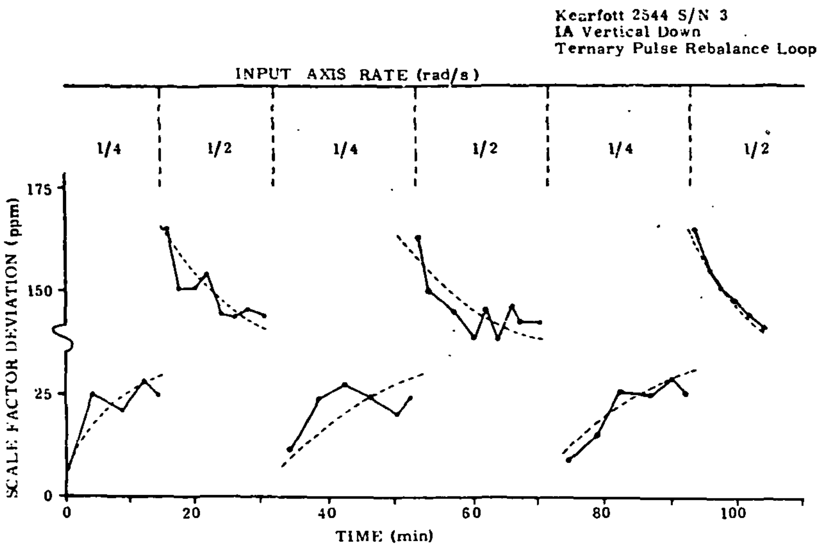

Fig. 3.2-12 Scale Factor Transients after IA Rate Changes

3.2.2.2.3 Ternary Scale Factor Deviation with Rate. Ternary pulse rebalance loop tests were run on the 2544 gyroscope to determine the scale factor deviation as a function of input rate. Figure 3.2-13 shows a scale factor rate deviation of 60 ppm for an applied input rate range of ±0.06 to ±1.0 rad/s. The entire test is completed within 20 minutes, therefore reducing the effect of long term scale factor transients. The plus-to-minus scale factor difference (ΔSF) of 479 ppm at 0.25 rad/s indicates a large SG to TG misalignment. This is consistent with the ac sensitivity test results discussed in Section 3.2.2.1.6. For all pulse torque rate tests, the average SF for a positive rate about the gyroscope input axis was greater in magnitude than for a negative rate about IA. The PTBL scale factor deviation with rate curves showed the same magnitude of ΔSF as the dc torquer linearity (Fig. 3.2-8). The difference in the shape of the two curves is the result of the torque-coil tuning in the PTBL test. The response of the pulse torque electronics is very dependent upon the reactance of the torque-coil load. This is discussed in Section 4.4.

3.2.2.2.4 Forced-Binary Scale-Factor Stability. A United Aircraft Corporation (UAC) forced-binary pulse torque-to-balance loop was interfaced to the 2544 instrument. This loop maintains a nearly constant torque-coil power regardless of gyroscope input-axis rate. Tests were performed with this loop to see if the scale factor transients were eliminated with constant torque-coil power. Figures 3.2-14 and 3.2-15 show the results of a 17-hour and a 68-hour forced-binary, scale-factor stability test. A constant rate of 0.25 rad/s was applied about the IA and the nominal

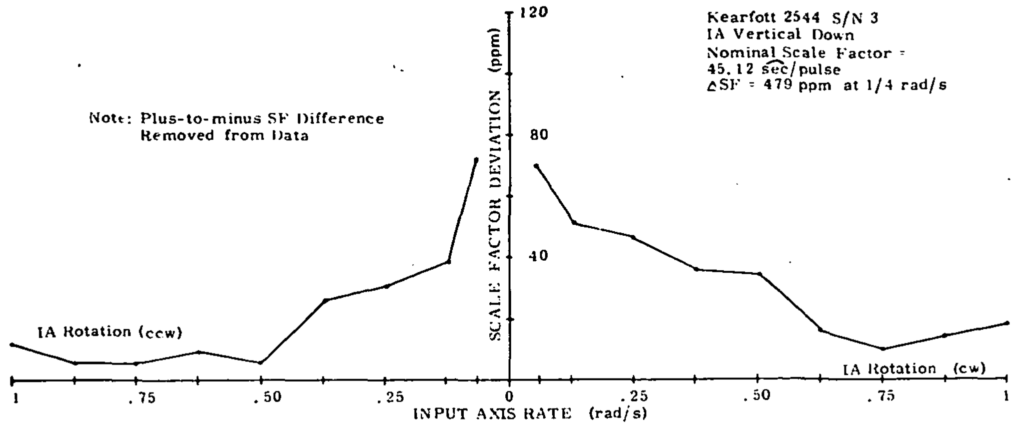

Fig. 3.2-13 Scale Factor Deviation vs Rate (Ternary Loop)

scale factor of 4.816 seconds of arc per pulse was sampled every 2 minutes. The average point-to-point scale factor uncertainty was typically 10 to 20 ppm for the two tests. Fig. 3.2-14 shows a +6 ppm/h slope in scale factor which settled out after 7 hours. Figure 3.2-15 shows a similar slope which settled out after 56 hours. The forced-binary loop tests exhibited similar long term transients and scale factor uncertainties as shown in the dc torque generator sensitivity and ternary loop tests. The constant torque-coil power with the forced-binary loop did not reduce the long term scale factor transients.

3.2.2.2.5 Forced-Binary Scale-Factor Deviation with Rate. Forced-binary pulse rebalance loop tests were run on the 2544 instrument to determine how scale factor varied with input rate. With this loop the scale factor deviation with rate (Fig. 3.2-16), for a limited test range of ±0.06 to ±0.5 rad/s, was 25 ppm. This variation with rate was less than the ternary scale-factor vs. rate results (Fig. 3.2-13), probably due to the constant power applied by the binary loop.

3.2.3 Conclusions

1. The bias and acceleration sensitive drift stabilities for this unit in long and short term continuous operation were 0.015 deg/h and 0.1 deg/h/g, respectively.

2. The bias and acceleration sensitive drift repeatability across cooldowns and wheel turn-off to turn-on was typically 0.15 deg/h and 0.15 deg/h/g, respectively.

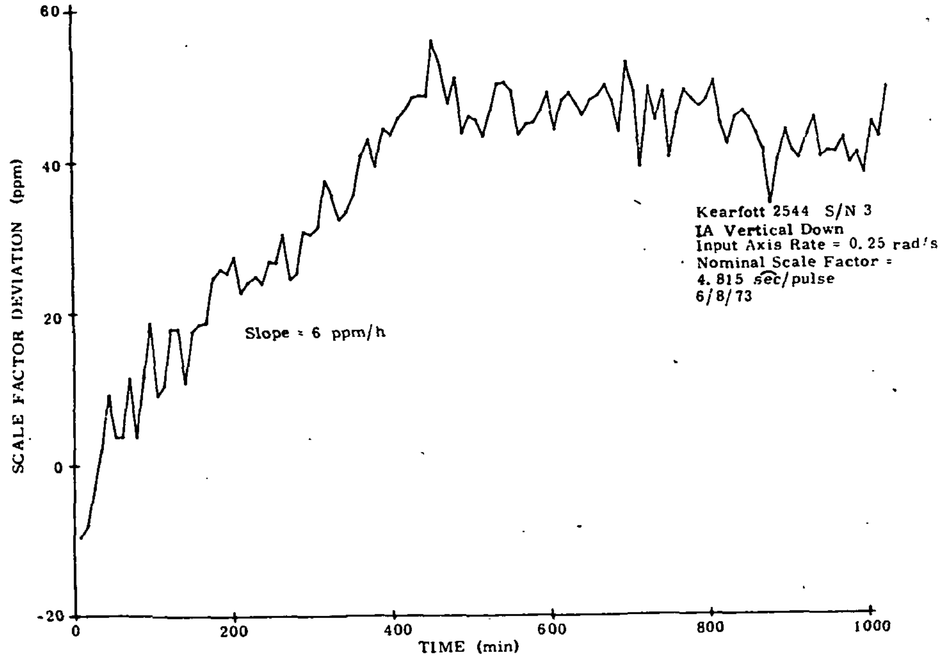

Fig. 3.2-14 Scale Factor Stability (Forced-Binary Loop)

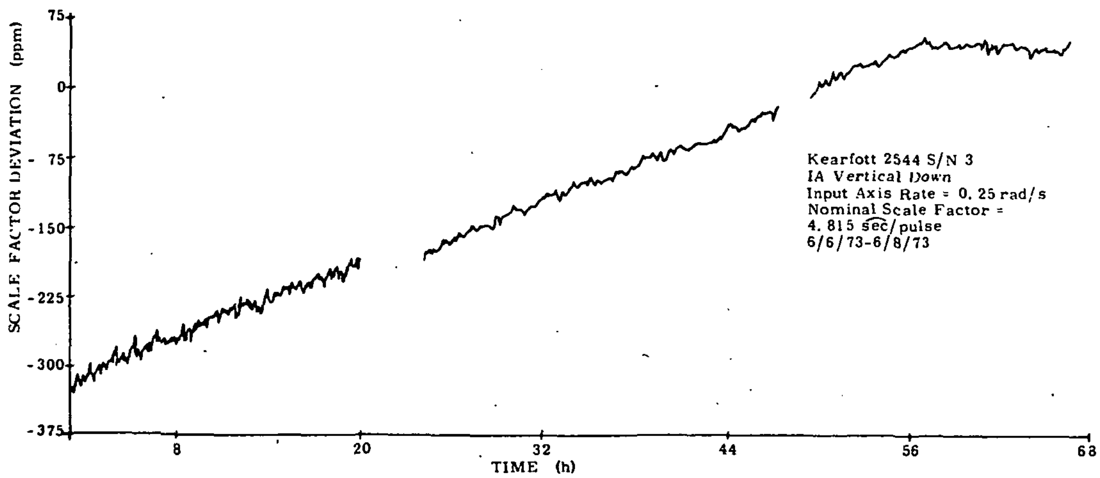

Fig. 3.2-15 Scale Factor Stability (Forced-Binary Loop)

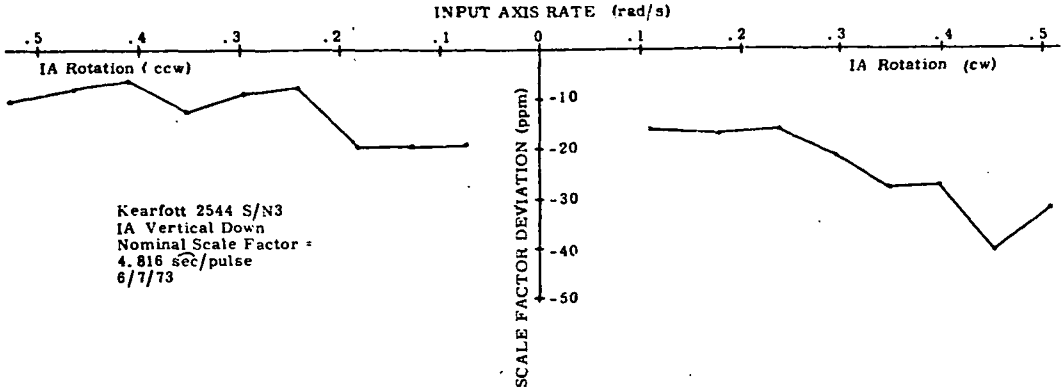

Fig. 3.2-16 Scale Factor Deviation vs Rate (Forced-Binary Loop)

3. The signal generator and torque generator nulls were misaligned by approximately 10 mrad.

4. The torquer exhibited an apparent sensitivity to input power. Scale factor transients, settling out within minutes, resulted from torquer current changes. Longer scale factor transients, which settled out after a number of hours, could have been due to thermal gradients set up in the instrument as a result of the applied torque-coil current.

5. The torquer scale factor magnitude was erratic. Random changes in the scale factor value occurred between tests. The cause of this nonrepeatability was internal to the instrument and was a torquer problem with this particular unit.

3.3 ANGULAR OSCILLATION TESTS

3.3.1 Background

The dynamic test program was conducted to experimentally measure the apparent average input rate of rotation indicated by a pulse-rebalanced gyroscope when subjected to angular oscillations. This apparent input rate results from the instrument, the pulse-rebalance loop, and their combined interaction. Experimental results from tests run on various single-degree-of-freedom floated instruments compared well with theory and digital simulations in defining the gyroscopic response. This, however, was achieved only after carefully modeling the gyroscope, torquer and rebalance loop so that indicated error rates could be computationally removed

from the experimental data. These dynamic errors, which are superimposed on the gyroscopic response, result from instrument SG-to-TG misalignment[2], imperfections in the pulse-rebalance loop, torque-generator frequency[2] and power effects and torque-coil tuning. If these inputs are not compensated for in the strapdown system computer, an IA angular velocity is falsely indicated by the pulse-rebalanced gyroscope. Several of these dynamic error sources, which affect the IA drift rate measurement, will be presented for a gyroscope operated in the ternary pulse torque-to-balance loop[2], prior to a discussion of the dynamic test results.

3.3.1.1 IA Oscillations (closed-loop). The apparent input-axis rate, ω_{IA}, resulting from IA angular oscillations is:

$$\omega_{IA} = \frac{SF(N^+ - N^-)}{t} = \omega_G + \omega_{PTBL} \tag{3.1}$$

where:

SF	= nominal scale factor about IA (rad/pulse)
N^+, N^-	= number of positive and negative restoring-torque pulses resulting from an angular oscillatory input about IA, respectively (pulses)
t	= data sample time (s)
ω_G	= constant rates resulting from gyroscope drift and earth-rate inputs (deg/h)
ω_{PTBL}	= drift rates caused by the pulse torque-to-balance loop and the gyroscope-loop interaction when subjected to angular oscillations (deg/h)

(Terms such as gyroscope frequency response, IA misalignment and torque-loop leakage have been neglected.)

When the gyroscope is oriented with IA vertical-down, the constant drift rate, ω_G, under earth-rate input and without applied oscillations is:

$$\omega_G = -\omega_{IEV} - BD + ADIA \tag{3.2}$$

where:

ω_{IEV} = vertical component of earth rate at a specified latitude angle (deg/h)

BD = gyroscope bias drift coefficient (deg/h)

ADIA = drift coefficient as a result of an acceleration along the input axis (deg/h/g).

This constant drift rate can be accurately measured and compensated for prior to angular oscillatory tests. A constant input rate, without applied oscillations, demands only a single polarity of restoring-torque pulses. With a ternary loop, ω_{PTBL} equals zero since the loop does not cause a rectified drift when restoring-torque pulses of a single polarity are applied.

When input angular oscillations are applied, both positive and negative torque pulses result. Due to a plus-to-minus scale-factor difference (ΔSF), the float-restoring capability of the positive pulses is not the same as for the negative pulses. That is, the scale factor for a positive rate about IA differs from that for a negative rate. This scale factor difference which appears as an indicated drift rate, ω_{PTBL}, is primarily caused by:

1. SG-to-TG misalignment
2. imperfections in the pulse rebalance loop
3. torque-generator frequency and power effects
4. torque-coil tuning

The SG-to-TG misalignment and/or a pulse-loop unbalance result in a constant plus-to-minus scale-factor difference, ΔSF_R, that is independent of rate. This ΔSF_R is defined as:

$$\Delta SF_R = SF_{(+R)} - SF_{(-R)} \tag{3.3}$$

where:

$SF_{(+R)}, SF_{(-R)}$ = scale factor value for all positive and negative input rates, R, about IA, respectively (rad/pulse).

This constant plus-to-minus scale-factor difference causes an effective error in the indicated drift measurement when the instrument is subjected to sinusoidal oscillations. This error rate, $\omega_{PTBL(1)}$, can be determined and compensated for in the software algorithm by the relation:

$$\omega_{PTBL(1)} = \frac{\Delta SF_R(N^+ + N^-)}{2t} \tag{3.4}$$

The total number of torque-restoring pulses $(N^+ + N^-)$ is directly proportional to the input-angular amplitude and frequency. Thus an increase in indicated drift rate results from an increase in either angular-input frequency or amplitude for a given ΔSF_R. Figure 3.3-1 shows the rectified IA drift caused by a ΔSF_R of 10 ppm at various angular-input frequencies and amplitudes. To determine the rectified drift resulting from a constant plus-to-minus scale-factor difference in a system application, the peak angular-input velocity imposed by the environment must be defined.

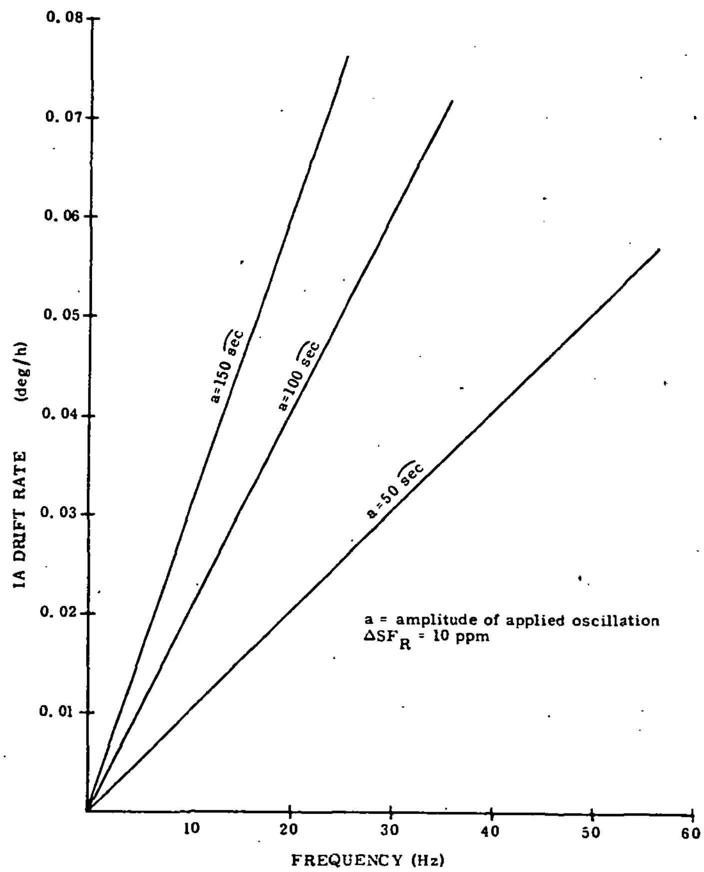

Fig. 3.3-1 Input Axis Drift Rate vs Applied Angular Frequency and Amplitude

An additional error in the indicated drift measurement is caused by torque-generator frequency and power effects and by torque-coil tuning. These effects cause the plus-to-minus scale-factor difference to vary with applied IA rate. This is demonstrated in the scale-factor deviation with rate plot (Fig. 3.3-2). To compensate for this changing ΔSF the scale-factor value for a negative IA rate is subtracted from the scale-factor value for the same magnitude of positive rate for the complete range of input-axis rates. The deviation in ΔSF with rate, which is superimposed on ΔSF_R, can then be determined (Fig. 3.3-3). The slope (SF_S) of the plus-to-minus scale-factor difference with rate can be implemented as a correction to the instrument's indicated drift rate when subjected to sinusoidal oscillations to compensate for the changing ΔSF with rate. For sinusoidal input oscillations the indicated drift rate, $\omega_{PTBL(2)}$, caused by a changing ΔSF with input-axis velocity, $V_{0(in)}$, is:

$$\omega_{PTBL(2)} = \frac{2}{\pi} SF_S V_{o(in)} \tag{3.5}$$

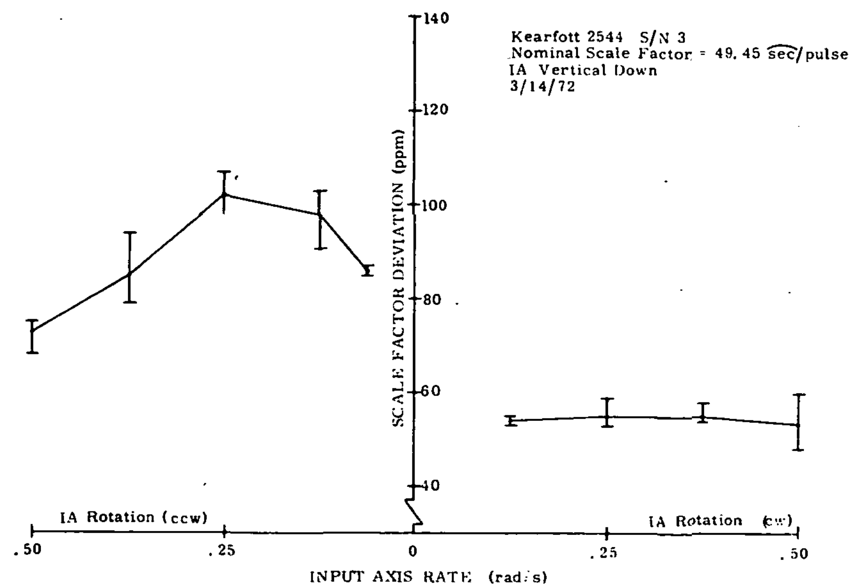

Fig. 3.3-2 Scale Factor Deviation vs IA Rate (Ternary Loop)

The rectified drift rates, ω_{PTBL}, caused by a constant and rate-dependent plus-to-minus scale-factor difference effects are thus:

$$\omega_{PTBL} = \omega_{PTBL(1)} + \omega_{PTBL(2)} \tag{3.6}$$

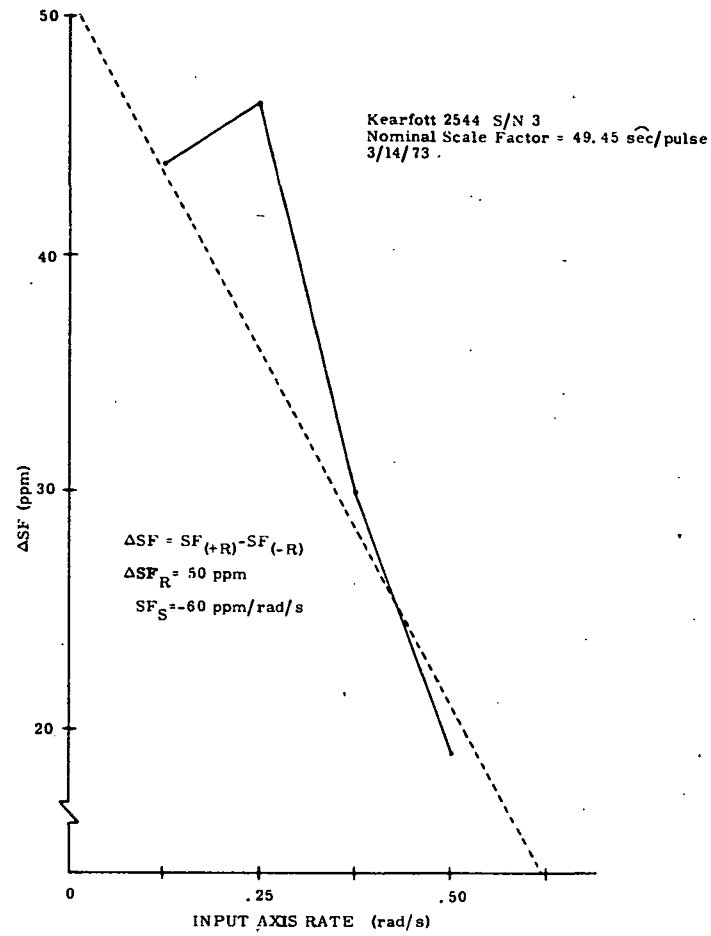

Fig. 3.3-3. Plus-to-Minus Scale Factor Difference vs Input Axis Rate

or

$$\omega_{PTBL} = \frac{\Delta SF_R(N^+ + N^-)}{2t} + \frac{2}{\pi} SF_S V_{o(in)} \tag{3.7}$$

The apparent input-axis rate, Eq. 3.1, resulting from IA angular oscillations becomes:

$$\begin{aligned} \omega_{IA} = \frac{SF(N^+ - N^-)}{t} &= -\omega_{IEV} - BD + ADIA \\ &+ \frac{\Delta SF_R(N^+ + N^-)}{2t} + \frac{2}{\pi} SF_s V_{o(in)} \end{aligned} \tag{3.8}$$

Knowledge of the drift rates and plus-to-minus scale-factor differences allows for an accurate instrument dynamic compensation. When these rates are removed from the ternary plus torque-to-balance loop measurement no rectified drift rate results from sinusoidal oscillatory inputs about IA.

3.3.1.2 IA-SA Oscillations (closed-loop). With the pulse-rebalanced gyroscope oriented as shown in Fig. 3.3-4, the apparent input-axis rate, ω_{IA}, with applied angular oscillations is:

$$\omega_{IA} = \frac{SF(N^+ - N^-)}{t} = \omega_G + \omega_{PTBL} + \omega_A + \omega_{cc} \tag{3.9}$$

where:

ω_A = drift rate caused by anisoinertia (deg/h)

ω_{cc} = drift rate caused by input and spin axis crosscoupling effects (deg/h)

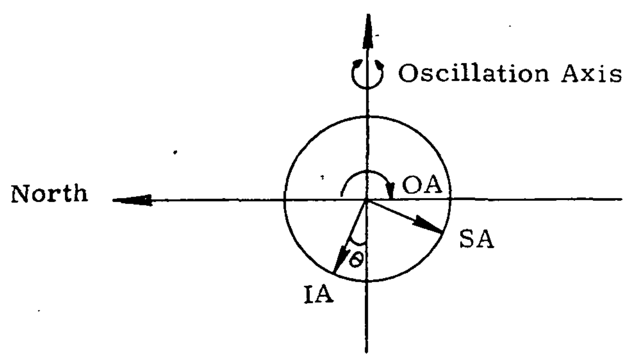

IA and SA lie in the North-South plane
$\theta \approx 32$ deg

Fig. 3.3-4 IA - SA Alignment for Two-Axes, In-Phase Oscillations

The constant drift rate, ω_G, for this gyroscope orientation is:

$$\omega_G = -\omega_{IEV} \cos\theta + \omega_{IEH} \sin\theta + \cos\theta \; ADIA + \sin\theta \; ADSRA - BD \tag{3.10}$$

where:

ω_{IEH} = horizontal component of earth rate at a specified latitude angle (deg/h)

θ = angle between IA and the applied oscillation axis (rad)

ADSRA = drift coefficient as a result of an acceleration along the spin reference axis (deg/h/g)

(All other terms were previously described in Section 3.3.1.1).

This constant drift rate can be similarly measured and compensated for prior to angular oscillatory tests. The apparent plus-to-minus scale-factor difference rate, ω_{PTBL}, can also be compensated for, as previously described.

The indicated input rate, for these two-axis in-phase oscillation tests, is influenced by the difference in IA and SA inertias (anisoinertia) and crosscoupling effects.

The basic equation[2] used in analyzing an IA-SA oscillation for drifts resulting from anisoinertia and crosscoupling is:

$$\begin{aligned} I_{OA}\ddot{A}_{OA} + C_{OA}\dot{A}_{OA} = {} & H_S\omega_{IA} + M_{TG} - I_{OA}\dot{\omega}_{OA} \\ & + (I_{SA} - I_{IA})\omega_{IA}\omega_{SA} \\ & + [(I_{SA} - I_{IA})(\omega_{IA}{}^2 - \omega_{SA}{}^2) \\ & - H_S\omega_{SA}]\ A_{OA} \end{aligned} \qquad (3.11)$$

where:

I_{IA}, I_{SA} and I_{OA} = moments of inertia about the gyroscope input, spin and output axes, respectively ($gm\text{-}cm^2$)

A_{OA} = angle about output axis (rad)

C_{OA} = gyroscope damping about the output axis (dyne-cm-s)

H_s = wheel angular momentum ($gm\text{-}cm^2/s$)

ω_{IA}, ω_{SA} and ω_{OA} = rate about input, spin and output axes, respectively (rad/s)

M_{TG} = torque generator command torque (dyne-cm).

For low frequency IA-SA oscillations a good approximation for a gyroscope oriented as shown in Figure 3.3-4 is:

$$
\begin{aligned}
C_{OA} \dot{A}_{OA} &= H_S \omega_{IA} + M_{TG} \\
&+ (I_{SA} - I_{IA}) \omega_{IA} \omega_{SA} \\
&- H_S \omega_{SA} A_{OA}
\end{aligned}
\tag{3.12}
$$

where:

$\omega_{IA} = a \omega \cos \theta \cos \omega t$
$\omega_{SA} = a \omega \sin \theta \cos \omega t$

The <u>anisoinertia term</u>[2] is:

$$
(I_{SA} - I_{IA}) \omega_{IA} \omega_{SA} = \frac{a^2 \omega^2}{4} \sin 2\theta \, (1 + \cos 2\omega t)(I_{SA} - I_{IA}) \tag{3.13}
$$

and the dc portion of the term is:

$$
(I_{SA} - I_{IA}) \frac{a^2 \omega^2}{4} \sin 2\theta = \frac{a^2 \omega^2}{2\sqrt{5}} (I_{SA} - I_{IA}) \tag{3.14}
$$

for $\theta \approx 32$ deg and/or $\theta = 1/2 \arctan 2$.

This yields a resulting drift (ω_A) due to anisoinertia of:

$$
\omega_A = \frac{C_{OA}}{H_S} \dot{A}_{OA} = \frac{I_{SA} - I_{IA}}{H_S} \frac{a^2 \omega^2}{2\sqrt{5}} \tag{3.15}
$$

The cross coupling term[2] is:

$$\omega_{cc} = \text{time average of} \left[\frac{C_{OA}}{H_S} \dot{A}_{OA}\right]$$

$$= \text{time averaged} \quad (-\omega_{SA} A_{OA}) \tag{3.16}$$

$$A_{OA} = \frac{H_S}{C_{OA}} [m \; \alpha \; \text{signum} \; (\omega_{IA}) + (T + \Sigma \; \tau_i)\omega_{IA}] \tag{3.17}$$

where:

α	= torque pulse weight about IA (rad/pulse)
m	= mean float hangoff (rad)
T	= interrogation time (s)
τ_i	= SG delays in response to torque command (s)

$$\text{signum } (x) = \begin{cases} 1, & x>0 \\ 0, & x=0 \\ -1, & x<0 \end{cases}$$

$$\dot{A}_{OA} = \frac{H_S}{C_{OA}} [m \; \alpha \; \text{signum} \; (\cos \omega t) + (T + \Sigma \; \tau_i) a\omega \cos\theta \cos\omega t] \; -\omega_{SA}A_{OA}$$

$$= -\frac{H_S}{C_{OA}} [m \; \alpha \; a\omega \sin\theta \;\; \text{signum} \; (\cos \omega t) \cos \omega t \tag{3.18}$$

$$+ \; (T + \Sigma \; \tau_i) \; a^2\omega^2 \sin\theta \cos\theta \cos^2 \omega t]$$

$$\omega_{cc} = \text{time average } (-\omega_{SA}A_{OA})$$

$$= -\frac{H_S}{C_{OA}} \left[\frac{2}{\pi} m \; \alpha \; a\omega \sin\theta + \frac{(T + \Sigma \; \tau_i) \; a^2\omega^2 \sin 2\theta}{4}\right] \tag{3.19}$$

Therefore, the drift due to cross coupling is:

$$\omega_{cc} = -\frac{H_S}{C_{OA}} \left[\sqrt{2(1 - \frac{1}{\sqrt{5}})} \;\; \frac{m \; \alpha \; a \; \omega}{\pi} + \frac{(T + \Sigma \; \tau_i) \; a^2\omega^2}{2\sqrt{5}}\right] \tag{3.20}$$

The apparent drift rate, Eq. 3.9, resulting from two-axis in-phase oscillations about the IA-SA axes is:

$$\omega_{IA} = \frac{SF(N^+ - N^-)}{t}$$

$$= -\omega_{IEV} \cos\theta + \omega_{IEH} \sin\theta + \cos\theta \text{ ADIA}$$

$$+ \sin\theta \text{ ADSRA} - \text{BD} + \frac{\Delta SF_R(N^+ + N^-)}{2t} + \frac{2}{\pi} SF_S V_{o(in)} \tag{3.21}$$

$$+ \omega_A + \omega_{cc}$$

After compensating for constant drift rates and plus-to-minus scale-factor difference effects, Eq. 3.21 reduces to:

$$\omega_{IA} = \frac{SF(N^+ - N^-)}{t} = \omega_A + \omega_{cc} \tag{3.22}$$

This is the gyroscopic drift rate resulting from IA-SA two-axis in-phase dynamic oscillatory inputs. Test results for IA-SA oscillations are discussed in Section 3.3.3.

3.3.2 Dynamic Test Facility

The dynamic test facility consists of a single-axis angular oscillator and a PDP/8L minicomputer. A block diagram illustrating the functional elements is shown in Fig. 3.3-5. This dynamic test apparatus and data acquisition system provided an on-line computation of gyroscope drift rate, under applied angular oscillations, as shown in Fig. 3.3-6. The versatile gyroscope mounting fixture enables numerous orientations of the instrument. Thus, single-axis and in-phase two-axis oscillations can be applied to the instrument.

The computer installation was necessary to perform and analyze data for the large quantity of tests required. Computer gyroscope testing provides flexibility, convenience, and utility far beyond that attainable with standard electronic instruments. Using analog-to-digital converters, the computer functions as an automatic test controller and sequencer. At the same time, it operates as a programmable data collection system of enormous proportions. Most important, perhaps, the program can reduce, scale to engineering units, and display data immediately after its collection. Many of the tests implemented were not practicable using conventional test equipment. Thus, the computer installation has reduced the

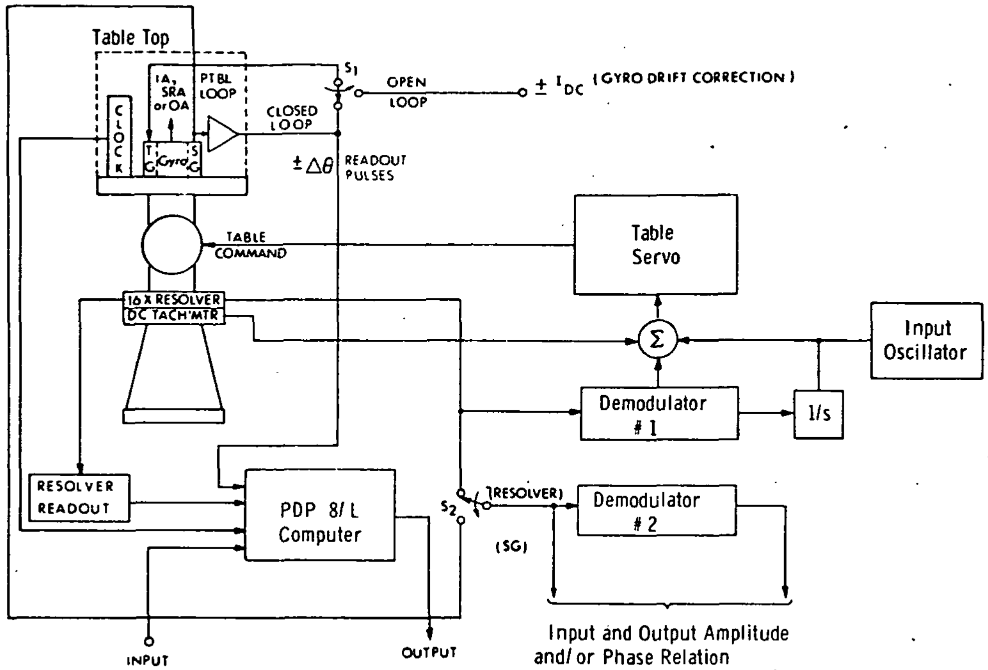

Fig. 3.3-5 Single-Axis Oscillator (open or closed loop)

level of data handling, greatly improved test accuracy, and allowed previously unattainable test techniques.

3.3.3 Dynamic Test Results

The angular oscillatory tests run on the 2544 gyroscope are described in this section. The measurements include:

1. Output-axis rate test
2. Single-axis oscillations
   a. Input axis
   b. Output axis
3. Two-axis in-phase oscillations
   a. Input axis-spin axis

```
INPUT
-----
     CLOCK FREQ (HZ) = 4800
     DURATION (S) = 300
     SCALE FACTOR (SEC/P) = 49.4495
     SF DIFF, ZERO RATE (PPM) = 50
     SF DIFF SLOPE (PPM/RAD/S) = -60
OUTPUT
------
     TEST DURATION = +0.2995287E+03 (S)
     # OF OSC. CYCLES = +0.1517600E+05
     OSC FREQ = +0.5066624E+02 (HZ)
     # OF + THETA'S = +0.2768999E+04
     # OF - THETA'S = +0.2708999E+04
     NET # OF THETA'S = +0.6000000E+02
     UNCORRECTED INPUT RATE = +0.9905458E+01 (DEG/H)
     PEAK AMPLITUDE = +0.2163423E-01 (MRAD)
     PEAK RATE = +0.6867159E-02 (RAD/S)
     CORRECTED INPUT RATE = +0.9928114E+01 (DEG/H)
```

Fig. 3.3-6 On-Line Computation of Single-Axis,Closed-Loop Oscillations

3.3.3.1 Output Axis Rate Tests. The change in apparent IA misalignment as a function of OA rate was measured in a ternary PTBL mode and is shown in Fig. 3.3-7. For applied rates from ±0.125 to ±1.0 rad/s about the gyroscope output axis, a 5 sec of arc uncertainty in apparent IA alignment occurred. This magnitude of uncertainty indicates that this unit has appproximately 25 to 30 microinches of clearance in the output-axis support. These results are discussed in greater detail in Chapter 2.

3.3.3.2 Input-Axis Oscillations. Figure 3.3-8 shows the gyroscope drift rate with and without applied sinusoidal oscillations about the input axis. The constant drift rate ($-\omega_{IEV}$ - BD + ADIA), measured with a ternary PTBL, without applied angular oscillation, was -15.085 deg/h. With input-axis oscillations, the maximum deviation, after compensating for ΔSF, from this constant drift rate was 0.1 deg/h. This was within the instrument's drift uncertainty.

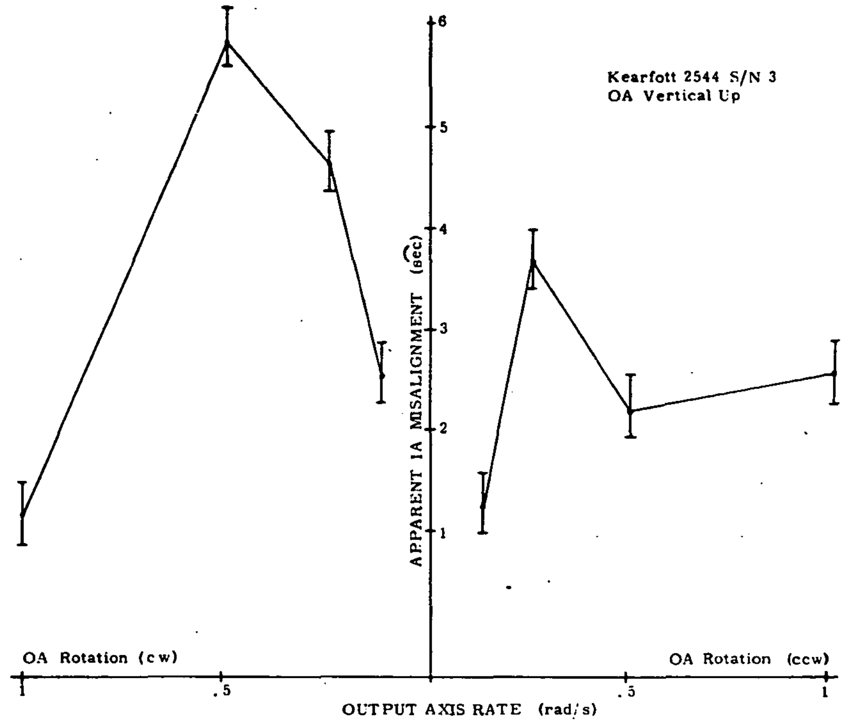

Fig. 3.3-7 Change in Apparent IA Misalignment vs Output Axis Rate

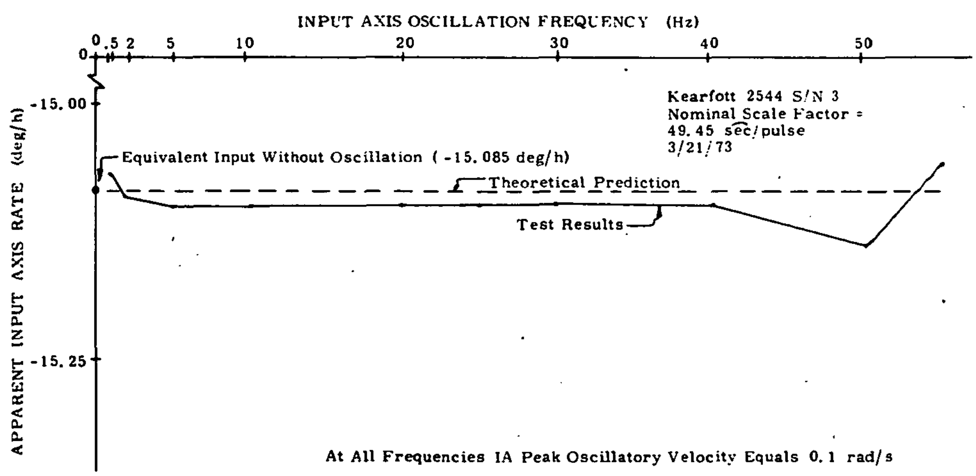

Fig. 3.3-8 Apparent IA Drift Rate for Angular Oscillations about IA (closed loop)

3.3.3.3 Output-Axis Oscillations. The gyroscope drift rate with and without applied angular oscillations about the output axis is shown in Figure 3.3-9. The constant drift rate ($+\omega_{IEH}$ - BD - ADOA) without applied oscillations and with the gyroscope oriented IA horizontal-north and OA vertical-up was +9.833 deg/h. The average drift rate, measured with a ternary PTBL, with applied angular oscillations about OA was +9.74 deg/h. The difference in drift between the two test conditions of 0.093 deg/h was again within the instrument's drift uncertainty.

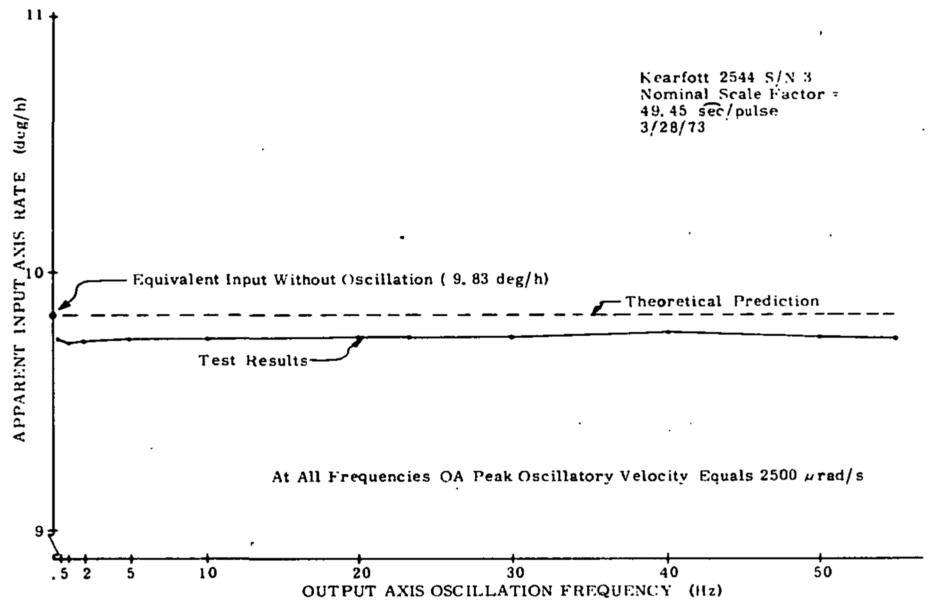

Fig. 3.3-9 Apparent IA Drift Rate for Angular Oscillations about OA (closed loop)

3.3.3.4 Input Axis - Spin Axis Oscillations. Figure 3.3-10 shows the predicted and measured drift rate of the Kearfott 2544 gyroscope for applied angular oscillations about the IA - SA axes. For this test the angular input frequency was held constant at 15 Hz and the peak angular input amplitude of applied oscillations was varied. The predicted response was calculated and plotted from the IA - SA oscillatory drift Eq. 3.21 and the 2544 nominal parameters. In addition, Figure 3.3-10 shows the constant drift rate of -14.2 deg/h without applied angular oscillations and the measured drift rate with and without the ΔSF correction for applied oscillations. The predicted and measured drift rate agreed to within test uncertainty. The rectified input drift rate results from anisoinertia and crosscoupling effects of IA-SA oscillations.

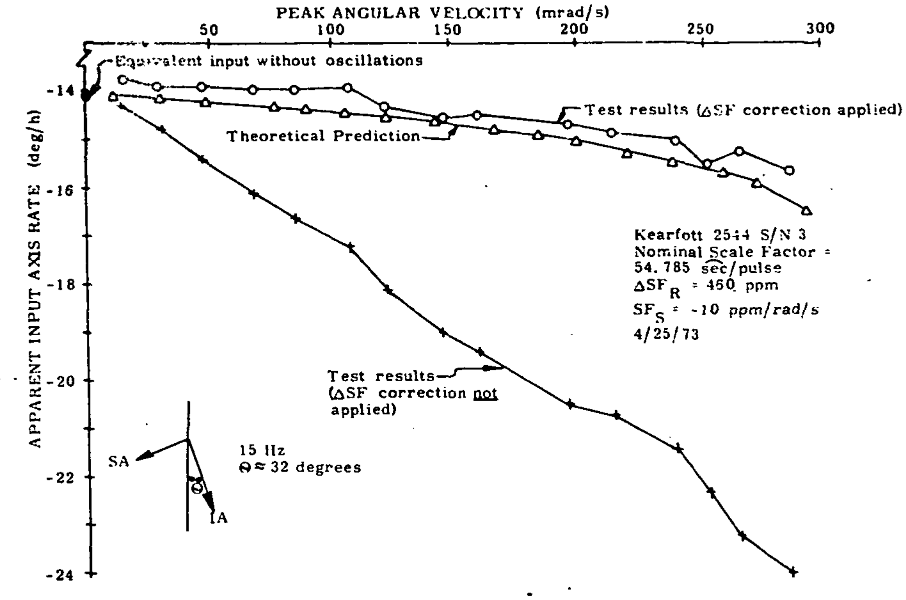

Fig. 3.3-10 Apparent IA Drift Rate for Angular Oscillations about IA - SA (closed loop)

3.3.4 Conclusions and Recommendations

3.3.4.1 Conclusions. The closed-loop dynamic performance showed:

1. The measured pulse-rebalanced drift rate under a severe oscillatory environment is dependent to a large extent upon the accurate extraction of the ΔSF error. This error is a function of the instrument and/or pulse-rebalance loop.

2. The IA and OA closed loop oscillation tests agreed with the predicted theory to within the drift uncertainty of the unit.

3. The IA-SA pulse-rebalanced loop dynamic results agreed within test uncertainty with the theoretical prediction. The rectified input drift rate is a function of $a\omega$ and $(a\omega)^2$ resulting from anisoinertia and crosscoupling effects.

4. The dynamic test results for this instrument have followed the theoretical predictions for a single-degree-of-freedom floated instrument. Further dynamic tests of this unit did not seem justified since the dynamic

performance was not a function of the output axis suspension. In addition, it was determined that the unit's drift uncertainties would have been greater than the rectified dynamic performance for OA-SA tests.

3.3.4.2 Recommendations. If ΔSF is a nonlinear function of input velocity, it will cause an error in a real system under severe dynamic inputs. The plus-to-minus scale-factor difference modeled in this phase of the report assumed ΔSF to be a linear function of rate. The magnitudes of ΔSF were also determined from constant input-rate data. These approximations do not necessarily model all systems. The ΔSF obtained from the constant-rate tests could be different from that obtained in a dynamic environment. The scale factor variation with rate and plus-to-minus scale-factor asymetries should be studied further to better model their effects on rectified drift in a random dynamic environment. Tests and analysis should be extended to binary and forced-binary torque-to-balance loops.

REFERENCES

1. O'Plinus, F., Product Specification, Gyroscope, Integrating Part No. C702544001-1, Singer-Kearfott Division, April 14, 1971.

2. Lory, C. B., Feldman, J., and Sinkiewicz, J. S., Dynamic Testing of a Single-Degree-of-Freedom Strapdown Gyroscope, MIT Draper Lab Report E-2618, October 1971.

CHAPTER 4

TESTING OF THE MAGNETICALLY-SUSPENDED C.S. DRAPER LABORATORY 18 IRIG MOD-B

4.1 INTRODUCTION

The intent of this program was to conduct static and dynamic performance tests on a variety of strapdown inertial instruments operating in pulse and analog rebalance modes. Tests were run to determine how these instruments performed as strapdown sensors. The tests were conducted on four instruments, the Honeywell GG334[1], the Kearfott 2544 (Chapter 3), the Teledyne SDG-2 (Chapter 5) and the C.S. Draper Laboratory (CSDL) 18 IRIG MOD-B. All instruments except the Teledyne SDG-2 are floated single-degree-of-freedom designs. The Teledyne instrument is a dry, two-degree-of-freedom, tuned, elastically-supported gyroscope. The three floated instruments have different types of output-axis (OA) supports. These support configurations and the results of their evaluation, which showed how the output-axis support affects the instrument's performance in a dynamic environment, are described in Chapter 2.

The evaluation of the Kearfott 2544 (ball-bearing OA support) is discussed in Chapter 3 of this report. The Honeywell GG334 (pivot-dithered jewel OA support) was evaluated in an earlier phase of this program[1]. This section of the report summarizes the evaluation of the magnetically-suspended CSDL 18 IRIG MOD-B. The areas discussed are:

1. A description of the CSDL 18 IRIG MOD-B (Section 4.2)
2. Torque generator and loop contributions to scale factor variation with rate (Section 4.3)
3. Methods of selecting the torquer tuning network and its effect on the scale factor variation with rate (Section 4.4)
4. Angular oscillation tests (Section 4.5)

4.2 THE MAGNETICALLY-SUSPENDED 18 IRIG MOD-B

The CSDL 18 IRIG MOD-B is a floated single-degree-of-freedom, strapdown instrument. A cutaway view of the 18 IRIG MOD-B is shown in Fig. 4.2-1. Tables 4.2-I and 4.2-II list a number of its operational and performance parameters. Its gas-bearing wheel rotates at 24,000 r/min, developing an angular momentum of 1.51×10^5 gm-cm^2/s. A four-pole, 800-Hz, two-phase, synchronous motor drives

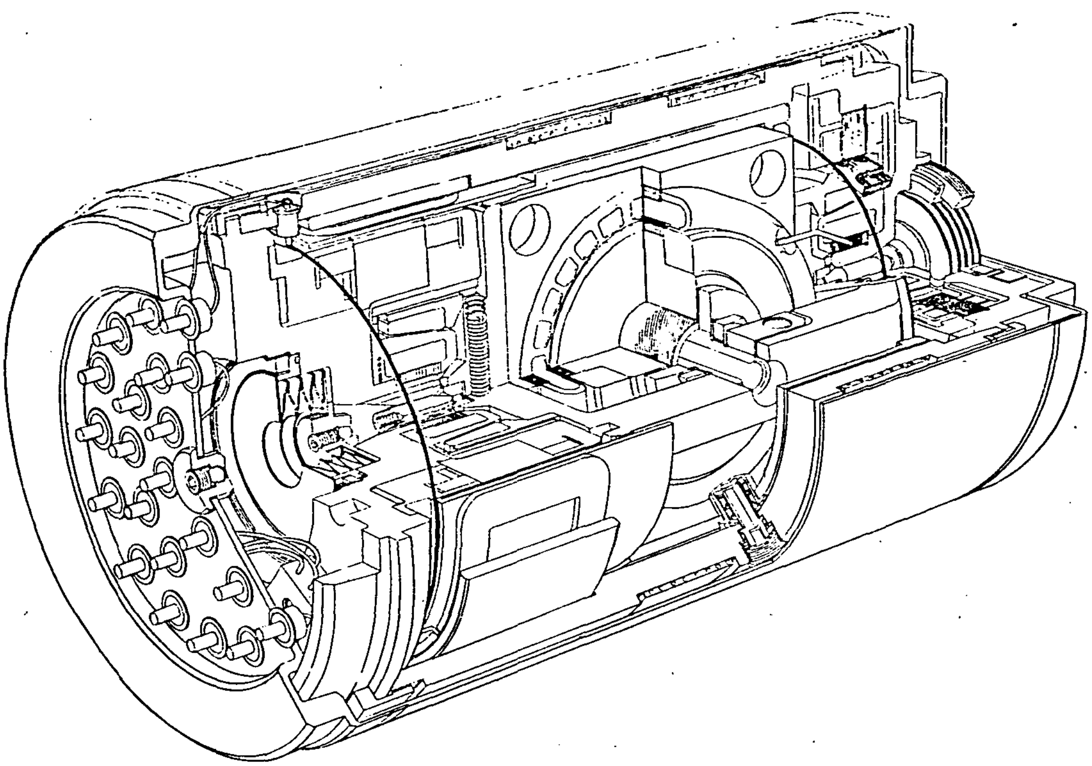

Fig. 4.2-1 CSDL 18 IRIG Mod-B

the wheel. The wheel and motor structure are mounted in an hermetically-sealed, cylindrical float surrounded by high density fluid. At operating temperature, the float is near neutral buoyancy. Bellows are provided in each end-housing to allow for fluid thermal expansion. An 8-pole, tapered, magnetic suspension is located at each end of the unit. It elastically restrains the axial and radial positioning of the float with respect to the case. At one end of the case is a signal generator whose output is proportional in magnitude and phase to the angular position of the float about the OA. It is a twelve-pole multiple-E-connected microsyn that is excited with 8.0 V (rms) at 9.6 kHz.

A permanent-magnet (PM) torque generator is at the opposite end of the case. It has an eight-pole, Alnico V permanent magnet, an Armco-iron return path mounted on the instrument's case, and eight torquing coils mounted on a beryllium-oxide holder attached to the float. A magnetic ring located on the permanent magnet provides torquer scale-factor temperature compensation.

Wrapped around the gyroscope case are four nickel, wire-wound temperature sensors for temperature control and monitoring. The gyroscope is enclosed in a mumetal vacuum envelope which provides magnetic shielding and reduces radial thermal gradients.

Table 4.2-I 18 IRIG Mod-B Mechanical and Dynamic Nominal Characteristics

PARAMETER	18 IRIG MOD-B	
Angular Momentum (H)	1.51×10^5	$gm\text{-}cm^2/s$
Output Axis Damping (C_{OA})	502,000	dyne-cm-s
Output Axis Inertia (I_{OA})	225	$gm\text{-}cm^2$
Float Time Constant	450	μ-s
Transfer Function	6	V/rad
Gimbal Freedom	±17	mrad
Operating Temperature	130	^oF
Size		
Diameter	1.8	in.
Length	3.86	in.
Weight	1.15	lb
Spin Motor Power		
Start	11	W
Run	5.2	W
Torquer Generator		
Scale Factor	1450	deg/h/mA
Temperature Coefficient	< 10	ppm/^oF
Maximum Input Power	0.9	W
Signal Generator Sensitivity	20	V/rad
Magnetic Suspension		
Radial Stiffness	8	gm/0.001 in.
Axial Stiffness	0.64	gm/0.001 in.
Heaters		
Warm-up	140	Ω
Control	80	Ω
Temperature Sensor		
Resistance at Operating Temperature	510	Ω
Coefficient	0.00226	$\Omega/\Omega/^oF$

Table 4.2-II 18 IRIG Mod-B Performance and Environmental Nominal Characteristics.

PARAMETER	18 IRIG MOD B	
Bias		
Magnitude	.4	deg/h
Stability		
Across Cooldowns	.05	deg/h
30 - day	.03	deg/h
Random (1h)	.001	deg/h
G-Sensitive Drift		
Magnitude	.1	deg/h/g
Stability		
Across Cooldowns	.07	deg/h/g
30 - day	.04	deg/h/g
Random (1h)	.005	deg/h/g
G^2-Sensitive Drift		
30 - day Stability	.009	$deg/h/g^2$
Scale Factor		
Stability (60 - hours)	±1.5	ppm
Deviation (±1.0 rad/s)	60	ppm
Environmental Capability (Conservative Estimates)		
Storage Temperature	25-190	°F
Vibration (60 - 400 Hz)	20	g
Acceleration	50	g
Shock	20	g
Rate	5.0	rad/s

4.3 TORQUE GENERATOR SENSITIVITY CHANGE WITH CURRENT

4.3.1 Introduction

Permanent-magnet torque generators were evaluated to determine their sensitivity change with current. The tests reported here were performed on the CSDL 18 IRIG Mod-B. These tests were run with either dc or ac input to the torque generator.

Similarities in the shape of the ternary-loop scale factor vs. rate curves and the dc sensitivity vs. current curves were observed in all tests. These similarities were first postulated as the result of power variation with rate and with changing dc inputs. Attempts to test verify this postulation showed that the torque generator variation with current could only be explained by a more comprehensive model since tests performed on a CSDL 18 IRIG Mod-B showed a sensitivity significantly higher when ac was superimposed on dc in the torque generator than for dc alone.

These studies identified design and assembly contributions to torque generator sensitivity changes with current. For example a variation in torque generator sensitivity with the ac frequency is obtained if the coil holder is a conductor and can support eddy currents. For this reason permanent magnet coil holders are typically constructed of potted epoxy or ceramic. In an actual instrument the torque generated is not identical when an equal magnitude of current is applied in one direction or in the opposite direction through the torque coil. This torque difference[1] occurs when the torque coil is operating at an angle, θ, rotated from the radially symmetric axis of the salient pole. The cause is armature reaction, an effect familiar in rotating dc machinery. A difference in positive and negative scale factor results in a net bias at null if the gyro is used in a binary torque-to-balance mode. Similarly, if conventional ac is fed to the coil, an output torque will result that is proportional to the angle θ and to the square of the current magnitude. If, during assembly of the instrument, the torque coil is aligned to the SG null until there is no ac torque sensitivity, the plus-to-minus scale-factor difference can be effectively minimized.

A theoretical model to explain this data was proposed by Salamin for the 18 IRIG MOD-B and is discussed in this section. The parameters of the model were determined for a particular gyroscope and the model was then used to predict the pulse torque scale-factor variation vs. input rate with various types of torque loops. The predicted variations were then compared to experimental results. Since this data is from a single instrument representing one specific design, it should not be identified as the nonlinearity model for all permanent magnet torque generators, but should only serve as a guide to the study of permanent magnet nonlinearities. These tests should be repeated using additional instruments representing different torquer designs to thoroughly understand these permanent-magnet characteristics.

4.3.2 Torquer Nonlinearity Model

The torque produced by a permanent-magnet torquer has been modeled by Salamin as:

$$M = (C_0 + C_1 P)I + C_2 I^2 + C_3 I^3 \tag{4.1}$$

where:

M	= torque (dyne-cm)
I	= current (mA)
P	= torquer power (W)
C_0	= coefficient of torque change with current
C_1	= coefficient of torque generator sensitivity change with torquer power
C_2	= coefficient of torque change with current squared
C_3	= coefficient of torque change with current cubed

The coefficient C_2 is proportional to the misalignment angle between the signal generator (SG) null and the torque generator (TG) point of maximum torque[1]. This angle can be adjusted during instrument assembly or test, allowing C_2 to be reduced or eliminated. The source of the C_3 coefficient is not understood at this time.

The current (I) is composed of ac (I_{ac}) and dc (I_{dc}) components, thus:

$$I = I_{dc} + I_{ac} \tag{4.2}$$

Substituting Eq. 4.2 into 4.1 yields:

$$M = (C_0 + C_1 P)\ (I_{dc} + I_{ac}) + C_2(I_{dc}^2 + 2I_{dc}I_{ac} + I_{ac}^2) + C_3(I_{dc}^3 + 3I_{dc}^2 I_{ac} + 3I_{dc}I_{ac}^2 + I_{ac}^3) \tag{4.3}$$

From Eq. 4.3, the time average of torque ($\overline{M}$) becomes:

$$\overline{M} = (C_0 + C_1 P)I_{dc} + C_2(I_{dc}^2 + \overline{I_{ac}^2}) + C_3(I_{dc}^3 + 3I_{dc}\overline{I_{ac}^2} + \overline{I_{ac}^3}) \tag{4.4}$$

where an overbar denotes time average.

When the ac has a single harmonic, $\overline{I_{ac}^3} = 0$ and Eq. 4.4 reduces to:

$$\overline{M} = (C_0 + C_1 P) I_{dc} + C_2 (I_{dc}^2 + \overline{I_{ac}^2}) + C_3 (I_{dc}^3 + 3 I_{dc} \overline{I_{ac}^2}) \tag{4.5}$$

Defining the deviation in torque generator sensitivity (D) as:

$$D = \frac{\overline{M}}{C_0 \overline{I}} - 1 \tag{4.6}$$

From Eq. (4.5) *D* becomes:

$$D = \frac{C_1}{C_0} P + \frac{C_2}{C_0} (I_{dc} + \frac{\overline{I_{ac}^2}}{I_{dc}}) + \frac{C_3}{C_0} (I_{dc}^2 + 3\overline{I_{ac}^2}) \tag{4.7}$$

Since $P = P_{dc} + P_{ac}$ where $P_{dc} \; \alpha I_{dc}^2$ and $P_{ac} \; \alpha \overline{I_{ac}^2}$ and assuming $C_2 = 0$ Eq. 4.7 can be expressed as:

$$D = (a + b) P_{dc} + (a + 3b) P_{ac} \tag{4.8}$$

where:

$a = C_1/C_0$
$b = C_3/C_0$

To determine the coefficients, a current is passed through the torquer and the test table is servoed to null the SG. This table rate is corrected for earth-rate input, gyroscope drift and the C_2 term. From Eq. 4.5 the coefficient C_2 is determined by measuring the average value of torque ($\overline{M}$) with no dc. Since the C_2 term is caused by a misalignment of the torque generator which is well understood, it will not be discussed in detail at this time. For the gyroscope used for the present tests, a CSDL 18 IRIG Mod-B (S/N 430B), the residual, after aligning the SG-to-TG null in the test lab was $C_2/C_0 = 0.045$ ppm/mA.

Figure 4.3-1 is the measured change in torque-generator sensitivity with dc input for this gyroscope. Its deviation (D) is linear with dc power. This gives the experimental value:

$$a + b = 0.0055 \text{ppm/mA}^2 \tag{4.9}$$

Figure 4.3-2 shows the variation in torque-generator sensitivity with ac superimposed on dc for this gyroscope. The variation is linear with ac power and yields the following value:

$$a + 3b = 0.014 \text{ ppm/mA}^2 \tag{4.10}$$

Previous tests showed that this ac power sensitivity is frequency independent. Tests results at 400, 1000, and 3200 Hz gave similar results.

Solving Eqs. 4.9 and 4.10 yields:

$$\begin{aligned} a &= 0.0012 \text{ ppm/mA}^2 \\ b &= 0.0043 \text{ ppm/mA}^2 \end{aligned} \tag{4.11}$$

The coefficient "a" is proportional to the change in thermal gradient between the torquer and the magnet. The 18 IRIG Mod-B was designed so that if the operating temperature increases, the increase in the moment arm of the torquer and the decrease in the magnetic flux compensate, leaving the torque constant. However, this does not compensate for thermal gradients across the torquer gap. Torquer current will cause a thermal gradient since it causes a higher coil temperature than magnet temperature. The increased moment arm of the torquer coil with this gradient causes a torque sensitivity increase with increasing current.

By running 10 and 100 mA through the torquer coils and measuring the voltages and resistance, the temperature change was obtained. The torquer temperature increased by 2.34°C for 100 mA.

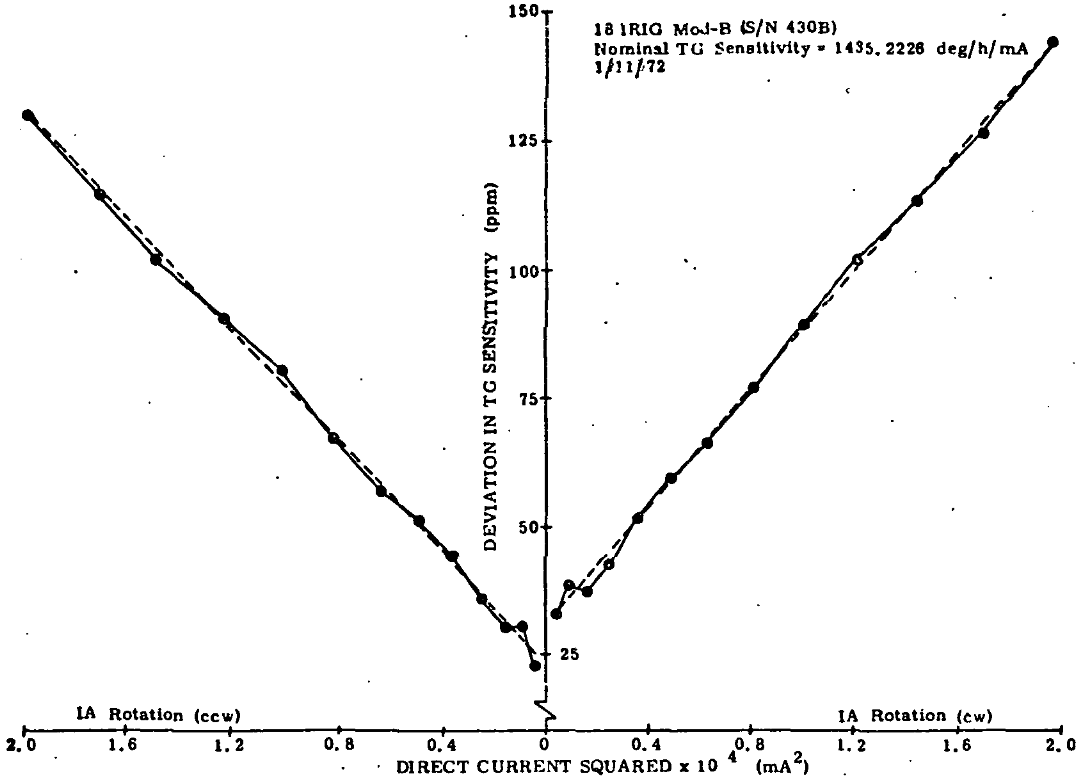

Fig. 4.3-1 DC Torque Generator Sensitivity.

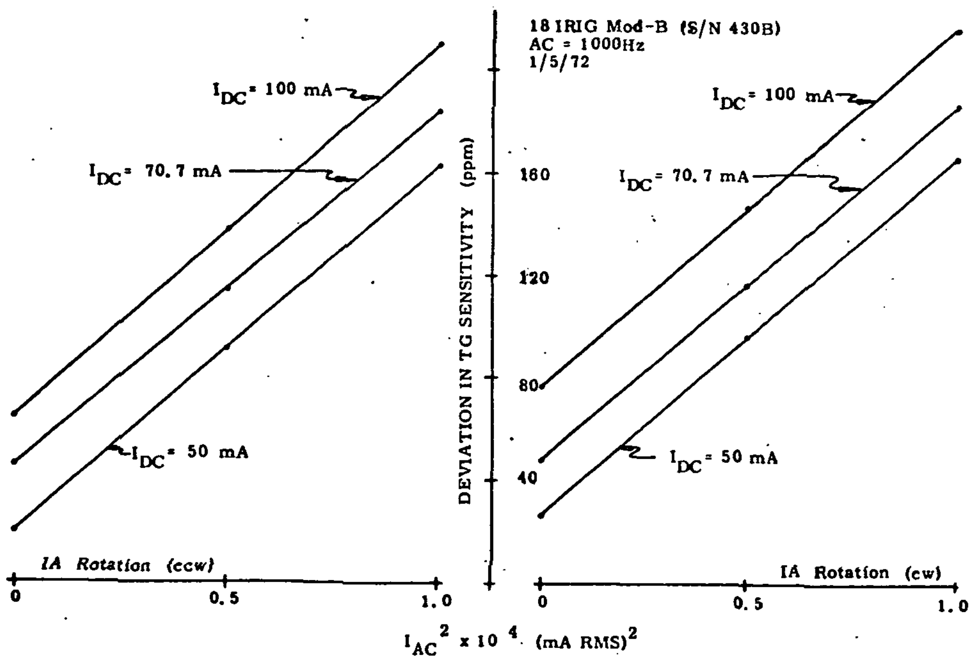

Fig. 4.3-2 TG Sensitivity to ac Superimposed on dc

The permanent magnet temperature cannot be measured directly. Instead, the temperature change of the magnetization winding was determined from its change in resistance. With 100 mA through the torquer coils, the temperature of the winding around the permanent magnet increased by 0.91°C.

Using this temperature difference of 1.43°C and the coefficient of expansion of copper the uncompensated moment arm expansion causes a 22 ppm scale factor change. Since part of the temperature gradient appears across the winding insulation and the expansion coefficient of the beryllium-oxide coil holder is smaller than that of copper, all we can conclude is that:

$$0 < a < 0.0022 \text{ ppm/mA}^2 \tag{4.12}$$

which is consistent with Eq. 4.11.

4.3.3 Torquer Nonlinearity for Various Torque-to-Balance Loops

Using Eq. 4.1 as a torquer model, the sensitivity deviation for various forms of pulse torquing can be predicted. Assume that the coefficient $C_2 = 0$, Eq. 4.1 becomes:

$$\overline{M} = (C_0 + C_1 P)\overline{I} + C_3\overline{I^3} \tag{4.13}$$

Using the definition of D from Eq. 4.6:

$$D = \frac{C_1}{C_0} P + \frac{C_3}{C_0}\frac{\overline{I^3}}{\overline{I}} \tag{4.14}$$

Using $P \ \alpha \overline{I^2}$ and "a" and "b" as previously defined.

$$D = a\overline{I^2} + b\,\frac{\overline{I^3}}{\overline{I}} \tag{4.15}$$

Computer simulations to illustrate the effects of the torque generator vs. current model on the performance of a gyro operating with various torque-to-balance

loops were performed. The simulation assumed the torque vs. current model previously developed for the 18 IRIG Mod-B. In addition, the computer simulation assumed the following conditions.

(1) Torquer time constant = 0.32 of interrogate time.

(2) Torque pulse duty cycle = 15/16.

(3) Gyroscope lag compensation[1] is used.

(4) In binary, ternary like decisions are made, i.e. non-zero threshold. If the ternary decision calls for no pulse, than an arbitrary pulse is given. These arbitrary pulses alternate in polarity. This is the fill-in binary technique discussed in Chapter 1.

(5) The torquer with its parallel tuning network appears as a pure resistance. Thus, the voltage across the torquer consists of sharp, square pulses.

(6) The torque current is normalized to 1 unit of current.

The simulation was only performed at rational multiples of maximum rate to insure a constant torquing pattern with time. For a given input rate, the computer simulation determined the pulse pattern. Starting with an arbitrary torquer current, the simulation repeatedly computed the current at the end of successive pulse pattern periods until a steady value was obtained. In addition, the integrals of I, I^2 and I^3 for one pulse pattern period were computed.

Figure 4.3-3 shows the average current squared, and Fig. 4.3-4 shows the average current cubed divided by the average current vs. input rate for binary and ternary torquing. The change in slope in the ternary curves at half rate are due to the occurrence of adjacent torque pulses above half rate and the non-occurrence below half rate. This discontinuity has a large, but finite, curvature. In actual gyroscopes, the discontinuity is smoothed by noise.

From Fig. 4.3-3 it is seen that the power variation in binary is 53% of the power variation in ternary. The binary power variation would be zero if the torquer time constant were zero. Furthermore, the current would consist of sharp, square pulses. Each pulse would produce the torque, $C_0I + C_3I^3$, and there would be no rate dependence from the I^3 term. If there is a finite torquer time constant, some power is dissipated in the tuning network (see Appendix B) and there is a corresponding power variation with rate for the binary torque loop.

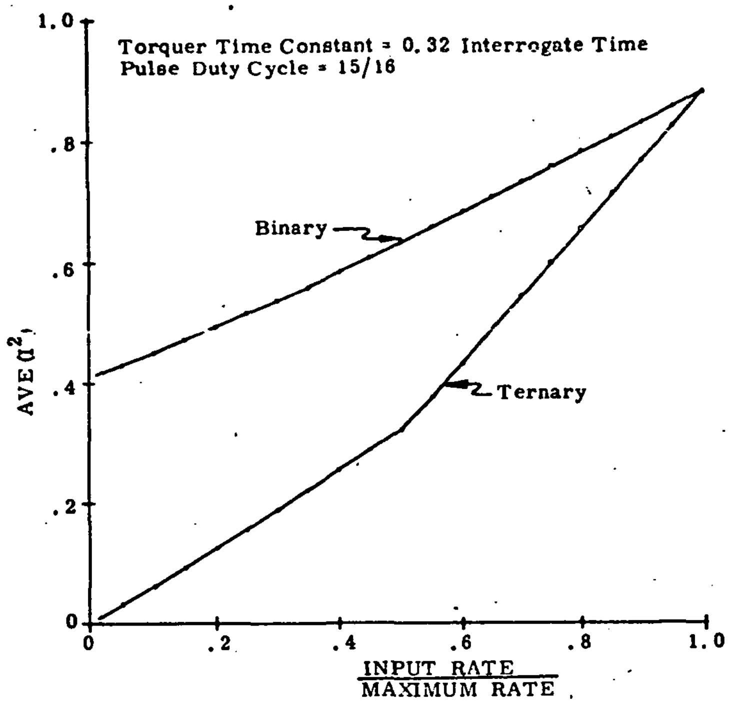

Fig. 4.3-3 Average Current Squared for Binary and Ternary Torquing

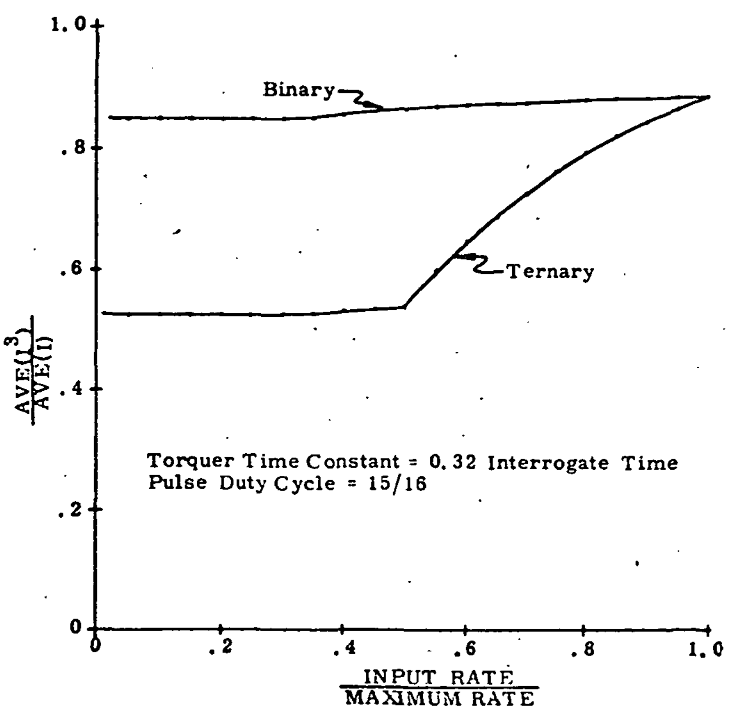

Fig. 4.3-4 Average Current Cubed for Binary and Ternary Torquing

The curves of Figs. 4.3-3 and 4.3-4 must be multiplied by the torque current squared and by the coefficients "a" and "b" as in Eq. 4.15 to give the predicted values of D for a particular gyroscope. Scale factor deviations computed in this manner for the torquer in the 18 IRIG Mod-B (S/N 430B) are shown in Fig. 4.3-5 for binary, ternary and analog torque-to-balance loops. These tests showed that, if considerations are directed specifically toward torque generator effects, the least scale factor deviation with rate occurred with the binary torque-to-balance loop (this is consistent with the results reported in Chapter 3), while the largest scale factor deviation resulted with the analog rebalance loop. The additional scale factor deviation vs. rate, caused by the torque electronics, will be discussed in the next section.

The I^3 term in the torquer model is necessary to account for a sensitivity variation with ac power 2.5 times as great as with dc power (see Eqs. 4.9 and 4.10). This model, however, should be verified experimentally using a number of torque generators of various designs.

4.3.4 Pulse Torque-to-Balance Electronics Rate Nonlinearity

In addition to the scale factor (SF) variation with rate caused by the torque generator, the torque-to-balance electronics causes a further scale factor variation with rate. For the ternary torque-to-balance loop, the SF variation with rate caused by the electronics, when combined with that caused by the torque generator results in the SF variation with rate shown in Fig. 4.3-6. Whether the loop is binary, ternary or analog torque-to-balance, a variation with rate would be expected from both the torque generator and the electronics. As described in Section 4.4 this variation with rate can be modeled and removed computationally. In addition to a variation in SF with rate, other loop problems such as dead zone, bias instability and quantization, as discussed in Chapter 1, must be considered in selecting the best torque loop for a particular application.

4.4 TORQUER TUNING

4.4.1 Background

Inertial components in strapdown systems have almost exclusively used permanent-magnet torque generators because of the high torque capability and the linear relationship between torque and coil current. In addition, the rebalance loop for strapdown systems is typically of the pulse torque-to-balance type. This rebalance technique provides the resolution needed and enables direct interfacing of the digital

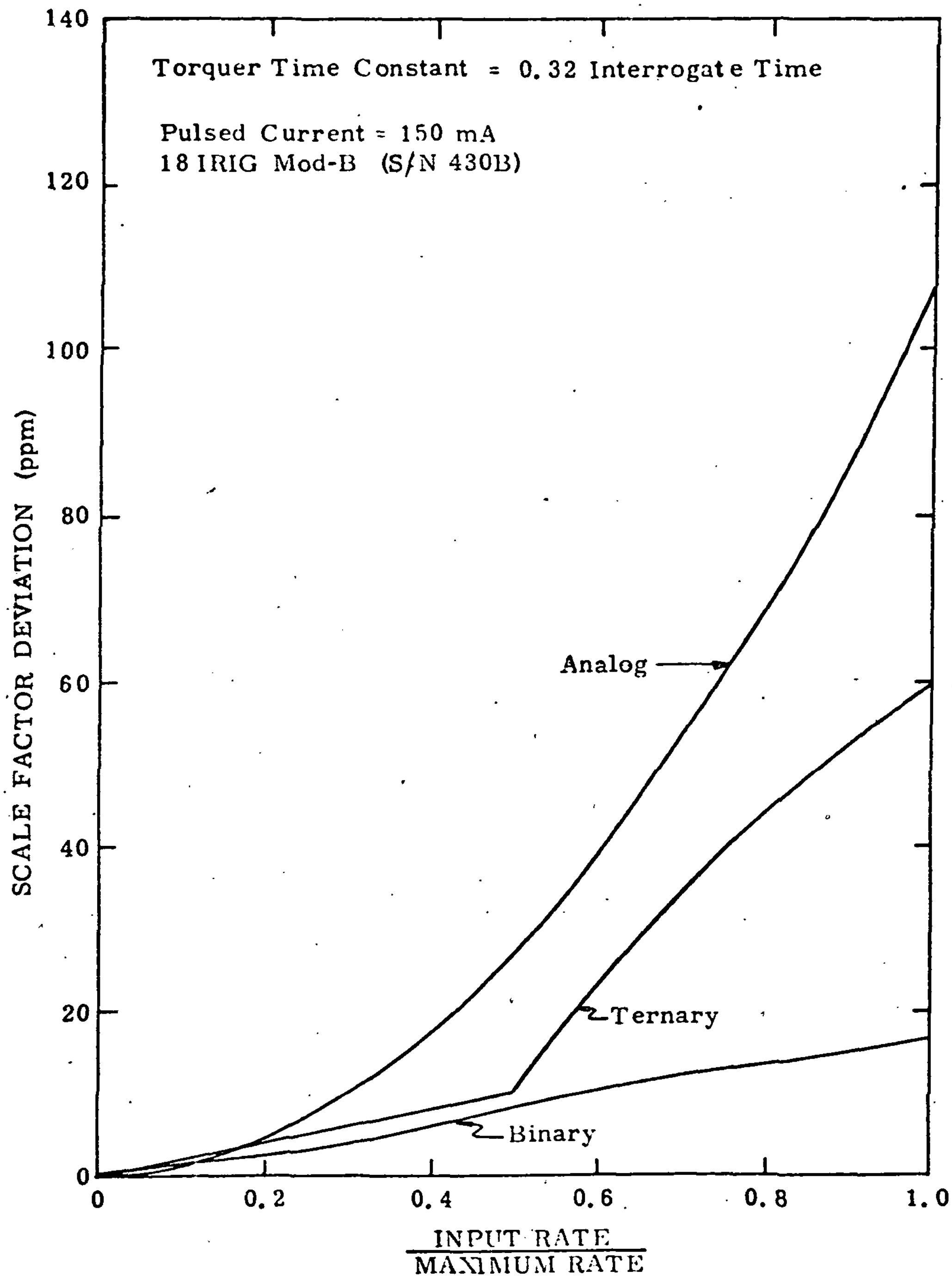

Fig. 4.3-5 Scale Factor Deviation Resulting from the Torquer for Binary, Ternary and Analog Torquing

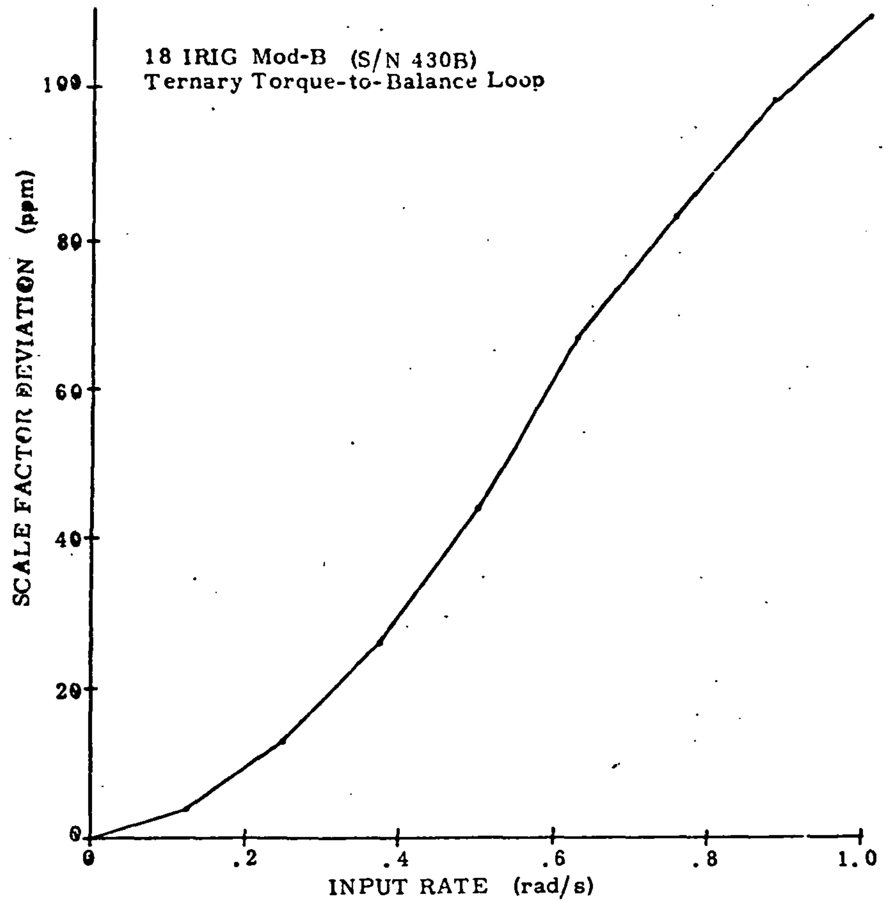

Fig. 4.3-6 Scale Factor Deviation vs Input Axis Rate

readout to a computer. In a digital rebalance loop, the current is applied in precision pulses to oppose precession or pendulous torque. Any variation in the charge of a pulse or the response to it will result in a scale factor deviation with applied rate. This scale factor variation with rate is affected by the torque generator characteristics, the rebalance electronics and the torquer tuning network. This section discusses methods of torquer tuning and the influence of these tuning techniques on scale factor variation with rate and on the pulse torque electronics response.

4.4.2 Torque Generator Tuning

The conventional method for tuning the permanent-magnet torque generator is to shunt the torque winding with an RC network (Fig. 4.4-1). This network is selected so that the load seen by the pulse torque electronics is purely resistive.

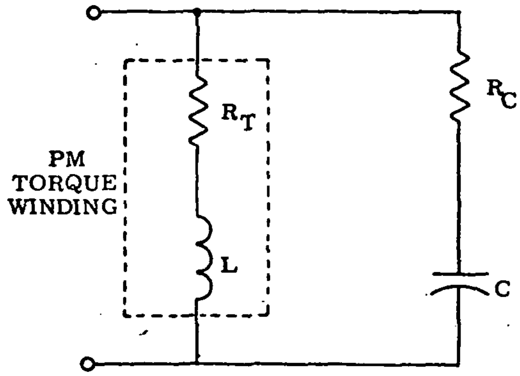

Fig. 4.4.-1 Primary - Torque Coil Compensation Network

The torque generator admittance is:

$$Y_T(s) = \frac{1}{R_T + L_s} = \frac{1}{L}\,\frac{1}{s + R_T/L} \qquad (4.16)$$

where:

L = torque generator inductance (H)
R_T = torque generator resistance (Ω).

The tuning network admittance is:

$$Y_C(s) = \frac{1}{R_C + 1/C_s} = \frac{1}{R_C} - \frac{1}{R_C{}^2 C}\,\frac{1}{s + 1/R_C C} \qquad (4.17)$$

where:

C = tuning capacitance (F)
R_C = tuning resistance (Ω).

The torque generator in parallel with its tuning network presents an admittance of:

$$Y(s) = Y_T(s) + Y_C(s) \tag{4.18}$$

If Y is to be a pure conductance, then the pole in Y_C must cancel the pole in Y_T. This imposes two conditions. First, the poles must coincide in the complex frequency plane:

$$\frac{1}{R_C C} = \frac{R_T}{L} \tag{4.19}$$

Second, the residues at these poles must be equal and opposite:

$$\frac{1}{R_C{}^2 C} = \frac{1}{L} \tag{4.20}$$

Equations (4.19) and (4.20) can be solved for the tuning network values:

$$R_C = R_T, \; C = \frac{L}{R_T{}^2} \tag{4.21}$$

The actual value of tuning network resistance and capacitance are generally selected for each individual gyroscope operating with its pulse torque electronics (PTE).

In reality, however, a single RC shunt does not eliminate PTE switching transients since the torquer model is really characterized by several RL time constants and a single RC shunt corrects only for the dominant first order lag. The switching devices in the PTE have basic lags which cause turn-on and turn-off transients in the current pulses to the torque coil. These transients can be reduced by applying an additional RC shunt network to the torque coil (Fig. 4.4-2). This network effectively minimizes the current pulse ringing and reduces its rise and decay time. The selection of the values for this secondary $R'_c C'$ tuning network and the final selection of the primary $R_c C$ network is best accomplished by adjusting the RC components such that the current pulses appear as square waves when monitored on an oscilloscope. Since the electronics are typically designed to drive a purely resistive load, these selected components are used as the torque-coil tuning network

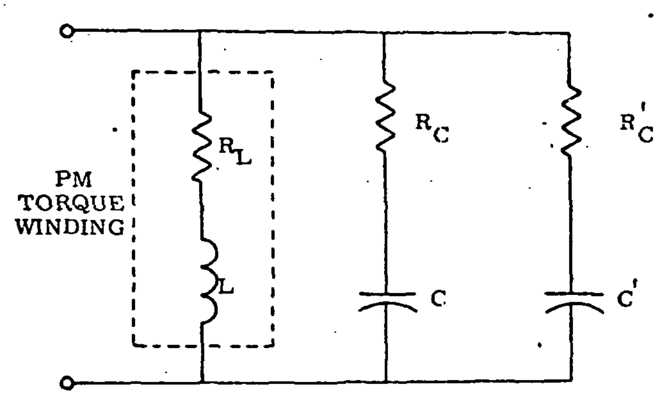

Fig. 4.4-2 Primary/Secondary - Torque Coil Compensation Network

to minimize the burden on the pulse rebalance electronics. The dynamic range and bandwidth of the PTE high gain amplifier, which has been designed to drive a resistive load, cannot typically handle overshoots because these overshoots can cause electronic instability.

4.4.3 Mistuning for Minimum Scale-Factor Deviation with Rate

The torque coil can be mistuned to cancel scale factor deviation with rate caused by the torque-coil power sensitivity and by the pulse torque electronics. Figure 4.4-3 shows the change in scale factor for an input rate range of ±0.06 to ±1.0 rad/s, with the torquer tuning network adjusted for a minimum deviation in scale factor. This adjustment was accomplished by systematically changing the resistance and the capacitance of the dominant first order (primary) tuning network to minimize the scale factor change with input rate. In doing so, the response of the pulse rebalance loop was also affected, thereby changing the charge of the current pulse. This method of mistuning the torque coil for minimum scale factor variation with rate is not considered desirable, since forcing the response of the PTE to effectively cancel an existing nonlinearity can cause transients. The transients, as previously stated, can saturate stages of the high-gain amplifier in the current control loop resulting in electronics instability.

Figure 4.4-4 shows the scale factor variation with rate for a resistively-tuned torque coil; the torquer-tuning network was adjusted so that the load seen by the PTE switches and current source was purely resistive. This condition satisfies the design criteria of the PTE and insures stable operating conditions through fast and accurate switching. In addition, the scale factor variation with rate can be

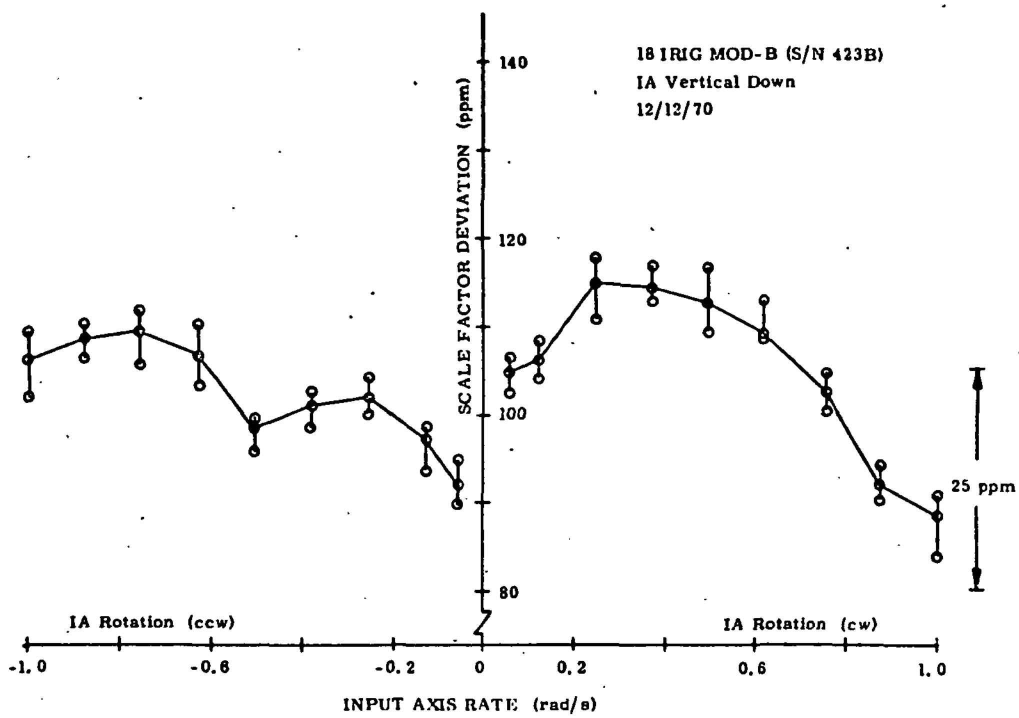

Fig. 4.4-3 Scale-Factor Deviation vs Rate (Torquer Mistuned for Minimum Scale-Factor Deviation)

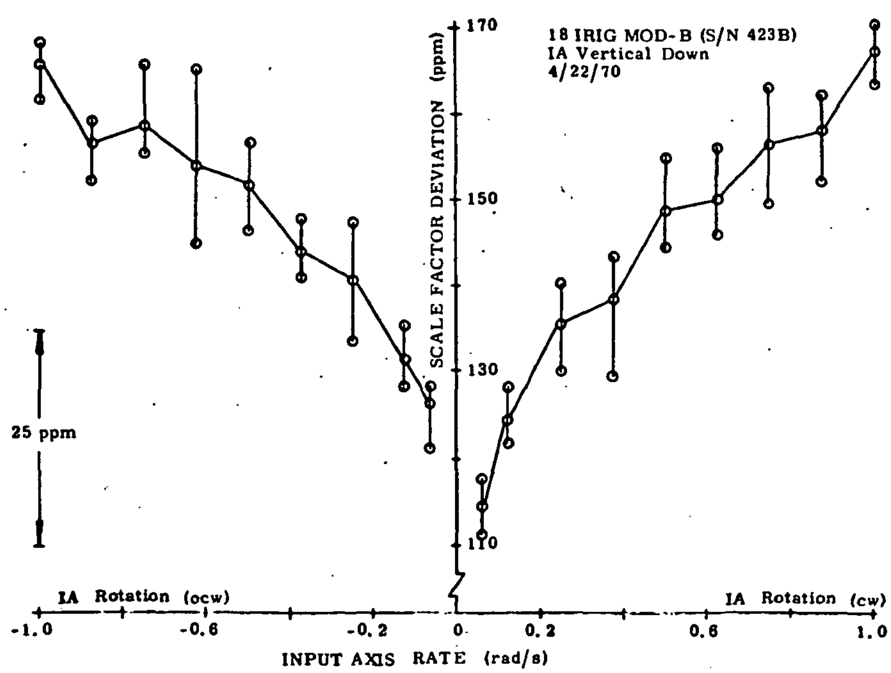

Fig. 4.4-4 Scale-Factor Deviation vs Rate (Torquer Resistively Tuned)

compensated in the software algorithm. Figure 4.4-5 shows the uncompensated and compensated scale factor as a function of rate for a resistively tuned condition. The uncompensated scale factor had a slope of 63 ppm/rad/s. The compensated algorithm removed this slope and resulted in a scale factor deviation with rate of less than 10 ppm over a rate range of ±0.8 rad/s.

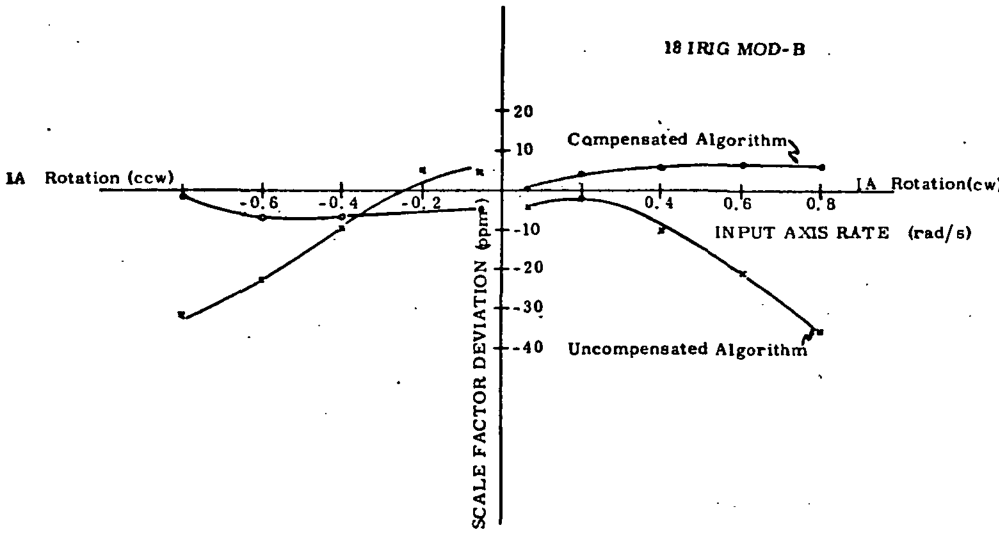

Fig. 4.4-5 Scale-Factor Deviation vs Rate (With and Without Computer Compensation)

This criterion for torque coil tuning is not restricted to the use of two RC networks. Additional RC shunt networks can be cascaded to eliminate other time constants and transients resulting from particular torquer and/or electronic characteristics. (For the Honeywell GG334 tests[1], three RC networks shunting the torque coil were used.) The major requirement in optimizing the tuning is to tune the specific torque coil with its selected rebalance electronics such that the current pulse response indicates a purely resistive load with no transients.

4.5 ANGULAR OSCILLATION TESTS

4.5.1 Background

Under a previous phase of this contract, facilities were assembled for testing inertial components under angular oscillatory environments. Comparative static, constant rate and angular oscillatory tests were performed for single-degree-of-

freedom ball-bearing, pivot-dithered jewel and magnetically suspended OA supports. The results of static and constant rate tests for the different OA supports is summarized in Chapter 2. The performance under angular oscillatory inputs was similar for the three types of suspensions. This section will summarize the angular oscillatory testing performed on the magnetically-suspended CSDL 18 IRIG Mod-B. The test facilities, described in Chapter 3, for the Kearfott 2544 tests, and in references 1, 2, and 3 of this chapter, were used for the testing of the 18 IRIG Mod-B.

4.5.2 Test Results

4.5.2.1 Introduction. Drift stability and constant rate test results for the CSDL 18 IRIG Mod-B are presented in Chapter 2. This section will present the single-axis angular oscillatory test results. Additional dynamic test evaluations of this instrument were performed on a triad system and are discussed in detail in reference 3.

4.5.2.2 Input Axis Transfer Function. The open loop transfer function for oscillations about IA is shown in Fig. 4.5-1. Test results are superimposed on two theoretical curves[4]. One curve assumes infinite structural rigidity of the wheel and float.

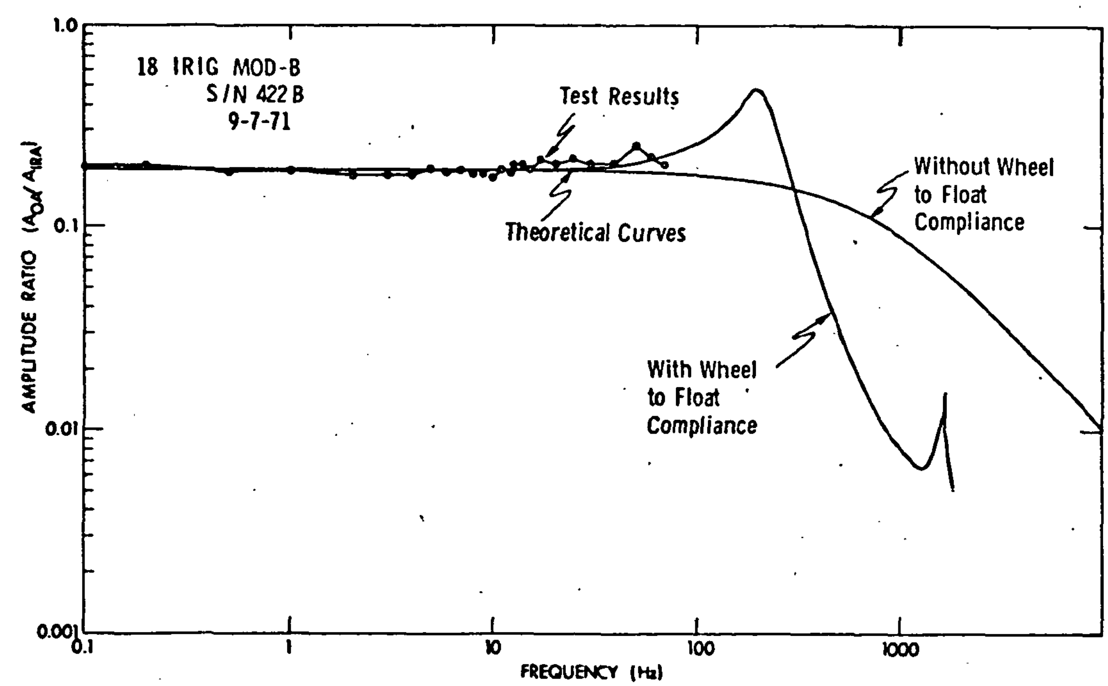

Fig. 4.5-1 Gyro Float Response to Sinusoidal Input Axis Case Motion (Magnitude)

The second curve considers the finite wheel-to-float structural rigidity and peaks in the vicinity of 200 Hz for this instrument. Both curves correspond in the low frequency range (less than 60 Hz). Data was obtained from 0.1 to 80 Hz. The test results follow the common portion of the two theoretical curves. A higher frequency angular vibrator would be required to determine which of the two models the test results followed. Reference 1 showed that the Honeywell GG334 tested to 600 Hz in the gimbaled angular vibrator followed the infinite structural rigidity model.

4.5.2.3 Output-Axis Transfer Function. The open loop transfer function for oscillations about OA is shown in Figs. 4.5-2 and 4.5-3. Test results are superimposed on the two theoretical curves, one assuming an infinite wheel-to-float structural rigidity, the second, assuming a finite wheel-to-float structural rigidity, peaked in the vicinity of 200 Hz for this unit. The test results for the 18 IRIG Mod-B follow the theoretical compliant model (Fig. 4.5-2). Similar agreement was obtained for the GG334 gyroscope as reported in reference 1.

4.5.2.4 Multiaxis Angular Oscillatory Testing. Multiaxis tests performed on a three-axis strapdown system[3] showed that the 18 IRIG Mod-B followed the expected theoretical models. Those results are discussed in reference 3. In addition, multiaxis tests similar to those described in Chapter 3 for the Kearfott 2544 were performed on the 18 IRIG Mod-B. These tests confirmed the significance of scale factor asymmetry on the rectified drift obtained during angular oscillations, and agreed well with the theoretical models.

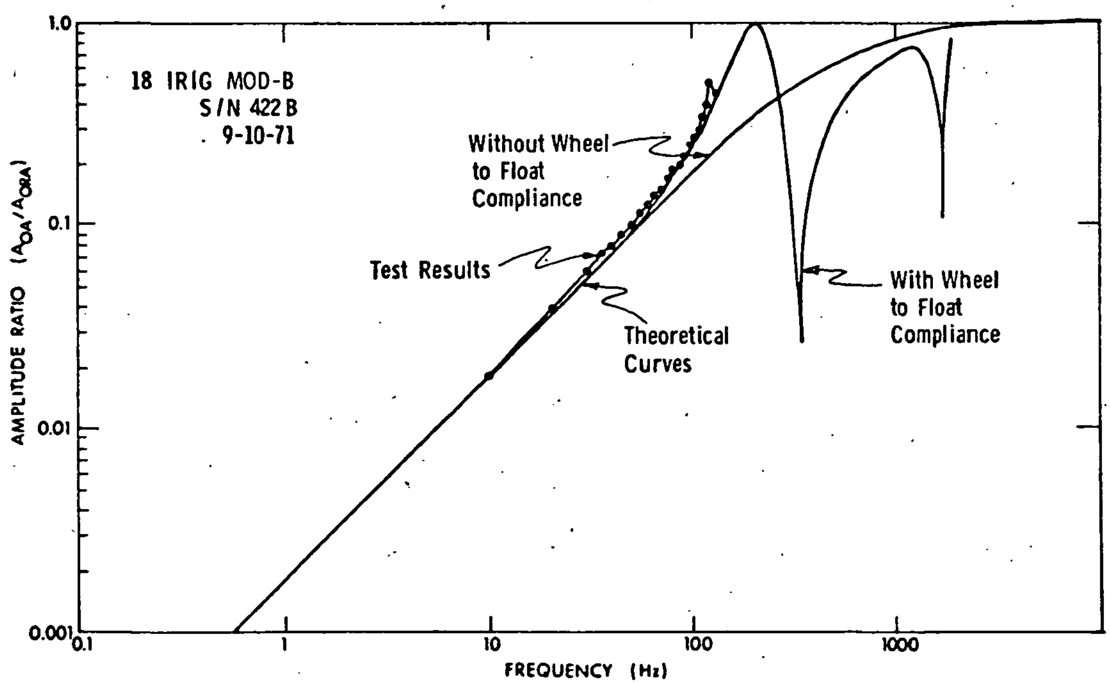

Fig. 4.5-2 Gyro Float Response to Sinusoidal Output Axis Case Motion (Magnitude)

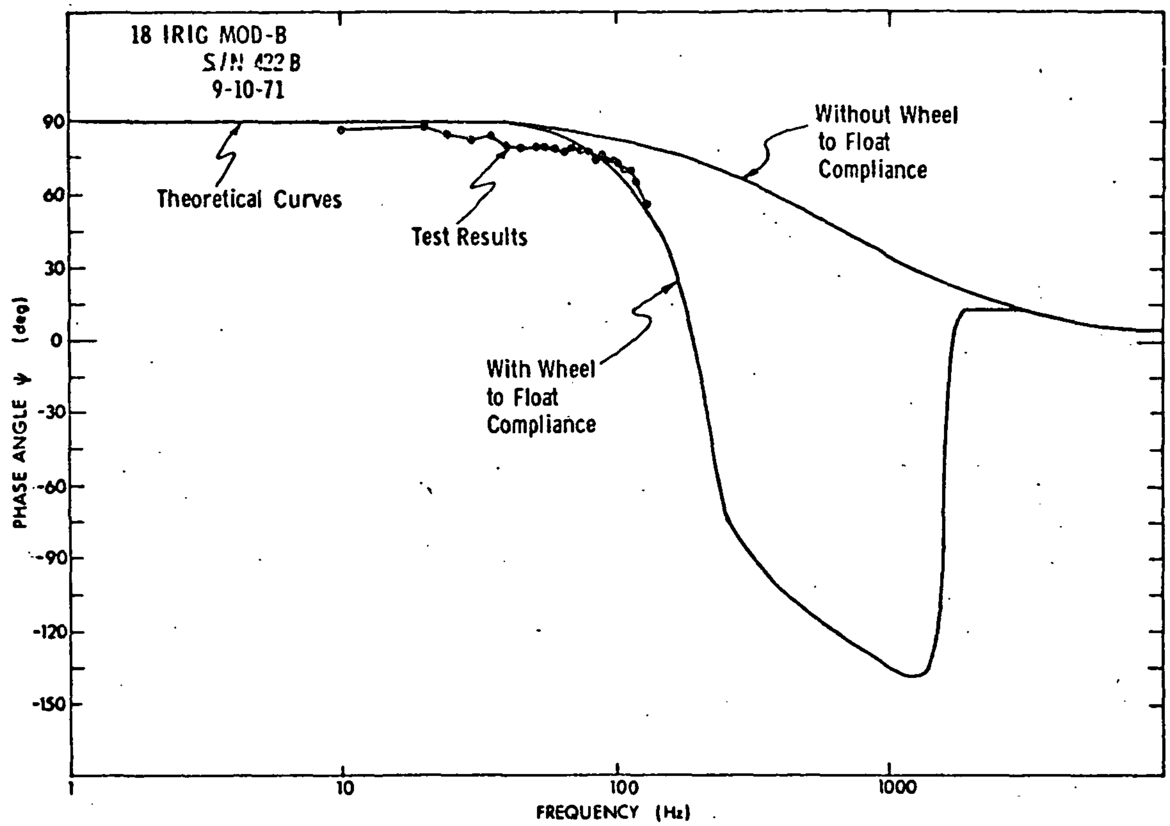

Fig. 4.5-3 Gyro Float Response to Sinusoidal Output Axis Case Motion (Phase Angle)

4.6 SUMMARY AND CONCLUSIONS

This chapter summarizes tests performed on the CSDL 18 IRIG Mod-B. The torque generator nonlinearity results, methods of tuning the torquer and angular oscillatory test results are presented.

The torque generator nonlinearity tests show results that can be explained by a torque proportional to torque coil current cubed. Additional tests are suggested for other PM torquers to confirm the torque generator nonlinearity model.

The torque coil tuning tests showed that scale factor variation with rate could be reduced by mistuning the RC tuning network, but this method of tuning achieved its purpose by sacrificing the stability of the pulse torque electronics. It is shown that a more satisfactory technique for correcting scale factor variations with rate proved to be to remove it computationally in the system software, since the scale factor deviation vs. rate characteristics as measured were stable and predictable. The software burden implied by this approach was insignificant, less than 30 words in a triad implementation.

The angular oscillatory test results performed on the CSDL 18 IRIG Mod-B are commensurate with performance data from the other single-degree-of-freedom, floated instruments tested.

REFERENCES

1. Lory, C., Feldman, J., and Sinkiewicz, J., Dynamic Testing of a Single-Degree-of-Freedom Strapdown Gyroscope, Charles Stark Draper Laboratory Report E2618, October 1971.

2. Cooper, R., Shuck, T., SIRU Development-Final Report-Volume II-Gyro Module, Charles Stark Draper Laboratory Report R-746, June 1973.

3. Blaha, R.J., Gilmore, J.P., Strapdown System Performance Optimization Test Evaluations (SPOT) Final Report on Contract NAS 9-6823 Modification 11, Charles Stark Draper Laboratory, Report R-743, February 1973.

4. Schneider, G.E., Studies on Dynamic Testing of a Single-Degree-of-Freedom Integrating Gyroscope Used in a Strapped-Down Environment, Charles Stark Draper Laboratory Report T-526, January 1970.

CHAPTER 5
TEST EVALUATION OF THE TELEDYNE TWO-DEGREE-OF-FREEDOM STRAPDOWN GYROSCOPE

5.1 INTRODUCTION

This chapter presents a test evaluation of the Teledyne, SDG-2, two-degree-of-freedom, strapdown gyroscope in both static and constant rate environments. The tests performed measured drift coefficients, drift stabilities, torquer stabilities, and torquer sensitivity changes with dc. In addition, the scale factor performance under constant rate inputs was demonstrated for the gyroscope-rebalance loop combination.

A description of the Teledyne instrument and the test facility and a discussion of the theory of an elastically-supported, tuned gyroscope are also presented.

The results and conclusions are based upon a sequence of evaluation tests performed on one instrument and its mating electronics. The report does not attempt to categorize the Teledyne SDG-2 family.

5.2 BACKGROUND

5.2.1 The Teledyne SDG-2 Gyroscope

The Teledyne SDG-2 gyroscope is a dry, two-degree-of-freedom, elastically-supported, tuned instrument. A cutaway view of the Teledyne gyroscope is shown in Fig. 5.2-1. Tables 5.2-I and 5.2-II list a number of its operational and performance parameters as quoted by Teledyne Systems Company. (Publishing of this performance data in this report does not infer CSDL verification except as indicated in the text). The unit has a multi-gimbal rotating suspension system, similar to that shown in Fig. 5.2-2, which torsionally decouples the rotor from the case-fixed shaft. Two sets of standard R4 ball-bearings enable shaft rotational freedom within the case. The shaft rotates at 6,000 r/min, developing an angular momentum of 1×10^6 gm-cm^2/s. An eight-pole, 400-Hz, three-phase, synchronous motor drives the shaft. To achieve the desired instrument performance a high angular momentum was required. Since the shaft speed (100 r/s) was selected to extend bearing life, a large rotor inertia and thus a large (3 in.-dia. x 3.25 in.-length), heavy (2.5 lb) instrument resulted.

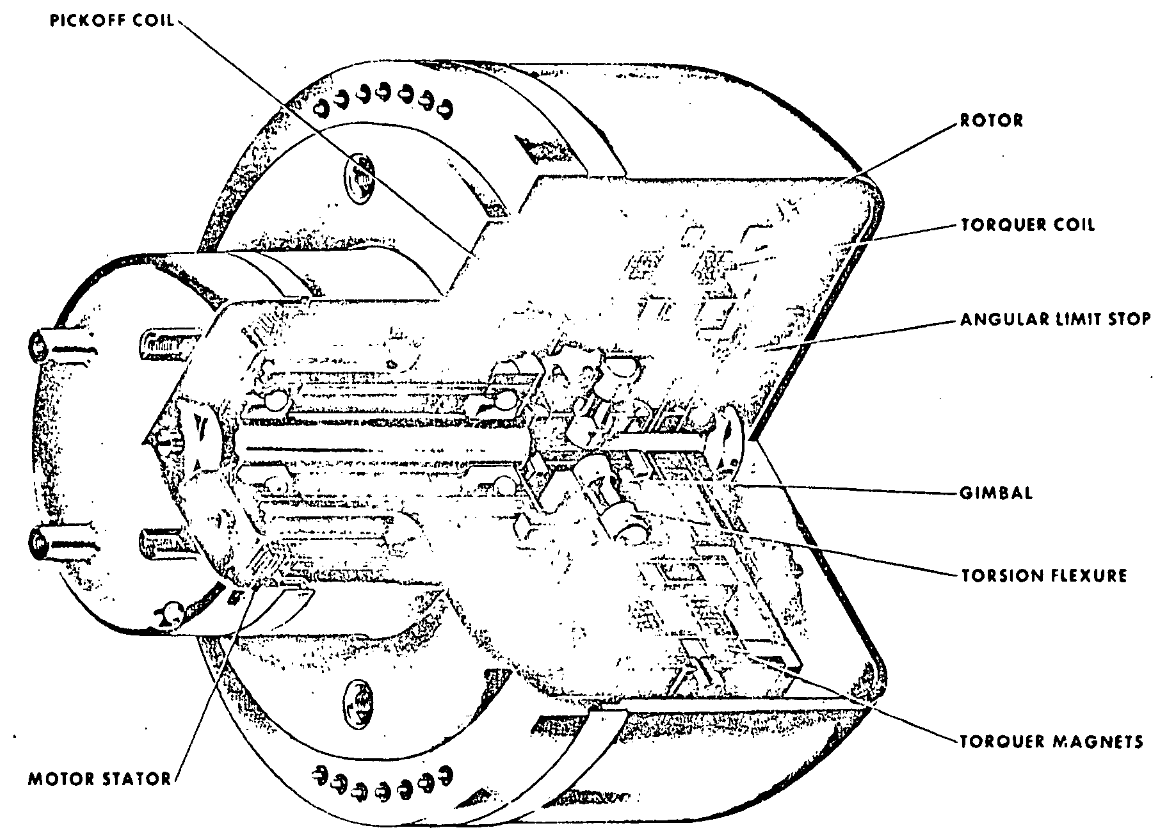

Photo Courtesy of Teledyne Systems Company

Fig. 5.2-1 Teledyne Inertial Rate Sensor

Table 5.2-I

Teledyne SDG* - Mechanical and Dynamic Nominal Characteristics**

PARAMETER	TELEDYNE SDG - 2
Size	
Diameter	3.0 in.
Length	3.25 in.
Weight	2.5 lb
Spin Motor Power	1.0 W
Angular Momentum (H)	1×10^6 gm-cm^2/s
Torque Generators	
Sensitivity (S_{TG})	200 deg/h/mA
Maximum Torquing Rate	
Transient	400 deg/s
Steady State	100 deg/s
Torquer Power	
Transient	640 W
Steady State	40 W
Torquer Current	
Transient	8 A
Steady State	2 A
Auxiliary Torque Generators	
Sensitivity (S_{TG})	20 deg/h/mA

* SDG - Suspended Dry Gyroscope

** As published by Teledyne Systems Company (Ref. 2, pp. 1-3)

Table 5.2-II

Teledyne SDG-Nominal Performance Characteristics*

PARAMETER	TELEDYNE SDG - 2
Bias Stability	
30 day	0.01 deg/h
Random drift	0.001 deg/h
G - Sensitive Torque	0.3 deg/h/g
Anisoelasticity	0.02 $deg/h/g^2$
Temperature Sensitivity	0.00005 $deg/h/^{o}F$
DC Torquer Stability	50 ppm

* As published by Teledyne Systems Company (Ref. 3, pp. 20)

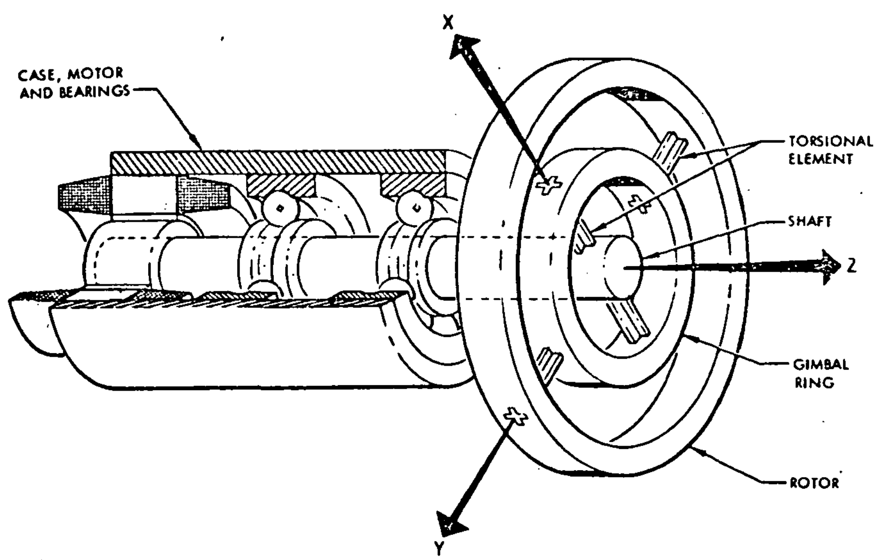

from Ref. 1, pp. 4

Fig. 5.2-2 Gyroscope Gimbal and Rotor Supported by Torsional Elements

The rotor is electromagnetically torqued with respect to the gyroscope case by a permanent magnet torque generator (TG). The TG consists of circular, samarium cobalt magnets mounted on the spinning rotor and case-fixed torque coils secured to beryllium-copper supports (Fig. 5.2-3). A steady-state torquer power of 40 watts is needed for a continuous torquing rate of 100 deg/s. Inductive pickoffs are used to provide an output proportional in magnitude and phase to the attitude change of the case with respect to the free rotor. The pickoffs are composed of winding pairs excited with 7.0 V (rms) at 48 kHz and fixed to the gyroscope case. Each winding pair defines one of the gyroscope input axes.

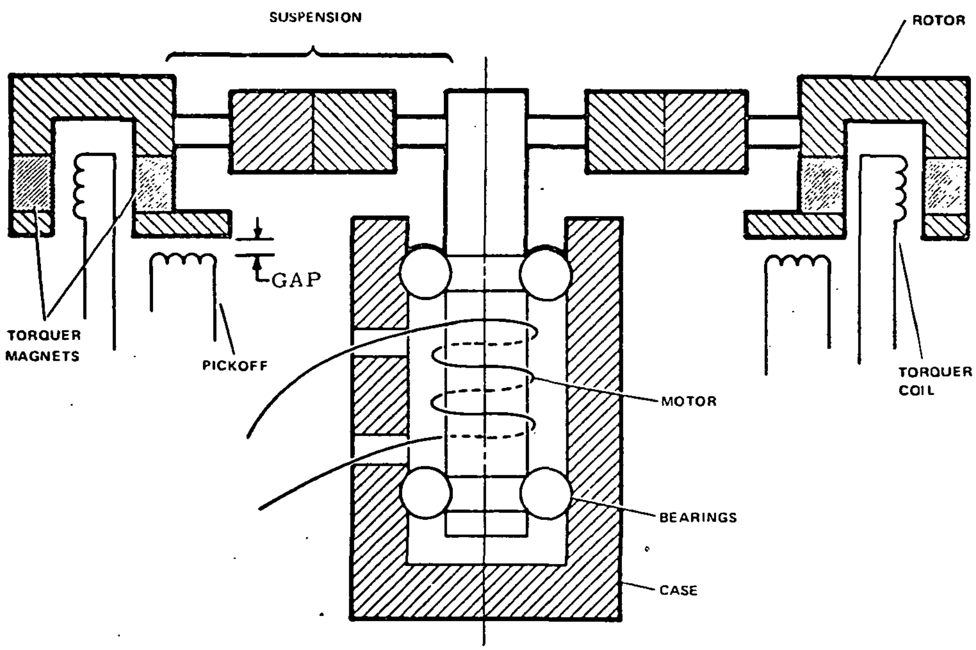

from Ref. 2, pp. 2

Fig. 5.2-3 Gyroscope Diagram

5.2.2 The Elastically-Supported, Tuned Gyroscope

A brief description of the principles of operation of a tuned gyroscope will be presented before discussing the performance evaluation of this instrument.

In an elastically-supported, tuned gyroscope, the spinning rotor and the gimbals are suspended by torsional elements (see Fig. 5.2-2). This rotating torsional support decouples the rotor from the case-fixed, motor-driven shaft through a number of gimbals to obtain a free-rotor, two-degree-of-freedom gyroscope.

The case of a free-rotor gyroscope can be displaced in any direction without transferring disturbance torques through the spinning rotor supports. Thus for a free-rotor gyroscope, the angular orientation of the rotor axis remains fixed relative to inertial space.

The elastically-supported, tuned gyroscope exhibits this free body characteristic when it is tuned. A tuned condition requires the gyroscope elastic restraints to sum to zero, i.e., that the dynamically induced spring restraint, which has a negative coefficient of spring rate, cancels the positive spring restraint produced by the torsional elements.

5.2.2.1 Equations of Motion. An analysis deriving the condition necessary for tuning was developed by Howe and Savet[4] for a single-gimbal configuration (Fig. 5.2-4). For a static, open-loop condition with no case motion they obtained a set of homogeneous, second-order, differential equations for the rotor deflection angles θ_x and θ_y (see Fig. 5.2-5). These equations of motion are:

$$\left(A + \frac{A_n}{2}\right) \ddot{\theta}_x + (C + A_n)N \dot{\theta}_y + (K - (A_n - \frac{C_n}{2})N^2)\theta_x + q_x \cos 2Nt + q_y \sin 2Nt + f\dot{\theta}_x + \lambda\theta_y = 0 \tag{5.1}$$

$$\left(A + \frac{A_n}{2}\right) \ddot{\theta}_y - (C + A_n)N \dot{\theta}_x + (K - (A_n - \frac{C_n}{2})N^2)\theta_y + q_x \sin 2Nt - q_y \cos 2Nt + f\dot{\theta}_y - \lambda\theta_x = 0 \tag{5.2}$$

where:

A, B, C	= inertias of the rotor about the principal axes x', y', z' (gm-cm^2)
A_n, B_n, C_n	= inertias of the gimbal about the principal axes x_n, y_n, z_n (gm-cm^2)
A	= B (gm-cm^2)
A_n	= B_n (gm-cm^2)
N	= shaft speed (rad/s)
K	= spring constant for the gimbal and rotor torsional elements (gm-cm^2/s^2)
θ_x, θ_y	= rotor deflection angles with respect to the shaft (rad)
f	= rotor damping coefficient[6] ((dyne-cm-s)/rad)
λ	= cross-axis torque constant of the rotor shaft[6] ((dyne-cm)/rad)

$$q_x = \frac{A_n}{2}\ddot{\theta}_x + A_n N \dot{\theta}_y - (A_n - \frac{C_n}{2})N^2 \theta_x \quad \text{(dyne-cm)}$$

$$q_y = \frac{A_n}{2}\ddot{\theta}_y - A_n N \dot{\theta}_x - (A_n - \frac{C_n}{2})N^2 \theta_y \quad \text{(dyne-cm)}$$

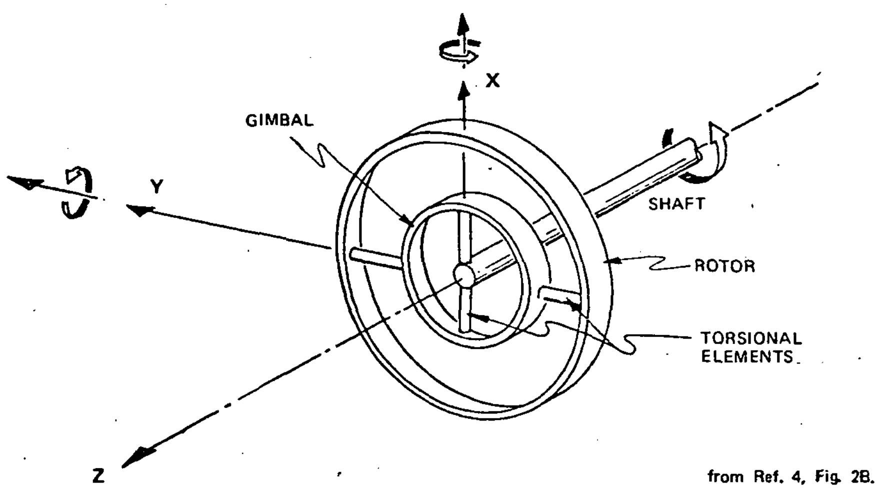

Fig. 5.2-4 Single Gimbal Configuration

For the purposes of this discussion, the effects of viscous damping (f) and cross-axis, rotor shaft torques (λ) are assumed to be negligible. In addition, the terms involving sin (2N) and cos (2N) may be eliminated. These sinusoidal expressions, at twice spin frequency, can cause a rectification error for a single gimbal configuration in the presence of a 2N-Hertz angular input. This error[5] is eliminated when a multi-gimbal arrangement is implemented. With the above simplifications, the open-loop equations of motion become:

$$\left(A + \frac{A_n}{2}\right)\ddot{\theta}_x + (C + A_n)N\dot{\theta}_y + (K - (A_n - \frac{C_n}{2})N^2)\theta_x = 0 \qquad (5.3)$$

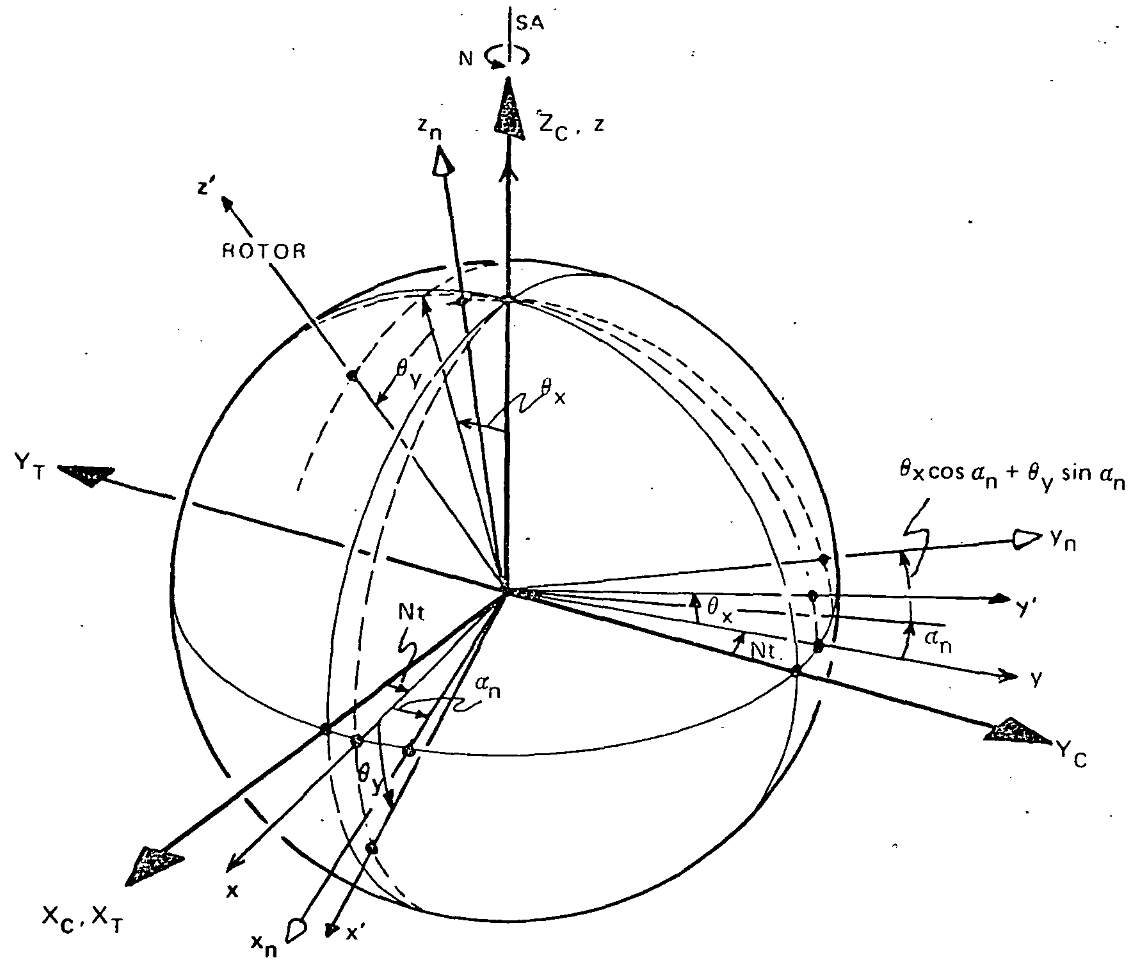

X_C, Y_C, Z_C	=	case fixed axes
x, y, z	=	coordinate set fixed to the shaft
x', y', z'	=	coordinate set fixed to the rotor
x_n, y_n, z_n	=	coordinate set fixed to the gimbal
X_T, Y_T	=	torquer axes
N	=	angular velocity of shaft
SA	=	shaft spin axis
α_n	=	angular displacement of the gimbal set with respect to the shaft set
θ_x, θ_y	=	rotor deflection angles

Fig. 5.2-5 Case, Shaft, Rotor and Gimbal Coordinate Sets

$$\left(A + \frac{A_n}{2}\right) \ddot{\theta}_y - (C + A_n)N\dot{\theta}_x + (K - (A_n - \frac{C_n}{2})N^2)\,\theta_y = 0 \tag{5.4}$$

To obtain a tuned condition and achieve a zero elastic restraint, the net restraint torque coefficient

$$K - (A_n - \frac{C_n}{2})N^2 \tag{5.5}$$

must be set equal to zero by balancing the positive torsional spring rate (K) with the negative dynamically induced spring rate $(A_n - C_n/2)N^2$. That is:

$$K = (A_n - \frac{C_n}{2})N^2 \tag{5.6}$$

5.2.2.2 Tuned Speed. The gyroscope tuned speed (N_0) can be determined, using Eq. 5.6, by the relation:

$$N_o = N = \sqrt{\frac{K}{A_n - \frac{C_n}{2}}} \tag{5.7}$$

This relationship for angular velocity can be extended to a multi-gimbal configuration, as shown by Craig[5]. His analysis shows that the square of the tuned speed is equal to the ratio of the given torsional restraint coefficient (K) relative to an n^{th} set of gimbal inertias (J). That is:

$$N_o^2 = \frac{K}{J} = \frac{\sum_1^n (Kx_n + Ky_n)}{\sum_1^n (A_n + B_n - C_n)} \tag{5.8}$$

For a tuned multi-gimbal gyroscope, the open-loop equations of motion thus reduce to:

$$\left(A + \frac{A_n}{2}\right) \ddot{\theta}_x + (C + A_n)N\dot{\theta}_y = 0 \tag{5.9}$$

$$\left(A + \frac{A_n}{2}\right) \ddot{\theta}_y - (C + A_n)N\dot{\theta}_x = 0 \tag{5.10}$$

5.2.3 Gyroscope Rebalance Electronics

The Teledyne gyroscope rebalance electronics (Fig. 5.2-6) consist of two direct-axis (X_D and Y_D), analog, torque-to-balance loops and two cross-axis loops (X_{CR} and Y_{CR}). The cross-axis loops were used by Teledyne to increase the bandwidth and achieve higher loop stiffness. This dual loop utilizes direct-axis rebalancing for angular input rate compensation and cross-axis rebalancing to compensate for input accelerations. This technique stems from the open-loop equations of motion (Eqs. 5.9 and 5.10). When these expressions are written in closed-loop form, they become:

$$I\ddot{\theta}_x + H\dot{\theta}_y = -M_x \tag{5.11}$$

$$I\ddot{\theta}_y - H\dot{\theta}_x = -M_y \tag{5.12}$$

where:

I	= rotor-gimbal inertias about input axes x', y' (gm-cm^2)
H	= gyroscope angular momentum (gm-cm^2/s)
M_x, M_y	= restoring torque for Y and X axis, respectively (dyne-cm)

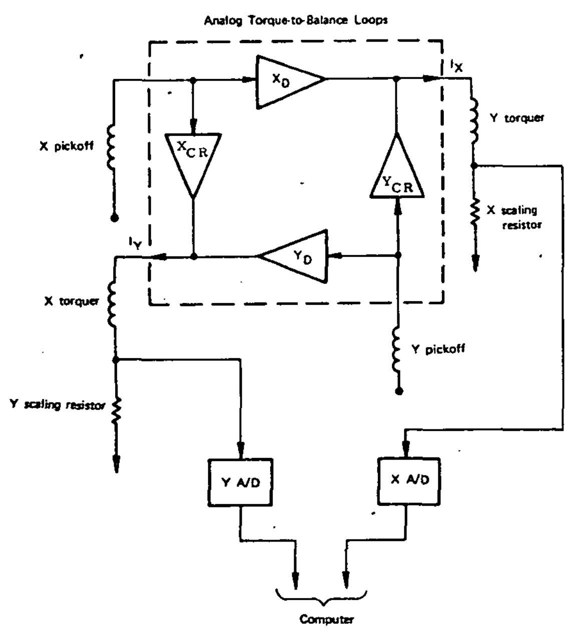

Fig. 5.2-6 Teledyne SDG: Rebalance Loop Diagram

When an input angular rate is applied to the gyroscope case, the inductive-pickoffs sense the resulting attitude change of the case axis relative to the rotor axis. The pickoff output signals are then applied as an input to the analog rebalance loops, which generate precision, direct rebalance currents. These currents are applied to the case-fixed torque coils, thereby providing the restoring torques needed to maintain instrument null. In addition, the torquer currents are monitored and used as a measure of input rate. Digital conversion of the precision direct currents provides the readout mechanization.

5.2.4 Mistuning and Offset Angle Errors

During instrument fabrication, the shaft is driven at a predetermined angular velocity and the gimbal inertias are adjusted to balance the restraints. If this adjustment is not precise, restraint torques on the rotor cause drifts with respect to inertial space.

This mistuned condition was shown by Craig[5] in his derivations of tuning errors. He develops expressions, from the open-loop transfer function, for the rotor to case angles of:

$$\theta_{x(t)} = - \phi_{x(t)} e^{-t/\tau} \cos \frac{\delta N}{F_m} t + \phi_{y(t)} e^{-t/\tau} \sin \frac{\delta N}{F_m} t \qquad (5.13)$$

$$\theta_{y(t)} = - \phi_{y(t)} e^{-t/\tau} \cos \frac{\delta N}{F_m} t - \phi_{x(t)} e^{-t/\tau} \sin \frac{\delta N}{F_m} t \qquad (5.14)$$

where:

θ_x, θ_y	= rotor to case angles for x and y axis, respectively (rad)
ϕ_x, ϕ_y	= input angular displacement of gyroscope case relative to rotor axis for x and y axis, respectively (rad)
τ	= gyroscope time constant (s) (see Section 5.2.5)
N	= shaft speed (rad/s)
N_o	= tuned speed (rad/s)
δN	= N_o-N (rad/s)
F_m	= figure of merit, ratio of gyroscope inertias (see Section 5.2.5)
t	= time (s)

The case axis displacements, ϕ_x and ϕ_y, require the gimbal to oscillate through the angles θ_x and θ_y relative to the case due to the rotor resistance to attitude

change. This relative motion between gimbal and shaft, and gimbal and rotor dissipates energy due to viscous and frictional effects. The resulting torques produced, tend to attenuate the amplitude of gimbal oscillation, with time constant, τ, and realign the rotor relative to the case. If the gyroscope is mistuned, the gimbal oscillation decays in the form of a damped sinusoid with period $T = F_m/\delta N$.

Equations 5.13 and 5.14 further show that mistuning causes bias drifts, $\dot{\theta}_x$ and $\dot{\theta}_y$. These drift rates occur for a constant rotor offset, closed-loop condition that is obtained by setting time $t = 0$. For the purpose of isolating the mistuning effect, τ is set to infinity. With these constraints Eqs. 5.13 and 5.14 become:

$$\dot{\theta}_x = \frac{\delta N}{F_m}\phi_y \tag{5.15}$$

$$\dot{\theta}_y = -\frac{\delta N}{F_m}\phi_x \tag{5.16}$$

Note that the sinusoidal terms, $\delta N/F_m$, in Eqs. 5.13 and 5.14 and the mistuning bias drift components in Eqs. 5.15 and 5.16 diminish as δN goes to zero—thus, the importance of running the gyroscope at a "tuned" speed.

An additional drift rate is introduced in a closed-loop mode. This drift rate is caused by the misalignment of the electrical pickoff nulls with respect to the instrument null. In a closed-loop mode, the rotor axis is aligned relative to the electrical nulls. This induces constant rotor offset angles, ϕ_x and ϕ_y. The offset angles, as shown by differentiating Eqs. 5.13 and 5.14 at time=0 and setting $\delta N=0$, produce drift rates of:

$$\dot{\theta}_x = \frac{\phi_x}{\tau} \tag{5.17}$$

$$\dot{\theta}_y = \frac{\phi_y}{\tau} \tag{5.18}$$

The combined expressions for error rates due to mistuning and rotor offset angles are:

$$\dot{\theta}_x = \frac{\phi_x}{\tau} + \frac{\delta N}{F_m}\phi_y \tag{5.19}$$

$$\dot{\theta}_y = \frac{\phi_y}{\tau} - \frac{\delta N}{F_m}\phi_x \tag{5.20}$$

These relationships show the effect and influence of rotor offset angles and shaft speed on the magnitude of bias drift.

5.2.5 Figure of Merit and Gyroscope Time Constant

The figure of merit (F_m) is the ratio of the rotor to gimbal inertias. For an n^{th} gimbal configuration, the figure of merit is[5]:

$$F_m = \frac{C + \sum_1^n A_n}{\sum_1^n (A_n + B_n - C_n)} \tag{5.21}$$

where:

A, B, C = inertias of the rotor about principal axes x', y', z' ($gm\text{-}cm^2$)

A_n, B_n, C_n = inertias of the n^{th} gimbal about principal axes x_n, y_n, z_n ($gm\text{-}cm^2$)

This gyroscope constant is a function of instrument design and is controlled by the diameter of the rotor. Equations 5.15 and 5.16 show that a large figure of merit is required to reduce drift uncertainties due to mistuning errors, thereby necessitating a relatively large instrument size. The figure of merit can be determined experimentally by the relation:

$$F_m = \frac{T_1 T_2 (\delta N_1 - \delta N_2)}{2\pi (T_1 - T_2)} \tag{5.22}$$

where:

T_1, T_2 = period of decaying oscillation for the mistuned shaft speed 1 and 2, respectively (s)

$\delta N_1, \delta N_2$ = the difference frequency between a referenced shaft speed and two mistuned shaft speeds 1 and 2, respectively (Hz)

In addition, the drift performance is a function of the gyroscope time constant (τ) as shown in Eqs. 5.17 and 5.18. The time constant is proportional to the rotor inertia and gimbal damping[5] as shown by:

$$\tau \approx \frac{I}{nD} \tag{5.23}$$

where:

$$I = 1/2\,(A + B + \sum_{1}^{n} A_n)$$

D = gimbal damping coefficient (due to air, eddy currents, etc,)

n = number of gimbals

(The damping coefficient due to rotor drag has been neglected.)

This inertia-damping ratio is determined in the instrument design and fabrication where τ is made large, so that offset-angle effects on drift performance are minimized.

5.3 TEST FACILITY

The test apparatus (Fig. 5.3-1) consists of a gyroscope rate table and a two-axis, Leitz dividing head. A block diagram illustrating the console and data-acquisition system adapted for supporting and monitoring the Teledyne instrument is shown in Fig. 5.3-2. On-line programs were written specifically for this instrument. These programs give misalignment angles, drift coefficients, and torquer stabilities and variations with rate. This facility provided the convenience of unattended long-term testing with automatic data processing. In addition, the computers simplified data handling, improved test accuracy, and displayed the data immediately after its collection.

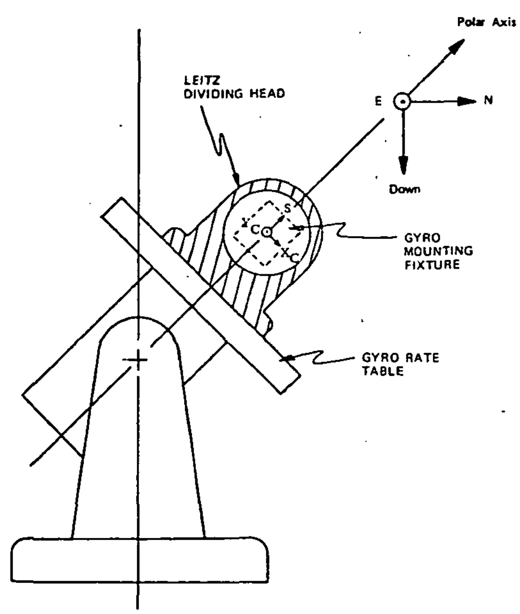

Fig. 5.3-1 Teledyne SDG:Test Apparatus

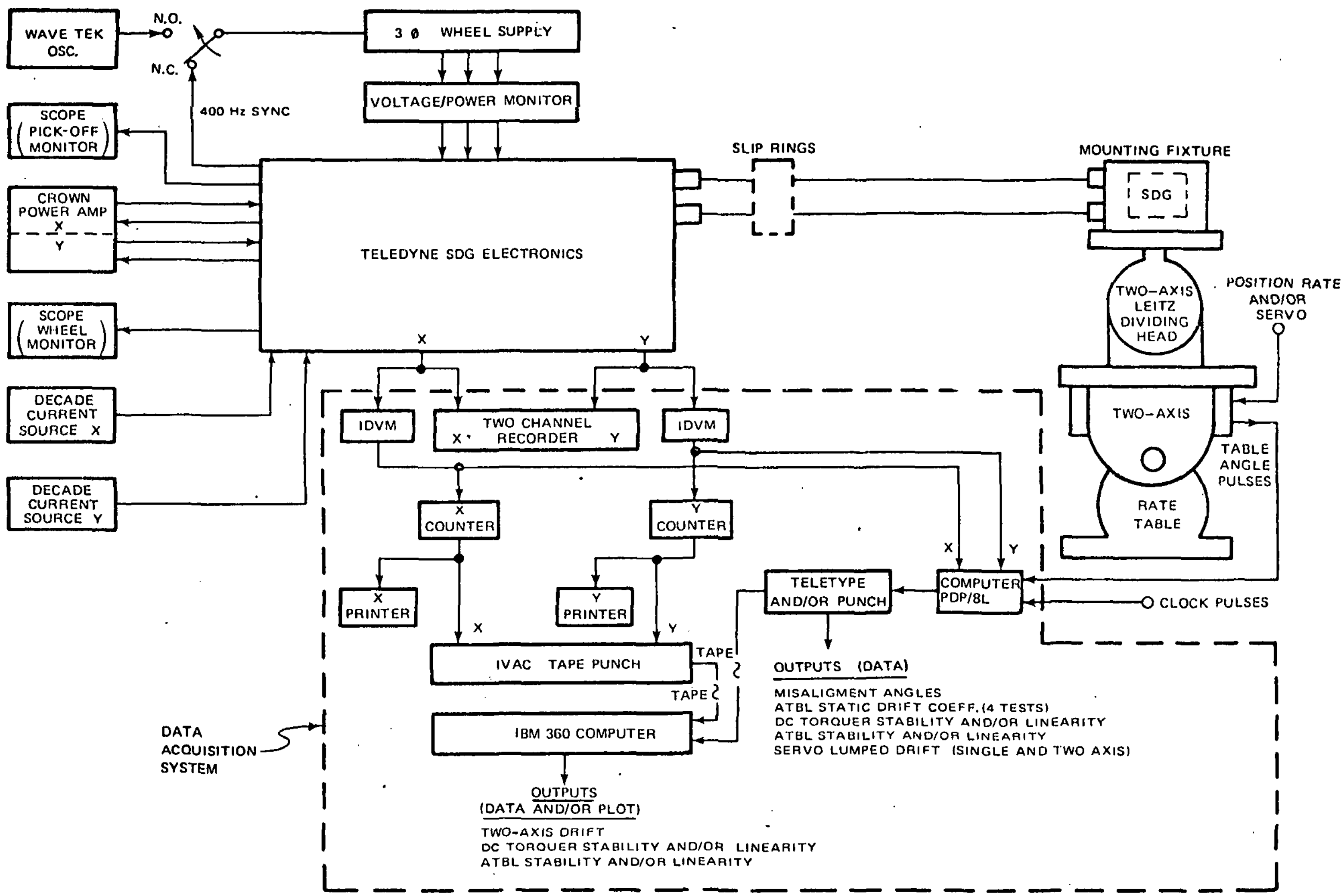

Fig. 5.3-2 Teledyne SDG: Test Setup and Data Acquisition System

5.4 TEST RESULTS

The tests run on the Teledyne gyroscope are described in this section. The measurements include:

1. Determination of the tuned speed
2. Offset angle adjustment
3. Determination of the figure of merit and the gyroscope time constant
4. Analog torque-to-balance loop calibration
5. Gyroscope drift performance
   a. Single-axis
   b. Two-axis
   c. Drift, line-voltage correlation
   d. Drift versus temperature
6. Bias and acceleration drift coefficients
7. Torque generator sensitivity
   a. Sensitivity measurement
   b. Stability
   c. Change with applied dc
8. Constant-rate scale factor
   a. Stability
   b. Scale factor versus rate

5.4.1 Measurement of the Tuned Speed

Figure 5.4-1 shows the rotor response after the torque-to-balance loop was opened (uncaged), as monitored by the demodulated pickoff outputs, for a shaft speed of 97 r/s. The decaying sinusoid indicates rotor oscillation resulting from a mistuned condition after an initial offset angle was induced. The period ($T \approx 114$ s) is a measure of the mistuning. Figure 5.4-2 is a similar test for a shaft speed of 100 r/s. The absence of the periodic sinusoid indicates a tuned condition for a shaft angular velocity of 100 r/s.

5.4.2 Offset Angle Adjustment

The rotor offset angles were minimized by adjustment of a pickoff dummy director on the Teledyne loop closure electronics. The offset angles were adjusted such that the open-loop pickoff nulls were coincident with the closed-loop pickoff nulls for zero input-axes rates.

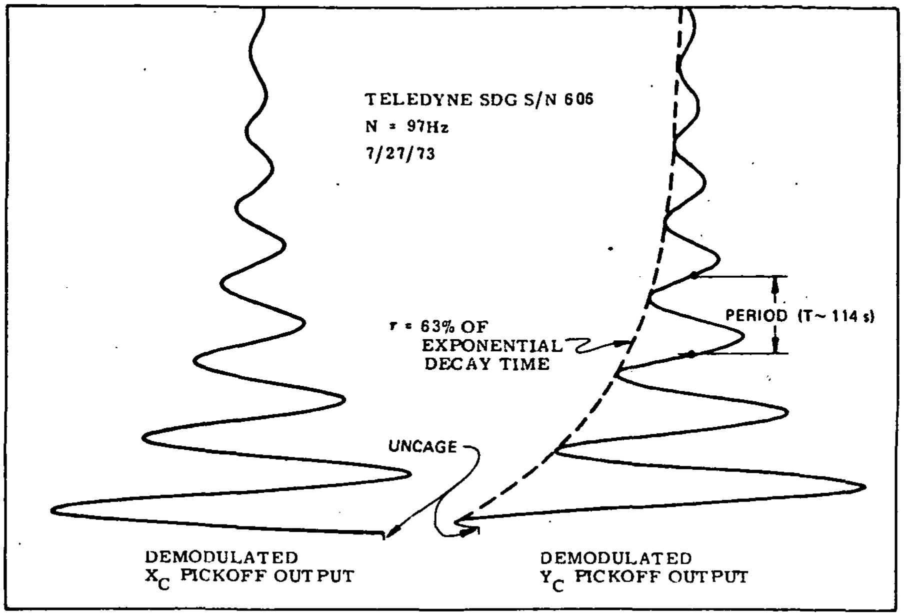

Fig. 5.4-1 Teledyne SDG: Mistuned Rotor Response

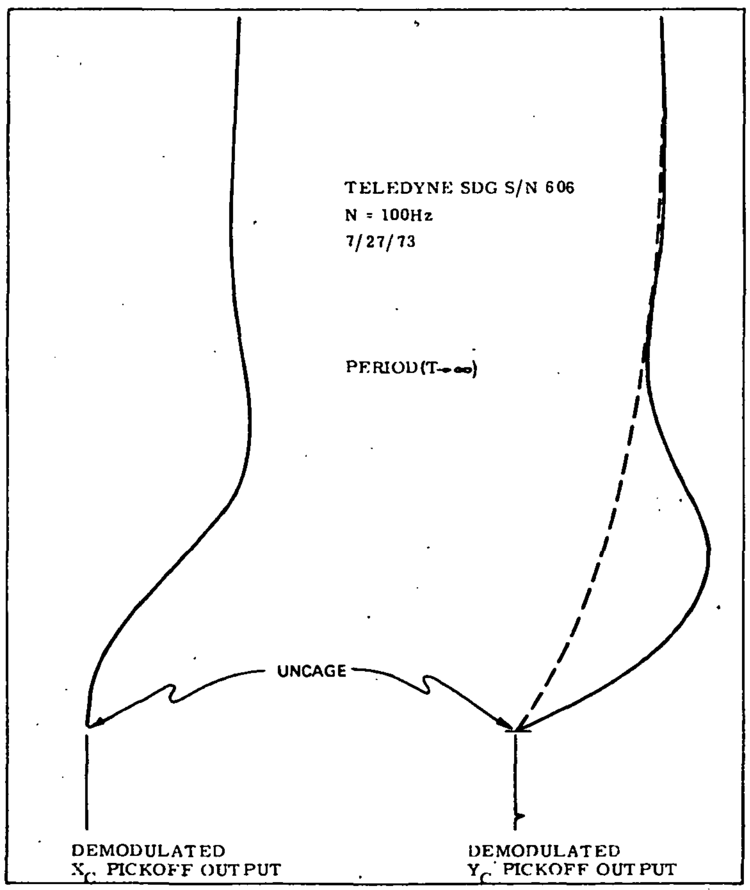

Fig. 5.4-2 Teledyne SDG: Tuned Rotor Response

5.4.3 Figure of Merit and Gyroscope Time Constant

The figure of merit and the gyroscope time constant were experimentally determined. Comparison of these test results with Teledyne data provided an additional check of instrument integrity. In these tests, the instrument's shaft speed was detuned by various selected frequencies. The figure of merit (F_m) was then determined from δN and the period (T) of the decaying sinusoid as monitored from the demodulated pickoff outputs. The tests indicated the figure of merit to be in the range of 310 to 327. The nominal figure of merit specification for this unit was 320.

The gyroscope time constant (τ) was determined from the detuning tests. Figure 5.4-3 shows that the time constant for this instrument was 178 seconds. The nominal time constant specification is 150 to 200 seconds.

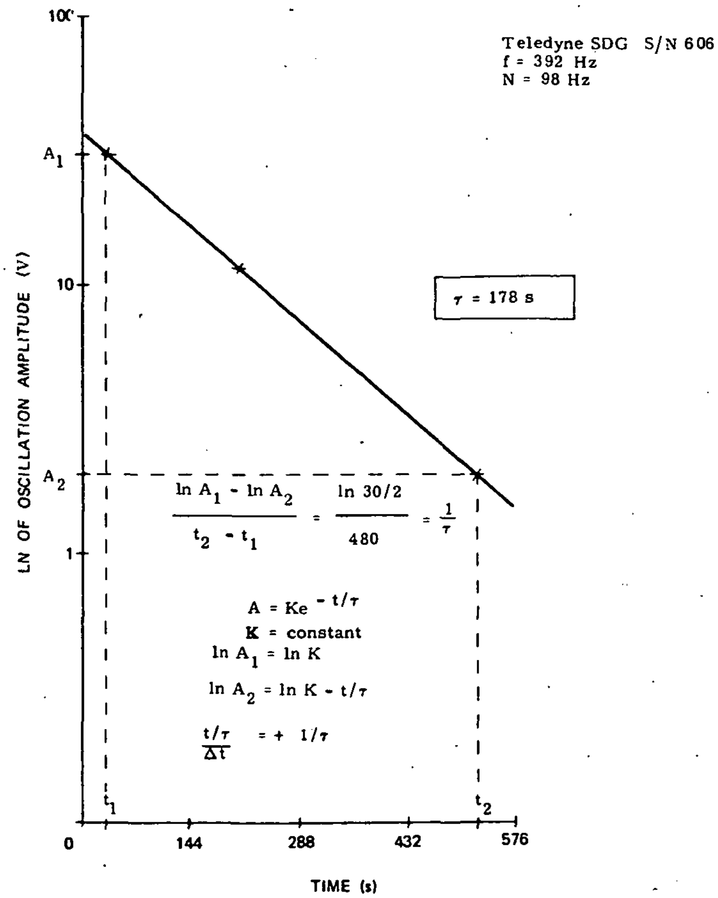

Fig. 5.4-3 Teledyne SDG: Time Constant

5.4.4 Analog Torque-to-Balance Loop Calibration

The calibration of both analog torque-to-balance loops (ATBL) was checked. For these tests the drift rates indicated by the ATBL readouts were compared with independent inertial reference servo measurements. The loop calibrations were also compared with earth-rate inputs. In addition, by use of the relationship

$$\omega_{IA} = S_{TG}\, I,$$

where:

ω_{IA}	= input axis rate (deg/h)
S_{TG}	= torquer sensitivity (deg/h/mA)
I	= torquer current (A)

the input-axis rate was determined. The measurements showed that the two-axis ATBL had a calibration error of approximately 5 percent.

5.4.5 Analog Torque-to-Balance Gyroscope Drift Performance

All drift performance tests were performed in an analog torque-to-balance mode.

5.4.5.1 Single-Axis Drift Stability. Figure 5.4-4 shows a 64-hour drift stability test with the $+X_C$ axis oriented horizontal-northwest. The drift stability was typically 0.01 deg/h with occasional changes in drift of 0.022 deg/h. There were three intervals in a quiescent environment when the drift was stable to 0.002 deg/h.

5.4.5.2 Two-Axis Drift Stability. A fifteen-hour, two-axis drift stability with the $+X_C$ axis oriented horizontal-north and the $+Y_C$ axis vertical-up is shown in Fig. 5.4-5. The standard deviation in drift for the $+X_C$ axis and the $+Y_C$ axis was 0.014 deg/h and 0.012 deg/h, respectively. The $+X_C$ axis drift showed a slope of -0.001 deg/h, whereas the slope of the $+Y_C$ axis drift was approximately zero. The $+X_C$ axis drift was essentially a mirror image of the $+Y_C$ axis drift. The linear correlation coefficient for this test was -0.914. The X_C versus Y_C drift slope was -1.081 with a sigma of 0.0059 deg/h. A forty-two-hour, two-axis drift stability yielded similar results.

5.4.5.3 Drift Stability, Line Voltage Correlation. Figure 5.4-6 is a seventeen-hour, single-axis drift stability test with $+X_C$ oriented vertical-up ($+Y_C$ horizontal-north), and a time sequenced plot of the deviation in line voltage supplied to the Teledyne

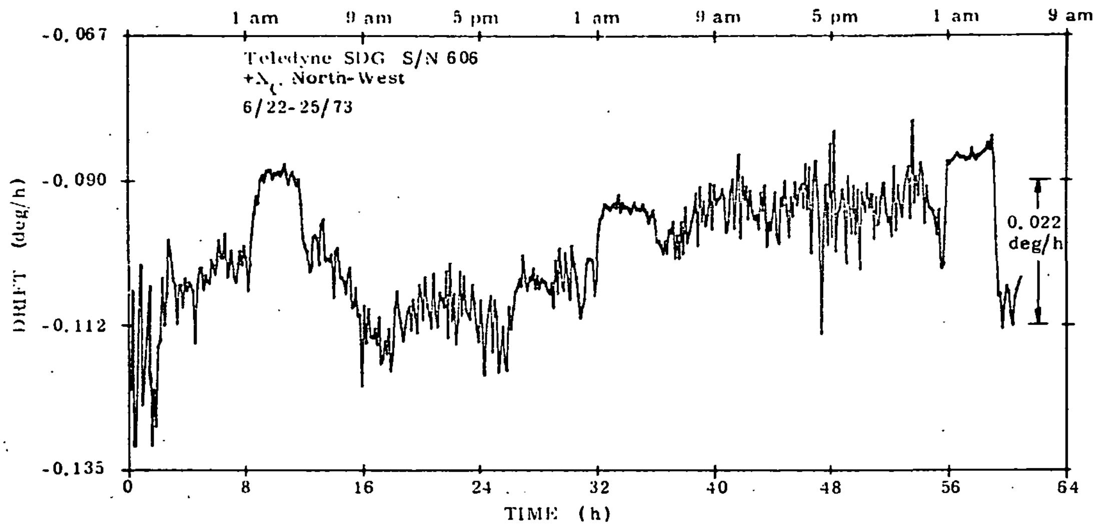

Fig. 5.4-4 Teledyne SDG: Single-Axis Drift Stability

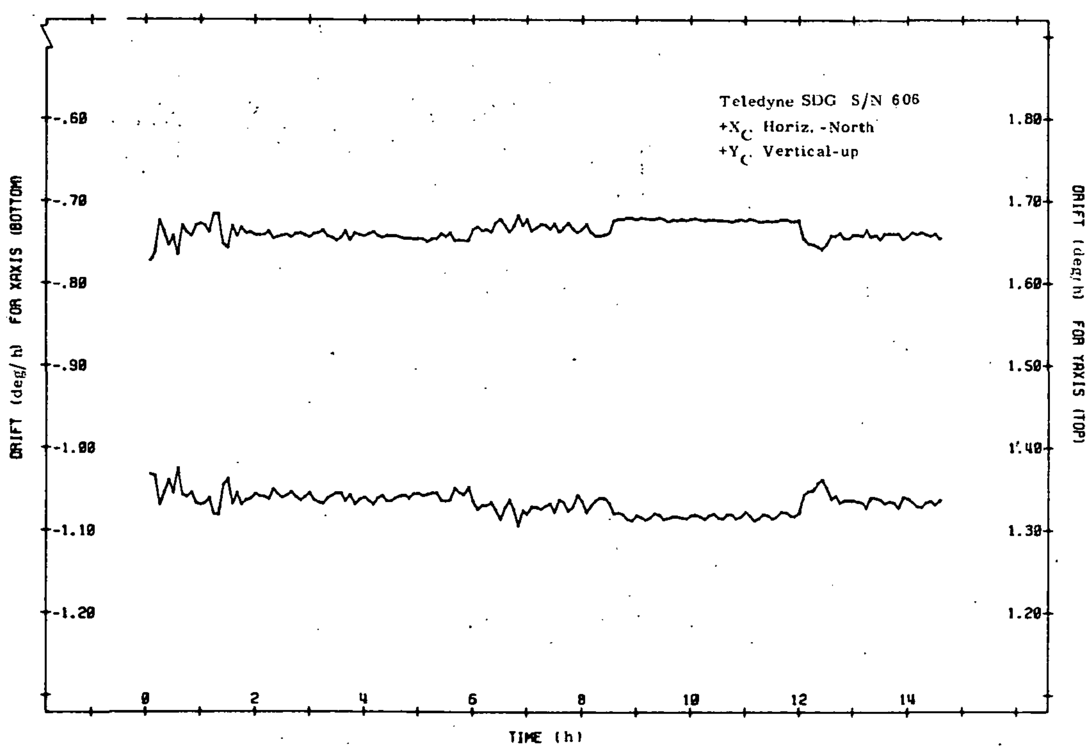

Fig. 5.4-5 Teledyne SDG: Two-Axes Drift Stability

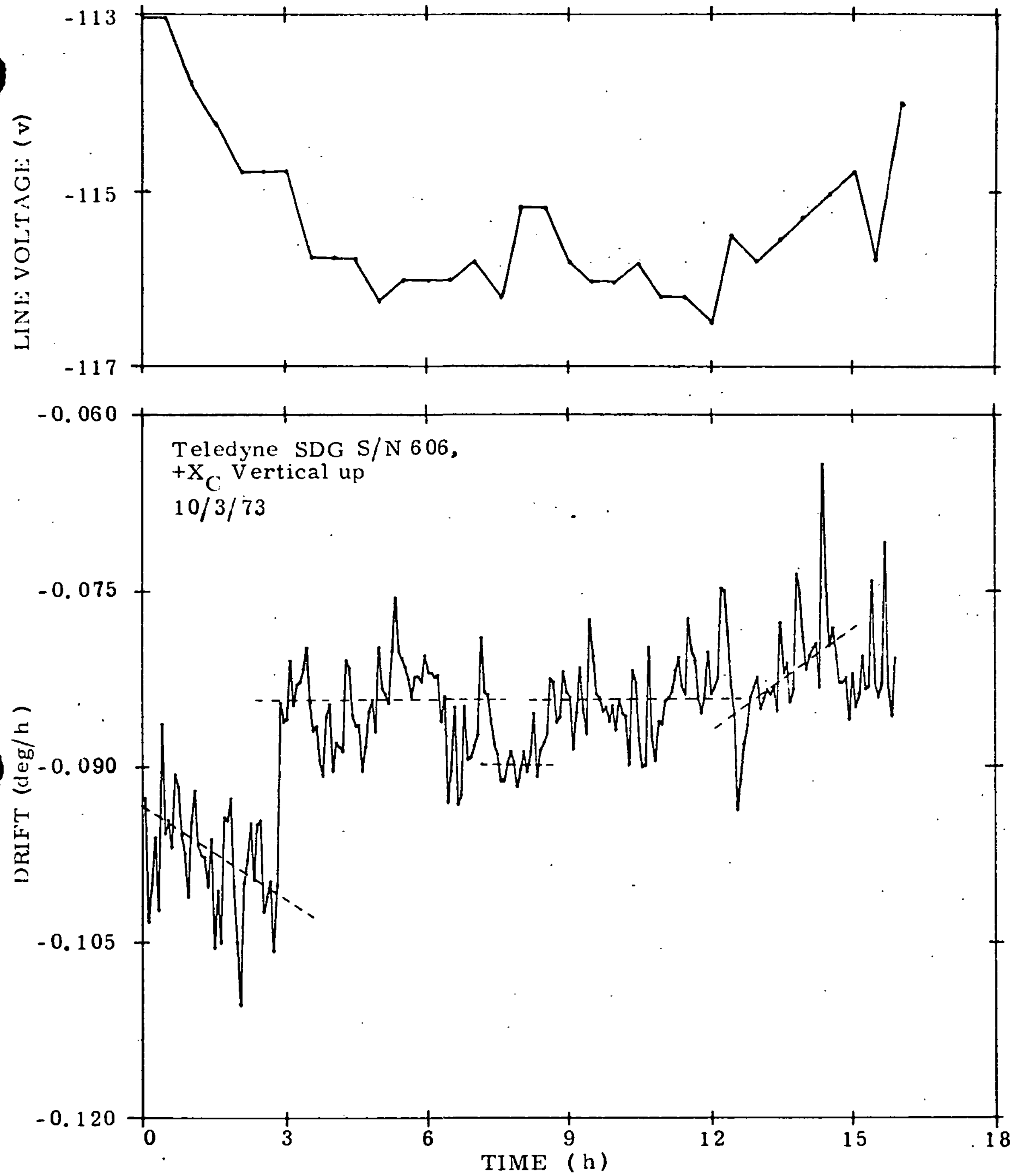

Fig. 5.4-6 Teledyne SDG: Drift Stability, Line-Voltage Correlation

test equipment. Note the correlation between drift amplitude and line voltage amplitude with the exception of the step change in drift at three hours of elapsed test time. This test showed a drift sensitivity to the ac line of approximately 0.01 deg/h/V.

5.4.5.4 Drift Performance versus Temperature. The unit, when mounted in its 5.5 cubic inch "heat-sink" block, as required by Teledyne for performance tests, showed no apparent transient or change in drift from a cold turn-on (wheel off condition) to a stabilized operating condition. Nor did it show any response to limited environmental changes in temperature ($\pm 2^{o}$F). The unit's performance as a function of temperature when removed from this block is unknown.

5.4.6 Bias and Acceleration-Sensitive Drift Measurement

Static multiple position tests were performed in the analog rebalance mode. These tests measured the drift coefficients, torquer sensitivities, anisoelastic coefficient, and gyroscope misalignment angles tabulated in Table 5.4-I.

The Teledyne decade current-source method (Fig. 5.4-7), previously used to obtain the drift terms, was abandoned due to the large inaccuracies in the measurements. An alternate method of inserting a precision resistor in series with the torque coil and measuring the voltages with an accurate meter was implemented. This alternate technique improved the accuracy of the measurements, however it was not adequate to determine the actual instrument performance. Some gyroscope orientations, in an earth-rate environment, require current measurements to be made that are less than a microampere. These measurement techniques had insufficient precision to obtain measurement repeatability of these magnitudes, thus the spread in the parameters in Table 5.4-I.

The static tests were also run with and without the offset angle compensations, so that offset angle contributions on bias drift (BX and BY) could be isolated. The tests, incorporating this offset angle compensation, are denoted by an asterisk (*) in Table 5.4-I.

The bias and g-sensitive drift magnitudes, without offset angle compensation, were less than 2.0 deg/h and 0.5/h/g, respectively, and showed a long-term peak-to-peak spread of less than 0.2 deg/h and 0.1 deg/h/g.

The $+X_C$ and $+Y_C$ bias drift measurements, with offset angle compensation, deviated from the uncompensated tests by approximately 0.75 deg/h and 5.0 deg/h,

Table 5.4-I

Static Drift Coefficients

	Date		$S_{TG(X)}$	$S_{TG(Y)}$	α	β	A	BX	BY	MX	MY	QX	QY	M	Q
			deg/h/mA	deg/h/mA	mrad	mrad	deg/h/g^2	deg/h	deg/h	deg/h/g	deg/h/g	deg/h/g	deg/h/g	deg/h/g	deg/h/g
SA Vertical	7/5/73		203.22	203.50	-1.044	-1.938		-1.774	0.551						
	10/1/73		203.00	204.30	1.838	-4.201		-1.642	0.531						
	10/11/73		204.12	204.49	0.920	-0.367		-1.610	0.532						
	10/11/73	*	203.74	204.68	1.842	-3.483		-0.982	-5.619						
SA Horizontal	7/5/73							-1.681	0.617	-0.127	-0.096	-0.418	-0.396		
	10/1/73							-1.639	0.575	-0.047	-0.131	-0.363	-0.391		
	10/11/73							-1.594	0.532	-0.084	-0.088	-0.413	-0.418		
		*						-0.734	-5.363	0.028	0.004	-0.474	-0.346		
SA Tumble About E-W	7/5/73						0.074	-1.783	0.624					0.014	-0.559
	10/1/73						0.051	-1.756	0.559					0.011	-0.626
	10/11/73						0.113	-1.725	0.565					-0.005	-0.649
		*					0.133	-0.734	-5.227					0.063	-0.635
SA Polar	7/5/73							-1.762	0.546	-0.130	-0.128	-0.458	-0.466		
	10/1/73							-1.594	0.562	0.005	-0.034	-0.426	-0.415		
	10/11/73							-1.587	0.501	-0.104	-0.103	-0.484	-0.443		
		*						-0.876	-5.526	-0.105	-0.019	-0.538	-0.402		

*Pickoff offset compensation IN

$\left.\begin{matrix} S_{TG(X)} \\ S_{TG(Y)} \end{matrix}\right\}$ Torque Generator Sensitivity

$\left.\begin{matrix} BX \\ BY \end{matrix}\right\}$ Bias Drift

α = X Torquer-Case Misalignment Angle

$\left.\begin{matrix} MX \\ MY \end{matrix}\right\}$ SA Mass Unbalance

$\left.\begin{matrix} QX \\ QY \end{matrix}\right\}$ Quadrature SA Mass Unbalance

β = Y Torquer-Case Misalignment Angle

M - SA Mass Unbalance

Q - Quadrature SA Mass Unbalance

A - Anisoelastic Coefficient

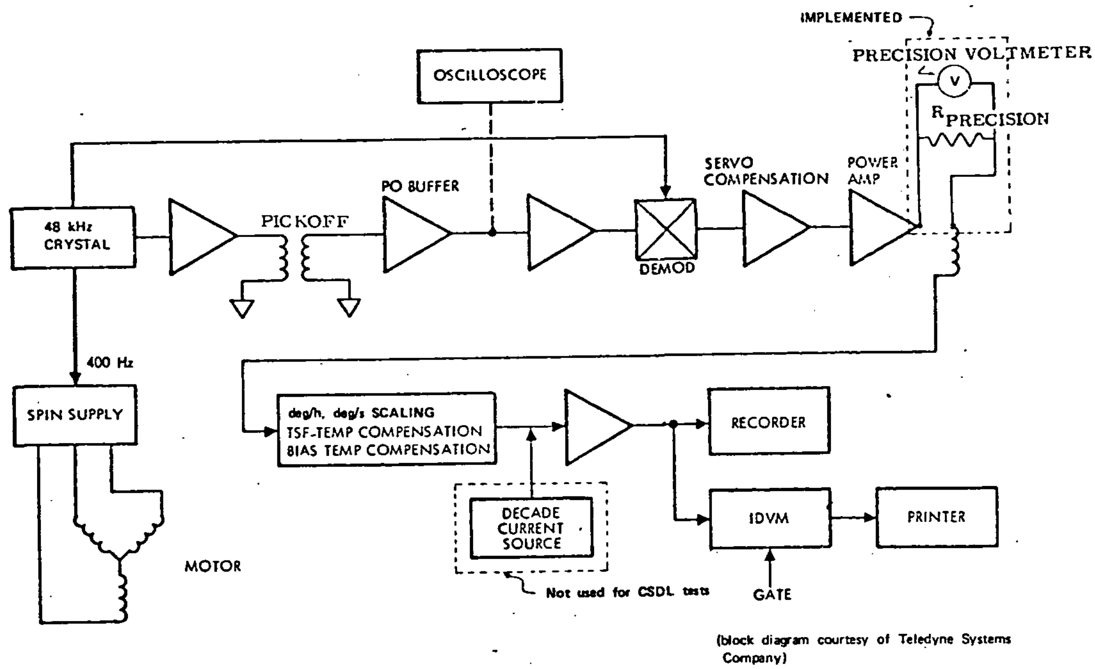

Fig. 5.4-7 Static Drift Measurement Technique

respectively. The offset angle compensation also changed the indicated torquer-case misalignment angles which are used in the computation of the remaining parameters in Table 5.4-I. This indicated that other responses, in addition to bias changes within the instrument, occur as a result of the offset angle compensation. The influence of offset angle compensation and its entire effect on the instrument, needs further investigation.

5.4.7 Torque Generator dc Sensitivities

The torque generator (TG) dc sensitivity was measured in an inertial reference mode. In that mode, the servo loop drives the table to oppose earth rate, gyroscope drift and dc inputs. The dc torque generator sensitivity is then calculated after the effects of gyroscope drift and earth-rate inputs are removed.

5.4.7.1 Torque Generator Sensitivity Measurement. The dc torque generator sensitivities $S_{TG(X)}$ and $S_{TG(Y)}$ measured were:

$$S_{TG(X)} = 203.33 \text{ deg/h/mA}$$

$$S_{TG(Y)} = 203.55 \text{ deg/h/mA}$$

5.4.7.2 Torquer Stability and Change with Applied dc. The dc stabilities and changes in sensitivity with applied dc of the torquers were determined. These measurements were performed on the instrument itself, independent of the rebalance loops. For the stability tests, a constant current of 100 mA was applied to torque coil while the gyroscope was servoed in an inertial reference mode. Figures 5.4-8 and 5.4-9 show nineteen-hour X torquer and thirty-two-hour Y torquer stability tests, respectively. The torquer sensitivities both showed a transient of 150 ppm which settled out after ten hours to a peak-to-peak stability of approximately 30 ppm.

Figures 5.4-10 and 5.4-11 show torque generator sensitivity change with applied dc of the X and Y torquers, respectively. These tests were run for applied direct currents of ±25 to ±150 mA. This applied current range corresponds to an input-rate range of ±0.025 to ±0.1 rad/s. Both $S_{TG(X)}$ and $S_{TG(Y)}$ showed a deviation of approximately 150 ppm for this limited rate range. The torquer sensitivity change with applied dc for higher torquer currents was not measured. Two amperes of torquer current was required to obtain input rates of approximately 100 deg/s. Accurate constant-current sources which exceeded 150 mA were not immediately available. The deviation in dc torquer sensitivity for an applied current range of 0 to ±2 A and/or 0 to ±100 deg/s should be determined.

5.4.8 Scale Factor Tests

Constant input rates were applied to the gyroscope and the analog rebalance loop response (scale factor) was monitored. Figure 5.4-12 shows a sixteen-hour scale factor (SF) stability run. For this test a constant rate of 0.025 rad/s was applied about the $+X_C$ input axis and the average SF was measured over ten table revolutions. An average point-to-point excursion of approximately 100 ppm was obtained. There was a downward trend in SF of -40 ppm/h.

Figure 5.4-13 is a plot of SF stability after an abrupt change in input rate. The SF was initially measured at an input rate of 0.25 rad/s and sampled for approximately 150 minutes. The applied $+X_C$ input-axis rate was then changed to 0. 75 rad/s. The scale factor showed a transient which settled out after 1.5 hours at -2300 ppm relative to its previous amplitude.

Figure 5.4-14 shows similar and repeatable SF transients and deviations in amplitude which were caused by alternating the applied input rate to the gyroscope between 0.25 and 0.75 rad/s. The scale factor transients and deviations were apparently due to power dissipation effects in the instrument and improper adjustment of the scale factor temperature compensation circuits.

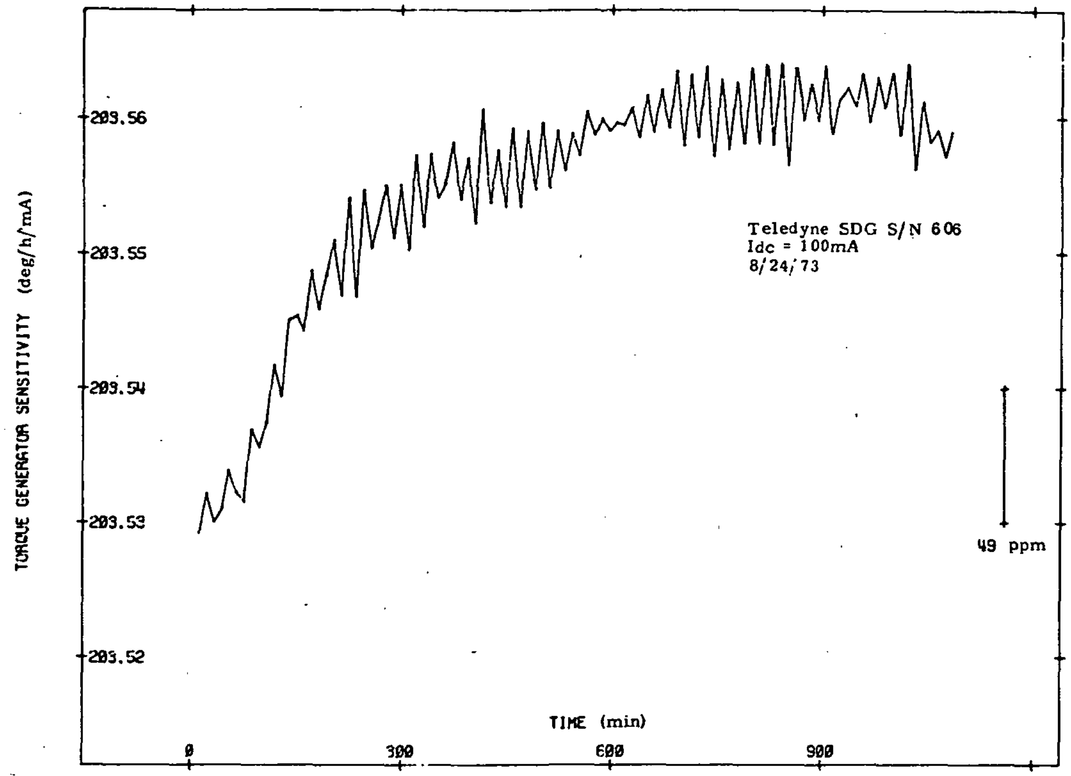

Fig. 5.4-8 Torque Generator Sensitivity (X_T)

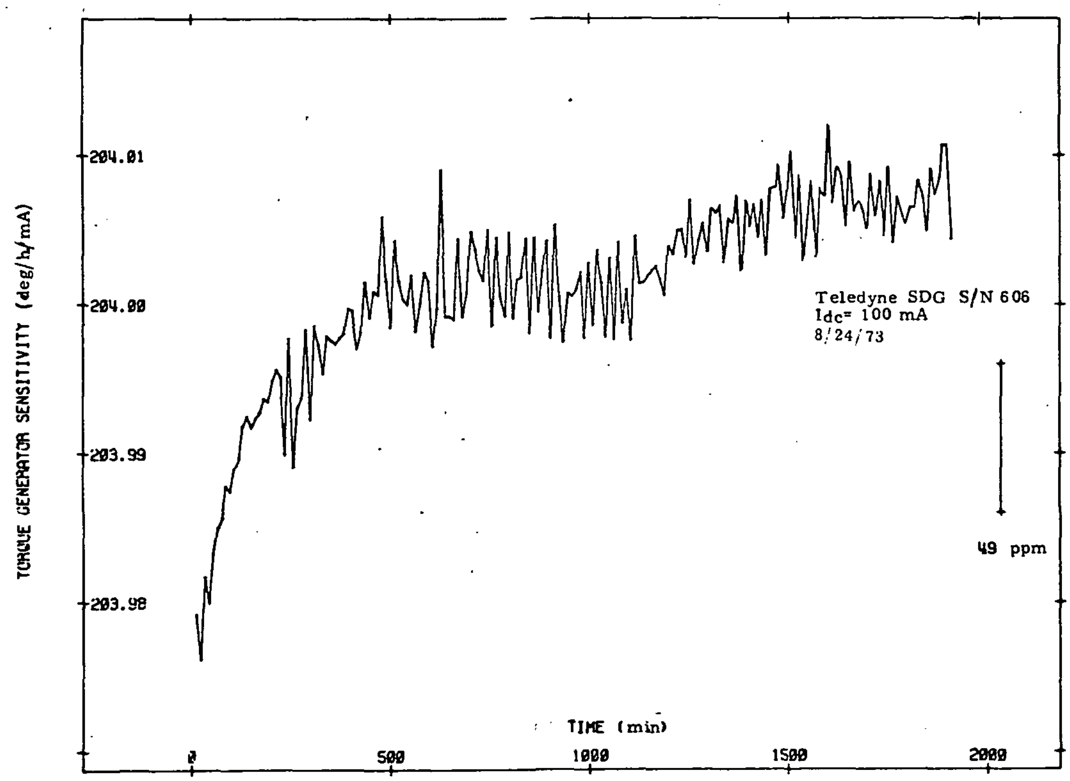

Fig. 5.4-9 Torque Generator Sensitivity (Y_T)

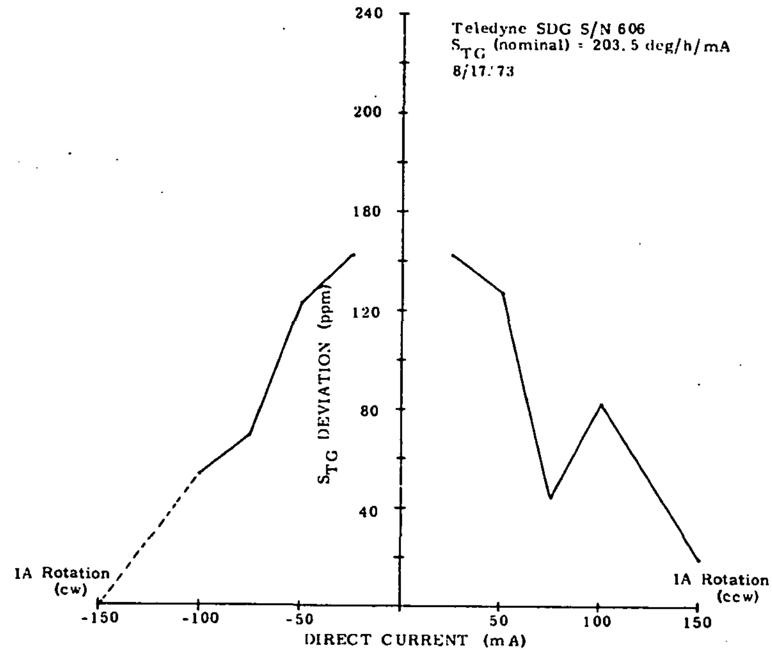

Fig. 5.4-10 Torquer Sensitivity Change with dc (X_T)

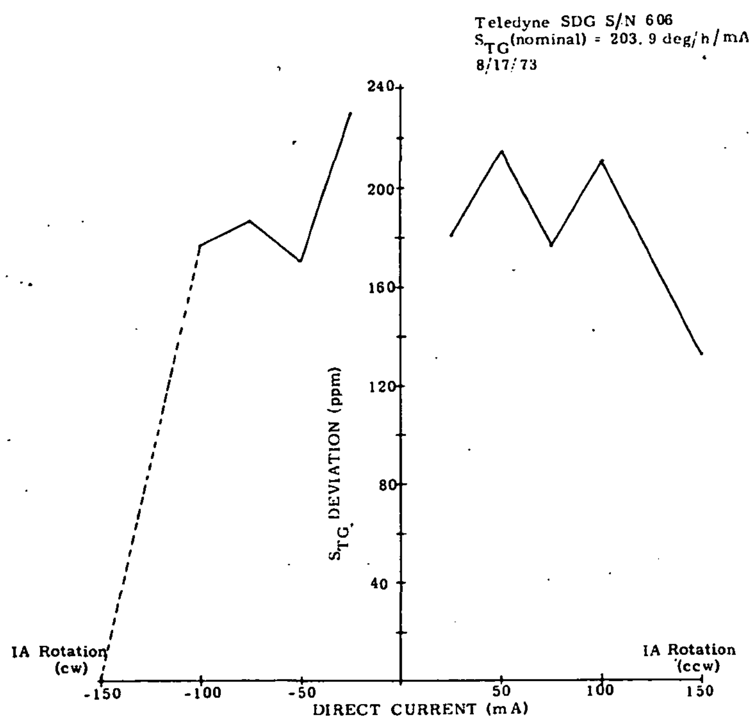

Fig. 5.4-11 Torquer Sensitivity Change with dc (Y_T)

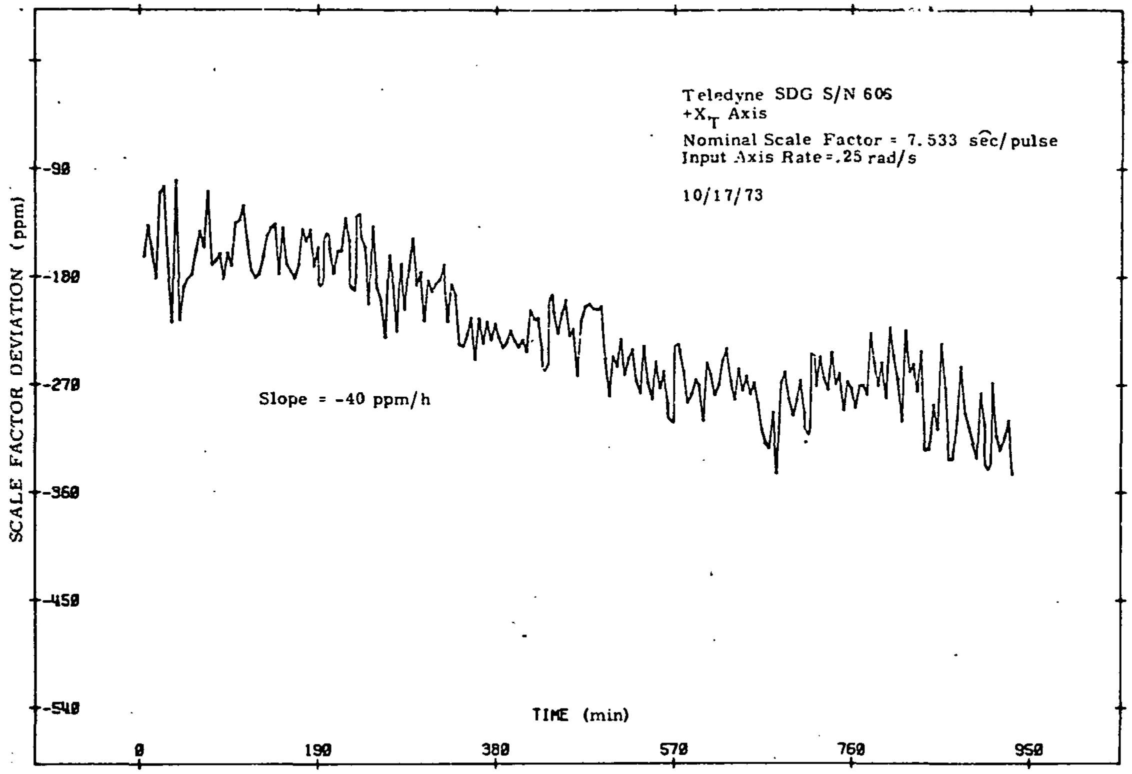

Fig. 5.4-12 Scale Factor Stability

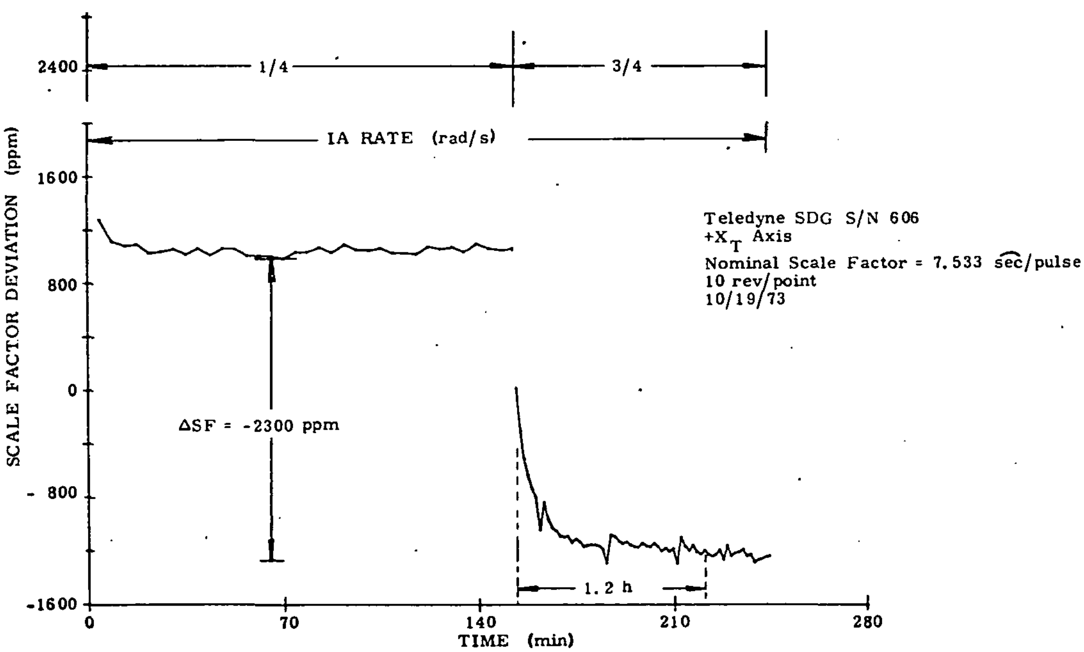

Fig. 5.4-13 Scale Factor Deviation after IA Rate Change

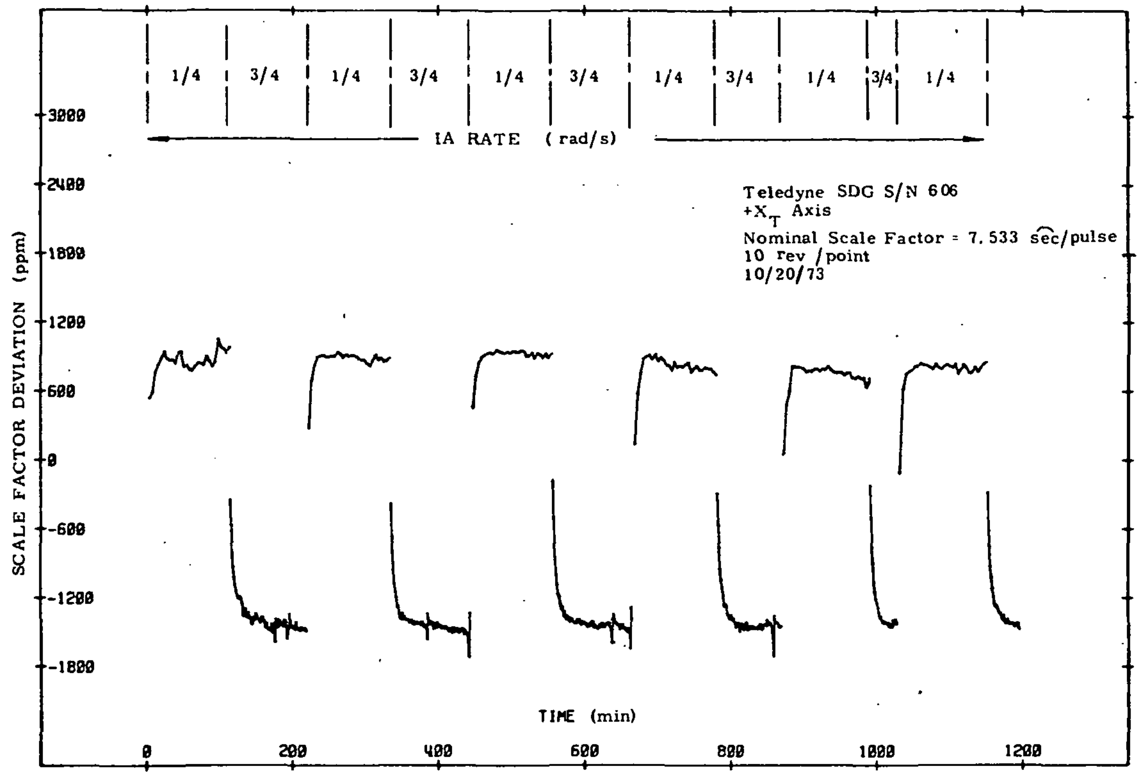

Fig. 5.4-14 Repeatability in Scale Factor after IA Rate Changes

5.5 CONCLUSIONS AND RECOMMENDATIONS

5.5.1 Conclusions

1. The instrument performed within the specifications for a static environment.
   a. The typical drift stability of 0.01 deg/h agreed with past performance. In addition, stable drift data of 0.002 deg/h was obtained in a controlled environment.
   b. Bias and g-sensitive coefficient amplitudes were less than 2.0 deg/h and 0.5 deg/h/g respectively, and demonstrated long-term repeatabilities of better than 0.2 deg/h and 0.1 deg/h/g.
2. The torquers exhibited a sensitivity to input power. Ten-hour settling transients of 150 ppm resulted from the application of 100 mA to the torque coil.
   a. After settle-out, the torquer sensitivities were stable to ±20 ppm.
   b. The torquer sensitivities changed by 150 ppm for a limited dc input range of ±25 mA to ±150 mA, which corresponds to an input rate range of ±0.025 to ±0.1 rad/s.

3. The SF measurement accuracy was limited by the analog torque-to-balance loop and read-out mechanization.
   a. The digital readout system, which was recommended by Teledyne, employed Integrating Digital Voltmeters (Model No. HP-2401A). These voltage-to-frequency converters were used to perform the analog-to-digital conversion. The repeatability of these meters is 100 ppm.
   b. Both scale-factor as well as dc torquer sensitivity tests showed that the torque generator was sensitive to power dissipation. This apparent TG thermal sensitivity is compensated external to the instrument, by Teledyne, in the analog rebalance loop. These compensation circuits may not have been properly adjusted by Teledyne. CSDL did not attempt to optimize the Teledyne circuitry.
4. The high magnitude of scale factor deviation, coupled with the rate dependent transient, prohibited the performance of meaningful testing in a dynamic environment. In addition, the readout mechanization does not provide adequate accuracy to perform dynamic tests.
5. A rebalancing torquer current of 2 amperes is required for input rates of 100 deg/s. This high current corresponds to 40 watts of torquer power.

5.5.2 Recommendations

It is recommended that:

1. the rebalance loops be updated to a usable system implementation. This would include the present analog-to-digital readout conversion technique used by Teledyne in more recent deliverable systems.
2. the performance of the instrument (i.e., thermal sensitivity) upon removal from the 5.5 cubic in. heat sink be investigated.
3. an improved technique be developed for measuring static drift coefficients since the present method does not have the required precision.
4. the loop closure electronics be adequately isolated from the ac line by appropriate input filtering.
5. the unit be mated with a pulse torque-to-balance loop for low rate applications. This would provide direct digital readout and accurate scale factor resolution. Pulse torquing the unit for high rate strapdown applications is not practical due to the low torque generator sensitivities. Amperes of current would have to be switched in a high rate (1.0 rad/s) loop. This would impose a problem to the electronic designer.

REFERENCES

1. Craig, R. J., Theory of Operation and Open Loop Transfer Function of a Tuned Elastically Supported Gyroscope, Teledyne Company, June 25, 1971.
2. Teledyne Systems Strapdown Gyroscope, Teledyne Systems Company, October 15, 1971.
3. Teledyne Strapdown Inertial System, Teledyne Systems Company, October 1971.
4. Howe, E. W., Savet, P. H., The Dynamically Tuned Free Rotor Gyro, Control Engineering, June 1964.
5. Criag, R. J., Theory of Errors of a Multi-gimbal, Elastically Supported, Tuned Gyroscope, Teledyne Systems Company, May 1972.
6. Bortz, Sr. J. E., Dynamic Errors in a Tuned Flexure-Mounted Strapdown Gyro, The Analytic Sciences Corporation Interim Scientific Report TR-147-5, September 1972.

APPENDIX A

MAGNETIC SUSPENSION

This appendix presents the magnetic suspension stiffness and anisoelasticity theoretical analyses.

A.1 Magnetic Suspension Stiffness

The magnetic suspension was described in Section 2.2. This appendix develops the relationship between magnetic suspension stiffness and circuit parameters.

Defining the terms:

$$Q_0 = \frac{\omega_0 L_0}{R} \tag{A.1}$$

$$Q_1 = \frac{\omega_0 L + \omega_0 L_0 - 1/\omega_0 C}{R} \tag{A.2}$$

and a dimensionless parameter

$$f(Q) = \frac{1 + Q_1^2 - Q_0 Q_1}{(1 + Q_1^2)^2} \tag{A.3}$$

where:

Q_0	=	the quality factor of the suspension coil
Q_1	=	the overall quality factor of the circuit
L_0	=	self-inductance of the coil (H)
L	=	leakage inductance (H)
C	=	series capacitance (F)
R	=	effective resistance (Ω)
Ω_0	=	excitation frequency (rad/s)

The relationship for suspension stiffness becomes

$$\frac{dF_r}{dg} = \frac{L_0}{(g_0)^2} \frac{V^2}{R^2} f(Q) \tag{A.4}$$

where:

V	=	excitation voltage (V)
g_0	=	centered air-gap value (m)

In order to have a stable restoring force, f(Q) must be negative and Q_1 must be greater than zero. A family of curves showing the values of f(Q) as a function of Q_1, for different values of Q_0, is shown in Fig. A-1. The maximum suspension stiffness occurs near the three quarter power point, where $Q_1 = 1/\sqrt{3}$.

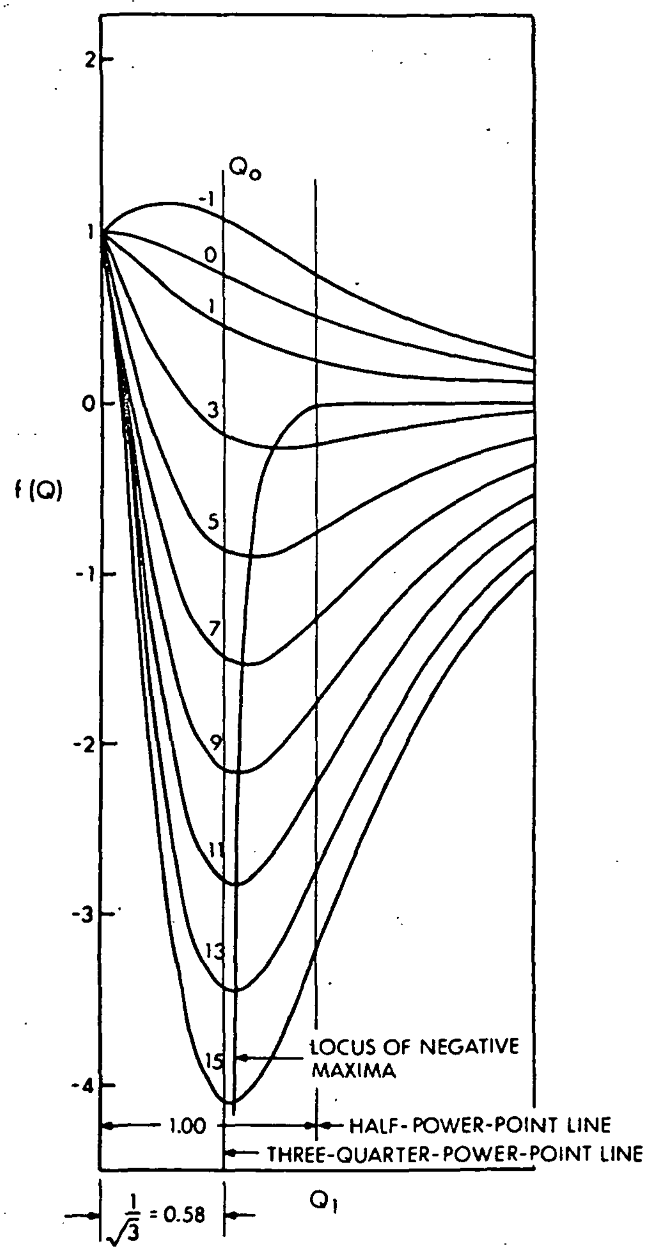

Fig. A-1 Locus of Maxima and Minima of f(Q), Shown to Enlarged Scale for $0<Q_1<2$

The normal operating point for magnetic suspension instruments is the second (inductive) half-power point, shown on the curve. This point is chosen to insure a stable suspension for all possible values of g_0, resulting from axial motion of the float.

A.2 Magnetic Suspension Anisoelasticity

Section 2.4.5 described the anisoelasticity of the 18 IRIG Mod-B magnetic suspension. In this appendix a theoretical analysis is performed to determine the change in IA alignment (about SRA) due to an unbalance in the suspension capacitor.

Figure 2.4-6 (upper-half) shows that a change of 1.82 rad/s can cause the IA alignment to change by 3.6 seconds of arc or 2 sec of arc/rad/s. After drawing a straight line between end points in Fig. 2.4-8, the corresponding slope is 24 sec of arc/rad/s. Hence, a change of 610 pF in the four capacitors indicated in Fig. 2.4-8 results in a measured change of 22 sec of arc/rad/s.

Referring to Fig. A-2 for definitions of terms, and to Reference 1 for gyroscope parameters, we find:

$$\text{Radial Stiffness} = F/d = 32 \times 10^6 \text{ dyne/cm} \tag{A.5}$$

$$\text{Distance between suspensions} = L = 5.57 \text{ cm} \tag{A.6}$$

For a rotational displacement of the float, again referring to Fig. A-2:

$$\begin{aligned}\text{Angular Displacement} &= \alpha \\ &= 2d/L \text{ (rad)}\end{aligned} \tag{A.7}$$

$$\begin{aligned}\text{Restoring Torque} &= \tau \\ &= FL/2\end{aligned} \tag{A.8}$$

$$\begin{aligned}\text{Angular Stiffness} &= \tau/\alpha \\ &= FL^2/4 \\ &= 1250 \text{ dyne-cm/sec}\end{aligned} \tag{A.9}$$

Increasing the capacitors by 610 pF or 4.35 percent decreases the stiffness by 26.5 percent.[2]

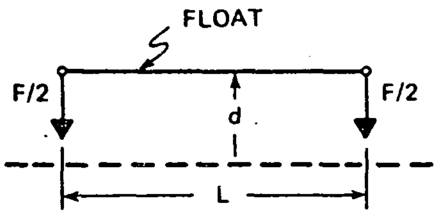

Float displaced by distance d and has restoring force F.

(a)

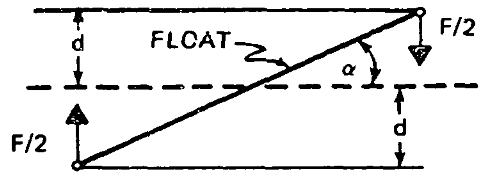

Float displaced by angle α.

(b)

Fig. A-2 Translational and Rotational Float Displacement

In Fig. A-3, we show the IA and SRA directions as well as the two principal directions denoted by 1 and 2. Let α with an axis subscript denote the component of angular displacement about that direction, and similarly let τ denote components of torque. By geometry (see Figure A-3):

$$\begin{pmatrix} \alpha_1 \\ \alpha_2 \end{pmatrix} = \frac{1}{\sqrt{2}} \begin{pmatrix} 1 & 1 \\ -1 & 1 \end{pmatrix} \begin{pmatrix} \alpha_{SRA} \\ \alpha_{IA} \end{pmatrix} \tag{A.10}$$

$$\begin{pmatrix} \tau_{SRA} \\ \tau_{IA} \end{pmatrix} = \frac{1}{\sqrt{2}} \begin{pmatrix} 1 & -1 \\ 1 & 1 \end{pmatrix} \begin{pmatrix} \tau_1 \\ \tau_2 \end{pmatrix} \tag{A.11}$$

Referring to Figs. 2.4-7, A-3 and 2.4-8, we see that the weakened suspension occurs when the ends of the float are displaced in the "2" direction. By cross products, this is the same as an angular displacement about the "1" direction. Thus, we have:

$$\begin{pmatrix} \tau_1 \\ \tau_2 \end{pmatrix} = -\left(1250 \ \frac{\text{dyne-cm}}{\text{sec}}\right) \begin{pmatrix} .735 & 0 \\ 0 & 1 \end{pmatrix} \begin{pmatrix} \alpha_1 \\ \alpha_2 \end{pmatrix} \tag{A.12}$$

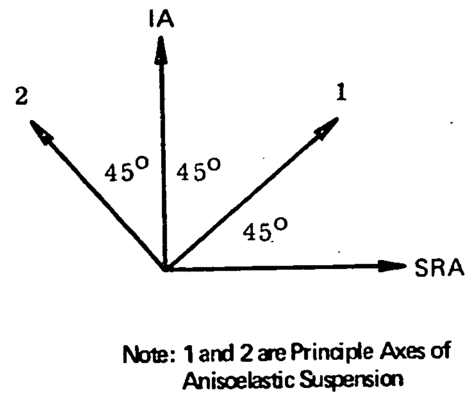

Fig. A-3 Orientation of Gyro and Suspension Axes

Multiplying out matrices,

$$\begin{pmatrix} \tau_{SRA} \\ \tau_{IA} \end{pmatrix} = -\left(625 \ \frac{\text{dyne-cm}}{\widehat{\text{sec}}}\right) \begin{pmatrix} 1.735 & -0.265 \\ -0.265 & 1.735 \end{pmatrix} \begin{pmatrix} \alpha_{SRA} \\ \alpha_{IA} \end{pmatrix} \tag{A.13}$$

and inverting,

$$\begin{pmatrix} \alpha_{SRA} \\ \alpha_{IA} \end{pmatrix} = -\left(\frac{1}{625\text{x}2.94} \ \frac{\widehat{\text{sec}}}{\text{dyne-cm}}\right) \begin{pmatrix} 1.735 & 0.265 \\ 0.265 & 1.735 \end{pmatrix} \begin{pmatrix} \tau_{SRA} \\ \tau_{IA} \end{pmatrix} \tag{A.14}$$

The wheel angular momentum is 150,000 dyne-cm-sec. If the gyroscope is given an input of 1 rad/s about the OA in the positive sense, the required suspension torque, from Fig. 2.4-8, is in the positive IA direction and its magnitude is 150,000 dyne-cm.

$$\begin{pmatrix} \tau_{SRA} \\ \tau_{IA} \end{pmatrix} = \begin{pmatrix} 0 \\ 150,000 \end{pmatrix} \quad \text{(dyne-cm)} \tag{A.15}$$

From the above, we get:

$$\begin{pmatrix} \alpha_{SRA} \\ \alpha_{IA} \end{pmatrix} = \begin{pmatrix} -21.6 \\ -14.2 \end{pmatrix} \quad (\widehat{\text{sec}}) \tag{A.16}$$

The α_{IA} is not measured by the method of this test. The α_{SRA} of 21.6 seconds of arc agrees with the measured value of 22 seconds of arc. This agreement is fortuitously good since the response curve of Fig. 2.4-8 is nonlinear.

It is important to check whether the above theory yields the correct polarity. The predicted displacement α_{SRA} is negative. From Fig. 2.4-7, the IA must move away from the OA. Figure 2.4-8 shows that for positive input about the OA, the IA does move away from the OA.

REFERENCES

1. Booth, R., 18 IRIG Mod-B Instrument Parameters, CSDL Report IC-1230, December 1969.

2. Garcia, G.E., The Effects of Variations in Working Capacitors and Frequency on 8 Pole Magnetic Suspension Microsyns, CSDL Report E-692, March 1958.

APPENDIX B
TORQUE GENERATOR POWER DISSIPATION

Part of the power output of the current source for pulse-torque electronics is dissipated in the tuning network rather than in the TG coil. The tuning makes the total power into the coil and tuning constant, but the portion dissipated as ac power in the tuning varies with the switching rate. Thus neither binary nor ternary PTE's keep dissipation in the coil constant.

As an example, consider a compensated binary loop having the TG coil tuned as in Fig. B-1. The combined load is excited with a square wave of current having a half amplitude I_s. As shown in Fig. B-2, the initial current in the tuning after switching is I_o. The voltage across the load is constant between switching times. Thus the current decays to $I_o\, e^{(-T/\tau)}$ by the next switchtime. Due to its inductance, the coil cannot change current instantaneously. At the switch time, therefore, the entire change in current, $2\, I_s$, occurs in the tuning. We have then:

$$2\, I_s = I_o + I_o\, e^{-T/\tau} \tag{B.1}$$

$$I_o = \frac{2\, I_s}{1 + e^{-T/\tau}} \tag{B.2}$$

The current during the positive transient is

$$i(t) = I_o\, e^{-t/\tau} \tag{B.3}$$

and the energy dissipated in the tuning resistor is

$$W_T = \int_0^T i^2(t)\, R\, dt \tag{B.4}$$

$$W_T = I_o^2\, R \int_0^T e^{-2t/\tau}\, dt \tag{B.5}$$

$$W_T = \frac{1}{2}\, I_o^2\, R\, \tau\, (1 - e^{-2T/\tau}) \tag{B.6}$$

Substituting Eq. B.2 into Eq. B.6 and simplifying,

$$W_T = 2\, I_s^2\, R\, \tau\, \frac{1 - e^{-T/\tau}}{1 + e^{-T/\tau}} \tag{B.7}$$

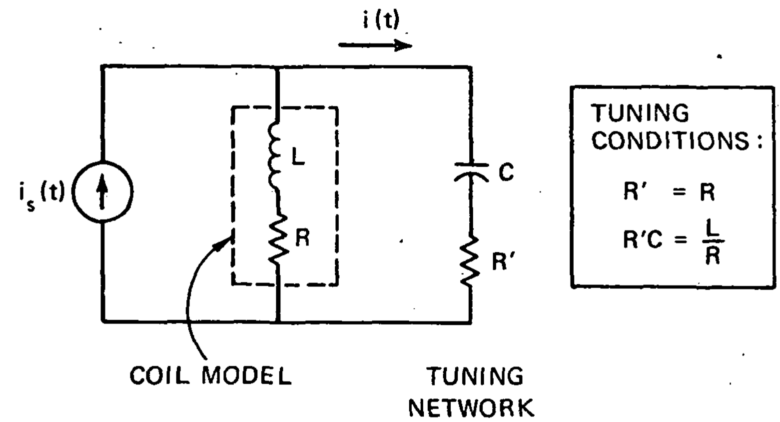

Fig. B-1 Tuning of First-Order Coil Model

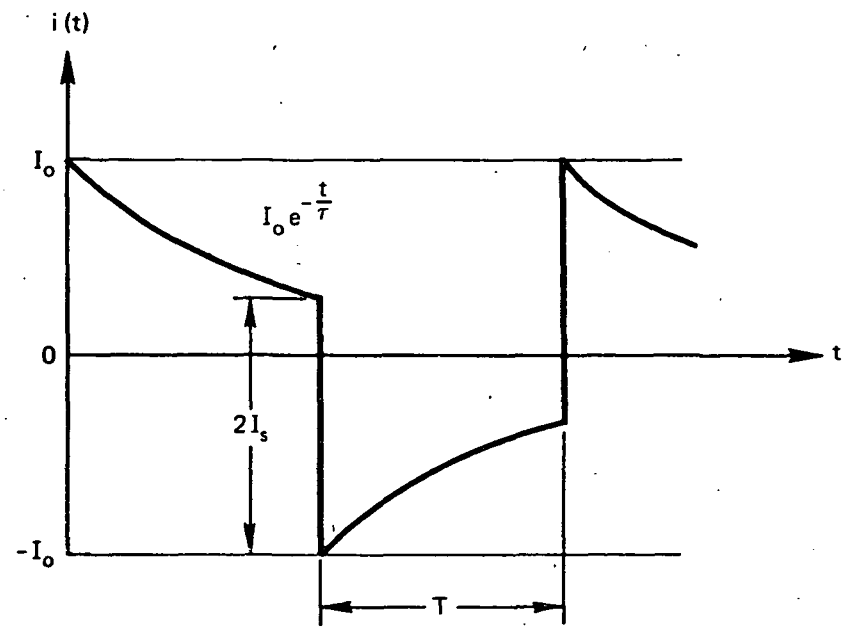

Fig. B-2 Current in Tuning Network

$$W_T = 2\, I_s^2\, R\, \tau \tanh\left(\frac{T}{2\tau}\right) \qquad (B.8)$$

During the same period, the total energy delivered by the source is

$$W_s = I_s^2\, R\, T. \qquad (B.9)$$

The ratio of energy dissipated in the tuning to the total energy delivered is:

$$\eta = \frac{2\tau}{T} \tanh\left(\frac{T}{2\tau}\right) \qquad (B.10)$$

for a symmetric square wave of current applied. This function is shown in Fig. B-3. It shows that as $\frac{2\tau}{T}$ approaches zero less power is dissipated in the tuning network and move power in the torque coils. The finite time constant (τ) results in energy dissipated in both the torquer and tuning networks. The energy dissipated in the tuning networks means that a binary loop does not supply constant power to the torque coils and a power dependent nonlinearity would be expected from the torque generator.

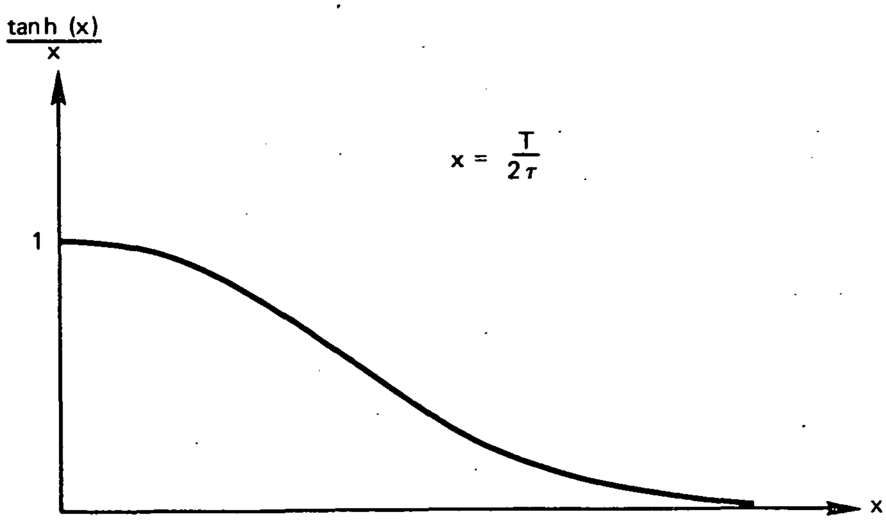

Fig. B-3 Ratio of Energy Dissipated in Tuning

END